The Role of Adaptor Proteins in the Dynamics of Clathrin Coat Disassembly

by

Katherine Mary Wood

A thesis submitted in partial fulfilment of the requirements for the degree of

Doctor of Philosophy in

Interdisciplinary Biomedical Research

University of Warwick, Warwick Medical School

November 2021

Contents

List of Figures xiii

List of Tables xviii

List of Abbreviations xviii

Acknowledgments xxiv

Declaration of Material xxv

Summary xxvi

1. Introduction 1

1.1 Endocytosis 2

1.2 Clathrin-Mediated Endocytosis 5

1.2.1 Nucleation and assembly 9

1.2.2 Stabilisation and maturation 11

1.2.3 Constriction and scission 14

1.2.4 Clathrin uncoating 14

1.3 CME and Health 19

1.4 The Structure of Clathrin 21

1.4.1 Clathrin triskelia 21

1.4.2 Clathrin coats and cages 22

1.4.3 The clathrin terminal domain 24

1.5 Unanswered Questions on the… 27

1.5.1 Structural basis of clathrin adaptor interactions 27

1.5.2 Potential competition between adaptors 28

1.6 Research Questions and Aims 30

2. Materials and General Methods 33

2.1 Materials and Equipment 34

2.2 Buffers 37

2.3 Buffers and Agar Plates Prepared and Sterilised by University of Warwick Prep Services 39

2.4 Protein Constructs 40

2.5 Methods 42

2.5.1 Preparation of competent cells 42

2.5.2 Transformation of competent cells 42

2.5.3 SDS-PAGE 43

2.5.4 DNA and protein quantification 43

2.5.5 Negative staining 43

2.5.6 Data, map and model visualisation 44

3. Protein Purifications 45

3.1 Methods 46

3.1.1 ACTA FPLC 46

3.1.2 Clathrin purification 46

3.1.3 Expression of adaptor proteins 48

3.1.4 Purification of GST-tagged proteins 48

3.1.5 Purification of His-tagged proteins 51

3.2 Clathrin Cage Purification 53

3.2.1 Negative staining of clathrin cages 54

3.3 Purification of GST-tagged Proteins 57

3.3.1 Auxilin 57

3.3.2 β_2-adaptin 59

3.3.3 ARH 59

3.4 Purification of His-tagged Proteins 62

3.4.1 Hsc70 62

3.4.2 Epsin 1 62

3.4.3 AP180 64

4. Cryo-EM of Clathrin 67

4.1 Background to Cryo-EM 68

4.1.1 Why is cryo-EM appropriate? 68

4.1.2 The cryo-EM workflow 69

4.1.3 Local reconstruction workflow 73

4.2 Methods 75

4.2.1 Cryo-EM sample preparation 75

4.2.2 Cryo-EM data collection 75

4.2.3 Cryo-EM data refinement of cages 76

4.2.4 Localised reconstruction 78

4.2.5 PDB model generation 80

4.2.6 Rosetta and BUDE analysis 80

4.3 Clathrin Cage Structures 82

4.3.1 2D and 3D classification 82

4.3.2 Clathrin cage structures 85

4.4 Localised Reconstruction of Hub Region 88

4.4.1 PPP, PPH and PHH hubs 88

4.4.2 Consensus hub structure 89

4.4.3 Clathrin hub model generation 91

4.5 Discussion 96

4.5.1 Clathrin hub model 96

4.5.2 Study limitations 101

4.5.2.1 Particle number 101

4.5.2.2 Pixel size 102

4.5.2.3 Nyquist frequency and aliasing 102

4.5.2.4 *In vitro* sample 103

4.5.3 Conclusion 104

5. Cryo-EM of Clathrin with Bound Auxilin 105

5.1 Clathrin Auxilin Complex Questions 106

5.2 Methods 107

5.2.1 Clathrin binding assays 107

5.2.2 Cryo-EM sample preparation 107

5.2.3 Cryo-EM data collection 108

5.2.4 Cryo-EM data processing 108

5.2.5 Localised reconstruction 110

5.2.6 Difference mapping 112

5.2.7 PDB model generation 112

5.2.8 Rosetta and BUDE analysis 113

5.3 Preparation of Cryo-EM Samples 114

5.3.1 Clathrin binding assays 114

5.3.2 Screening of clathrin adaptor grids 114

5.4 Processing of Clathrin Auxilin Complexes 116

5.4.1 2D and 3D classification 116

5.4.2 Clathrin auxilin cage structures 119

5.5 Localised Reconstruction for Locating Auxilin 122

5.5.1 3D classification of clathrin auxilin hubs 122

5.5.2 Clathrin auxilin model generation 124

5.5.3 Rosetta and BUDE analysis 130

5.6 Discussion 136

5.6.1 Clathrin auxilin model 136

5.6.2 Study limitations 140

5.6.2.1 Lower resolutions of lower hub regions 141

5.6.2.2 3D classification limitations 142

5.6.3 Conclusion 142

6. Visualising Clathrin Disassembly 145

6.1 Background to Tomography 146

6.2 Methods 148

6.2.1 Clathrin disassembly assays 148

6.2.2 Cryo-ET sample preparation 148

6.2.3 Cryo-ET data collection 148

6.2.4 Tomography data processing 149

6.3 Results 150

6.3.1 Sample preparation 150

6.3.2 Tomogram generation and processing 151

6.4 Discussion 155

6.4.1 Study limitations and possible solutions 155

6.4.1.1 Tilt series 155

6.4.1.2 High electron dosage 156

6.4.1.3 CTF measurements 157

6.4.1.4 Low number of fiducials 157

6.4.1.5 Producing interpretable reconstructions 158

6.4.2 Conclusion 158

7. Interactions Between Clathrin and Adaptors 161

7.1 Background to Fluorescence Anisotropy 162

7.1.1 How does fluorescence anisotropy work? 162

7.1.2 Biologic MOS-450 anisotropy measurements 165

7.1.3 Measuring the dissociation constant using anisotropy 166

7.1.4 Why anisotropy as opposed to other methods? 168

7.2 Methods 169

7.2.1 PLS 169

7.2.2 DLS 169

7.2.3 Fluorescent labelling of cysteine residues 170

7.2.4 Anisotropy 170

7.2.5 Stopped flow PLS 170

7.2.6 Stopped flow anisotropy 171

7.3 Confirming the Activity of Hsc70 and Auxilin 172

7.3.1 Clathrin disassembly assays 172

7.3.2 Fluorescent labelling of constructs 174

7.4 Measuring Binding with Anisotropy 178

7.4.1 Equilibrium binding of auxilin to clathrin cages 178

7.4.2 Determining competition between adaptors 179

7.4.3 Stopped flow PLS studies 180

7.4.4 Stopped flow anisotropy studies 183

7.5 Discussion 184

7.5.1 Anisotropy for studying clathrin-adaptor interactions 184

7.5.2 Study limitations 187

7.5.2.1 Fluorescent labelling 187

7.5.2.2 Limited library of adaptor proteins 188

7.5.3 Conclusion 189

8. Overall Conclusions 191

8.1 Overview 192

8.2 Impact of Research 193

8.2.1 Updating the model for clathrin disassembly 193

8.2.2 CME adaptors are competitive by nature 196

8.3 Future Research Prospects 198

8.3.1 Further clathrin adaptor complex structures 198

8.3.2 Assessing interactions between auxilin and CLC 198

8.3.3 Anisotropy for assessing competition and interactions 199

8.3.4 Production of clathrin cages from *E. coli* 200

8.4 Final Remarks 201

References 203

Appendix – Publications 234

List of Figures

Figure 1.1.1	Forms of endocytosis	3
Figure 1.2.1	CME	6
Figure 1.2.2	Clathrin-coated vesicle formation pathways	12
Figure 1.2.3	Clathrin uncoating mechanisms	16
Figure 1.4.1	Structure of clathrin triskelia	21
Figure 1.4.2	Electron cryotomography of CCV's	23
Figure 1.4.3	Structure of a clathrin cage	24
Figure 1.4.4	Adaptor binding sites in the clathrin terminal domain	25
Figure 3.2.1	Clathrin purification traces and SDS-PAGE gels	53
Figure 3.2.2	Clathrin quantification	55
Figure 3.2.3	Negative staining of clathrin	56
Figure 3.3.1	Auxilin purification traces and SDS-PAGE gels	58
Figure 3.3.2	β_2-adaptin purification traces and SDS-PAGE gels	60
Figure 3.3.3	ARH purification traces and SDS-PAGE gels	61
Figure 3.4.1	Hsc70 purification traces and SDS-PAGE gels	63

Figure 3.4.2	Epsin 1 purification traces and SDS-PAGE gels	64
Figure 3.4.3	AP180 purification traces and SDS-PAGE gels	65
Figure 4.1.1	Preparing and imaging cryo-EM samples	70
Figure 4.1.2	SPA workflow	71
Figure 4.1.3	Localised reconstruction workflow	73
Figure 4.2.1	Clathrin cryo-EM screening and data collection	75
Figure 4.2.2	28-minicoat polishing B-factors	77
Figure 4.2.3	Extracted regions from localised reconstruction	79
Figure 4.3.1	Selection of clathrin particles with different defocus levels	82
Figure 4.3.2	Selected 2D classes of clathrin cages	83
Figure 4.3.3	3D classification of clathrin	84
Figure 4.3.4	Selected 2D classes of 28-minicoat and 36-barrel particles	85
Figure 4.3.5	Post-processed clathrin cage structures	86
Figure 4.4.1	Post-processed structures of different hub types	88
Figure 4.4.2	3D classification of lower hub region	89
Figure 4.4.3	Post-processed consensus hub structure	90

Figure 4.4.4	Local resolution of the clathrin consensus hub	91
Figure 4.4.5	New clathrin consensus hub model	92
Figure 4.4.6	Rosetta analysis of clathrin domain interactions	94
Figure 4.5.1	Comparison of consensus hub with published clathrin structures	98
Figure 5.2.1	Clathrin-auxilin complex cryo-EM screening and data collection	108
Figure 5.3.1	Clathrin auxilin binding assay	114
Figure 5.3.2	Initial freezing attempts	115
Figure 5.3.3	Clathrin auxilin sample and grid preparation	116
Figure 5.4.1	Selection of clathrin auxilin particles using Cryolo	117
Figure 5.4.2	3D classification of clathrin auxilin complexes	118
Figure 5.4.3	Selected 2D classes of clathrin cage particles	119
Figure 5.4.4	Post-processed clathrin auxilin cage structures	119
Figure 5.4.5	3D classification of clathrin auxilin 28-minicoat complexes	121
Figure 5.5.1	Clathrin auxilin hub densities	122
Figure 5.5.2	Refined clathrin auxilin hub classes	123

Figure 5.5.3	Global difference analysis of the clathrin auxilin hub structure	125
Figure 5.5.4	Auxilin J-domain adopts different positions when bound	127
Figure 5.5.5	Fitting of the auxilin J-domain in the class 4 auxilin densities	128
Figure 5.5.6	CLC N-terminal α-helical density present in clathrin auxilin map	129
Figure 5.5.7	Clathrin-auxilin interactions	131
Figure 5.5.8	Clathrin heavy and light chain interactions	133
Figure 5.5.9	Clathrin terminal and ankle domain interactions	135
Figure 5.6.1	Impact of variable auxilin positioning	137
Figure 6.1.1	Acquisition of clathrin structures using cryo-ET	147
Figure 6.3.1	Preparation of cryo-ET grids with disassembling clathrin cages	150
Figure 6.3.2	Images taken at different angles for each tilt series	152
Figure 6.3.3	Selected fiducials for tilt series alignment	152
Figure 6.3.4	Tomogram slices	153
Figure 6.3.5	Extracted cage from each tomogram	153

Figure 6.3.6	3D maps of cryo-ET clathrin cages	154
Figure 7.1.1	Photo-selective excitation of fluorophores by polarised light	164
Figure 7.3.1	Clathrin disassembly analysed *via* perpendicular light scattering	173
Figure 7.3.2	Clathrin disassembly analysed *via* dynamic light scattering	174
Figure 7.3.3	SDS gels of AF488 labelled S835C auxilin and S603C Hsc70	175
Figure 7.3.4	Assessing the use of AF488 labelled adaptors for anisotropy	176
Figure 7.4.1	Equilibrium binding of clathrin to AF488 labelled auxilin mutants	178
Figure 7.4.2	Competition between different adaptors for clathrin binding	180
Figure 7.4.3	PLS of clathrin cage disassembly with competitive adaptors	181
Figure 7.4.4	Competitive adaptors reduce maximum clathrin disassembly rate	182
Figure 7.4.5	Characterising anisotropy for measuring clathrin disassembly	183

Figure 8.2.1 Entropic pulling/collision pressure model 194

Figure 8.2.2 Proposed model for initial clathrin uncoating steps 196

List of Tables

Table 1.2.1 List of CME accessory proteins and their key roles 6

Table 2.4.1 DNA constructs used for protein expression and purification 40

Table 3.1.1 Expression conditions for constructs 48

Table 4.2.1 EM map statistics for processed clathrin cages 78

Table 4.2.2 EM map statistics for processed clathrin hub structures 80

Table 5.2.1 EM map statistics for processed clathrin-auxilin cages 110

Table 5.2.2 EM map statistics for processed clathrin-auxilin hubs 111

List of Abbreviations

AAK1	AP2 associated kinase
Abp1	Auxin binding protein 1

AEBSF	4-(2-Aminoethyl) benzene sulfonyl fluoride hydrochloride
AIM	Auto induction media
APS	Ammonium persulphate
AP2	Adaptor-protein 2
ARH	Autosomal recessive hypercholesterolemia
Arp2/3	Actin-related proteins 2/3 complex
ATP	Adenosine triphosphate
ATP-Agarose	ATP-agarose 4B cyanogen bromide activated
A_{280}	Absorbance at 280 nm
BIN1	Bridging integrator 1
$CaCl_2$	Calcium chloride
CALM	Clathrin assembly lymphoid myeloid leukaemia
CCP	Clathrin coated pit
CCV	Clathrin coated vesicle
CHC	Clathrin heavy chain
CLC	Clathrin light chain
CME	Clathrin-mediated endocytosis

Cryo-EM	Cryo-electron microscopy
Cryo-ET	Cryo-electron tomography
CTF	Contrast transfer function
Dab2	Disabled-2
DGKγ	Diacylglycerol kinase γ
DLS	Dynamic light scattering
DTT	Dithiothreitol
E. coli	*Escherichia coli*
EDTA	Ethylene-diamine-tetra acetic acid
EGTA	Ethylene-glycol-bis(ß aminoethyl ether)-tetra acetic acid
Eps15	EGF-receptor phosphorylation substrate
Eps8	Epidermal growth factor receptor pathway substrate 8
FA	Fluorescence anisotropy
FCHo1/2	Fer/Cip4 homology domain-only proteins ½
FRAP	Fluorescence recovery after photobleaching
FSC	Fourier shell correlation
GAK	Cyclin G associated kinase

GSH	Reduced glutathione
GST	Glutathione sepharose transferase
HCl	Hydrochloric acid
HIP1	Huntingtin-interacting protein 1
HIP1R	Huntingtin-interacting protein 1 related
HPPH	Hexagon-pentagon-pentagon-hexagon proximal region
Hrb	Human immunodeficiency virus Rev-binding protein
Hsc70	Heat shock protein 70 kDa
IPTG	Isopropyl ß-D-1-thiogalactopyranoside
KCl	Potassium chloride
LB	Luria broth
LDL	Low-density lipoprotein
LϕXϕ[DE]	L(L, I)(D, E, N)(L, F)(D, E)
NaCl	Sodium chloride
NADH	Nicotinamide adenine dinucleotide reduced
NaOH	Sodium hydroxide
NECAP	Adaptin-ear-binding coat-associated protein

N-WASP	Neural Wiskott-Aldrich syndrome protein
$MgCl_2$	Magnesium chloride hexahydrate
$MgSO_4$	Magnesium sulphate
$MnCl_2$	Manganese chloride
OCRL	Oculocerebrorenal Lowe syndrome protein
OD_{600}	Optical density at 600 nm
PHH	Pentagon-hexagon-hexagon hub
PIP2	Phosphatidylinositol 4,5-bisphosphate
PIPKIγ	Phosphatidylinositol (4) phosphate 5 kinase type I γ
PIPSK	Phosphatidylinositol phosphate
PI3KC2a	Phosphatidylinositol 3-kinase C2a
PLS	Perpendicular light scattering
PPH	Pentagon-pentagon-hexagon hub
PPHP	Pentagon-pentagon-hexagon-pentagon proximal region
PPP	Pentagon-pentagon-pentagon hub
PPPH	Pentagon-pentagon-pentagon-hexagon proximal region
RbCl	Rubidium chloride

RME	Receptor-mediated endocytosis
RME-6	RME protein 6
RMSD	Root mean square deviation
SAT	Single angle tomography
Sd	Standard deviation
SDS	Sodium dodecyl sulphate
SGIP1	SH3 domain GRB2 like endophilin interacting protein 1
SHIP2	SH2 domain containing inositol 5-phosphatase 2
SNX9	Sorting nexin 9
S.O.C.	Super optimal broth with catabolic repression
SPA	Single particle analysis
SPR	Surface plasmon resonance
TEA	Triethylamine
TEMED	Tetra-methyl-ethylene-diamine
Tris-base	Tris-(hydroxymethyl)-amino-methane
Tris-HCL	Tris-(hydroxymethyl)-aminomethane-hydrochloride

Acknowledgments

I acknowledge the University of Warwick Interdisciplinary Biomedical Research Doctoral Training Programme for providing exceptional training and guidance, and for providing the opportunity to conduct a PhD at the University of Warwick. The PhD project is funded by the MRC Doctoral Training Partnership [grant number MR/N014294/1]. I acknowledge my supervisors, Dr Corinne Smith and Dr Nikola Chmel, for providing exceptional training, support and guidance during the project throughout all stages. I acknowledge Dr Sarah Smith for providing exceptional training and support during the project, and for providing frozen cryo-EM grids for continuation of the clathrin-auxilin complex studies during the COVID-19 pandemic. I acknowledge Dr Michael Baker for providing DNA constructs of Hsc70 and auxilin cysteine mutants, which enabled the fluorescence anisotropy studies to be conducted. I also wish to extend thanks to the members of Dr Corinne Smith's group and Dr Nikola Chmel's group, particularly Dr Sarah Smith, Veronica Foiser, Liam Riley, Dr Joe Jones and Dr Michael Baker, for their support and friendship throughout the project.

For provisions of sterile chemical consumables and waste management facilities, I acknowledge the technical support and preparation room technicians based at the University of Warwick School of Life Sciences. For use and training of cryo-EM and cryo-ET equipment and facilities we acknowledge the following facilities: the Midlands Regional Cryo-EM Facility, hosted at the Warwick Advanced Bioimaging Research Technology Platform, for use of the JEOL 2100Plus, supported by MRC award reference MC_PC_17136; the University of Warwick Advanced Bioimaging Research Technology Platform supported by BBSRC ALERT14 award BB/M01228X/1; the Midlands Regional Cryo-EM facility at LISCB, major funder MRC (Leicester institute of structural and chemical biology). We further wish to extend are thanks to Dr Christos Savva, Dr TJ Ragan, and Dr Saskia Bakker, for their advice and support during training, sample preparations and data collections.

Declaration of Material

This thesis is submitted to the University of Warwick in support of my application for the degree of Doctor of Philosophy. It has been composed by myself and has not been submitted in any previous application for any degree. The work presented (including data generated and data analysis) was carried out by the author except in the cases outlined below:

- Dr Michael Baker produced the DNA constructs of cysteine mutants used in chapter 7. Protein expression and purification was conducted by the author.
- Dr Sarah Smith produced the frozen clathrin auxilin complex cryo-EM grids that were subsequently used for data collection and analysis. Figure 5.3.3 contains images taken by Dr Sarah Smith showcasing the quality of the purified auxilin, and the overall quality of the frozen grids.

Parts of this thesis have been published by the author:

- The material in sections 1.1, 1.2 and 1.4 draws heavily on the author's previously published literature review (1), which has been attached to the end of this thesis in the appendix
    - Wood, K. M., & Smith, C. J. (2021). Clathrin - The Molecular Shapeshifter. *Biochemical Journal*, *478*(16), 3099–3123. https://doi.org/10.1042/BCJ20200740
- The 28-minicoat cage density presented in section 4.3.2 was previously published in Smith *et al.* (2021)(208) which has been attached to the end of this thesis in the appendix.. The map density was used for difference map analysis of the clathrin β2-adaptin complex to identify β2-adaptin densities.
    - Smith, S. M., Larocque, G., Wood, K. M., Morris, K. L., Roseman, A. M., Sessions, R. B., Royle, S. J., & Smith, C. J. (2021). Multi-modal adaptor-clathrin contacts drive coated vesicle assembly. *EMBO Journal*, *40*, e108795. https://doi.org/10.15252/embj.2021108795

Summary

Clathrin mediated endocytosis (CME) allows selective uptake of extracellular molecules into cells using cell surface receptors. CME is associated with different diseases (*e.g.,* Parkinson's disease) where mutations and differing expression levels of CME adaptor proteins are observed. The current understanding of clathrin-adaptor interactions is limited to low-resolution cryo-EM structures and crystal structures of the clathrin terminal domain with bound peptides derived from adaptor proteins, despite the wealth of data on the role of adaptor proteins within endocytosis. There are also still many questions with regards to how multiple adaptor proteins interact and bind to clathrin cages to enable controlled clathrin coat assembly and disassembly. This project aimed to gain a greater understanding of how adaptor proteins interact with clathrin, and the impact these interactions have on clathrin cage disassembly.

Initially cryo-EM was conducted to determine the structure of a clathrin cage hub with no adaptor proteins bound and terminal domains resolved, providing new insights into clathrin-clathrin interactions in the absence of adaptor proteins. This was followed by cryo-EM of clathrin cages with the disassembly adaptor protein auxilin bound, to acquire higher resolution details on auxilin binding to clathrin cages. Finally, effects of clathrin-adaptor interactions on clathrin disassembly were further analysed using fluorescence anisotropy (FA) to assess adaptor protein competition for clathrin binding sites. Overall, structures of the clathrin cage complex and the clathrin auxilin complex were successfully produced providing information on how auxilin interacts with clathrin during clathrin disassembly. The FA technique has been developed for measuring clathrin-adaptor interactions and clathrin disassembly rates, enabling competition between adaptor proteins auxilin, AP180, epsin, ARH and β_2-adaptin to be identified. Further use of FA will be beneficial for assessing clathrin adaptor interactions and adaptor competition to understand how adaptor protein mutations and expression levels may cause or contribute to disease states.

Chapter 1:

Introduction

Chapter Overview

This chapter shall provide the background for this PhD thesis, including information on the clathrin-mediated endocytosis (CME) process and relevant proteins. Information on the aims and objectives of this work can be found in section 1.6. The material in sections 1.1, 1.2 and 1.4 of this introduction draws heavily on the author's previously published literature review (1), which has been attached to the end of this thesis in the appendix.

1.1 Endocytosis

Endocytosis is a cellular process where cells produce internal membranes from the plasma membrane, causing the internalisation of plasma membrane lipids, integral proteins and extracellular fluid (2,3). Endocytosis thus allows the cell to carry out or contribute to multiple processes including regulation of cell surface receptors to control cell sensitivity to certain ligands, uptake of ligands within extracellular media, remodelling the plasma membrane, cell migration, mitosis, antigen presentation, and positive regulation of signalling cascades (2,4). Endocytosis can also be exploited by bacteria and viruses to allow their internalisation into cells (5,6). Understanding the general mechanisms of endocytosis is therefore important for understanding how endocytosis is used and exploited, and how defects in endocytosis can lead to disease. Our understanding of endocytosis and how it recruits cargo, however, is still lacking despite having a wealth of information on endocytic cargoes. Many questions remain as to the role of different proteins during endocytosis, the mechanisms in which the proteins act, and how they cooperate or compete with other proteins to fulfil their roles. This issue is partly due to the multiple types of endocytosis; all of which are very complex due to the large number of proteins that they utilize.

Historically, endocytosis was considered to take place *via* three distinct mechanisms termed phagocytosis, pinocytosis, and receptor-mediated endocytosis (RME). There are multiple forms of pinocytosis and RME that differ based on their morphology and associated proteins; types include CME, micropinocytosis, caveolae-dependent endocytosis, flotillin-dependent endocytosis, and more (2,3). Figure 1.1.1 demonstrates the differences between phagocytosis, pinocytosis and RME.

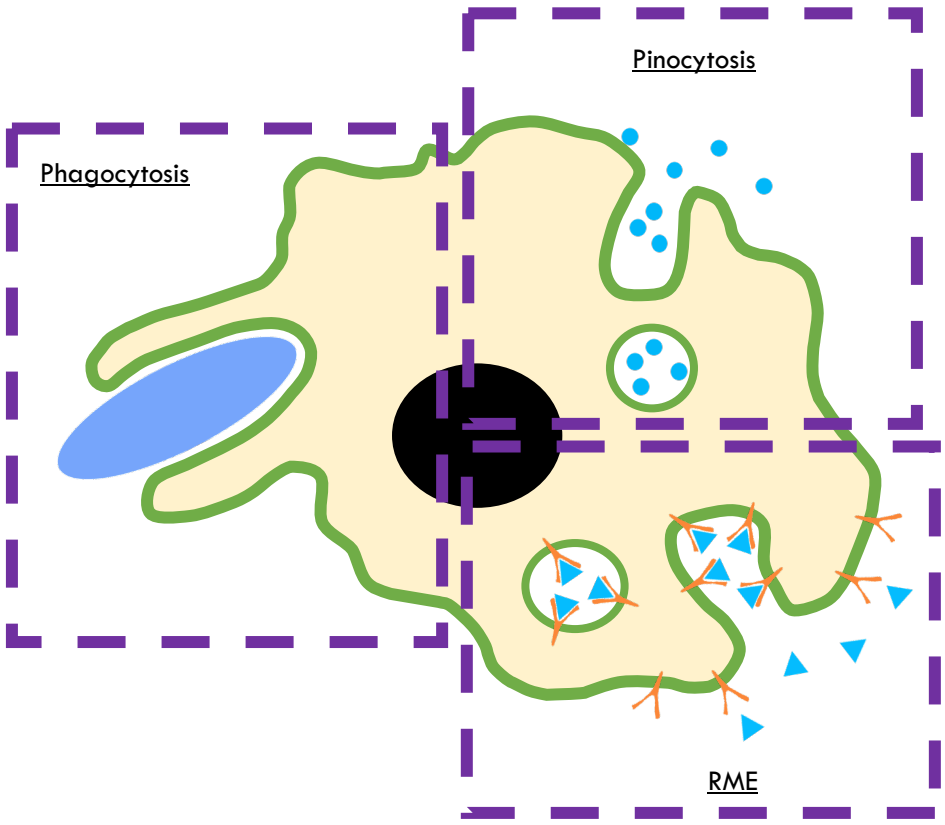

Figure 1.1.1 – Forms of endocytosis

Schematic diagram describing the differences between phagocytosis, pinocytosis and endocytosis. Lipid membranes are green, molecules are blue, receptors are orange, extracellular fluid is white, the cytoplasm is yellow and the cell nucleus is black. Purple dashed boxes separate the different types of endocytosis. Figure is not to scale.

Phagocytosis allows the cell to engulf macromolecules including cellular debris, bacteria and whole cells, by remodelling cell membrane around the macromolecule (7,8). Fusion of the membrane creates a phagosome in which the macromolecule resides within the cell; lysosomes will fuse with the phagosome to create a phagolysosome, causing the macromolecule to be degraded by lysosomal hydrolases (7,8). Pinocytosis differs from phagocytosis as the plasma membrane invaginates to create pits before pinching off to form intracellular vesicles, allowing molecules in the extracellular fluid to be ingested (8,9). These vesicles are then trafficked to either endosomes or lysosomes for further trafficking or degradation respectively. RME is very similar to pinocytosis, however, receptors on the cellular surface are required for RME which allows

selective uptake of molecules from the extracellular environment, unlike pinocytosis which is non-specific (8,9).

The most studied form of RME is CME which is believed to be the major endocytic route in most cells, as clathrin-independent pathways appear to not contribute significantly to endocytic flux (10). CME plays roles in several key processes such as hormone desensitisation, intracellular trafficking, mitosis, sperm development and more (11–14). Understanding how CME occurs is therefore important for understanding how CME impacts different processes and how defects can lead to disease. The focus of this thesis will therefore be centred around CME: more specifically how accessory proteins interaction with clathrin leads to clathrin cage disassembly.

1.2 Clathrin-Mediated Endocytosis

CME was first discovered in 1964, and was found to create clathrin coated vesicles (CCV) from cell membranes and *trans*-Golgi network with the vesicles having a diameter of around 60 – 120 nm (15–19). The coat that forms around these vesicles is created from the scaffold protein clathrin and multiple accessory proteins (17–19). CME has been described in four key stages termed nucleation and assembly, stabilisation and maturation, constriction and scission, and clathrin uncoating. A summary of the CME stages is shown in figure 1.2.1. Each of the CME stages requires the involvement of multiple accessory proteins whose functions can be classified as follows: nucleation and assembly, neck constriction, scission and movement, and uncoating (20). There are around 50 different accessory proteins, the names and abbreviations of which are detailed in table 1.2.1, which coordinate with one another to allow CME to occur (17,20,21). Due to the high number of accessory proteins involved, recruitment of CME accessory proteins to the plasma membrane must occur in a highly ordered sequential fashion, with recruitment of certain accessory proteins only occurring upon the CME process reaching a certain stage (21–25).

But why are so many accessory proteins required? The key protein involved in CME, clathrin, cannot bind to membranes or integral protein on its own; so in order for clathrin to assemble at the membrane, accessory proteins are required which can interact with clathrin and each other to link clathrin to membrane-attached cargo and assemble clathrin to produce a CCV (26,27). These accessory proteins are termed CME adaptors. CME adaptors are also required to produce forces to the order of picoNewtons, so that a variety of cell membrane parameters can be overcome that make membrane bending a challenge; this includes high membrane tension, internal hydrostatic pressure, and cargo properties (17,28–30). Such a complex process thus requires a coordinated series of precise binding interactions, which shall be discussed in sections 1.2.1 to 1.2.4.

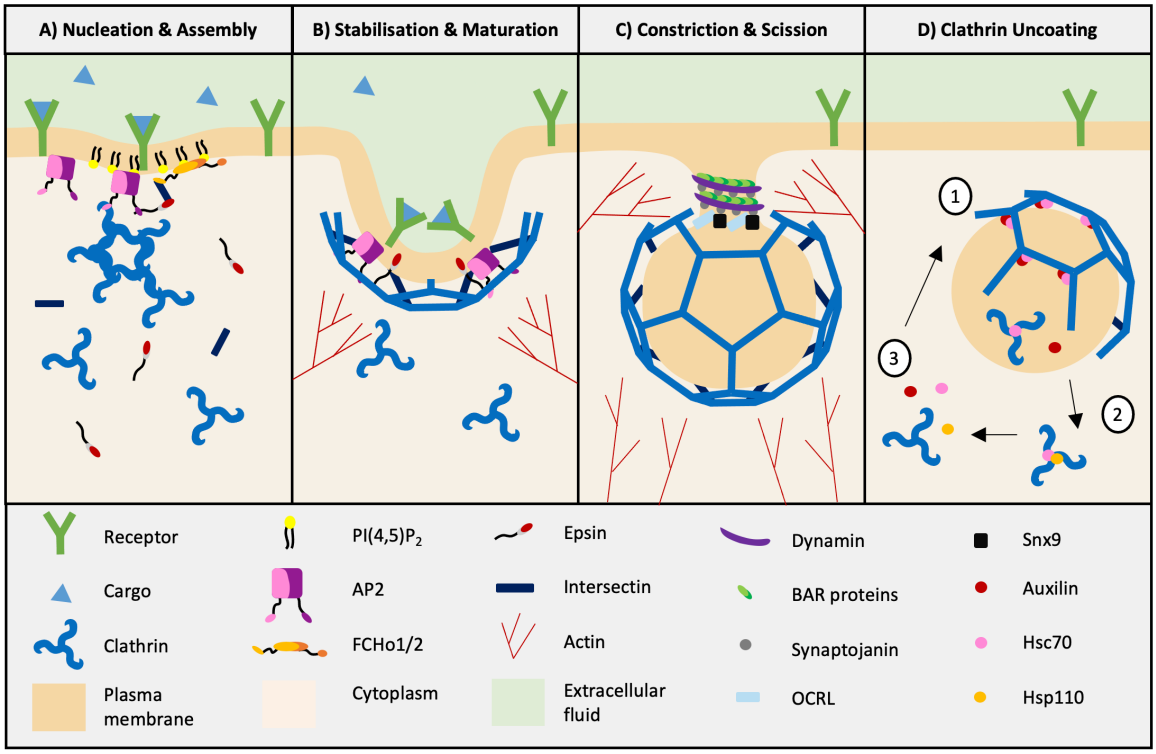

Figure 1.2.1 – CME

Schematic of the CME process. Nucleation and assembly: ligand binding to cargo receptors in the plasma membrane causes AP2 and FCHo1/2 to bind to PIP2 in the membrane and create a nucleation site, allowing clathrin to be recruited by AP2 for CCP formation (31–34). Stabilisation and maturation: Adaptor proteins stabilise and extend the clathrin coat as the membrane is bent further, aiding with the development and stabilisation of a larger pit and ensuring the CCP is enriched with cargo (16,35). Constriction and scission: Once the CCP is ready to be released and form a vesicle, BAR domain proteins will constrict the neck and recruit the scission protein dynamin to the neck of the pit. Dynamin will assemble around the neck and pinch off the clathrin coated vesicle from the plasma membrane (36–39). Clathrin uncoating: [1] disassembly of the clathrin coat from the CCV occurs upon auxilin recruiting Hsc70 to the clathrin coat for adenosine triphosphate (ATP) hydrolysis; [2] Hsc70 will remain bound to disassembled clathrin triskelia until the nucleotide exchange factor Hsp110 binds, which [3] dissociates hsc70 from clathrin to allow auxilin, clathrin and hsc70 to be recycled for further CME processes (40–46). Figure is not to scale. Republished with permission of Portland Press, from Clathrin: the molecular shape shifter, Wood KM and Smith CJ, 478 (16), 2021(1); permission conveyed through Copyright Clearance Center, Inc. Licence: 1163059-1.

Table 1.2.1 – List of CME accessory proteins and their key roles

Role	Protein name	Abbreviation
	Clathrin heavy chain	CHC
	Clathrin light chain a/b	CLCa/CLCb

Nucleation and Assembly	Adaptor-protein 2	AP2
	Clathrin assembly lymphoid myeloid leukemia	CALM
	AP180	-
	Huntingtin-interacting protein 1	HIP1
	Adaptin-ear-binding coat-associated protein	NECAP
	AP2 associated kinase 1	AAK1
	β-arrestin	-
	Autosomal recessive hypercholesterolemia	ARH
	Disabled-2	Dab2
	Human immunodeficiency virus Rev-binding protein	Hrb
	Receptor-mediated endocytosis protein 6	RME-6
	Diacylglycerol kinase γ	DGKγ
	Phosphatidylinositol(4) phosphate 5 kinase type I γ	PIPKIγ
	SH2 domain containing inositol 5-phosphatase 2	SHIP2
	Epsin 1/2	-
	Stonin 2	-
	Connecdenn	-
	Fer/Cip4 homology domain-only proteins 1/2	FCHo1/2
	Intersectin	-
	SH3 domain GRB2 like endophilin interacting protein 1	SGIP1
	EGF-receptor phosphorylation substrate	Eps15
Neck Constriction	Bridging integrator 1	BIN1
	Endophilin	-

	Amphiphysin	-
Scission and Movement	Dynamin 1/2	-
	Synaptojanin 1/2	-
	Syndapin	-
	Myosin VI	-
	Neural Wiskott-Aldrich syndrome protein	N-WASP
	Cortactin	-
	Actin	-
	Myosin 1E	-
	Huntingtin interacting protein-1 related	Hip1R
	Epidermal growth factor receptor pathway substrate 8	Eps8
	Sorting nexin 9	SNX9
	Profilin	-
	Cofilin	-
	Coronin	-
	Actin-related proteins 2/3 complex	Arp2/3
	Auxin binding protein 1	Abp1
	Phosphatidylinositol 3-kinase C2a	PI3KC2a
	Phosphatidylinositol phosphate	PIPSK
Uncoating	Auxilin	-
	Heat shock protein 70 kDa	Hsc70
	Cyclin G associated kinase	GAK
	Ack	-
	Oculocerebrorenal Lowe syndrome protein	OCRL

The table was developed from details from Mettlen *et al.* (2018)(21) and Traub (2011)(20).

1.2.1 Nucleation and assembly

CME is initiated when the first accessory proteins come together at the membrane, forming a nucleus for subsequent interactions to allow for the formation of a clathrin coat. The FCHo1/2 or the AP2 complex could act as the primary initiator for nucleation site formation, or nucleation could be due to the actions of several accessory proteins (31,32,47–50). It is known in mammals that the key accessory proteins involved in initiation are FCHo1/2, AP2, Eps15, Eps15R, and intersectins 1/2, however, other adaptors could still play a role (23,31,48). Upon forming a CME nucleus, accessory proteins can then recruit cargo by binding to cytosolic regions of transmembrane cargo, allowing specific cargo and associated lipids to be recruited into the forming vesicle for selective endocytosis (51–53). An example of endocytic cargo would be the low-density lipoprotein (LDL) receptor which bind to LDL's (54). Some accessory proteins associated with initiation such as AP2, FCHo1, Eps15, and CALM, act as cargo adaptors (55). Use of accessory proteins as cargo adaptors suggests specific cargoes can recruit and cluster initiation accessory proteins to the plasma membrane, thereby triggering initiation of CME, however, it also allows the production of a biochemical checkpoint to ensure a sufficient quorum is reached before CME is initiated (56–58).

The location at which initiation of CME occurs tends to be at spatially distinct sites in the cell membrane and is dependent on cortical actin integrity and the availability of CME accessories such as AP2 and Phosphatidylinositol 4,5-bisphosphate (PIP2) (59). This allows CME to occur repeatedly in the same location or within certain regions of the cell, such as a neuron synapse, allowing the creation of dynamic clathrin coated pits (CCP) which produce multiple CCVs in succession (60). Some nucleation sites can occur at random positions in the cell membrane which could be due to stochastic collisions between CME accessories, however, the majority of nucleation sites are at spatially distinct sites (32,52). The sites at which CME accessory proteins are recruited could be dependent on the location of PIP2 in the membrane, as binding of CME

accessory proteins to PIP2 is necessary for nucleation site formation, and depletion of PIP2 leads to a complete loss of endocytic CCPs (33,34). CME accessory proteins could also be recruited in areas with higher localised concentrations of cargo-binding adaptors across membranes, which could be due to localised exocytosis of cargo adaptors from the cell or from interactions that may occur between cargo adaptors (56,61). To spatially organise initiation, the action of nucleation factors and nucleation organisers is required (59). FCHo1/2 and SNX9 are two accessory proteins which impact on the number or spatial organisation of CCPs respectively (31,59). FCHo1/2 helps sculpt the initial bud site upon AP2 engagement, by recruiting the scaffold proteins eps15 and intersectin to the membrane (31,32). Changes in FCHo1/2 expression levels influence the number of CCPs forming, whereas changes in SNX9 expression levels impacts the spatial clustering of CCPs (31,59).

Abortion of intermediate CCPs is another way in which CME is controlled, with a proportion of nucleation events in cells being weak and short lived (52). This checkpoint which determines the turnover of nucleation events could be controlled by the concentration of cargo and the accessory protein dynamin, which is involved in vesicle scission, since knockdown of dynamin in cells using siRNA is shown to increase the number of persistent CCPs, and reintroduction of dynamin to these cells reduces the number of persistent CCPs (62). Cargo can also cause disassembly or delayed completion of a forming vesicle if the number of cargo present is not substantial, ensuring that all vesicles formed are filled with cargo. This is dependent on multiple factors such as ubiquitination of cargo adaptors and the amount of cargo present (52,58,63–65). The exact molecular mechanism by which nucleation sites are formed and regulated though still has many questions remaining. This includes what accessories are required and how they interact with one another to form the nucleation site, and the role of membrane domains and cargo for regulating nucleation site formation.

1.2.2 Stabilisation and maturation

After initiation of CME, formation of a clathrin coated pit will occur which leads to the formation of a vesicle bud as the coated pit grows and matures. Curvature of the vesicle can initiate during different stages of clathrin recruitment as shown in figure 1.2.2; here vesicle curvature occurs immediately after initiation, during clathrin recruitment, after completion of clathrin recruitment, or from a section of a flat clathrin patch (66). Several CME accessories contribute to this process of stabilisation and maturation including clathrin, actin filaments and scission proteins.

For the CCP to form, the membrane needs to bend through the action of accessory proteins. The ability for clathrin to polymerise into polyhedral cages consisting of pentagon and hexagon arrangements, and more rarely heptagon and square arrangements, suggests the shape of polymerised clathrin could induce curvature of membranes (16,35). Clathrin could achieve this in two ways: (1) forming a flat lattice on a membrane surface followed by gradual lattice reorganisation to form a spherical coat; (2) polymerisation of clathrin into a curved lattice on the membrane, with a progressive increase in the surface area covered by clathrin. Contradictory evidence though has put the two models under debate. Electron microscopy studies have shown the appearance of clathrin lattices with varying curvature, which requires clathrin exchange as the vesicle grows. This supports model 1, however, several clathrin-clathrin interactions would require modification for a flat clathrin lattice to become spherical (67–70). Thus model 1 would impact vesicle size and shape, with vesicle development from larger clathrin patches being more energetically costly than smaller clathrin patches. Clathrin polymerisation must also compete with membrane tension that increases with membrane curvature in model 2, which would prevent or stall clathrin polymerisation (71,72).

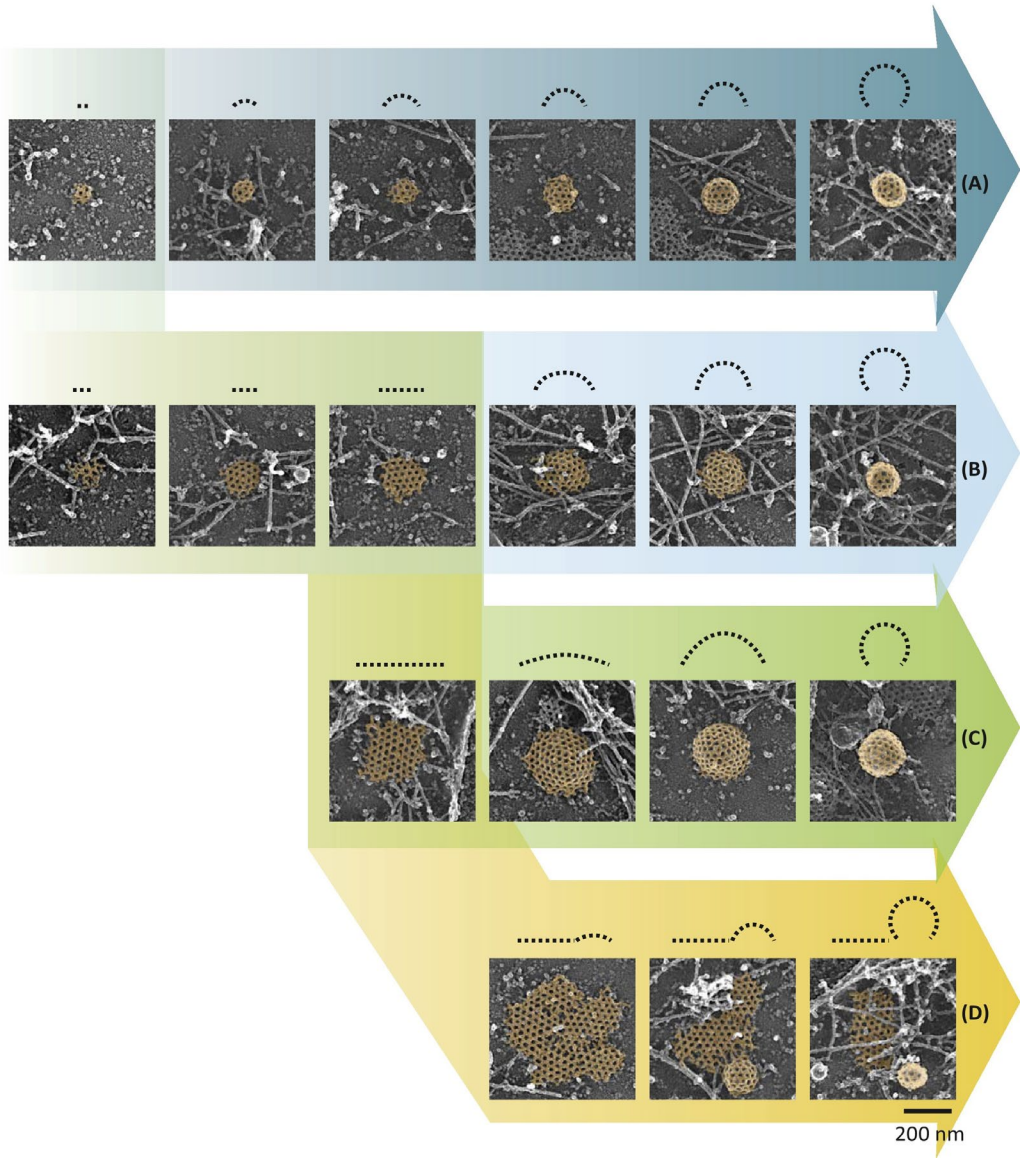

Figure 1.2.2 - Clathrin-coated vesicle formation pathways

There are four points in which clathrin-coated vesicle curvature can initiate. Membrane and lattice curvature can start at either A) structure initiation, B) during clathrin recruitment, C) after completion of clathrin recruitment, or D) from a section of a clathrin patch. Reprinted from Trends in Cell Biology, 29 (3), Kem A. Sochacki and Justin W. Taraska, From Flat to Curved Clathrin: Controlling a Plastic Ratchet, 241-256 (2019) (12), with permission from Elsevier. Licence: 5077170164269.

Adaptor proteins also impact the bending of membranes, with several adaptor proteins such as Epsin, CALM and CLCs promoting curvature induction. Epsin and CALM contain amphipathic helices in their structure, which when bound to polymerised clathrin, will wedge into the membrane to create local curvature (19,71,73). CLCs act differently as they promote membrane curvature by

making clathrin lattices more rigid upon binding to CHCs; this allows the rigidity of the clathrin lattice to be dynamically modulated (74). Uncoating adaptor proteins may also play a role in membrane curvature, as hsc70, auxilin and GAK have been associated with earlier stages of clathrin assembly despite their major role in uncoating CCV's (75,76). This is further backed by fluorescence recovery after photobleaching (FRAP) experiments, which show a high turnover rate of clathrin in clathrin lattices *in vivo,* suggesting reorganisation of the clathrin lattice (70,77,78). As reorganisation requires energy, the action of the chaperone protein hsc70 may provide the necessary energy for the remodelling, and thereby provides support for model 1 over model 2 (79).

Clathrin coats and adaptors, however, are not the only elements that can impact membrane curvature, as the actin cytoskeleton also makes a significant contribution. Live cell imaging studies show actin assembling at endocytic sites, and other studies show that actin cytoskeleton perturbation leads to inhibition of endocytosis, indicating that actin is required for CCV formation (22,60,80–84). Microscopy studies have shown actin polymerisation occurs around the clathrin coat and at the base of forming vesicles (85,86). This polymerisation of actin at endocytic sites is aided and regulated by additional actin-binding proteins including filament crosslinkers, depolymerisation factors, cappers and myosin motors (87). For actin polymerisation to impact membrane bending, it needs to be coupled to CME adaptors. Epsin and HIP1R fulfil this role as they bind to and couple clathrin, PIP2 and actin (72,88–91). This allows actin filament polymerisation to generate and transmit a force when coupled to clathrin coats, leading to membrane bending (92,93). HIP1R, however, can also interact with CLC, which upon binding leads to negative regulation of HIP1R actin interactions (94).

1.2.3 Constriction and scission

Once the matured vesicle is ready to be separated from the membrane, the GTPase dynamin will assemble around the neck of the vesicle and pinch the vesicle from the membrane; this step is called scission. Dynamin forms tight oligomers of around 10 nm in radius around the neck of the vesicle (39). Binding and hydrolysis of GTP causes a conformational change in dynamin, leading to dynamin to constrict and allow membrane scission to occur (39). The exact mechanism in which this reaction proceeds and is regulated *in vivo,* however, is still unresolved, despite the reaction being reconstituted *in vitro* and dynamins known interaction with BAR domain proteins (95–97). The unresolved mechanism is due to the presence of several dynamin partners, such as actin for example, which are required to control membrane tension to allow fission to occur, as fission cannot occur by dynamin constriction alone (98–101). Understanding how dynamin partners interact to drive scission thus requires further investigation.

BAR domain proteins recruit dynamin to the neck of the vesicle (102–104). The recruitment of different BAR domain proteins is dependent upon the changing membrane curvature at the endocytic site, with F-Bar domain proteins being recruited at low membrane curvature and N-BAR domain proteins being recruited at higher membrane curvature (104,105). When BAR domain proteins bind to membranes at high density, they cause membranes to tubulate and, therefore, allow the neck of the vesicle to form so that dynamin can perform its function (36–38).

1.2.4 Clathrin uncoating

Disassembly of clathrin coats from CCVs allows the vesicle to be trafficked to and fuse with the early endosome, while also freeing up CME adaptors for additional bouts of CME. For uncoating to occur, synaptojanin and OCRL1 dephosphorylate PIP2 found within the CCV membrane in order to recruit the

chaperone auxilin to clathrin, allowing the auxilin J-domain to recruit the ATPase Hsc70 to clathrin. Upon binding of Hsc70 to clathrin and completion of ATP hydrolysis, Hsc70 disassembles the clathrin coat (75,76,106–115). Auxilin's phosphatase and tensin homolog deleted on chromosome ten (PTEN) domain allows auxilin to bind to the CCV membrane *via* interactions with the dephosphorylated negatively charged PIP2 lipids (116). The presence of the PTEN domain increases uncoating efficiency by orienting auxilin in the ideal orientation for disassembly, however, the PTEN domain is not essential for clathrin uncoating to occur (116–118). Unlike the PTEN domain, auxilins J-domain is essential for uncoating as it recruits Hsc70 in a catalytical manner by recruiting several Hsc70 molecules for the uncoating reaction (40,41). When Hsc70 is bound to both auxilin and clathrin, its activity is heightened to enable rapid disassembly of CCVs (119). They key interactions that occur between Hsc70 and auxilin are electrostatic interactions at auxilin residues Lys847, Tyr866, Arg867, Lys868, His874, Asp876, Lys877, Thr879, Gln881, Phe891, Asn895, and Asn903 (120,121). Upon Hsc70 being recruited by auxilin to a CCV and binding of ATP, the Hsc70-ATP complex binds the CHC carboxy-terminals QLMLT motif; this allows Hsc70 to bind to up to three sites per clathrin triskelion (41,107,122–124). The clathrin Hsc70 interaction is tightened upon ATP hydrolysis, which in turn dissociates auxilin from hsc70 and clathrin, and destabilises proximal-distal contacts between clathrin triskelia (123,125,126).

Two models, called the steric wedge/Brownian ratchet model and the entropic pulling model, have been proposed so far to explain how Hsc70 might disrupt proximal-distal contacts between clathrin triskelia. A schematic diagram of each model is presented in figure 1.2.3. In the steric wedge/Brownian ratchet model, binding of auxilin and Hsc70 on the inner face of the clathrin coat increases the excluded volume below clathrin coat vertices, producing a strained clathrin coat conformation (107,123). Then upon ATP hydrolysis, Hsc70's Brownian motion will increase causing collisions with the clathrin coat to further weaken clathrin-clathrin interactions until the coat disassembles (79,107,123). In the entropic pulling model, ATP hydrolysis by Hsc70 dissociates auxilin from clathrin and

tightens Hsc70 binding to clathrin, which in turn restricts Hsc70 movement and entropy (127–129). This in turn causes Hsc70 to move away from clathrin vertices to increase entropy and freedom of movement, creating a directional force that pulls on the clathrin carboxy domain to break clathrin proximal-distal interactions (127–129). Of the two models discussed the entropic pulling model appears the most reasonable and efficient, however, more research needs to be done to determine the correct mechanism of Hsc70 driven clathrin uncoating.

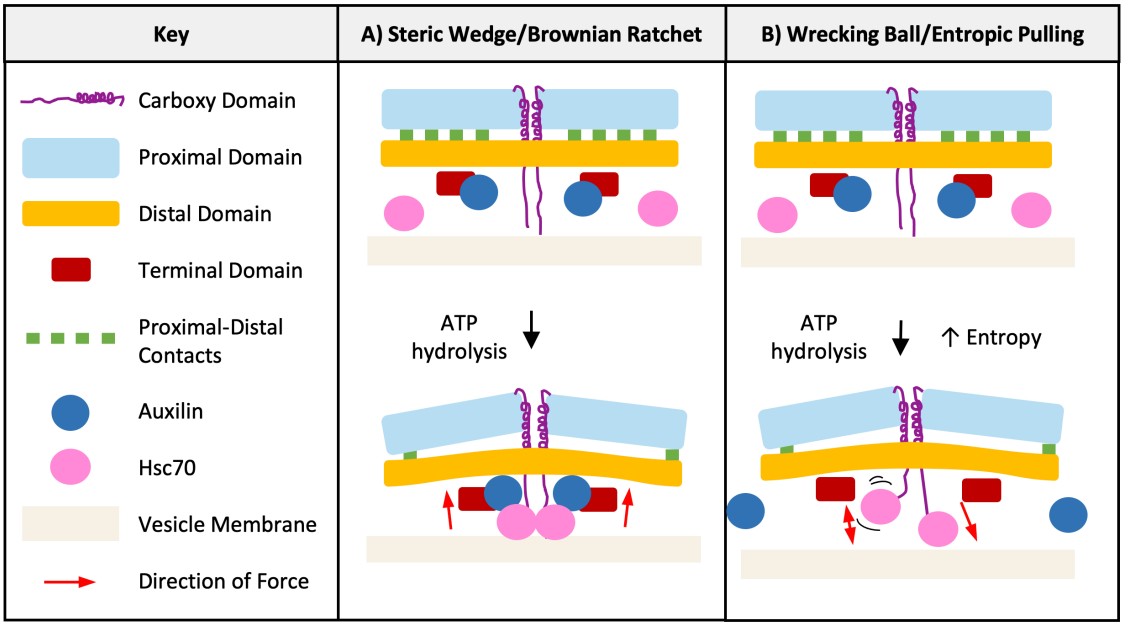

Figure 1.2.3 - Clathrin uncoating mechanisms

Schematic diagram demonstrating the two models for hsc70 driven uncoating of clathrin cages; the steric wedge model and the entropic pulling model. Diagram is not to scale. Domains presented are from the clathrin heavy chain. Republished with permission of Portland Press, from Clathrin: the molecular shape shifter, Wood KM and Smith CJ, 478 (16), 2021(1); permission conveyed through Copyright Clearance Center, Inc. Licence: 1163059-1.

The rate in which uncoating proceeds not only depends on the quantity of ATP and CME adaptors present but also the stability of the clathrin coat, of which determines the number of structural perturbations needed for disassembly to occur (125). The cytoplasmic pH has an impact on the ratio of Hsc70 to clathrin triskelia required for disassembly, the highest ratio observed so far being 1:6 Hsc70 to clathrin triskelia (124,125,130). A drop in pH causes more histidine residues in CHCs to become protonated, specifically the proximal-distal residues

H867, H876, H1275, H1279, H1432 and H1458, which in turn strengthens the connections between triskelia leading to more Hsc70 and ATP being required for uncoating (125). Auxilin-clathrin interactions also increase coat stability, which is regulated by CLCs to control the level of coat stability and auxilins ability to perform catalytically. Regulation of auxilin by CLCs is achieved through CLC phosphorylation, causing auxilin dissociation from clathrin coats (41,131). *In vitro*, the optimal auxilin to clathrin concentration ratio for uncoating has been determined to be 1:1, with higher auxilin concentrations having minimal impact on uncoating; additional auxilins can still bind to clathrin cages though with up to three auxilins per vertex (118). *In vivo*, a smaller ratio of auxilin has been found to bind to clathrin coats, with around 2 to 20 auxilins bound to CCVs formed of between 36 and 100 triskelions (132). The results from *in vitro* and *in vivo* experiments thus suggests the concentration ratio of auxilin to clathrin does not necessarily match the number of auxilin molecules that will bind to CCV's (1). Despite this auxilin is still capable of acting catalytically, as auxilin can recruit multiple Hsc70 molecules to a clathrin vertex in sequence after successive rounds of ATP hydrolysis (118,124,132).

During clathrin uncoating, triskelia will separate from the CCV either individually or as partially uncoated intermediates (133). Auxilin will dissociate from the clathrin coats once Hsc70 conducts ATP hydrolysis, and as the coat disassembles, Hsc70 and adenosine triphosphate (ADP) will remain bound to the clathrin triskelia which explains why *in vitro* experiments of clathrin disassembly follows burst kinetics (118,119,124). Burst kinetics is where addition of limited quantity of protein or substrate causes rapid reaction rates initially followed by a slower steady-state as the protein or substrate is used and the amount of free protein or substrate becomes more scarce. The nucleotide exchange factor Hsp110 allows ADP to dissociate from the Hsc70-clathrin complex so that ATP hydrolysis by Hsc70 can occur to remove Hsc70 from the clathrin triskelia (42–46). Hsp110's ability to free up Hsc70 for additional rounds of uncoating could explain why differences in *in vitro* and *in vivo* kinetic

experiments are observed. *In vitro*, Hsc70 needs to be in excess for the maximum disassembly rate as Hsc70 remains bound to triskelia during disassembly, however, *in vivo* less Hsc70 is required to uncoat a CCV with a sixty triskelion clathrin coat being observed to only require ten Hsc70 molecules at a time for uncoating (118,132). As Hsp110 is present *in vivo* but not *in vitro*, Hsc70 can be recycled and would therefore follow steady kinetics as opposed to the burst kinetics seen *in vitro*.

1.3 CME and Health

CME has been shown to be associated with a range of different diseases such as Alzheimer's disease, Parkinson's disease and ARH. The association of CME with diseases varies from changes in CME protein expression to mutations in CME adaptors. Further details on the link between CME and Parkinson's disease, ARH, and Alzheimer's disease are detailed below.

Parkinson's disease leads to abnormality of movement, muscle tone and postural stability, which is caused by neuronal loss in the *substantia nigra* of the brain (134). Homozygosity mapping and whole exome sequencing has identified a deleterious mutation in auxilin associated with juvenile Parkinsonism, which leads to abnormal transcripts and reduced auxilin mRNA levels (134). Cellular analysis of the auxilin deleterious mutation is shown to confer a toxic gain-of-function and impairs endosomal transport (135). This is further supported by a *drosophila* Parkinson's disease model which showed reduced expression of auxilin leads to symptoms seen in Parkinson's disease (136). Phosphorylation of auxilin also has an impact as PD-linked leucine-rich repeat kinase 2 mediated phosphorylation of S627, which is found in the clathrin-binding region of auxilin, leads to differential clathrin binding causing synaptic CME to be disrupted; the Parkinson's disease phenotype can be partially recovered here by restoring auxilin function (137). Other CME adaptors besides auxilin are also associated with Parkinsonism. A homozygous mutation in the Sac domain of synaptojanin leads to development of Parkinson's disease in mice; these brains had elevated levels of parkin and auxilin levels, as well as endocytic defects (138). Therefore, research into auxilin would be advantageous for identifying new treatments for Parkinson's disease.

Alzheimer's disease is another neurodegenerative disease. Alzheimer's disease causes loss of neurons and synapses in the cerebral cortex and subcortical regions of the brain; this causes memory loss in sufferers and eventually leads to death (139). The loss of neurons is caused by an accumulation of misfolded

amyloid-β, called amyloid-β plaques, as well as aggregation of tau protein (139). Genome wide studies of Alzheimer's disease have found an association with the PICALM gene, of which encodes a phosphatidylinositol-binding clathrin assembly protein (140). The *PICALM* rs3851179 polymorphism allele G was found to increase the risk of Alzheimer's disease, whereas allele A decreased the risk (140). A depletion of PICALM in the brain has also been found to reduce levels of intracellular amyloid precursor protein, which could be beneficial for slowing or preventing Alzheimer's disease (141). Further research has shown that partial loss of PICALM leads to decreased amyloid-β production by regulating the CME of γ-secretase, an enzyme responsible for the formation of amyloid-β plaques (142). Therefore, research into CME assembly adaptor proteins could identify new ways in which Alzheimer's disease could be prevented or delayed, such as by inhibiting or controlling expression levels of adaptor proteins like PICALM.

Autosomal recessive hypercholesterolemia (ARH) is the last disease that will be discussed. ARH, unlike Alzheimer's disease and Parkinson's disease, is caused by defects in the LDL receptor gene; this leads to some cells being unable to mediate LDL receptor-dependent internalisation of LDL's, leading to high levels of plasma LDL's which in turn promotes atherosclerosis (143). ARH mediates LDL uptake by binding to LDL receptors and recruit clathrin and/or AP2 in order to initialise CME (144). Understanding how ARH interacts with clathrin is therefore important so that a greater understanding of the ARH disease mechanism can be understood, and to identify how mutations within ARH impact the CME of LDL's. CME accessory proteins are also associated with other pathways including mitosis, cell migration, spermiogenesis, hormone desensitisation and spermiogenesis (1). Mutations within CME accessory proteins or changes in their expression levels could therefore impact other pathways which may lead to different disease states. Further investigations of the impact of mutations and differing expression levels on different pathways would therefore be beneficial for better understanding the role of CME and CME accessory proteins on disease pathways.

1.4 The Structure of Clathrin

Clathrin's central role in CME, and the relevance of clathrin and its interaction with adaptors in health and disease has led to considerable efforts to obtain a structural understanding of clathrin assemblies (145). The current research on clathrin structure shall now be discussed.

1.4.1 Clathrin triskelia

Clathrin is a protein complex formed of a heavy chain of ~190 kDa in size, and a light chain of ~ 25 kDa in size, which come together to form a tripod-like triskelion structure, with each leg of the triskelion consisting of a heavy chain and a light chain as demonstrated in figure 1.4.1 (146,147).

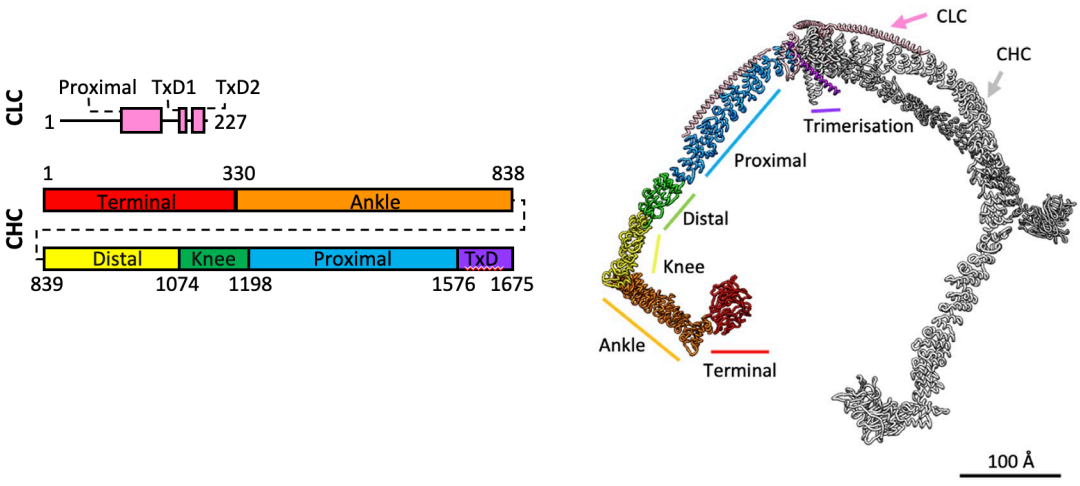

Figure 1.4.1 – Structure of clathrin triskelia

Schematic diagram showing the length and domains found within a CHC and CLC (left), and a ribbon diagram of a clathrin triskelion (right). The Clathrin triskelion consists of three CHCs ~190 kDa in size [grey] and three CLCs ~25 kDa in size [pink]. The CHCs are joined together at the trimerization domain [purple]. Republished with permission of Portland Press, from Clathrin: the molecular shape shifter, Wood KM and Smith CJ, 478 (16), 2021(1); permission conveyed through Copyright Clearance Center, Inc. Licence: 1163059-1.

The CHC consists of a 45-residue carboxy-terminal segment, followed by 42 alpha helices arranged in a zigzag-like structure that form the curved legs of the

triskelion, followed by a seven WD40 repeat β-propeller domain at the amino terminal (148). The CLCs, of which there are two spliced variants in mammals called CLCa and CLCb, interact with the proximal segment of the CHC *via* several residues with tryptophan residues as the key binding determinants. The segment of the CLC interacting with the CHC has an alpha-helical structure, with the terminal regions of the CLC being disordered and not interacting with the CHC (148–151).

1.4.2 Clathrin coats and cages

During CME, clathrin triskelia will assemble to create CCV's. The size and shapes of these coats are heterogenous, with tomographic reconstruction demonstrating a variety of different clathrin lattices from *bovine* brains, as shown in figure 1.4.2 A (152,153). These CCV's obtained from *bovine* brains have clathrin coats of around 700 - 800 Å in diameter, which enclose a vesicle of around 400 Å in diameter, however, much larger coats can be formed as CCV's obtained from a human placenta have been shown to range between 1000 – 1350 Å in diameter (152,154). The traces of the clathrin coats, as shown in figure 1.4.2 B, demonstrate a lattice containing primarily pentagons and hexagons, with some lattices containing heptagons and squares (152).

Clathrin can also assemble into cages *in vitro*, which are empty coat-like structures formed in the presence of Mg^{2+} or Ca^{2+} at pH 6.5 or less (146). The *in vitro* assembly of clathrin cages has allowed high resolution analysis *via* cryo-electron microscopy (cryo-EM), leading to the production of a 7.8 Å structure of a D6 clathrin coat, as demonstrated in figure 1.4.3 A, and recently the 4.7 Å structure of the clathrin coat consensus hub, as demonstrated in figure 1.4.3 B (35,148,155). The clathrin triskelia within cages have their centre associated with each lattice point, with the legs of the triskelia bending clockwise inwards as they interact with triskelia positioned at other lattice points to aid coat assembly (35,148). The bending of the triskelion legs suggests a level of flexibility within them that enables them to form cages as well as flat lattice

arrangements; this could be due to the zig-zag arrangement of α-helices within the legs of the clathrin triskelia, as changes in the conformation of the alpha helices would alter the position of the clathrin triskelion legs (35,148).

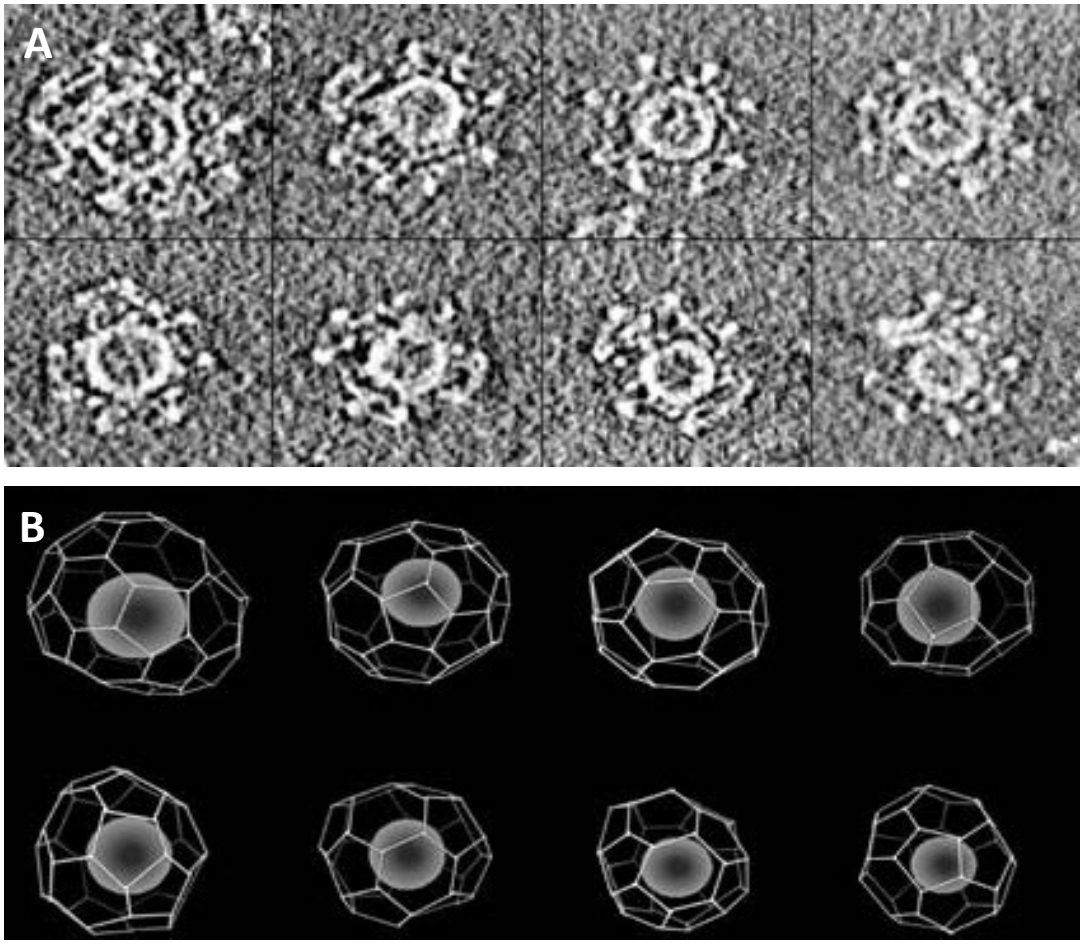

Figure 1.4.2 – Electron cryotomography of CCV's

Electron cryotomography images of CCV's obtained from brain cells. A) Original electron cryotomography images of CCV's. B) Traces of the clathrin coat (white) surrounding a lipid vesicle (grey). Reprinted from Journal of Molecular Biology, 365 (3), Yifan Cheng, Werner Boll, Tomas Kirchhausen, Stephen C. Harrison, and Thomas Walz, Cryo-electron Tomography of Clathrin-coated Vesicles: Structural Implications for Coat Assembly, 892-9, (2007) (152), with permission from Elsevier. Licence: 5153581147755.

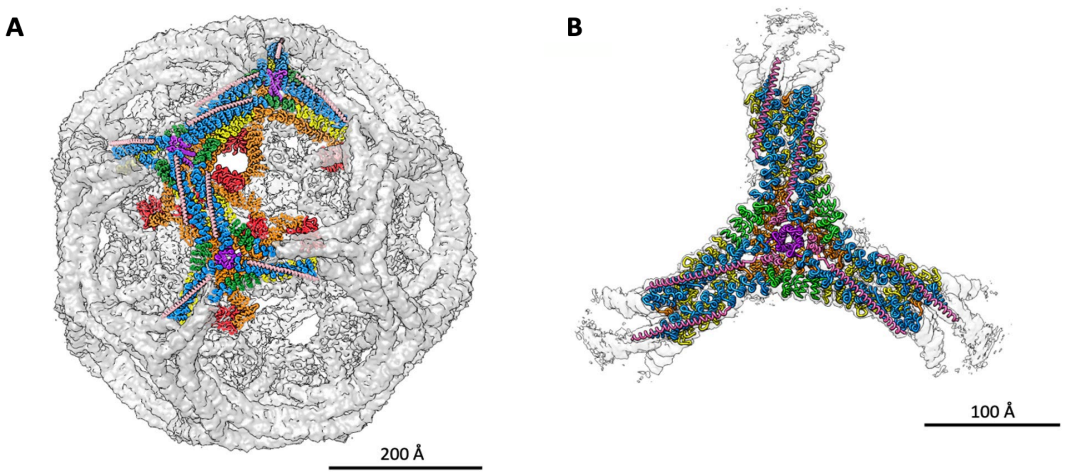

Figure 1.4.3 – Structure of a clathrin cage

Structure of CHCs and CLCs within a clathrin cage. Clathrin components shown include CLCs (pink), and CHC trimerisation domain (purple), proximal domain (blue), distal domain (green), knee region (yellow), ankle domain (orange) and terminal domain (red). A) Structure of a clathrin barrel cage [light grey] resolved to 7.9 Å [EMDB: 5119], of which was obtained from the structure of a clathrin AP2 complex, with fitted triskelion model [PDB: 1XI5] (1,148,155). B) Structure of a clathrin cage consensus hub [light grey] [EMDB:0126] resolved to 4.7 Å with fitted hub model [PDB: 6SCT] (35). Republished with permission of Portland Press, from Clathrin: the molecular shape shifter, Wood KM and Smith CJ, 478 (16), 2021(1); permission conveyed through Copyright Clearance Center, Inc. Licence: 1163059-1.

1.4.3 The clathrin terminal domain

The majority of interactions between clathrin and adaptors occurs at the terminal domain. But where and how do adaptors bind on the clathrin terminal domain? Figure 1.4.4 A shows the structure of the clathrin terminal domain which was determined using x-ray diffraction and has a resolution of 2.6 Å (156). The terminal domain has a 7-bladed β-propeller structure connected to short alpha-helices which form the start of the legs of clathrin triskelia (156). At present, four binding sites within the clathrin terminal domain have been identified which play a role in adaptor-clathrin interactions; these sites are called the clathrin box, the W-box, the arrestin box and the Royle box (27). Further details on these sites will now be discussed.

The clathrin box motif comprises of acidic and bulky hydrophobic residues L(L, I)(D, E, N)(L, F)(D, E) (LϕXϕ[DE]), and is highly conserved within adaptors including the β3-appendage of AP3, amphiphysin, arrestin3 segments, and β-arrestin 1 and β-arrestin 2 (160–164). Structures of clathrin terminal domain complexes with peptides derived from AP2, β-arrestin 2 and the β subunit of AP3 identified the location of the clathrin box motif binding site, with peptides binding in an extended conformation within the groove found between blades 1 and 2 of the clathrin terminal domain (162,165). Figures 1.4.4 A and 1.4.4 B demonstrates the binding site of the clathrin box motif on the clathrin terminal domain.

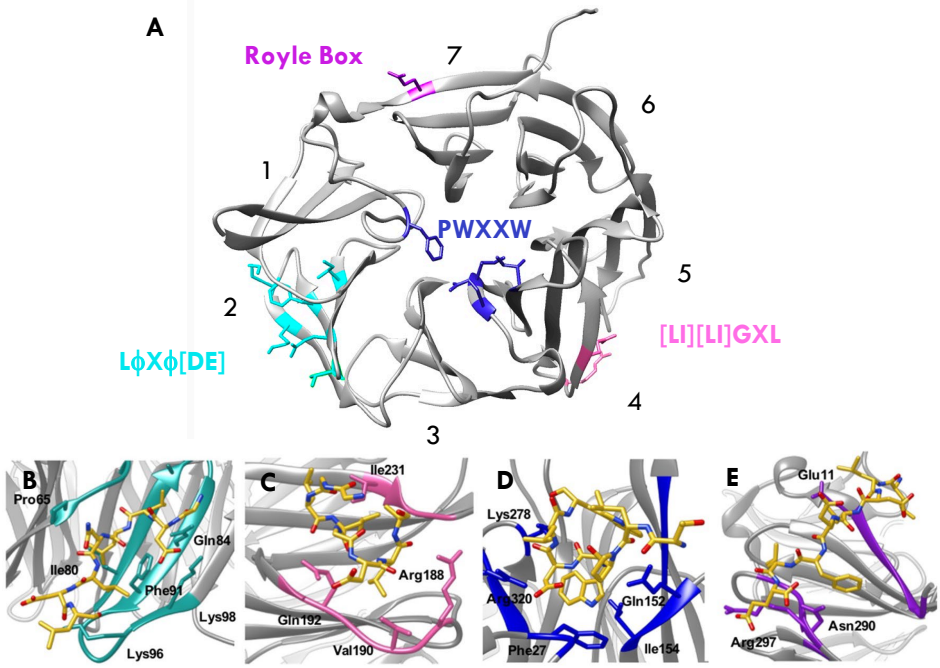

Figure 1.4.4 – Adaptor binding sites in the clathrin terminal domain

Structure of the clathrin terminal domain and the four known adaptor binding sites within. A) The clathrin terminal domain consists of a 7-bladed β-propeller containing four known adaptor binding sites. The clathrin box (LϕXϕ[DE]) is highlighted in cyan, the W-box (PWXXW) is highlighted in blue, the Arrestin-box ([LI][LI]GXL) is highlighted in pink, and the Royle box is highlighted in purple. B) β2-adaptin (CGDLLNLDLG) bound to the clathrin box. C) β-arrestin1L peptide (ALDGLLGG) bound to the arrestin box. D) amphiphysin peptide (TLPWDLWTT) bound to the W-box. E) An amphiphysin peptide bound to the Royle box. PDB codes: A) 1BPO (156); B) 5M5R (157); D) 3GD1 (158); D) 1UTC (159); E) 5M5T (157). Figure adapted from Frontiers in Molecular Biosciences, 4 (72), Smith SM, Baker M, Halebian M and Smith CJ, Weak Molecular Interactions in Clathrin-Mediated Endocytosis, (2017) (27) under the terms of the Creative Commons Attribution License (CC BY).

The arrestin box motif consists of residues [LI][LI]GXL, and binds between blades 4 and 5 of the clathrin terminal domain, as demonstrated in figures 1.4.4 A and 1.4.4 C (158). The W-box motif comprises of residues PWXXW within adaptors, and was identified from a 2.3 Å structure of the clathrin terminal domain bound to an amphiphysin 1 peptide (159). The W-box motif differs from the other box motifs as it binds within the centre of the β-propeller with a compact helical structure, as demonstrated in figures 1.4.4 A and 1.4.4 D (159). The final motif is called the Royle box motif which binds to blade 7 of the clathrin terminal domain as demonstrated in figures 1.4.4 A and 1.4.4 D, however, the motif required in adaptors to bind to this site is currently unknown (166).

1.5 Unanswered Questions on the…

1.5.1 Structural basis of clathrin-adaptor interactions

The structures obtained so far have only been of the clathrin terminal domain bound to peptides derived from adaptor proteins; all of which suggest unique binding to individual sites on the clathrin terminal domain (158,159,165). Solution-based NMR studies, however, have shown that clathrin-box peptides from AP180 can simultaneously bind to the clathrin box, W-box and the Royle box, suggesting multiple interactions are either required or possible for a stable interaction between the clathrin terminal domain and adaptors; this is further backed by glutathione sepharose transferase (GST) binding assays which show weak interactions that occur between clathrin and box motifs peptides derived from adaptors (164,169,170).

The multiple interaction theory was later confirmed by Muenzner *et al.* (2017) (157), who showed that the arrestin box and clathrin box motifs can bind to the arrestin box binding site on the clathrin terminal domain; this was achieved by crystallizing the clathrin terminal domain with the box peptide motifs. With the ability of different box motifs being able to bind to different box sites on the clathrin terminal domain, as well as the variability of sequences that can bind to the Royle box site, the idea of a single box motif being only able to bind to one binding site appears to be invalid (157,166). This leads to questions of where on the clathrin terminal domains accessory proteins bind, and are multiple conformations or binding locations observed? To better understand adaptor interactions with clathrin and its terminal domain, structures of adaptors bound to clathrin are required such as the clathrin-auxilin structure for example (107). As clathrin cage samples produce low resolution in cryo-EM, a new approach is required that will improve the resolution of the sample, which will allow identification of where adaptors are bound to the clathrin terminal domains and the residues involved in clathrin-adaptor binding.

1.5.2 Potential competition between adaptors

As mentioned previously, there are multiple regions in the clathrin terminal domain that can interact with adaptors, and the presence of multiple clathrin box motifs and DLL/DLF motifs allows adaptors to interact with multiple sites (167,169). This poses the questions, do adaptors compete for similar binding sites, to what extent does competition occur, and what impact does this have on adaptor function in CME? To better understand the potential competition that occurs between adaptors, kinetic based studies are required in the presence of multiple adaptor proteins to identify the effect competition may have on strength of adaptor binding, and the timings of CME processes. These hypotheses could be tested using techniques such as perpendicular light scattering (PLS), fluorescence anisotropy (FA), and surface plasmon resonance (SPR).

If PLS were to be used, a CME process would be required that can be conducted *in vitro*. As PLS observes the level of light scattering from particles, clathrin assembly or disassembly would be ideal processes to use as clathrin cage disassembly has previously been tested using PLS (118). The disadvantage of using PLS however, is that only the effect of individual adaptors on either auxilin, epsin and hsc70 binding to clathrin could be assessed due to the need for a process to create changes in light scattering. FA would remove this issue as the technique instead relies on changes in the anisotropy of particles, which are the changes to the level of rotational diffusion of fluorophores upon protein-protein interaction (171). This would allow the effects of competition between multiple adaptors to be studied, providing that fluorescent labelling does not impact the function of the adaptor or clathrin binding, and that binding of the adaptor to clathrin produces a significant change in anisotropy. SPR would go further to improve experimentation conditions as it would allow competition to be studied without the need for fluorescent labelling, thereby allowing clathrin-adaptor interactions and competition to be studied in their native state. But despite the several advantages of SPR , which include high sensitivity,

binding event specificity, and real time measurements, there are several disadvantages which make SPR less favourable to attempt initially over FA, including the expense of sensor chips and instrumentation, non-specific binding to surfaces, immobilisation effects, and the steric hindrance that occurs with binding events (172). In conclusion, FA would be the most beneficial technique for initial kinetics-based studies, however, SPR, perpendicular light scattering and other techniques such as isothermal calorimetry for example, are complimentary to FA and could be conducted alongside or after FA experiments have been completed to further support FA findings.

1.6 Research Questions and Aims

The current understanding of the interactions that occur between individual adaptor proteins and clathrin is limited to low-resolution cryo-EM structures and crystal structures of the clathrin terminal domain with bound peptides derived from adaptor proteins, despite having a growing databank on the role of adaptor proteins within endocytosis. There are still many questions with regards to how multiple adaptor proteins interact with clathrin cages, as well as the molecular details of these interactions. The overarching aim of this PhD project is thus to gain a greater understanding of how adaptor proteins interact with clathrin, and the impact these interactions have on the disassembly of clathrin cages. To achieve this, the following questions will be tested:

1. What is the structure of clathrin? What is the structure and orientation of the clathrin terminal domains and ankle regions in clathrin cages? Can we improve the resolution to visualise positioning of amino acids in clathrin cages and interactions that occur between them?

Despite the publication of several clathrin cage structures, all have been produced in the presence of at least one adaptor (35,107,123,155). To verify the structure of clathrin and the presence of adaptor densities bound to clathrin cages, a structure needs to be produced from a sample containing clathrin only. By using cryo-EM single particle analysis (SPA), this project aims to produce and develop clathrin cage and clathrin hub models which include the lower hub regions. By using localised reconstruction alongside SPA, as previously conducted by Morris *et al.* (2019) (35), this project also aims to obtain higher resolution information on CLCs and CHCs so that amino acids in upper hub regions and secondary structure details in lower hub regions can be resolved.

2. Where and how do adaptors bind to clathrin cages? Do different adaptors share the same binding sites?

Obtaining structural information on how adaptors interact with clathrin will provide insights into how these adaptors conduct their specific functions. Upon development of a structure of clathrin, this project aims to use cryo-EM SPA and localised reconstruction to develop and produce models of clathrin bound to adaptor proteins, to determine where on the clathrin terminal domain adaptors bind, and also to obtain a high enough resolution to distinguish which regions or residues of the adaptors interact with clathrin.

3. How do clathrin cages disassemble? Is it all the cage at once or in stages?

Mechanisms have been proposed to describe how auxilin and hsc70 can cause clathrin disassembly, however, no studies have been conducted so far to try and visualise this process in real time. By using cryo-electron tomography (cryo-ET) on clathrin cages incubated with ATP, Hsc70 and auxilin, this project aims to visualise the clathrin disassembly process and capture intermediate states of disassembling clathrin cages, enabling new information on the clathrin disassembly mechanism to be discerned.

4. How tightly do adaptors bind to clathrin and how quickly do they interact with one another? Is this impacted when other adaptors are present?

Studies using PLS have been previously conducted to assess clathrin disassembly by hsc70 and auxilin, however, no studies so far have analysed competition that may occur between adaptor proteins (118). Using fluorescently labelled versions of hsc70 and auxilin, this project aims to use PLS and FA to determine whether FA can be utilised to assess the binding affinity of adaptors with clathrin, and determine which adaptors compete with hsc70 and auxilin for similar binding sites. Use of stopped flow FA will also be pursued to gain information on the timing of adaptors binding to clathrin, and how the presence of potentially competitive adaptors may impact this rate.

This page is intentionally left blank

Chapter 2:

Materials and General Methods

Chapter Overview

Details on the general materials and methods used for the experiments in this thesis can be found within this chapter. This will also include details on where materials and equipment have been acquired, the composition of buffers, what protein constructs were used and how they are quantified, and the generation and use of competent cells.

2.1 Materials and Equipment

Agar Scientific (UK): Formvar/Carbon 300 mesh copper grids.

Agilent: Cary UV-Vis spectrophotometer.

AMRESCO (USA): HEPES free acid.

Applichem Lifesciences (USA): Dithiothreitol (DTT), Sodium dodecyl sulphate (SDS).

Beckman: JA8.1 rotor, JLA25.5 rotor, Ti45 rotor, TLA100.3 rotor, TLA120.1 rotor, Avanti high speed centrifuge, XPN-80 ultracentrifuge, Optima max E benchtop ultracentrifuge.

Benchmark scientific: MyTEMP mini digital incubator.

Bio-logic SAS: MOS-450 with SFM-400 attachment, Bio-Kine32 software.

Biorad: Gel electrophoresis gel casting kits and tetra-running tanks.

Expedeon (UK): Instant Blue.

First Link Ltd. (UK): Porcine brain.

Fisher Scientific (UK): Ammonium sulphate, Glycerol, Magnesium acetate tetrahydrate, Calcium chloride ($CaCl_2$), Potassium acetate, Potassium chloride (KCl), Sodium chloride (NaCl), Sodium hydroxide (NaOH), Magnesium sulphate ($MgSO_4$), Fisherbrand model 50 sonic dismembrator, Biosafety cabinets, Vacuum pump.

Gatan: OneView IS camera, K2 counting electron detector.

GE Healthcare (USA): Ficoll TM PM70, Glutathione Sepharose 4B, GSTrap FF column, HiTrap Q HP anion exchange column, HiLoad 26/600 Superdex 200 column, HiPrep 26/60 Sephacryl S-500 HR, XK 16/100 Superdex 75 column, ÄKTA FPLC system.

GenScript: Prescission protease.

IVYX Scientific: Digital water bath

Jasco: FP-6500 fluorimeter.

JEOL: 200 kV 2100 Plus TEM, 200 kV 2200FS TEM.

Melford Laboratories Ltd. (UK): Isopropyl ß-D-1-thiogalactopyranoside (IPTG).

Medicell Membranes Ltd. (UK): Visking dialysis tubing 19 mm 12-14 kDa cut-off.

National Diagnostics (USA): 30% w/v Accugel 29:1 acrylamide to bis-acrylamide.

New Brunswick Scientific: Innova large capacity stackable shacking incubator.

New England Bioscience (USA): Color pre-stained protein standard broad range (11-245 kDa).

PanReac AppliChem (USA): 4-(2-Aminoethyl) benzenesulfonyl fluoride hydrochloride (AEBSF).

Qiagen (Germany): QIAprep Spin Miniprep Kit.

Roche Diagnostics Ltd. (Switzerland): c0mplete HisTrap (5 mL) column, c0mplete Protease Inhibitor Tablets.

Sanco: Ultra low temperature freezer 500L capacity with condensor.

Sartorius Stedim (Germany): Analytical balance, Precision balance, Vivaspin 20 centrifugal concentrators.

Sigma-Aldrich (UK): Ammonium per sulphate (APS), Ampicilin, ATP-agarose 4B cyanogen bromide activated (ATP-Agarose), Adenosine triphosphate (ATP) disodium, Ethylene-diamine-tetraacetic acid (EDTA), Ethylene-glycol-bis(ß aminoethyl ether)-tetraacetic acid (EGTA), Reduced glutathione (GSH), MOPS, Hydrochloric acid (HCl), Imidazole, Kanamycin, Magnesium chloride hexahydrate ($MgCl_2$), Manganese chloride ($MnCl_2$), Sucrose, Triethylamine (TEA), Tetra-methyl-ethylene-diamine (TEMED), Thrombin, Tris-(hydroxymethyl)-amino-methane (Tris-base), Tris-(hydroxymethyl)-aminomethane-hydro-chloride (Tris-HCl), Rubidium chloride (RbCl), Nicotinamide adenine dinucleotide reduced (NADH), Pyruvate kinase/Lactic dehydrogenase enzyme mix from rabbit muscle, Phosphoenol pyruvate monopotassium salt, Apyrase from potato.

Stuart: Magnetic stirrer plates.

TAAB Laboratories equipment Ltd: Quantifoil r 1.2/1.3 300 mesh copper grids, Quantifoil r 3.5/1 200 mesh copper grids, Tweezers type 5 Revia SS A/Mag.

Thermo fisher scientific: Zebra spin desalting columns 7K MWCO 0.5 mL, Reagecon buffer solutions at pH 4, 7 and 10, Alexa Fluor 488 C_5 maleimide, NanoDrop 2000, FEI Titan Krios G3.

University of Warwick Stores: Disposable consumables (*i.e.*, PPE, Eppendorf tubes, pipette tips, inoculation loops, spreaders, foil, clingfilm, tape, *etc.*).

VWR Chemicals (UK): Bromophenol blue, Ethanol, Methanol.

2.2 Buffers

Buffers used within this thesis are detailed below. The pH of these buffers was measured using a Mettler Toledo Seven Easy pH meter and adjusted using HCl and NaOH. The probe attached to the meter was calibrated using standards at pH 4, 7 and 10.

10 × HKM Buffer pH 7.2: 250 mM HEPES, 1.25 M potassium acetate and 50mM magnesium acetate.

Ficoll/Sucrose solution: 6.25% Ficoll PM70 (w/v) and 6.25% Sucrose (w/v) in HKM Buffer pH 7.2.

2 M Tris pH 7.1: 100 mM Tris-base, 1.9 M Tris-HCl, 2 mM EDTA and 2 mM DTT.

Saturated ammonium sulphate: 77% ammonium sulphate (w/v) in 10 mM Tris 0.1 mM EDTA pH 7. Buffer was boiled and stirred for 30 minutes before storage.

Depolymerisation Buffer pH 8: 20 mM TEA, 1 mM EDTA and 1 mM DTT.

Polymerisation Buffer pH 6.4: 100 mM MES, 1.5 mM $MgCl_2$ and 0.2 mM EGTA.

SDS-PAGE Loading Dye: 250 mM Tris-HCl pH 6.8, 5% SDS, 25% glycerol, 50 mM DTT and 350 μM bromophenol blue.

TFB1 Buffer pH 5.8: 30 mM Potassium acetate, 10 mM $CaCl_2$, 50 mM $MnCl_2$, 100 mM RbCl and 15% glycerol [pH was adjusted with acetic acid].

TFB2 Buffer pH 6.5: 10 mM MOPS, 75 mM $CaCl_2$, 10 mM RbCl and 15% glycerol.

Buffer A pH 7: 20 mM HEPES, 25 mM KCl, 3 mM $MgCl_2$ and 1 mM DTT.

Buffer B pH 7: 20 mM HEPES, 25 mM KCl, 10 mM EDTA and 1 mM DTT.

Buffer C pH 7: 40 mM HEPES, 75 mM KCl, 4.5 mM Magnesium acetate and 1 mM DTT.

Buffer D pH 7.9: 25 mM Tris-HCl, 500mM NaCl and 1 mM DTT.

High Salt Buffer pH 7: 20 mM HEPES, 1 M KCl, 1 M NaCl, 3 mM $MgCl_2$ and 1 mM DTT.

Low Salt Buffer pH 7: 20 mM HEPES, 3 mM $MgCl_2$ and 1 mM DTT.

2.3 Buffers and Agar Plates Prepared and Sterilised by University of Warwick Prep Services

SDS-PAGE Running buffer pH 8.3: 25 mM Tris, 150 mM Glycerol, and 35 mM SDS.

Luria broth (LB): 10:5:5 w/w ratio of Peptone, Yeast extract and NaCl in 1 L of water.

2YT: 16:10:5 w/w ratio of Tryptone, Yeast extract and NaCl in 1 L of water.

Auto induction media (AIM): Formedium AIM 2YT with trace elements media was used, which contains 16:10:3.3:6.8:7.1:0.5:2:0.15:0.004 w/w ratio of Tryptone, Yeast extract, Ammonium sulphate, KH_2PO_4, Na_2HPO_4, Glucose, Lactose, $MgSO_4$, and 100X Trace elements in 1 L of water.

LB Ampicillin Agar plates: 15:10:5:5 w/w ratio of Agar, Peptone, Yeast extract and NaCl in 1 L of water with 100 μg/mL Ampicillin.

Super optimal broth with catabolic repression (S.O.C.): 2% Tryptone, 0.5% yeast extract, 10 mM NaCl, 2.5 mM KCl, 10 mM $MgCl_2$, 10 mM Magnesium sulphate, and 20 mM glucose.

Ampicillin: 100 mg/ml Ampicillin in water.

2.4 Protein Constructs

Table 2.4.1 provides details on the DNA constructs used for protein expression and purification.

Table 2.4.1 – DNA constructs used for protein expression and purification

Construct	Properties	Reference	Source
WT auxilin (401-910) in pGEX4T2	GST-tagged auxilin (401-910) from *Bovine.*	(173)	Helen Kent (MRC LMB)
SC auxilin (401-910) mutants in pGEX4T2	A cysteine-less version of GST-tagged auxilin (401-910) with one cysteine remaining at either position 427, 438, 835 or 899 from *Bovine.*	NA	Alice Rothnie (University of Warwick)
WT Hsc70 in pET15b	His-tagged Hsc70 from *Bovine.*	NA	Michael Baker (University of Warwick)
S603C Hsc70 in pET15b	A cysteine-less version of His-tagged Hsc70 with one cysteine at position 603 from *Bovine.*	NA	Michael Baker (University of Warwick)
ARH (180-270) in pGEX4T2	GST-tagged ARH (180-270) from *Homo sapiens.*	NA	Sarah Smith (University of Warwick)

Epsin 1 (1-575) in pET32c	His-tagged Epsin 1 (1-575) from *Rattus norvergicus.*	(174)	Ernst Ungewickell (Hannover Medical School)
AP180 (328-896) in pQE31	His-tagged AP180 (328-896) from *Rattus norvegicus.*	(174)	Ernst Ungewickell (Hannover Medical School)
β_2-adaptin (616-951) in pGEX6p1	GST-tagged β_2-adaptin (616-951) from *Homo sapiens.*	(175)	Steve Royle (University of Warwick)

Details the names and lengths of constructs, what plasmids they are within, what organisms their sequences originated from, the original references where they were first used, and where the constructs were sourced from.

2.5 Methods

2.5.1 Preparation of competent cells

Escherichia coli (*E. coli*) BL21 (DE3) cells were streaked onto an LB Agar plate and grown at 37 °C overnight. A single colony was taken and grown overnight in 5 ml LB at 37 °C. The overnight culture was used to inoculate 250 ml LB with 20 mM $MgSO_4$, which was grown at 37 °C until the optical density at 600 nm (OD_{600}) reached 0.4 - 0.6. Cells were pelleted at 4,500 ×g for 5 minutes at 4 °C. The cell pellet was resuspended in 100 ml of TFB1 Buffer pH 5.8 at 4 °C. Resuspended cells were incubated at 4 °C for 5 minutes, before being pelleted again at 4,500 ×g for 5 minutes at 4 °C. The cell pellet was resuspended in 10 ml of TFB2 Buffer pH 6.5 at 4 °C. Resuspended cells were incubated at 4 °C for 1 hour, before being separated into 50 µl aliquots, frozen in liquid nitrogen and stored at – 80 °C for up to 1 year.

2.5.2 Transformation of competent cells

A 50 µl aliquot of *E. coli* BL21 (DE3) competent cells were thawed on ice alongside the desired plasmid for no more than 5 minutes. A negative control was prepared by taking 10 µl of the competent cells. 1 µl of plasmid was added to the remaining 40 µl of competent cells and mixed by flicking. The cells were incubated on ice for 20 minutes, followed by a heat shock at 42 °C for 30 seconds. The cells were placed back on ice for 5 minutes before warm S.O.C. media was added [60 µl for the negative control; 240 µl for the transformation]. The cells were grown at 37 °C for 30 minutes at 180 rpm. The cells were then spread onto LB agar plates with 100 µg/ml Ampicillin [70 µl Negative control; 50 µl transformation; 50 µl of a 1 in 10 dilution of the transformation]. Plates were incubated overnight at 37 °C

2.5.3 SDS-PAGE

12 % acrylamide resolving gels consisting of 370 mM Tris-HCl pH 8.8, 0.1 % SDS, 0.1 % APS and 0.09 % TEMED were made, with a 4% acrylamide stacking gel consisting of 130 mM Tris-HCl pH 6.8, 0.1 % SDS, 0.1 % APS and 0.09% TEMED. SDS-PAGE loading dye was added to samples with a 1:1 v/v ratio to denature the proteins. Samples were loaded onto the gels alongside a colour pre-stained broad range protein marker (11-245 kDa). Gels were run at 180 V using BioRad electrophoresis equipment filled with SDS-PAGE running buffer pH 8.3.

2.5.4 DNA and protein quantification

Quantification of clathrin is detailed in section 2.8. Other proteins as well as plasmid DNA, which was prepared using a QIAprep spin miniprep kit, were quantified using a Thermo Scientific NanoDrop 2000 spectrophotometer. For DNA the mg/ml reading was taken, and for proteins the absorbance at 280 nm (A_{280}) was taken. An average was taken from three readings. Beer's law was then used to determine the protein concentration based on their extinction coefficients and A_{280} reading.

2.5.5 Negative staining

Formvar/carbon film 200 mesh copper grids were used for preparing negative stain samples. These grids were glow-discharged immediately prior to use to reduce the hydrophobicity of the grids. A volume of 5 µl of sample was added onto a grid and left for one minute. The grid was then blotted, and a drop of 2 % uranyl acetate was applied for one minute for staining purposes before the grid was blotted again; this staining and blotting process was conducted four times. Upon completing the staining and blotting process, the grid was left to dry for one minute before it was visualised on a 200 kV JEOL 2100Plus transmission

electron microscope fitted with a Gatan OneView IS camera at a nominal magnification of 20,000×.

2.5.6 Data, map, and model visualisation

Maps and models were visualised using UCSF Chimera (176). Quantitative data was analysed and plotted using GraphPad Prism version 9.2.0 for Windows, GraphPad Software, San Diego, California USA, www.graphpad.com.

Chapter 3:

Protein Purifications

Chapter Overview

This chapter provides details on the purification of proteins used for the experiments within this thesis. This includes purification of clathrin from porcine brains, and purification of recombinant proteins from *E. coli*.

3.1 Methods

3.1.1 ACTA FPLC

UV absorbance of proteins was measured at 280 nm. Solutions were injected onto columns at 1ml/min. Size exclusion columns were washed up to 3ml/min with a max pressure of 0.5 MPa, while all other columns were washed up to 5ml/min with a max pressure of 0.5 MPa. 10 ml fractions were collected for all purifications with the exception of β_2-adaptin, AP180 and epsin1 size exclusion purifications where 2ml fractions were collected.

3.1.2 Clathrin purification

Clathrin was purified from a porcine pig brain source. Up to 12 porcine brains were removed from -80 °C storage and left to defrost for 10 minutes in HKM Buffer pH 7.2 supplemented with protease inhibitor tablets, before blending to a liquid puree using a standard kitchen blender. Blended brains were spun at 12,000 ×g for 30 minutes at 4 °C in a high-speed centrifuge. Collected supernatant was further spun at 140,000 ×g for 45 minutes at 4 °C using an ultracentrifuge. Pellets were homogenised in HKM Buffer pH 7.2 to release CCVs from cells. An equal volume of Ficoll/Sucrose solution was added to the homogenised pellet which was then spun at 44,000 ×g for 25 minutes at 4 °C in a high-speed centrifuge. Four times the volume of HKM Buffer pH 7.2 was added to the collected supernatant, which was subsequently spun at 140,000 ×g for 1 hour at 4 °C in an ultracentrifuge to pellet down the CCVs. Pellets were stored at 4 °C overnight. Pellets were resuspended in HKM Buffer pH 7.2 and homogenised. The homogenate was spun at 13,000 rpm for 10 minutes at 4 °C in a microcentrifuge. An equal volume of 2M Tris pH 7.1 was added to the supernatant and left at 4 °C for 1 hour to strip the clathrin coat from lipid vesicles. The solution was spun at 135,000 ×g for 30 minutes at 4 °C in a benchtop ultracentrifuge to remove the majority of lipids. Remaining lipids and

adaptor proteins were removed *via* size exclusion chromatography using an XK26/100 Sephacryl S500 column connected to an ÄKTA FPLC system and equilibrated in 1M Tris pH 7.1. SDS-PAGE of fractions was conducted to confirm purity before clathrin fractions were mixed with an equal volume of saturated ammonium sulphate and stored overnight at 4 °C.

Clathrin precipitate was pelleted at 48,000 ×g for 30 minutes at 4 °C using a high-speed centrifuge. The pellet was resuspended in 1M Tris pH 7.1 before being dialysed in depolymerisation buffer for 4 hours with one buffer change. Insoluble aggregates were pelleted at 130,000 ×g for 30 minutes at 4 °C using a benchtop ultracentrifuge. Supernatant was loaded onto a Superdex 200 column connected to an ÄKTA FPLC system and equilibrated in 1M Tris pH 7.1 to remove remaining contaminants. SDS-PAGE of fractions was conducted to confirm purity, before the clathrin-containing fraction were mixed with an equal volume of saturated ammonium sulphate and stored overnight at 4 °C. Clathrin was pelleted at 48,000 ×g for 30 minutes at 4 °C using a high-speed centrifuge. Pellets were resuspended in 1 M Tris pH 7.1 and dialysed against depolymerisation buffer pH 8 for 4 hours at 4 °C with one buffer change, followed by dialysis in polymerisation buffer pH 6.4 overnight at 4 °C with one buffer change after 2 hours. Polymerised clathrin was harvested by spinning the sample at 140,000 ×g for 20 minutes at 4 °C using a benchtop ultracentrifuge, followed by resuspension of the pellet in 200 µl of polymerisation buffer pH 6.4. Clathrin cages were stored at 4 °C for up to 3 weeks.

Purified clathrin was quantified using a Cary 100 UV-VIS spectrophotometer. The absorbance between 250 nm and 350nm was recorded for a 200 µl solution of 1 M Tris pH 7.1 followed by a dilution series of clathrin which involved adding 2 - 8 µl of clathrin solution to 200 µl of 1 M Tris pH 7.1. The dilution series was used to determine what the absorbance reading would be for the clathrin stock. Clathrin concentration was determined using Beer's law and extinction coefficient for CHC with CLCb [222780 M^{-1} cm^{-1}].

3.1.3 Expression of adaptor proteins

Constructs were expressed in *E. coli* BL21 (DE3) cells. Small 10 ml cultures were grown in LB with 100 μg/ml Ampicillin at 37 °C 180 rpm for up to 16 hours. Large cultures were prepared in 2L flasks, with ARH *E. coli* cells specifically grown in baffled flasks, by mixing a 10 ml overnight culture with 800 ml media containing 100 μg/ml Ampicillin and 10 mM $MgCl_2$. Details of incubation conditions are within table 3.1.1 for each construct.

Table 3.1.1 – Expression conditions for constructs

Construct	Media	Initial temp (°C)	Desired OD_{600}	IPTG induction (mM)	Final temp (°C)	Time (hours)
Auxilin	LB	37	0.8-1.0	1	25	18
β_2-adaptin	LB	37	0.6-0.8	0.8	22	18
ARH	AIM	37	-	-	37	4
Hsc70	LB	37	0.3-0.4	0.5	16	19
Epsin 1	LB	37	0.6-0.8	1	22	4
AP180	LB	37	0.6-0.8	0.5	22	18

Details the expression conditions used for GST-tagged protein constructs. All cultures were grown at 180 rpm.

Induced cultures were pelleted at 4,000 ×g for 10 minutes at 4 °C using a high-speed centrifuge. Pellets were stored at -20 °C for up to three months.

3.1.4 Purification of GST-tagged proteins

Pellets were thawed and resuspended in 25 ml Buffer A pH 7 with a crushed protease inhibitor tablet. The resuspension was sonicated on ice five times at

40 – 50 % power for 15 seconds with 30 second breaks which included mixing *via* inversion. The sonicated cell suspension was spun at 44,000 ×g for 30 minutes at 4 °C using a high-speed centrifuge to separate the soluble and insoluble fractions. The soluble fraction was loaded onto a GSTrap FF column connected to an ÄKTA FPLC system which was equilibrated in Buffer A pH 7 at 4 °C. The column was washed with Buffer A pH 7 until UV absorbance returned to baseline. The GST-tagged construct was eluted using Buffer A pH 7 supplemented with 10 mM GSH. SDS-PAGE of fractions was conducted to confirm adaptor presence, before fractions were collated and dialyzed against Buffer A pH 7 overnight at 4 °C to remove GSH.

For GST-auxilin, 10 units of thrombin per mg of protein was added to cleave the GST-tag. The auxilin thrombin mix was dialyzed against Buffer A pH 7 for 4 hours at 4 °C, before 0.2 mM AEBSF was added to inhibit further thrombin cleavage. For GST-β_2-adaptin, 2 units of PreScission protease per 100 µg of protein was added to cleave the GST-tag. The β_2-adaptin PreScission mix was dialyzed against Buffer D pH 7 supplemented with 1 mM EDTA for 3 hours at 4 °C. ARH did not have its GST-tag removed due to its small size. For auxilin and β_2-adaptin, the adaptor was loaded onto a GSTrap FF column connected to an ÄKTA FPLC system at 4 °C, which was equilibrated in either Buffer A pH 7 for the auxilin purification or Buffer D pH 7 supplemented with 1 mM EDTA for the β_2-adaptin purification. The column was washed with the same buffer used to equilibrate the column until the UV absorbance returned to baseline. GST-tag was eluted using the wash buffer supplemented with 10 mM GSH. SDS-PAGE of fractions was conducted to confirm adaptor presence in the flow-through before adaptor fractions were collated.

A final purification step was conducted to remove additional contaminants from each adaptor, with a different technique used for each construct. For auxilin and ARH constructs, the adaptor was spin concentrated at 4 °C using a VIVAspin 10,000 MWCO until a final volume of <1 ml was reached. The adaptor solution was made up to 20 ml using Low Salt Buffer pH 7 and loaded onto a HiTrap Q

HP anion exchange column equilibrated in Low Salt Buffer pH 7, of which was connected to an ÄKTA FPLC system at 4 °C. The auxilin construct was washed with 3 % High Salt Buffer pH 7 until the UV absorbance returned to baseline, followed by an elution with 6 % High Salt Buffer pH 7 until the UV absorbance returned to baseline, followed by a wash with 30 % High Salt Buffer pH 7 to remove contaminants from the column. The ARH construct was washed with 8.5 % High Salt Buffer pH 7 until the UV absorbance returned to baseline, followed by an elution with 14 % High Salt Buffer pH 7 until the UV absorbance returned to baseline, followed by a wash with 50% High Salt Buffer pH 7 to remove contaminants from the column. SDS-PAGE of fractions was conducted to confirm adaptor presence in the elution step before adaptor fractions were collated and dialyzed against either Buffer C pH 7 (for interaction studies) or Polymerisation Buffer pH 6.4 (for Cryo-EM studies) overnight at 4 °C.

For β_2-adaptin, the adaptor was spin concentrated at 4 °C using a VIVAspin 10,000 MWCO until a final volume of <10 ml was reached. The adaptor solution was loaded onto a HiLoad 26/600 Superdex 200 column connected to an ÄKTA FPLC system at 4 °C, which was equilibrated in 1 M Tris pH 7. The column was washed with 1 M Tris pH 7 until UV absorbance returned to baseline. SDS-PAGE of fractions was conducted to confirm adaptor presence before adaptor fractions were collated and dialyzed against Buffer C pH 7 overnight at 4 °C.

All adaptors were spin concentrated at 4 °C using a VIVAspin 10,000 MWCO and quantified as stated in section 2.8 using the extinction coefficients 58565 M^{-1} cm^{-1} for auxilin, 55725 M^{-1} cm^{-1} for ARH, and 29910 M^{-1} cm^{-1} for β_2-adaptin. The adaptor was aliquoted into 40 µl aliquots once a concentration of > 200 µM was reached. Aliquots were frozen in liquid nitrogen and stored at – 80 °C for up to 12 months.

3.1.5 Purification of His-tagged proteins

Pellets were thawed and resuspended in 25 ml of buffer with a crushed protease inhibitor tablet, with Hsc70 placed in Buffer A pH 7, and epsin 1 and AP180 placed in Buffer D pH 7.9. Resuspended pellets were sonicated on ice five times at 40 – 50 % power for 15 seconds, with 30 second breaks with mixing with inversions. AP180 sonicated suspensions were heated in a boiling water bath for 3 minutes, followed by shock cooling in an ice water bath for 5 minutes. Adaptor suspensions were spun at 4 °C at 44,000 ×g for 30 minutes for Hsc70 and epsin 1, and 1 hour for AP180 to separate the soluble and insoluble fractions. The soluble fraction was loaded onto a HisTrap column connected to an ÄKTA FPLC system at 4 °C, which was equilibrated in Buffer A pH 7 for Hsc70, or Buffer D pH 7.9 for epsin 1 and AP180. The column was washed with buffer until UV absorbance returned to baseline. His-tagged adaptors were eluted using buffer supplemented with 250 mM Imidazole. SDS-PAGE of fractions was conducted to confirm adaptor presence before collating adaptor containing fractions.

For Ap180 and epsin 1, the adaptor was spin concentrated at 4 °C using a VIVAspin 10,000 MWCO until a final volume of <10 ml was reached. The adaptor was loaded onto a HiLoad 26/600 Superdex 200 column connected to an ÄKTA FPLC system at 4 °C and equilibrated in Buffer D pH 7.9. The column was washed with Buffer D pH 7.9 until UV absorbance returned to baseline. SDS-PAGE of fractions was conducted to confirm adaptor presence before adaptor-containing fractions were collated and dialyzed against Buffer C pH 7 overnight at 4 °C.

For Hsc70, the adaptor solution was supplemented with 1/50th the volume of 0.5 M EDTA pH 8, before being dialyzed against Buffer B overnight at 4 °C to remove imidazole. Magnesium was added to the solution after dialysis by adding 1/500th the volume of 2M $MgCl_2$. Hsc70 was loaded onto an ATP Agarose column connected to an ÄKTA FPLC system at 4 °C and equilibrated in Buffer A pH 7. The column was washed with Buffer A pH 7 supplemented with 1 M KCl until

UV absorbance reading returned to baseline, followed by 50 ml Buffer A pH 7. Hsc70 was eluted using 100 ml Buffer A pH 7 supplemented with 3 mM ATP. SDS-PAGE was conducted to confirm adaptor presence before Hsc70 containing fractions were collated and spin concentrated at 4 °C down to < 10 ml using VIVAspin 10,000 MWCO. Hsc70 solution was loaded onto a Superdex 75 16/60 column connected to an ÄKTA FPLC system at 4 °C and equilibrated in Buffer A pH 7. The column was washed with Buffer A pH 7 to separate Hsc70 from ATP. SDS-PAGE of fractions was conducted to confirm Hsc70 presence, before fractions were collated and dialyzed against Buffer C pH 7 overnight at 4 °C.

Hsc70, epsin 1 and AP180 were spin concentrated using a VIVAspin 10,000 MWCO and quantified as stated in section 2.8 using the extinction coefficients 33350 M^{-1} cm^{-1} for Hsc70, 76430 M^{-1} cm^{-1} for epsin 1, and 23490 M^{-1} cm^{-1} for AP180. The adaptors were aliquoted into 40 µl aliquots once a concentration of > 200 µM was reached. These were frozen in liquid nitrogen and stored at – 80 °C for up to 12 months.

3.2 Clathrin Cage Purification

Size exclusion chromatography was used to separate clathrin from lipids and adaptor proteins, as demonstrated in figure 3.2.1 A. A further size exclusion chromatography step was conducted on depolymerised clathrin to remove insoluble aggregates, as shown in figure 3.2.1 B.

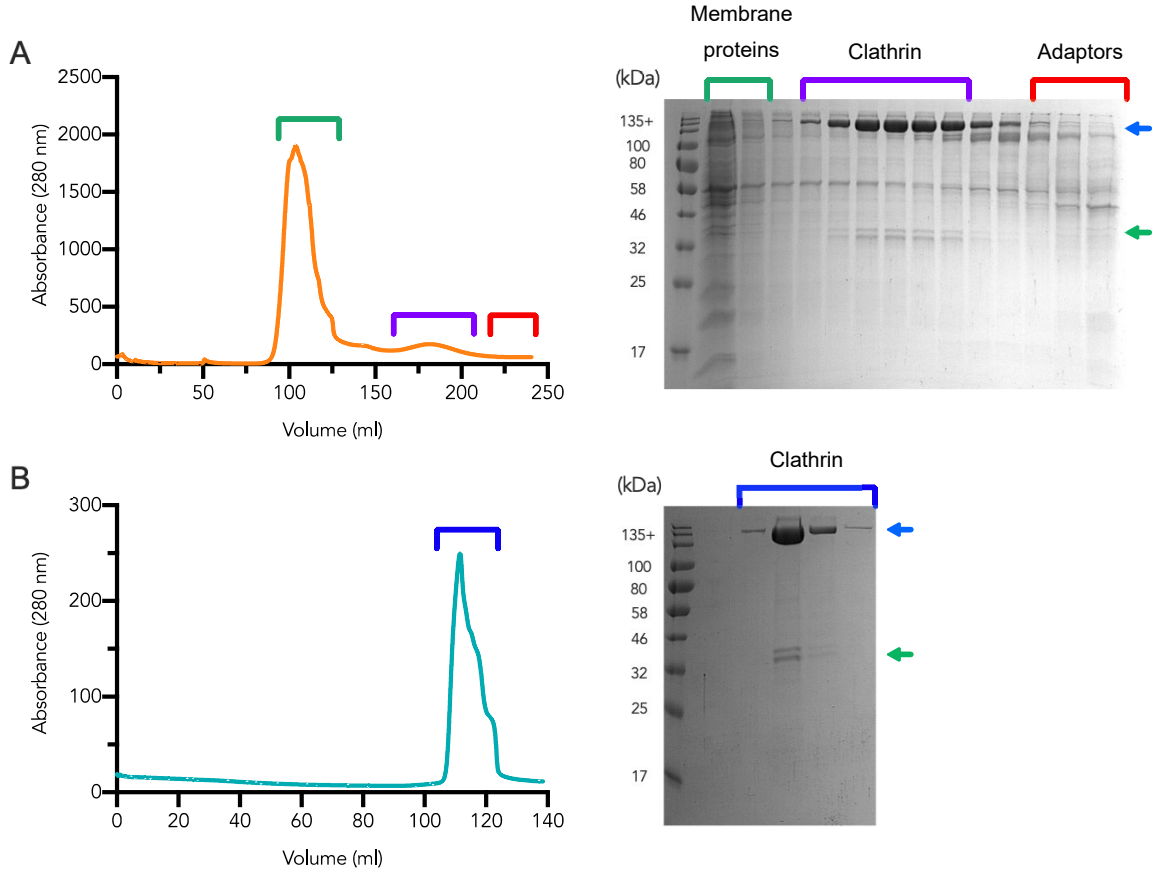

Figure 3.2.1 – Clathrin purification traces and SDS-PAGE gels

A280 absorbance traces and SDS-PAGE gels are presented on the left and right of the figure respectively. CHCs and CLCs are indicated by blue and green arrows respectively. A) Initial XK26/100 Sephacryl S500 size exclusion chromatography purification separating lipids and adaptor proteins from clathrin cages. Lipid runs off the column first between 90 ml and 140 ml, with clathrin running off the column after around 160ml to 210 ml of washing with a trail of adaptors following. B) Final Superdex 200 size exclusion chromatography purification separating depolymerised clathrin from insoluble aggregates. The clathrin appears to run off the column after 100 ml to 130 ml of washing, as confirmed by SDS-PAGE.

To quantify the clathrin stock, A280 readings from a dilution series was used to create a linear model, as shown in figure 3.2.2, allowing the A280 of the clathrin stock to be determined by setting the value of x to 1. The R^2 value of the linear model is 0.99. The stock concentration was then determined as stated in section 2.8 using the extinction coefficient for 1:1 CHC:CLCb [222780 M^{-1} cm^{-1}]. The CHC:CLCb extinction coefficient was used as use of the CHC extinction coefficient results in an overestimation of clathrin concentration due to its small extinction coefficient, and determination of the ratio of CLCs that varies per prep by mass spectrometry is too expensive. The extinction coefficient of CHC:CLCb [222780 M^{-1} cm^{-1}] is in the middle of the extinction coefficients for clathrin heavy chain [201810 M^{-1} cm^{-1}], and CHC:CLCa [229770 M^{-1} cm^{-1}], and is therefore a sufficient compromise.

3.2.1 Negative staining of clathrin cages

To confirm that clathrin had repolymerised into clathrin cages, negative staining of 0.1 μM of clathrin stock was performed. Negative stain images are presented in figure 3.2.3. These images showed that the clathrin had polymerised into cages of different sizes and had successfully been separated from lipid vesicles during purification. We can also conclude that the clathrin cages had not degraded during the purification and whilst in storage.

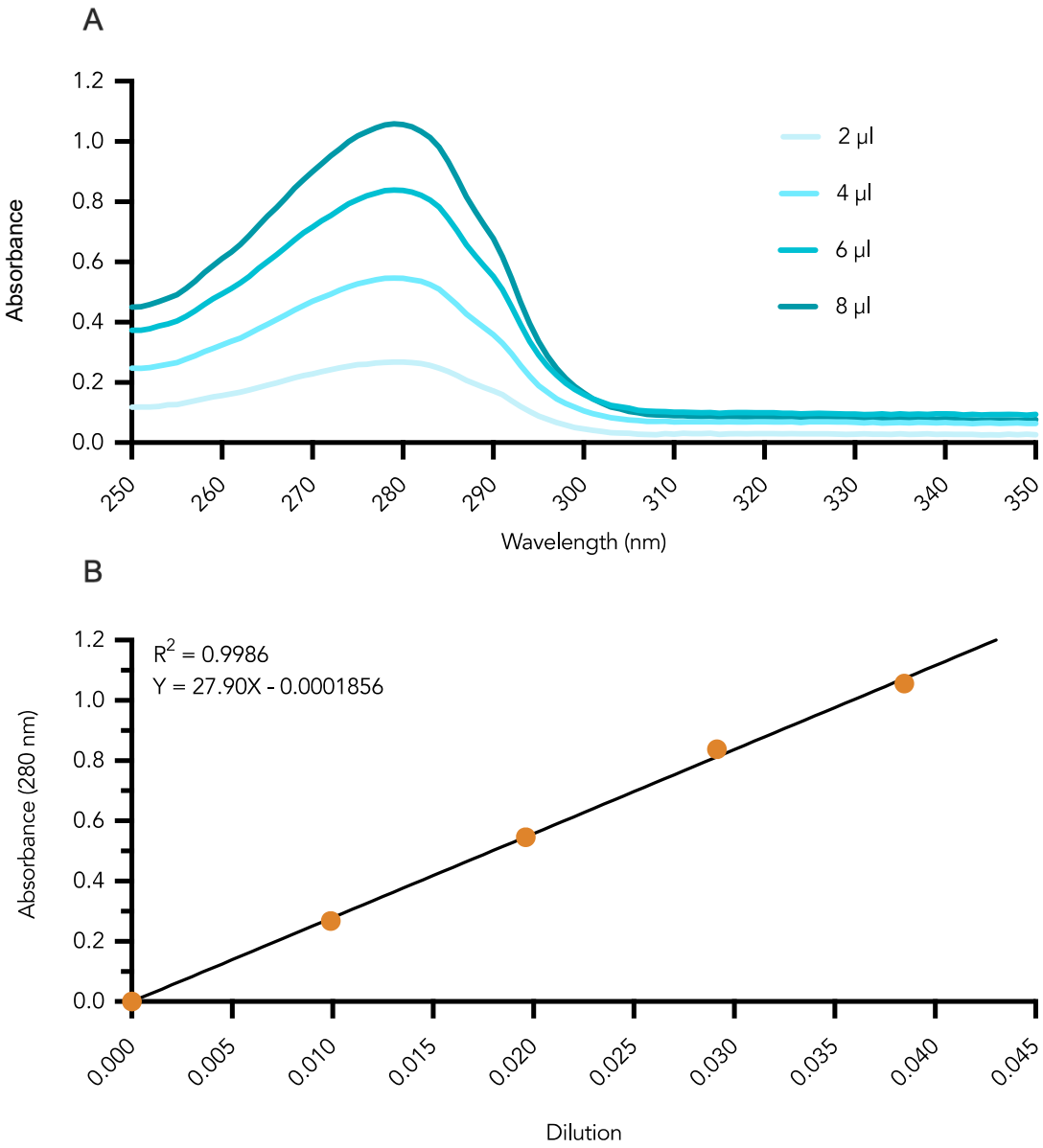

Figure 3.2.2 – Clathrin quantification

Graphs used to interpret A280 readings from the UV-visible spectrophotometer in order to quantify the purified clathrin cages. A) Corrected absorbance readings from 250 nm to 350 nm after accounting for tris buffer absorbance. The peak of absorbance is at 280 nm. B) A linear model produced from the corrected absorbance values at 280 nm. The equation of the linear model is used to calculate clathrin concentration, by setting X to 1.

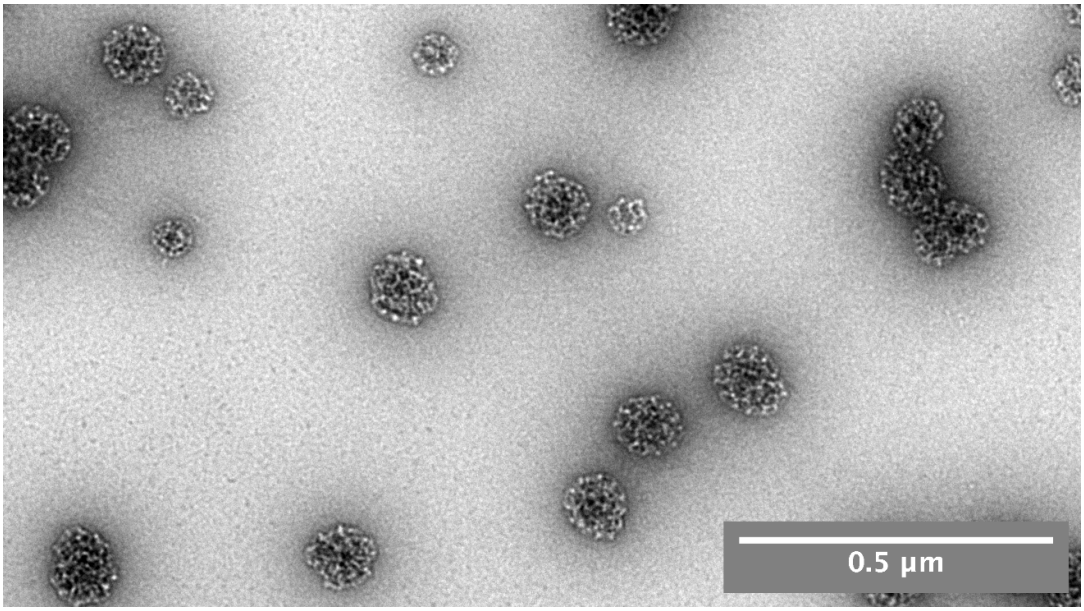

Figure 3.2.3 - Negative staining of clathrin

Transmission electron microscopy images of negatively stained clathrin. Images show clathrin had polymerised into cages and had not degraded. Visualisation of the lattice structure of the clathrin cage is apparent upon closer inspection.

3.3 Purification of GST-tagged Proteins

3.3.1 Auxilin

A three-step purification of auxilin constructs was conducted using a GSTrap FF column, which involved separation of auxilin from *E. coli* proteins followed by cleavage and removal of the GST-tag, and a HiTrap Q anion exchange column, which involved further removal of *E. coli* protein contaminants. The GST-tag was removed to ensure auxilin was in its native state, and to ensure there were no additional cysteines present from the GST-tag within the auxilin structures, as the mutant auxilin structures would be fluorescently labelled for use in fluorimetry experiments.

The purification steps are demonstrated in figure 3.3.1. Auxilin was successfully separated from the majority of *E. coli* proteins during the first affinity purification, as shown from the elution fractions of figure 3.3.1 A. The thrombin cleavage step removed the majority of the GST-tag from auxilin, as shown from the post-cleave fraction of figure 3.3.1 B. The majority of the GST-tag was separated from auxilin upon completing the second affinity purification, with auxilin coming off in the flow-through fractions, and the GST-tag coming off in the elution fraction as shown in figure 3.3.1 B. Ion-exchange removed a significant number of contaminants with auxilin coming off in the 6% High Salt Buffer pH 7 elution, as shown in figure 3.3.1 C.

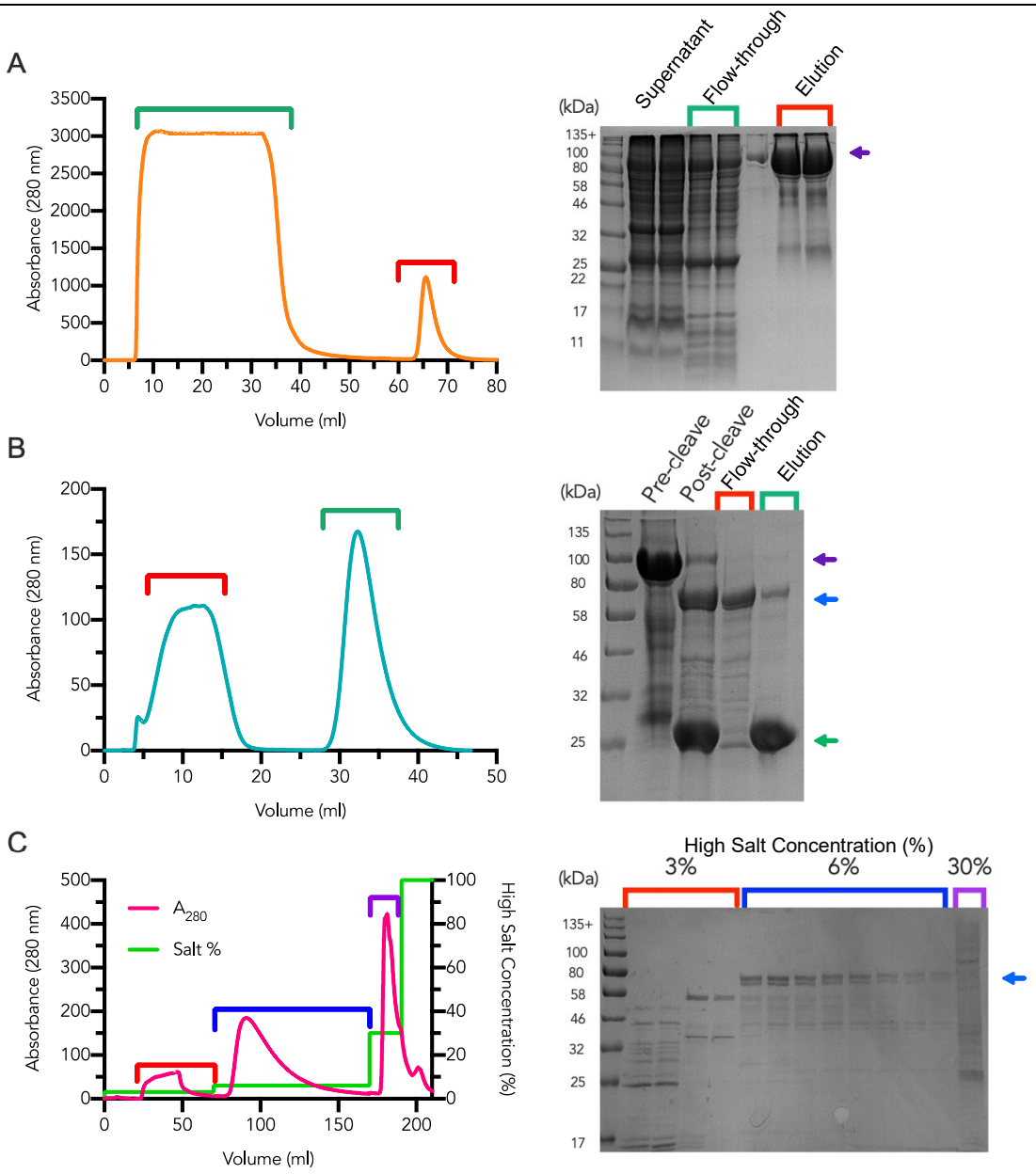

Figure 3.3.1 – Auxilin purification traces and SDS-PAGE gels

A280 absorbance traces and SDS-PAGE gels are presented on the left and right of the figure respectively. GST-auxilin is indicated by purple arrows, auxilin is indicated by blue arrows, and GST is indicated by the green arrow. The molecular weight of GST-auxilin, auxilin and GST-tag is 80 kDa, 54 kDa and 26 kDa respectively. A) Initial GSTrap FF affinity purification separating GST-tagged auxilin from *E. coli* proteins. B) Final GSTrap FF affinity purification step conducted after GST-tag cleavage, separating the cleaved GST-tag from auxilin. C) Final HiTrap Q anion exchange purification to remove additional *E. coli* protein contaminants.

3.3.2 β_2-adaptin

A three-step purification of β_2-adaptin was conducted using a GSTrap FF column, which involved separation of β_2-adaptin from *E. coli* proteins followed by cleavage and removal of the GST-tag, and a HiLoad 26/600 Superdex 200 column, which involved further removal of *E. coli* protein contaminants. The GST-tag was removed to ensure β_2-adaptin was in its native state. The purification steps are demonstrated in figure 3.3.2. β_2-adaptin was successfully separated from the majority of *E. coli* proteins during the first affinity purification, as shown from the elution fractions of figure 3.3.2 A. The Prescission cleavage step removed the majority of the GST-tag from β_2-adaptin, as shown from the post-cleave fraction of figure 3.3.2 B. The majority of the GST-tag was separated from β_2-adaptin upon completing the second affinity purification, with β_2-adaptin coming off in the flow-through fractions, and the GST-tag coming off in the elution fraction as shown in figure 3.3.2 B. Size-exclusion chromatography removed several contaminants from β_2-adaptin, as shown in figure 3.3.2 C.

3.3.3 ARH

A two-step purification of ARH was conducted using a GSTrap FF column, which involved separation of ARH from *E. coli* proteins, followed by a HiTrap Q anion exchange column, which involved further removal of *E. coli* protein contaminants. The GST-tag was not removed due to the small size of ARH, which is 14 kDa. The purification steps are demonstrated in figure 3.3.3. ARH was successfully separated from the majority of *E. coli* proteins during the first affinity purification, as shown from the elution fractions of figure 3.3.3 A. Ion-exchange removed some contaminants with ARH coming off in the 14% High Salt Buffer pH 7 elution, as shown in figure 3.3.3 B, however, a significant number of contaminants still remained.

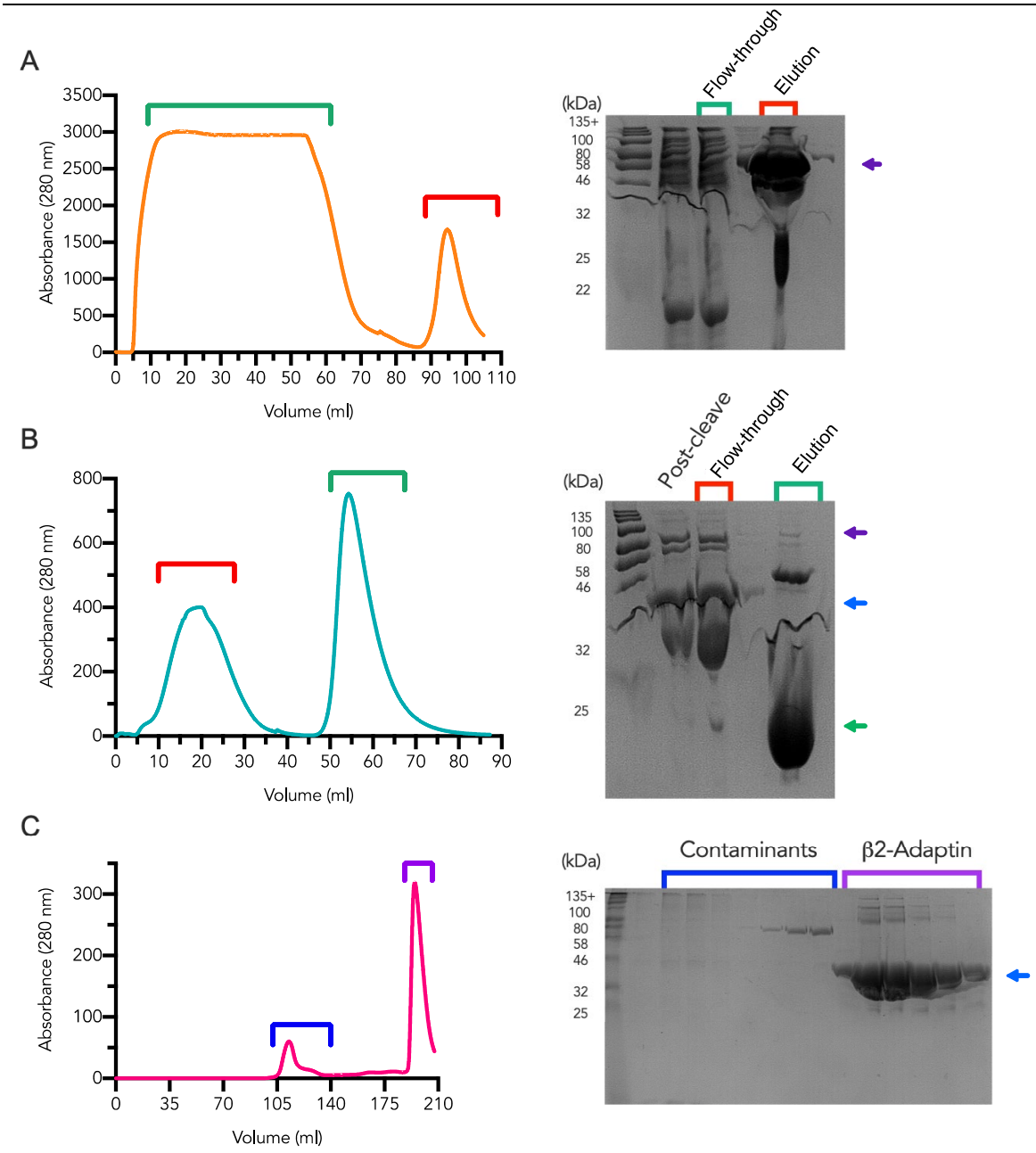

Figure 3.3.2 – β_2-adaptin purification traces and SDS-PAGE gels

A280 absorbance traces and SDS-PAGE gels are presented on the left and right of the figure respectively. GST-β_2-adaptin is indicated by purple arrows, β_2-adaptin is indicated by blue arrows, and GST is indicated by the green arrow. The molecular weight of GST-β_2-adaptin, β_2-adaptin and GST-tag is 62 kDa, 36 kDa and 26 kDa respectively. A) Initial GSTrap FF affinity purification separating GST-tagged β_2-adaptin from *E. coli* proteins. B) Final GSTrap FF affinity purification step conducted after GST-tag cleavage, separating the cleaved GST-tag from β_2-adaptin. C) Final size-exclusion chromatography purification to remove additional *E. coli* protein contaminants.

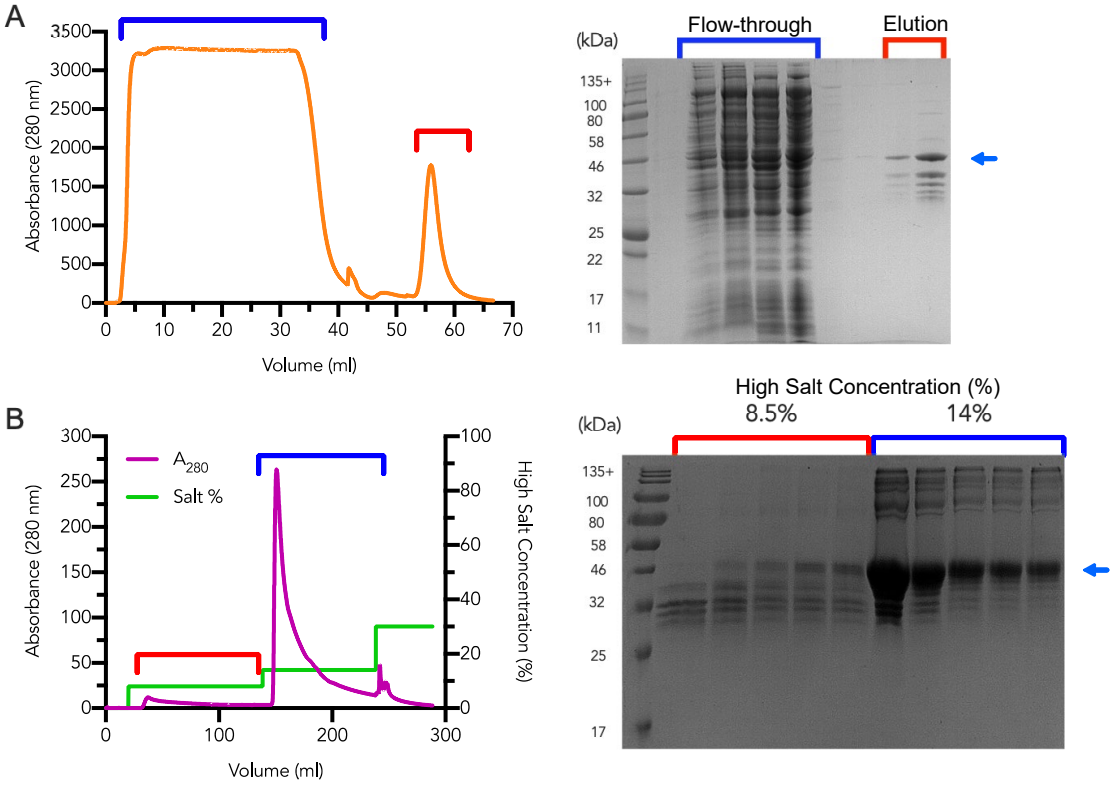

Figure 3.3.3 – ARH purification traces and SDS-PAGE gels

A280 absorbance traces and SDS-PAGE gels are presented on the left and right of the figure respectively. GST-ARH is indicated by blue arrows. The molecular weight of GST-ARH is 40 kDa. A) Initial GSTrap FF affinity purification separating GST-tagged ARH from *E. coli* proteins. B) Final HiTrap Q anion exchange purification to remove additional *E. coli* protein contaminants.

3.4 Purification of His-tagged Proteins

3.4.1 Hsc70

A three-step purification of hsc70 was conducted using a complete HisTrap column, which involved separation of hsc70 from *E. coli* proteins, an ATP-Agarose 4B column, which involved separation of hsc70 from non-ATP binding proteins, and a Superdex 75 16/60 column, which involved removal of ATP from hsc70. The purification steps are demonstrated in figure 3.4.1. Hsc70 was successfully separated from the majority of *E. coli* proteins during the first affinity purification, as shown within the elution fractions of figure 3.4.1 A. The ATP-Agarose 4B affinity purification removed additional *E. coli* protein contaminants, as shown within the elution fractions in figure 3.4.1 B. Size-exclusion chromatography removed ATP from hsc70, as shown in figure 3.4.1C.

3.4.2 Epsin 1

A two-step purification of epsin 1 was conducted using a complete HisTrap column, which involved separation of epsin 1 from *E. coli* proteins, followed by a HiLoad 26/600 Superdex 200 column, which involved further removal of *E. coli* protein contaminants. The purification steps are demonstrated in figure 3.4.2. Epsin 1 was successfully separated from the majority of *E. coli* proteins during the first affinity purification, as shown from the elution fractions of figure 3.4.2 A. Size-exclusion chromatography removed several contaminants from epsin 1, as shown in figure 3.4.2 B.

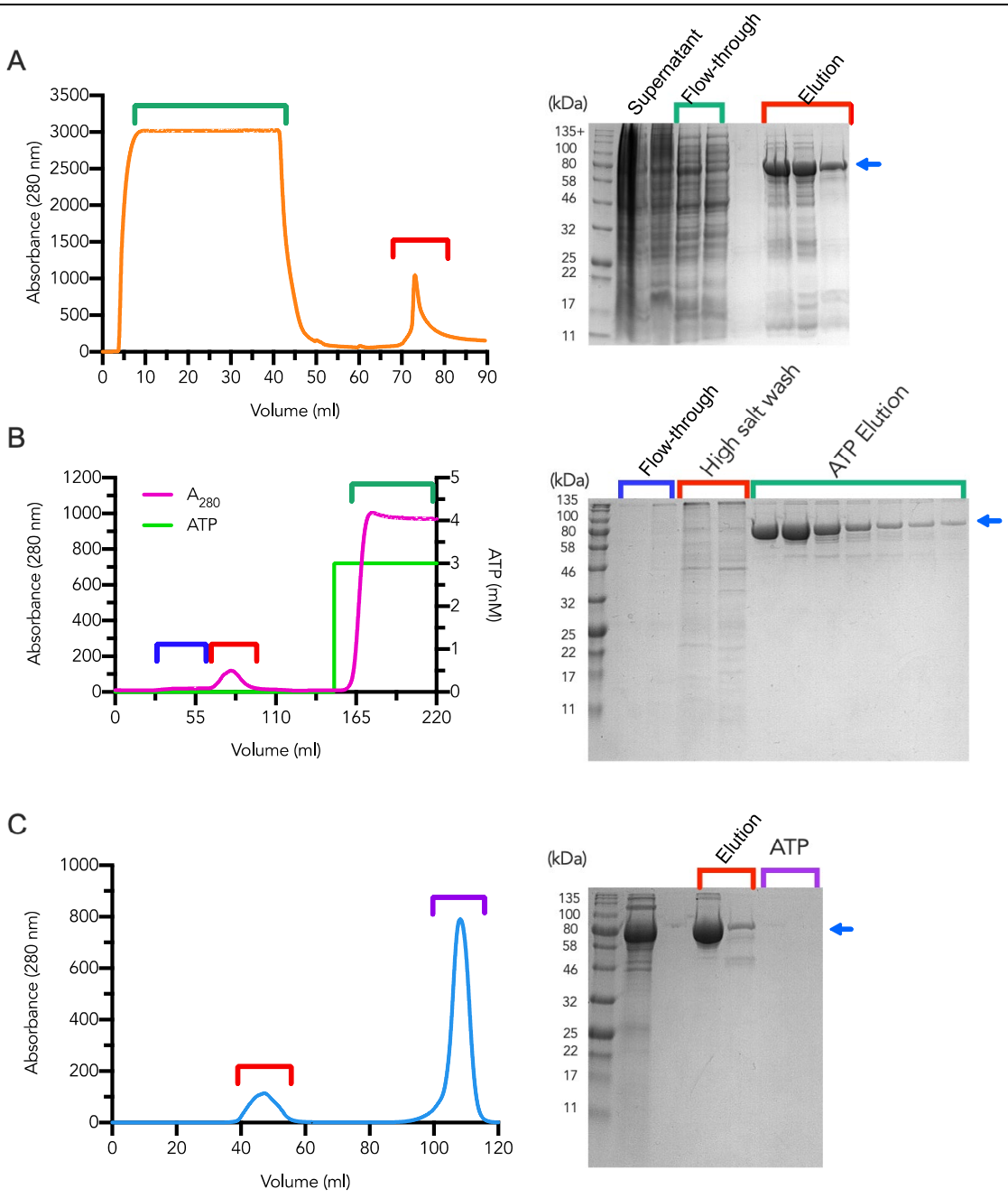

Figure 3.4.1 – Hsc70 purification traces and SDS-PAGE gels

A280 absorbance traces and SDS-PAGE gels are presented on the left and right of the figure respectively. The molecular weight of hsc70 is 72 kDa and is indicated by blue arrows. A) Initial HisTrap affinity purification separating his-tagged hsc70 from *E. coli* proteins. B) ATP-Agarose 4B affinity purification step to separate hsc70 from non-ATP binding proteins. C) Final size-exclusion chromatography purification to remove ATP contaminants.

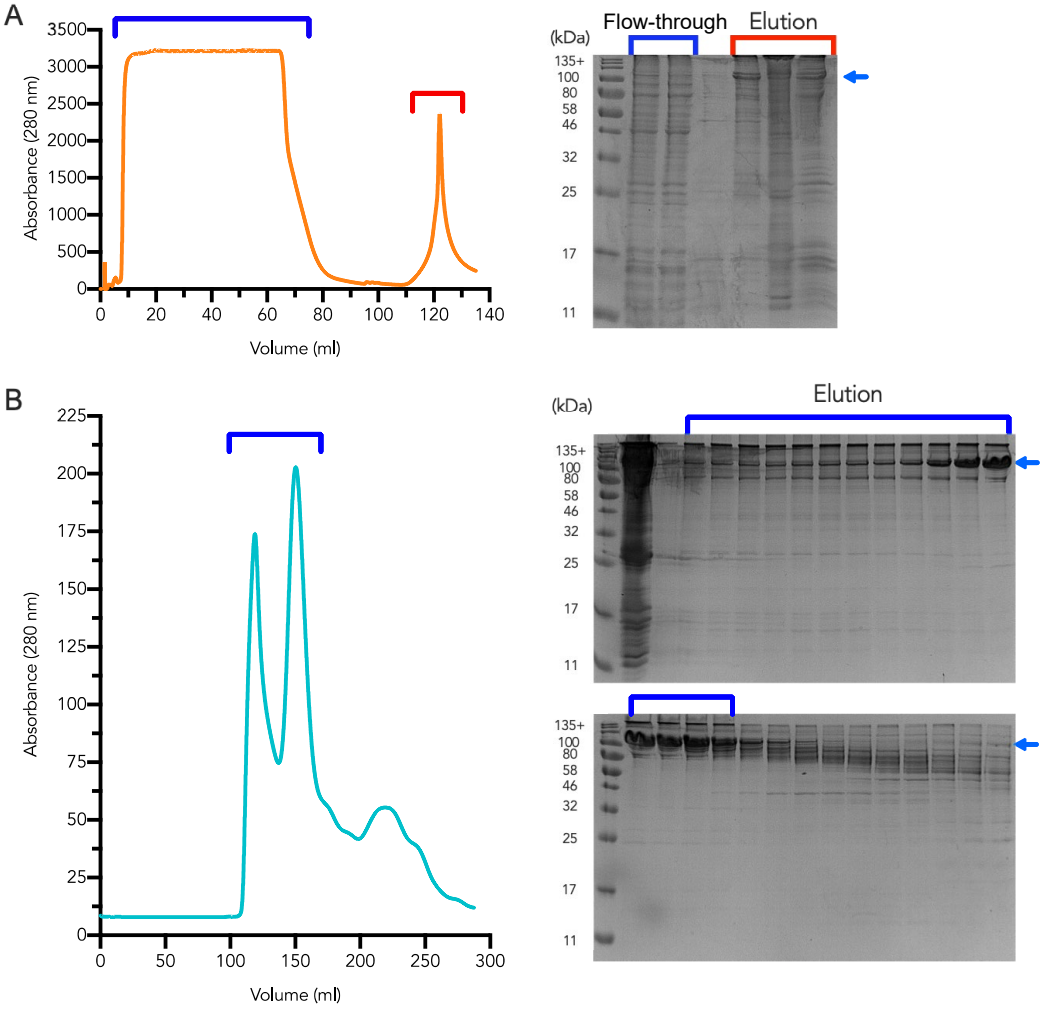

Figure 3.4.2 – Epsin 1 purification traces and SDS-PAGE gels

A280 absorbance traces and SDS-PAGE gels are presented on the left and right of the figure respectively. Epsin 1 is indicated by blue arrows. The molecular weight of epsin 1 is 60 kDa. A) Initial HisTrap affinity purification separating his-tagged epsin 1 from *E. coli* proteins. B) Final size-exclusion chromatography purification to remove additional *E. coli* protein contaminants.

3.4.3 AP180

A two-step purification of AP180 was conducted using a complete HisTrap column, which involved separation of AP180 from *E. coli* proteins, followed by a HiLoad 26/600 Superdex 200 column, which involved further removal of *E. coli* protein contaminants. The purification steps are demonstrated in figure 3.4.3. AP180 was successfully separated from the majority of *E. coli* proteins during

the first affinity purification, as shown from the elution fractions of figure 3.4.3 A. Size-exclusion chromatography removed several contaminants from AP180, as shown in figure 3.4.3 B.

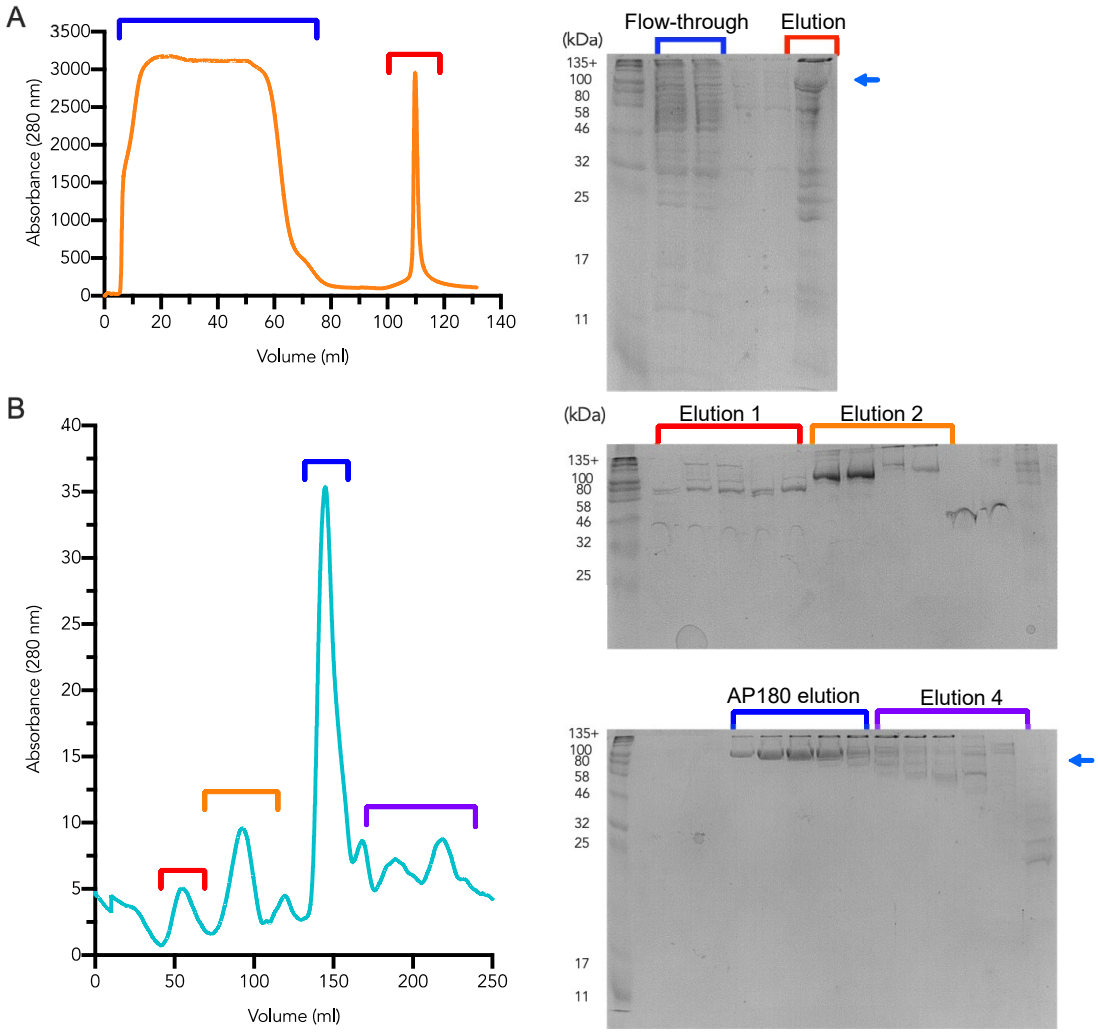

Figure 3.4.3 – AP180 purification traces and SDS-PAGE gels

A280 absorbance traces and SDS-PAGE gels are presented on the left and right of the figure respectively. AP180 is indicated by blue arrows. The molecular weight of AP180 is 55 kDa. A) Initial HisTrap affinity purification separating his-tagged AP180 from *E. coli* proteins. B) Final size-exclusion chromatography purification to remove additional *E. coli* protein contaminants.

This page is intentionally left blank

Chapter 4:

High Resolution Cryo-EM Structure of Clathrin

Chapter Overview

This chapter details the development of the clathrin cage structure using cryo-EM, as well as localised reconstruction analysis to develop a higher resolution structure of the clathrin hub domain with terminal domains included.

4.1 Background to Cryo-EM

The first aim of this thesis is to obtain the structure of clathrin with no adaptors present, containing both the upper and lower hub regions at a higher resolution. To obtain the structure of clathrin cages, cryo-EM and localised reconstruction techniques were utilised, but what are the cryo-EM and localised reconstruction techniques, how are they conducted, and why are they appropriate for obtaining higher resolution structures of clathrin? Sections 4.1.1 to 4.1.3 will provide the answers to these questions

4.1.1 Why is cryo-EM appropriate?

Cryo-EM is a technique which can determine the structure of macromolecular complexes and assemblies at high resolutions, without the need for developing protein crystals (178). This would thus allow a 3D structure of a macromolecular complex, which is more than 100 kDa in size, to be determined while in its functional form (179). Although structures produced by X-ray crystallography tend to be of higher resolution than those produced by cryo-EM, cryo-EM can also produce structures up to atomic resolution, with the structure of a 334 kDa glutamate dehydrogenase determined by cryo-EM reaching a resolution of 1.8 Å (180). Several structures of clathrin complexes have been produced by cryo-EM, including the clathrin auxilin complex and the clathrin, auxilin and hsc70 complex (107,123). For clathrin cage model development and comparative purposes, cryo-EM would thus be a suitable technique as it can obtain the structure of a clathrin cage, it has potential to reach high resolutions, and cryo-EM has been used previously for other clathrin adaptor complex to determine their structures.

4.1.2 The cryo-EM workflow

To image macromolecular complexes in the EM whilst maintaining their functional form, the macromolecular complex is frozen rapidly. To achieve this, a small aliquot of the sample in solution or suspension is placed onto an EM grid and blotted until only a thin layer of solution remains on the grid (181). The grid is then plunged immediately into a -180 °C solution of liquid ethane in order to rapidly freeze the sample so vitreous ice is formed, which is when water forms a glass like amorphous structure instead of ice crystals upon being shock-cooled below -140 °C (181). A schematic of the plunge freezing method is demonstrated in figure 4.1.1 A. Once the sample grid has been prepared, the grid is placed into an EM holder that is cooled with liquid nitrogen, as demonstrated in figure 4.1.1 B. The holder is then inserted in the EM *via* the specimen port so that it can be imaged (182). A schematic of an EM is shown in figure 4.1.1 C.

To image the sample, an electron beam is produced by an electron gun which is then focused *via* the action of condenser lenses to remove high angle electrons (182). To ensure the electron beam does not collide with gases, the EM is placed under a high vacuum, with a pressure between $1.\dot{3} \times 10^{-3} - 1.\dot{3} \times 10^{-7}$ mbar (182). Upon contact with the sample, parts of the electron beam will pass through the sample (182). Biological specimens are sensitive to electron damage because electrons break bonds, therefore a low electron dose is used, however, this results in low contrast images due to low electron scattering (183,184). To preserve high resolution details, cryo-EM samples must be imaged under low dose conditions of around 10-20 $e^-/Å^2$ (184). The objective lens focuses the electron beam that has passed through the sample towards a direct electron detector camera, which upon hitting leads to the production of an image (182).

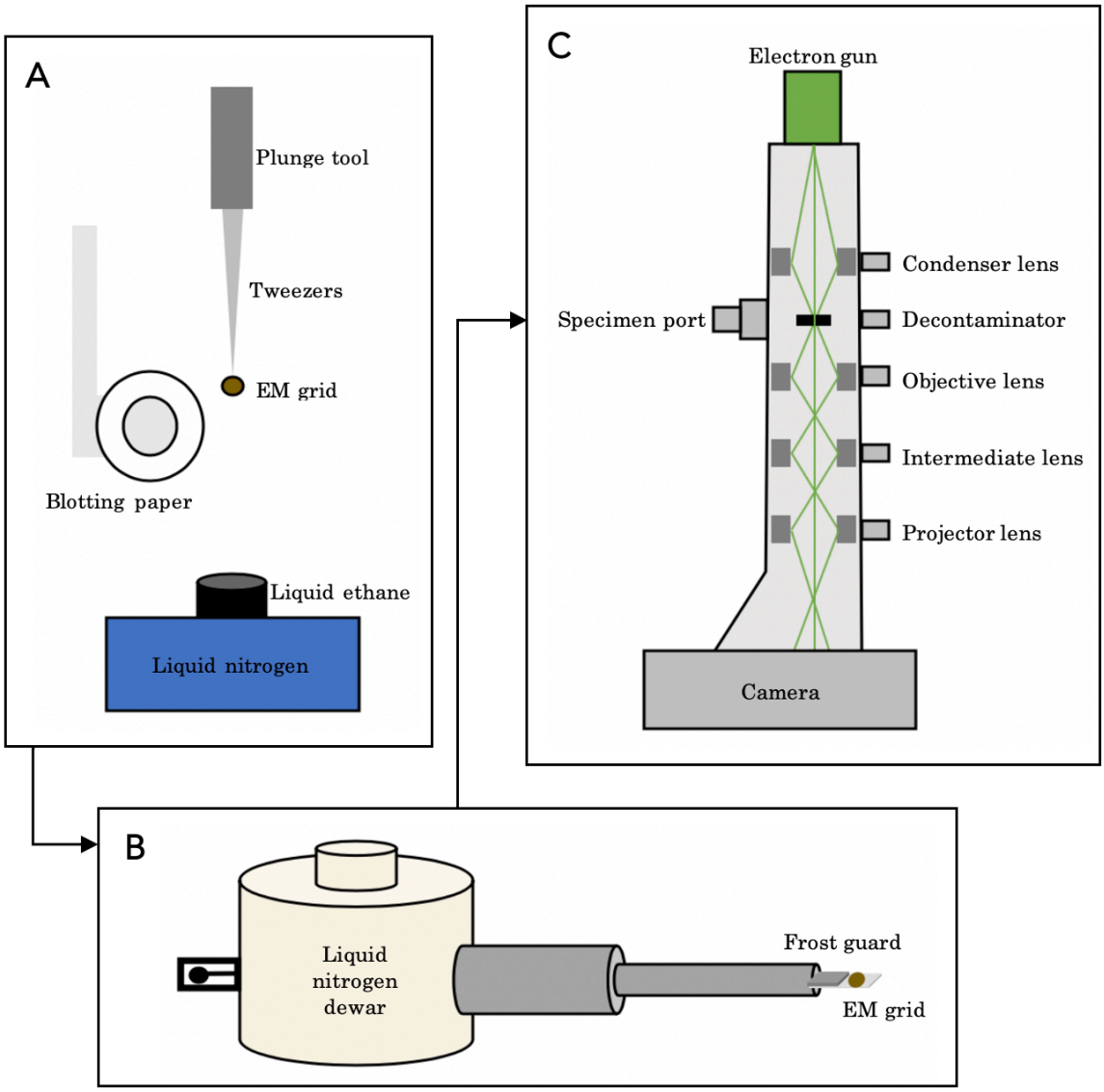

Figure 4.1.1 – Preparing and imaging cryo-EM samples

Schematics for preparing and imaging cryo-EM samples. A) Plunge freezer apparatus. The blotting paper is attached to a mechanical arm which moves to blot the grid. Upon blotting, the plunge tool submerges the grid into liquid ethane (182). B) The EM grid is placed at the tip of an EM holder cooled with liquid nitrogen. A frost guard is used to protect the grid from ice contamination during transfer (182). C) TEM set-up. The electron beam is presented as green lines (182).

Once 2D images of the sample have been acquired, which are projections of the electron potential, the 2D images will need to be processed to produce a 3D volume. To reconstruct a 3D several projections at different tilt angles must be combined. This can be achieved in two ways: 1) by collecting single images of a high number of similar particles which are randomly rotated in the sample, and

then using SPA techniques to determine their relative orientation; or 2) by collecting tilted images of the same sample and using them directly to obtain a 3d reconstruction (tomography). A schematic of the SPA processing pipeline is shown in figure 4.1.2.

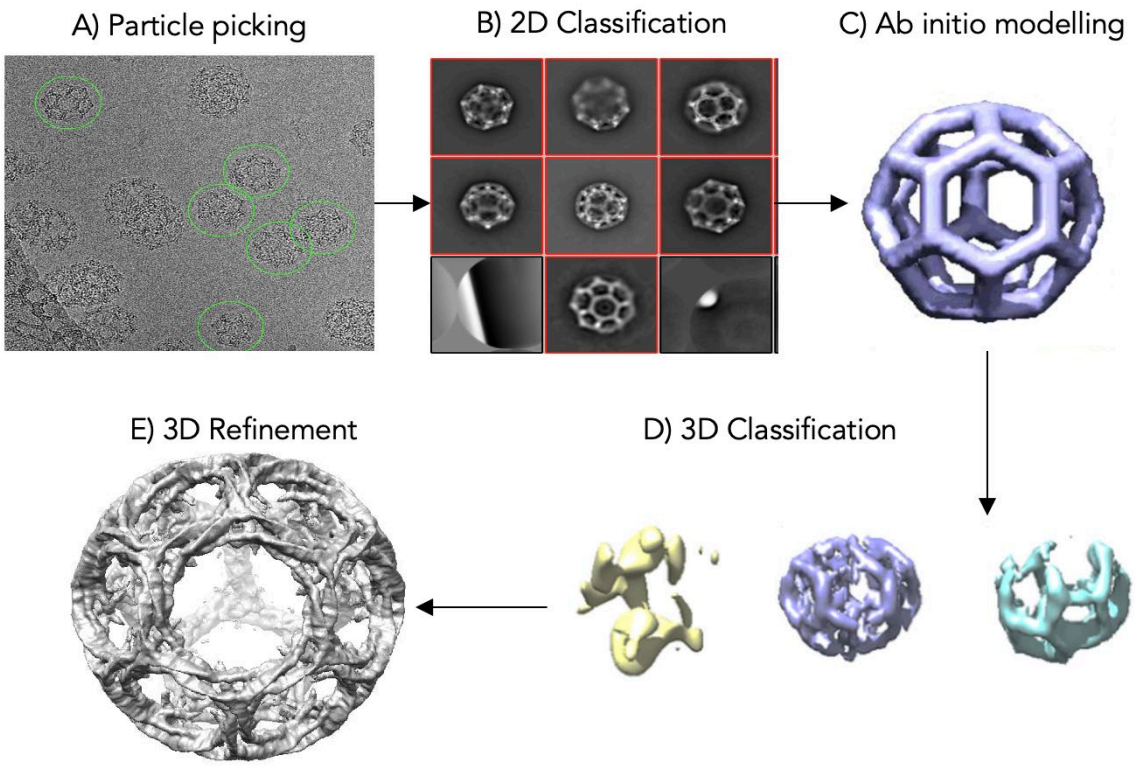

Figure 4.1.2 – SPA workflow

Processing pipeline for developing a 3D structure from 2D cryo-EM micrographs. A) Particles are selected within each micrograph. Green circle indicates the particle box. B) 2D classification of the selected particles. Only high-resolution particles and particles which look like a protein are selected. C) *Ab initio* modelling of selected 2D class particles produces a low-resolution reference model. D) 3D classification of particles using a reference model(s) allows structures with different conformations to be separated. E) 3D refinement of selected 3D class allows higher resolution structure to be produced by improving particle alignment.

First the micrographs will undergo motion correction to correct for blurring of particle images caused by particle movement. As the electron beam passes through the sample, the sample particle will move leading to blurring of images (185). To correct this, each 2D image is instead collected as a movie, allowing a motion correcting software package to be applied to track the movement of

particles so that a high resolution 2D image can be acquired (185). Following motion correction, the 2D images then undergo contrast transfer function (CTF) correction, to correct for interference in signal caused by electron scattering. When the electrons pass through the sample the electrons may scatter, with the amount of signal scattered being proportional to the sample spatial frequency spectrum (186). The scattered electrons are focused back into a beam by various lenses, however, because the electrons scatter at different angles the electrons end up with different path lengths, causing phase shifts in the electron wavefunction that interfere with the electron signal (186). The phase shift interference can be either constructive leading to an increase in signal, destructive leading to a decrease in signal, or inverting leading to a flip in the signal, and is mathematically modelled by the microscopes CTF (186). The CTF is calculated from the applied defocus, wavelength of incident electrons, microscopes spherical aberration, and the spatial frequency (186). The CTF model is a function of defocus, as the defocus impacts the strength of image spatial frequencies (186).

Once motion correction and CTF correction has occurred, particles can then be selected which fall within a certain box size either manually or automatically using a selection algorithm. Upon particle selection, particles can be sorted *via* 2D classification in order to remove any 2D classes that do not produce high resolution 2D images (187). The particles can then undergo *ab initio* model generation if a 3D model of the protein is unavailable in order to predict the structure and generate an initial low-resolution model (187). The model can then be used to conduct 3D classifications to separate particles with different 3D states (*e.g.,* open and closed conformations, bound and unbound adaptors, *etc.*), and conduct 3D refinements, whereby projection vectors are assigned to each particle image so that a 3D electron density map can be constructed.(187). Once the map has been refined, it can then be sharpened *via* applying a gaussian function with an inverse *ad hoc* B-factor (defines the quantity of uncertainty for each atom), allowing modelling of contrast lost through experimental and computational factors into the map (188). Application of an inverse *ad hoc* B-

factor thus enables resolutions greater than 3 Å to be obtained which would allow amino acid side chains to be discerned (188).

4.1.3 Localised reconstruction workflow

Localised reconstruction is a method for improving the resolution of symmetrical structures which consist of multiple repeated subunits, with the workflow demonstrated in figure 4.1.3 (189).

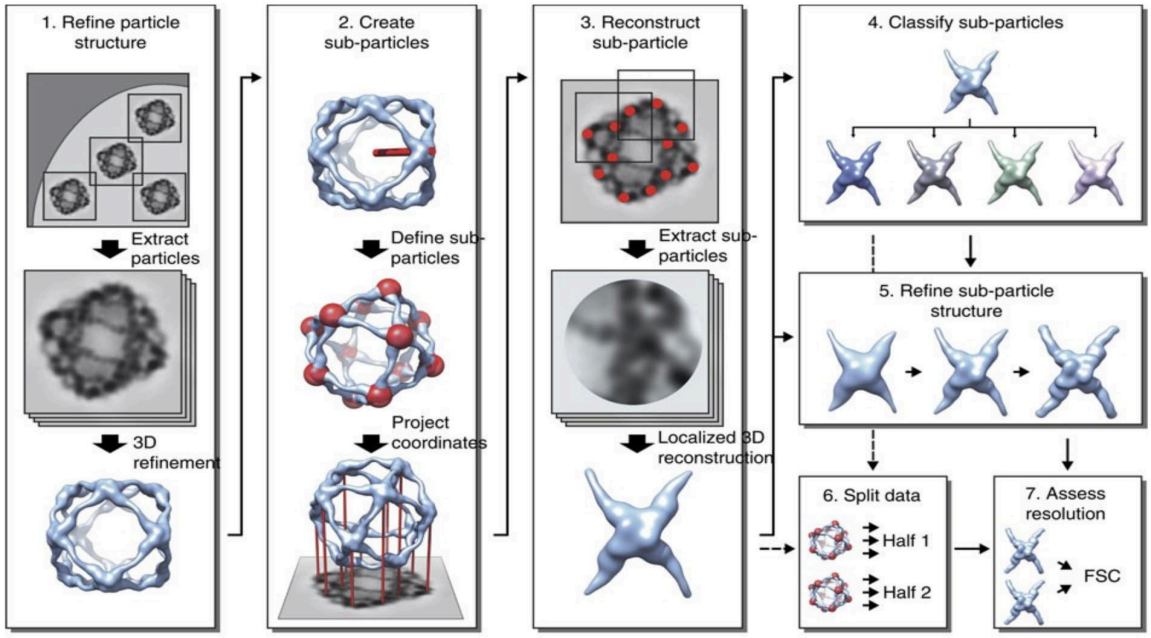

Figure 4.1.3 – Localised reconstruction workflow

Processing pipeline for localised reconstruction. 1) Structure of macromolecular complex solved using conventional SPA refinements with C1 symmetry. 2) Locations of subparticles are defined using vectors. 3) Subparticles are extracted from micrographs and used to calculate a 3D localised reconstruction. 4&5) Localised reconstruction is further classified and refined using 2D and 3D classification and 3D refinements. 6&7) Refined localised reconstruction is sharpened and its resolution is assessed. Reproduced from Nature Communications, 4 (72), Ilca SL *et al.*, Localized reconstruction of subunits from electron cryo-microscopy images of macromolecular complexes, (2015) (189) under the terms of the Creative Commons Attribution License (CC BY).

Use of localised reconstruction for improving the resolution of clathrin shows promise, as it has been used previously to improve the resolution of the upper hub region of clathrin cages from 9.1 Å to 4.7 Å (35). To conduct localised

reconstruction, a refined 3D structure needs to be produced using the methods described in section 4.1.2 with no symmetry applied to the structure (189). Subunits of interest and their positions are then identified by the creation of vectors, which includes information on the centre origin of the structure and the centre origins of the subparticles of interest, so that the position of each subparticle within the original particle images can be calculated (189). Subparticle images can then be extracted from the original micrographs using a smaller box size so that they can be treated as individual particles in future refinements (189). Once the subparticle images have been extracted, they can be combined together to increase the overall particle number. For example, if there are 4000 particles in a structure which has 5 identical subunits, then upon extracting and combining the subparticles the total number of particles will be 5 times 4000 which is 20000 particles. The subparticles can then undergo 3D classification, refinements and reconstructions as described in section 4.1.2 to create a structure of the subunit with an improved overall resolution (189).

4.2 Methods

4.2.1 Cryo-EM sample preparation

Cryo-EM samples were prepared by adding 3 µl of 9 µM clathrin in polymerisation buffer onto glow-discharged Quantifoil R 1.2/1.3 holey carbon film 300 mesh copper grids, followed by a 4.5 second single side blot at 50 % chamber humidity before plunge freezing in liquid ethane using a Leica Automatic Plunge Freezer EM GP2. Grids were screened at the Midlands Regional Cryo-EM Facility at the University of Warwick on a 200 kV JEOL 2100 Plus EM fitted with a Gatan OneView IS camera at a nominal magnification of 20,000 ×, with a screening image shown in figure 4.2.1 A.

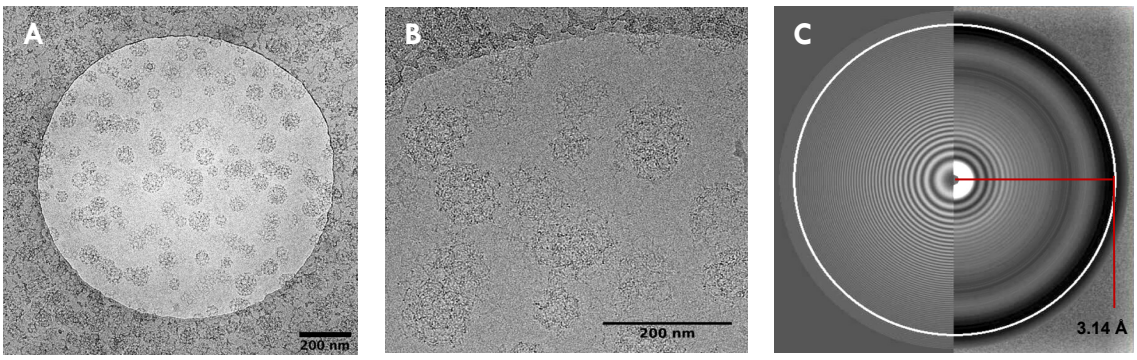

Figure 4.2.1 – Clathrin cryo-EM screening and data collection

Collected EM images of clathrin cages during screening and data collection. A) Image of screened grid obtained from a 200 kV JEOL 2100 Plus. Scale bar set to 200 nm. B) Clathrin cages imaged on a 300 kV Titan Krios during data collection. Scale bar set to 200 nm. C) CTF for presented micrograph. Oscillations are detected above noise levels up to a resolution of 3.14 Å

4.2.2 Cryo-EM data collection

Cryo-EM micrographs were collected automatically at the LISCB using an FEI 300 kV Titan Krios G3 equipped with a Falcon III counting detector. Images were collected in EFTEM mode using a nominal magnification of 59,000 ×, pixel (px) size of 1.39 Å/px, 100 µm objective aperture, 50 µm C2 aperture, spot

size of 5, 2.7 spherical aberration, and 800 nm^2 illuminated area. Due to an error in the electron counter, an accurate dose rate could not be determined, and so micrographs were collected with an estimated total dose of 46 – 92 $e^-/Å^2$ over 7 s at a dose rate of 1.2 – 2.4 $e^-/Å^2\ s^{-1}$. Micrographs were targeted for collection between 1.3 – 2.8 µm defocus with 300 nm steps. A representative micrograph image is presented in figure 4.2.1 B alongside its measured CTF (figure 4.2.1 C).

4.2.3 Cryo-EM data refinement of cages

Collected movie files were imported into Scipion(v3)(190) for data processing, which contains plugins for different EM processing software such as Relion (191,192), MotionCor2 (185), gctf (186), and ResMap (193). Motion correction of movie files was performed using MotionCor2 (185) and without dose weighting applied due to uncertainty in the actual dosage applied per frame during collection. The contrast transfer function (CTF) for each micrograph was estimated using gctf(v1.06) (186) with validation and EPA functions utilized. Clathrin cages were manually picked using Relion(v2.1) (192) with a 1000 px box size at 1.39 Å/px; a total of 22,827 particles were selected. Cage structures were processed using Relion(v2.1) using two-dimensional (2D) classification, three-dimensional (3D) classification, 3D refinement, movie refinement, Bayesian polishing, mask creation, and post-processing. Reference free 2D classifications were performed over 25 iterations. An asymmetric 3D classification was performed on selected 2D class particles using a previously described 10 cage library (35) as reference volumes, to separate the different cage types. An initial 3D refinement was performed for each cage type with no symmetry imposed and a 60 Å low pass filter applied, which was followed by movie refinement and Bayesian polishing (191,194) for dose weighting and sharpening, with applied B-factors presented in figure 4.2.2.

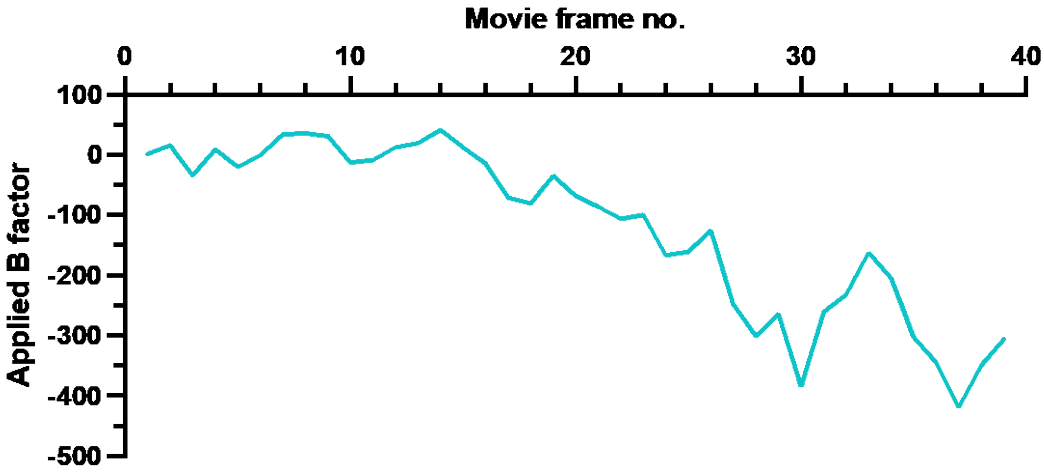

Figure 4.2.2 – 28-minicoat polishing B-factors

Calculated polishing B-factors plotted against movie frame number.

The 28-minicoat and 36-barrel cage structures were selected for further 3D refinements with imposed symmetry; an additional refinement was conducted with no symmetry imposed which would be used for the localized reconstruction procedure. Masks were generated from the reconstructions at 3σ, extended and softened by 3 px and 3 px respectively to employ solvent flattening and a Gaussian noise background to refined structures. Gold-standard Fourier shell correlation (FSC) measurement was performed during post-processing to calculate resolution, using a mask with 3σ contour level, 5 px expansion and 9 px softening, an MTF of the Falcon III camera operated at 300 kV, and automatic B-factor calculation (195,196). ResMap (193) was used to calculate local resolution of cage structures using a 8-14 Å range with 1.5 Å steps. Table 4.2.1 provides further details on the EM map statistics for processed cages, including applied symmetry, box size, particle number, MW, and map resolution at an FSC of 0.2.

Table 4.2.1 – EM map statistics for processed clathrin cages

	28-Minicoat	36-Barrel
Complex ordered MW	17.6 MDa	22.7 MDa
Box size (px)	1000	1000
Particle number (initial)	22,827	
Particle number (final)	8,137	2,073
Symmetry	T	D6
Map resolution (FSC 0.2)	9.3 Å	22.8 Å

4.2.4 Localised reconstruction

Localised reconstruction was conducted using the method published in Ilca *et al.* (2015) (189). The scripts for localised reconstruction were run using the programs Scipion and Relion-1.4 (190,194). Masks of the clathrin cage with a single hub region subtracted were developed in UCSF Chimera, allowing the extraction of hub domains from the 28-minicoat structure upon running the localised reconstruction script (176). Hub domains were extracted at a box size of 350 pixels and 1.39 Å/px pixel size. For the consensus hub, only particles obtained from the 28-minicoat were used. For additional analysis on symmetry structure effects, particles were split up depending upon the cage faces they were associated with, which is demonstrated in figure 4.2.3, with hub domains split into 3 classes called pentagon-pentagon-pentagon (PPP), pentagon-pentagon-hexagon (PPH), and pentagon-hexagon-hexagon (PHH). The PHH hub was obtained from the 36-barrel structure.

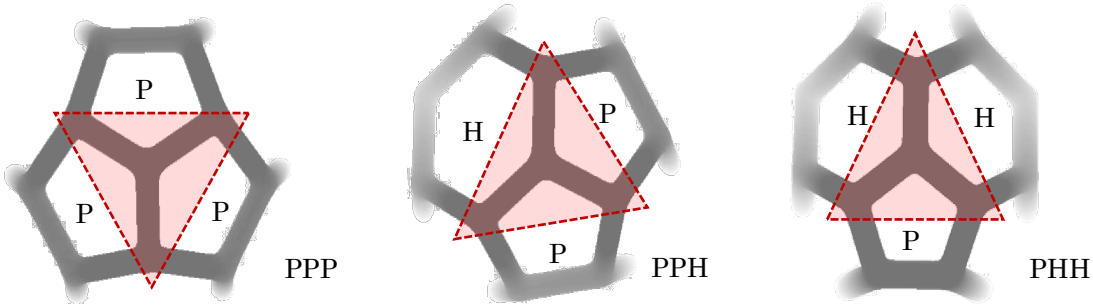

Figure 4.2.3 – Extracted regions from localised reconstruction

Schematic shows the classes of particles extracted *via* localised reconstruction. The red triangles indicate the area of particle extraction. P indicates a pentagon face, and H indicates a hexagon face.

Upon completion of the localised reconstruction script, particles were imported into Scipion(v3) (190) for additional classification and refinement. Relion(v3) (191) was used for 2D classifications, 3D classifications, 3D refinements, post-processing and mask creation (191). An initial low pass filter of 40 Å was used on reference maps for all 3D classifications and refinements. The 3D classifications were performed with no image alignment and a regularisation parameter of 10, to split particles into two classes to remove poorly aligned and low-resolution particles. 3D refinements were conducted with C1 symmetry imposed. For the consensus and PPP hub C3 symmetry was imposed, and for the PPH hub and PHH hub C1 symmetry was imposed. Upon completion of refinements, postprocessing was conducted using B-factor estimation and FSC weighting (195,196). The masks used for post-processing were created at 2σ with a 5 px extension and 9 px softening. Table 4.2.2 provides a summary of the EM map statistics for processed hubs. Local resolution was calculated using ResMap (193), between 4 – 10 Å with a resolution step size of 1 Å. Confidence maps of volume densities were calculated using SPoC(197,198).

Table 4.2.2 – EM map statistics for processed clathrin hub structures

	PPP	PPH	PHH	Consensus
Complex ordered MW	~965 kDa	~965 kDa	~965 kDa	~965 kDa
Box size (px)	350	350	350	270
Particle number (initial)	227,836		24,876	227,836
Particle number (final)	25,237	86,911	9,595	139,259
Symmetry	C3	C1	C1	C3
Map resolution (FSC 0.2)	4.7 Å	5 Å	11 Å	4.3 Å
Measured map B-factor (Å^2)	-11.3	-17.5	-12.3	-25.8

4.2.5 PDB model generation

To facilitate map interpretation, a new model of the full clathrin sequence was generated using the cryo-EM determined clathrin hub PDB file 6SCT (residues 635 - 1626), the X-ray crystallography determined clathrin terminal domain PDB file 1BPO (residues 1 – 493), and residues 494 - 634 from the cryo-EM determined clathrin triskelion model PDB file 1XI4 (35,148,156). Each model was fitted into the new consensus hub density discussed in this chapter, *via* UCSF Chimera using rigid body fitting (176). Atom number and chain ID in the model PDB file was altered using R, in order to combine components from different PDB files together (199). Coot was utilised to conduct minor translations and rotations of alpha helices, using the rotate/translate zone function, so that the hub model fits into the electron density maps (200).

4.2.6 Rosetta and BUDE analysis

To determine potential interactions between the N terminal domain and the ankle regions of the CHC, interface energy analysis was conducted using

Rosetta(v3.12) (201) on the consensus hub structure. The structure was prepared for energy scoring using the *relax* application, which alters the structure to remove any clashes between amino acids and improve its overall energy score (201,202). To ensure the structure remained similar to the original model, relaxation was conducted over 5 iterations with all atom constraints and no ramping, followed by a single iteration of backbone-only constrained relaxation. The RMSD between the starting and relaxed structure was calculated using the program VMD, with the RMSD for Cα position and all atoms being 0.24 Å and 1.39 Å respectively (203). The *residue_energy_breakdown* program and ref2015 scoring function in Rosetta was used to calculate and report the interface energy scores from the relaxed structure in Rosetta energy units (REU) (204,205).

Bristol University Docking Engine (BUDE)(v.1.2.10)(206,207) was configured to report the theoretical free energy (ΔG kJ mol^{-1}) of binding for the Rosetta relaxed input structure using the heavy_by-atom_2016-v1.bhff forcefield, as described previously (35). The ligand file was split into five residue segments with one residue increments using a windowing operation for the BUDE analysis only.

4.3 Clathrin Cage Structures

4.3.1 2D and 3D classification

Particles were selected *via* manual picking as shown in figure 4.3.1. A defocus series was used to obtain particle images at different spatial frequencies. Multiple different cage types are present in the sample, with several large cages being present. Due to the processing abilities of the computer and the size of the clathrin cage minicoat and barrel structures we wish to use for structural analysis, a box size of 1000 pixels was used. Overall, a total of 22,827 particles were selected from 7,190 images. 2D classification was conducted on the 22,827 particles selected from manual picking, with the results shown in figure 4.3.2.

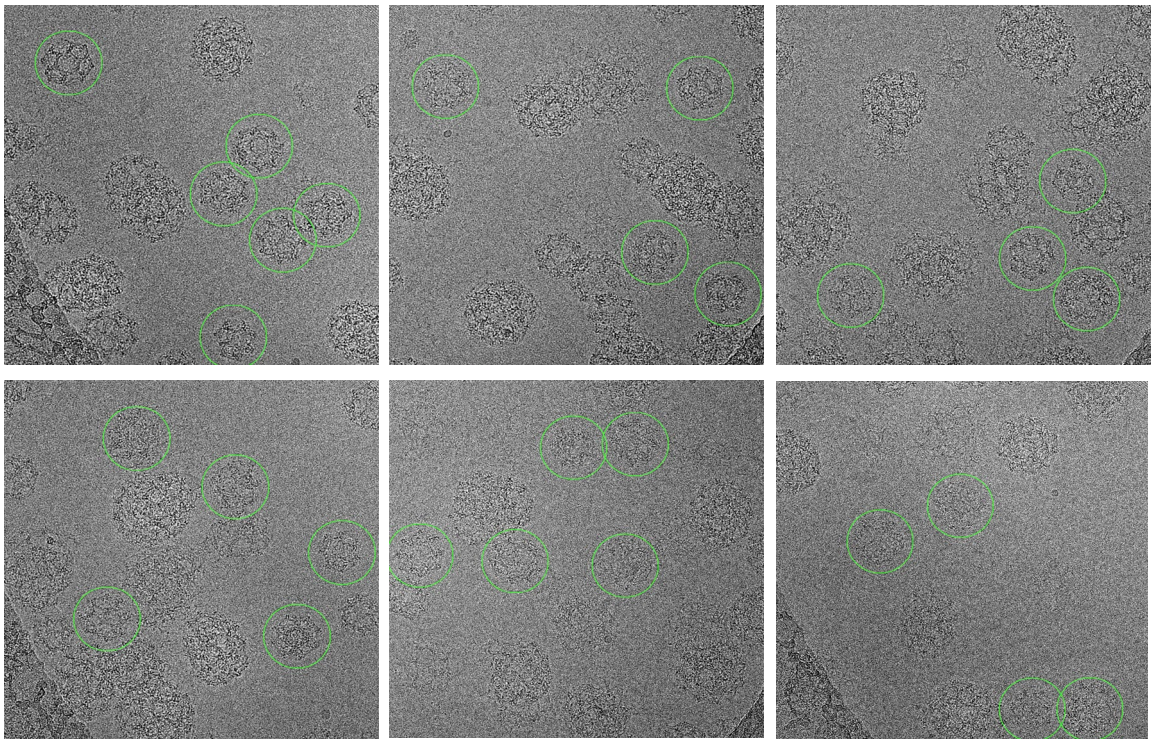

Figure 4.3.1 – Selection of clathrin particles with different defocus levels

A selection of clathrin cage micrographs from each defocus series. Particles selected *via* manual picking are surrounded by green circles.

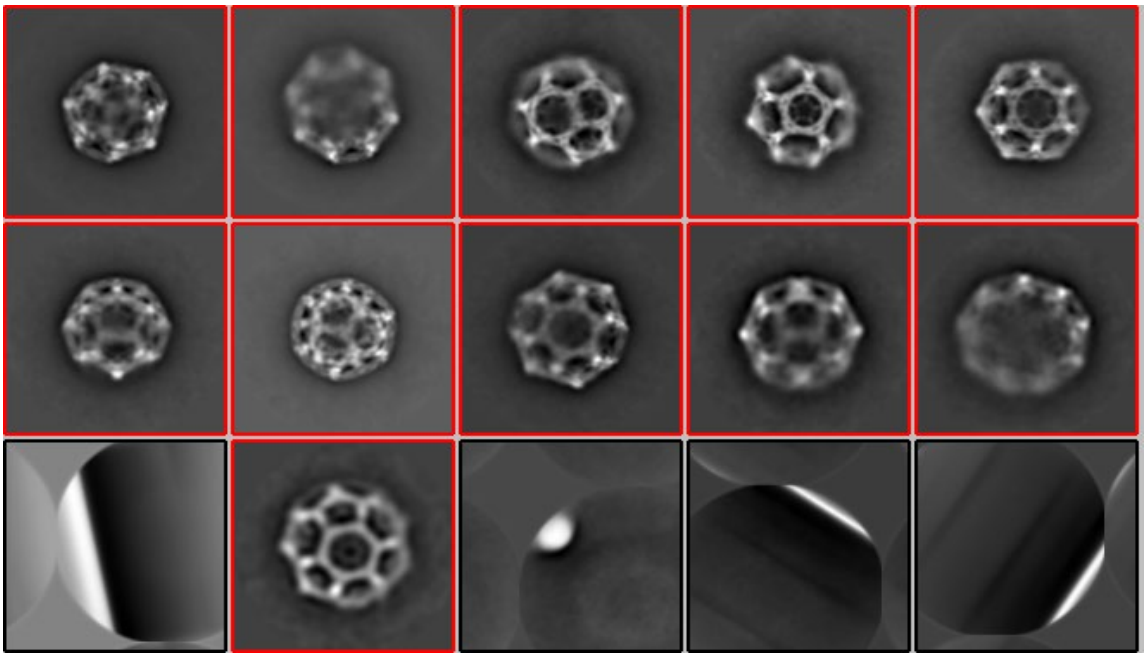

Figure 4.3.2 – Selected 2D classes of clathrin cages

Selected cages are outlined in red.

Classes which looked like clathrin cages were selected for use in 3D classification, with a total of 20,443 particles selected. This step was conducted to remove the majority of 'bad' particles; this includes particles which do not match the more popular cage types. 3D classification was then conducted using the reference structures shown in figure 4.3.3 A, with the results demonstrated in figure 4.3.3 B. Overall the 28-minicoat structure yielded the highest number of particles with 8,361 particles. 2D classifications of selected 28-minicoat particles and 36-barrel particles were conducted to ensure only high-quality particles are utilised during 3D refinement. Overall, 8,137 28-minicoat particles and 2,078 36-barrel particles were selected, with selected 2D classes shown in figure 4.3.4.

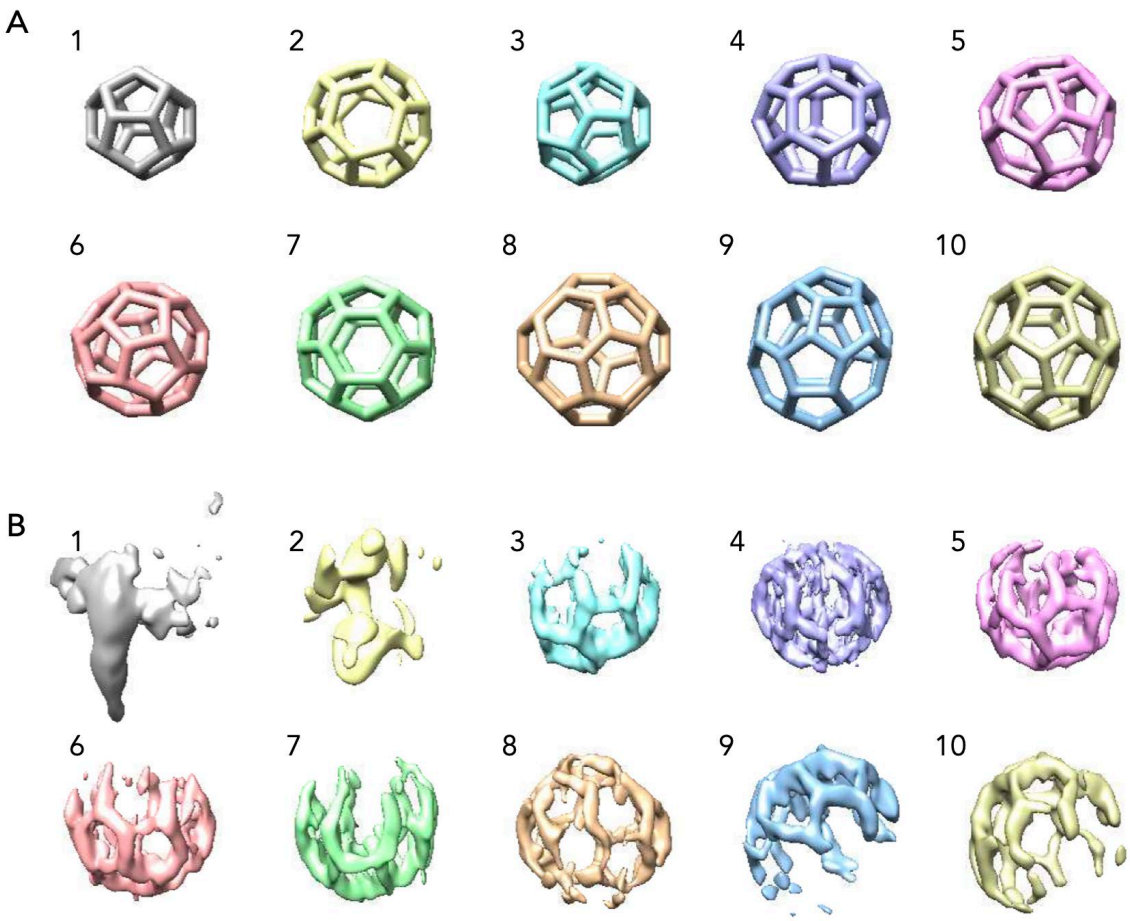

Figure 4.3.3 – 3D classification of clathrin

Initial 3D classification structures of clathrin. 1: 20-dodec, 2: 24-cage, 3: 26 cage, 4: 28-minicoat, 5: 32-sweet potato a, 6: 32-sweet potato b, 7: 36-barrel, 8: 36-tennis ball, 9: 38-big apple a, 10: 38-big apple b. A) Reference cage library from Springer Nature: Nature Structural & Molecular Biology, Cryo-EM of multiple cage architectures reveals a universal mode of clathrin self-assembly, Morris *et al.*, (2019) (35). B) 3D classification results.

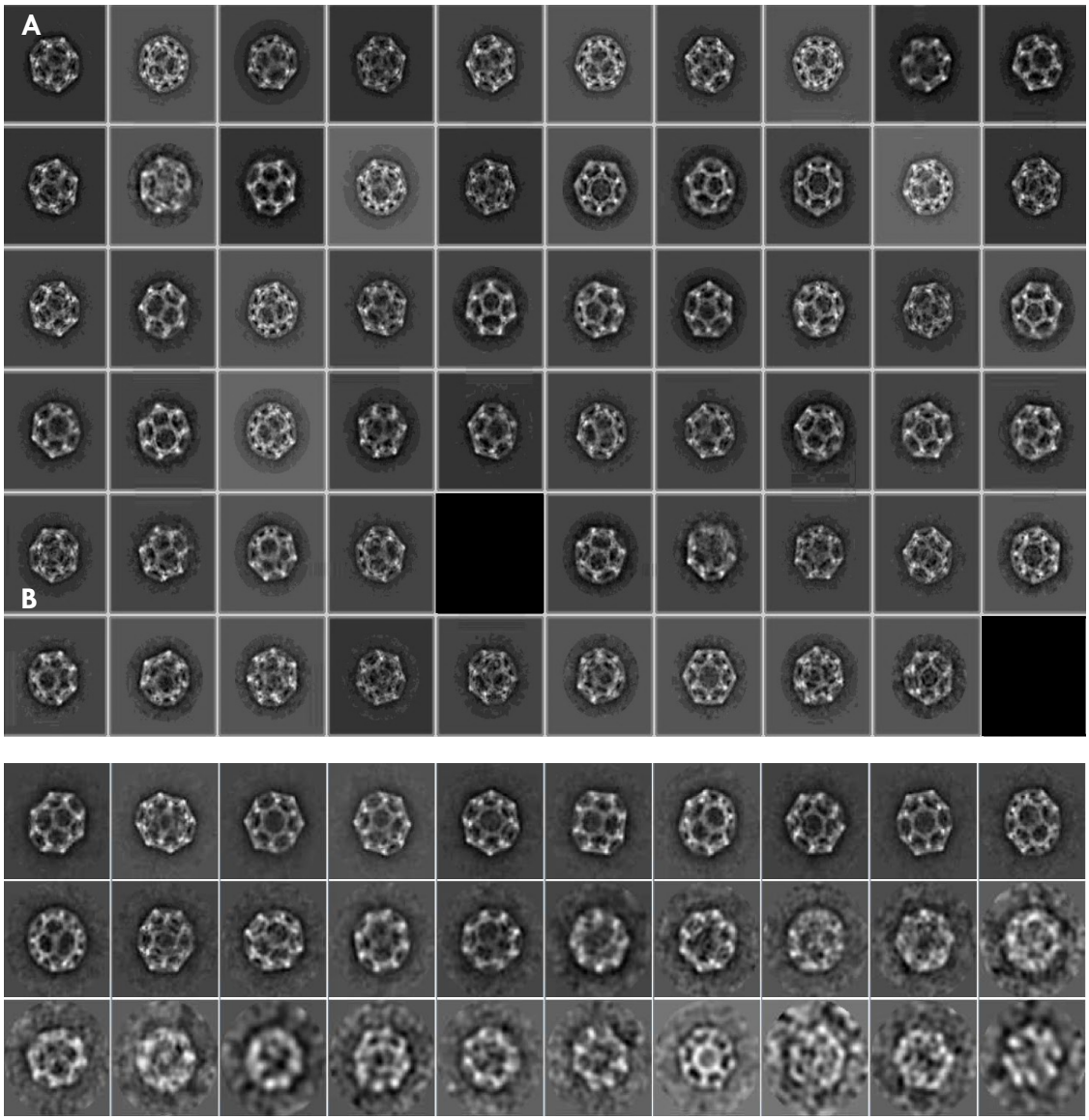

Figure 4.3.4 – Selected 2D classes of 28-minicoat and 36-barrel particles

2D classification results for 3D classified 28-minicoat and 36-barrel particles. A) Selected 2D classes for 28-minicoat structure development. B) Selected 2D classes for 36-barrel structure development.

4.3.2 Clathrin cage structures

The final post-processed map of the 28-minicoat and 36-barrel is shown in figure 4.3.5 A at different volume threshold levels, demonstrating cage resolution while also presenting lower resolution terminal domain regions. The 28-minicoat map was produced from 8,137 particles and has a resolution of

9.3 Å, and the 36-barrel map was produced from 2,073 particles and has a resolution of 22.8 Å, with the FSC curves of both cages presented in figure 4.3.5 C. From these maps we can identify the presence of terminal domains for all faces of the cages, however, higher resolution maps will be required to develop a more accurate model.

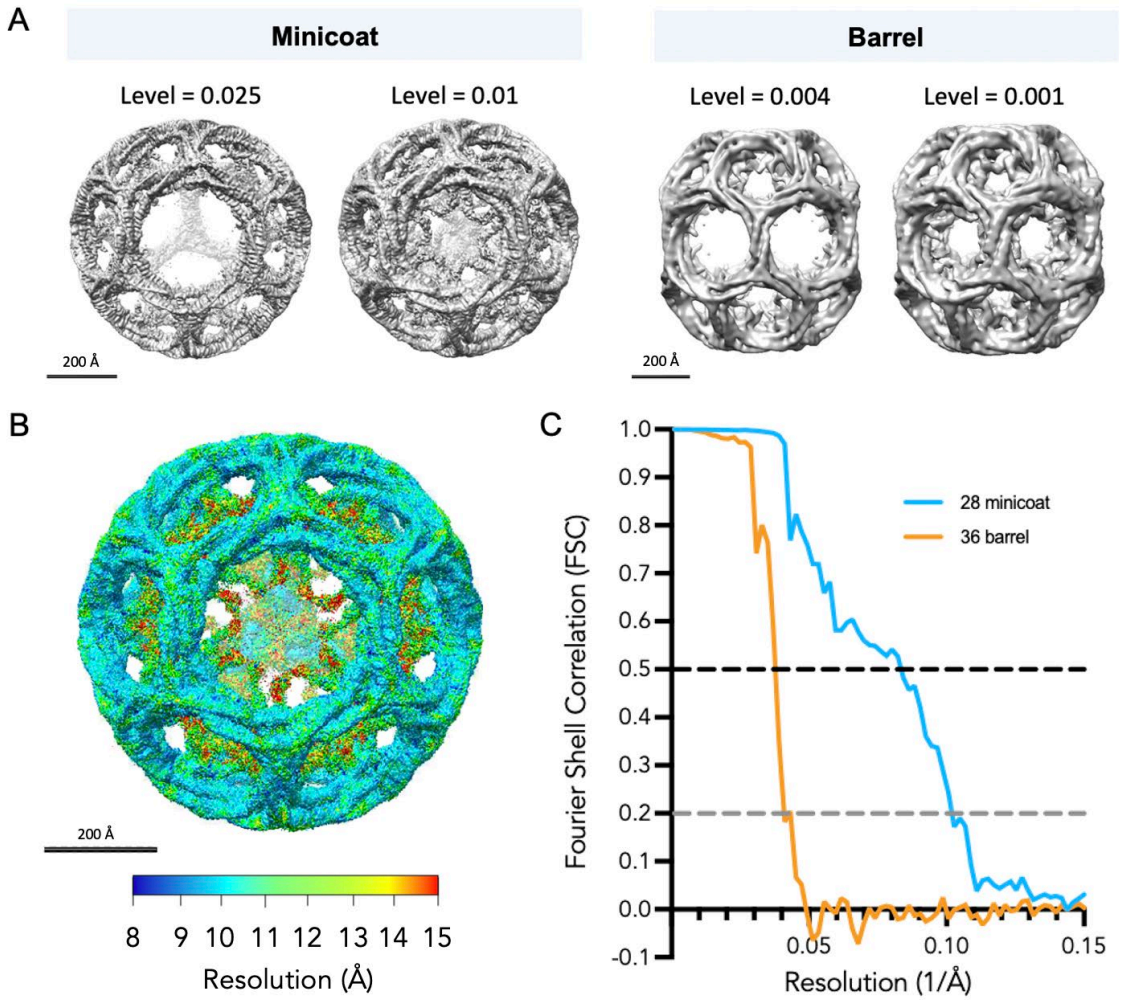

Figure 4.3.5 – Post-processed clathrin cage structures

Structure and resolution information on the post-processed cage structures. Scale bars set to 200 Å. A) Structures of the 28-minicoat (left) and 36-barrel (right) at different thresholds, with the volume threshold level shown above each cage. B) Local resolution colour-map structure presents changes in resolution across the 3D refined structure of the 28-minicoat. C) FSC curves of the 28-minicoat and 36-barrel structures. Grey dotted line at an FSC of 0.2 indicates where the resolution value was obtained.

Good definition of light chains and alpha helices can also be seen in the higher resolution 28-minicoat map, making the 28-minicoat map an ideal basis for further refinement of a consensus hub using localised reconstruction. The local resolution of the 28-minicoat was analysed using ResMap due to varying levels of resolution throughout the map, with results shown in figure 4.3.5 B. The resolution of the 28-minicoat determined by ResMap aligns well with the FSC curve values at $FSC^{0.2}$, with the ResMap resolution of the 28-minicoat being around 9-10 Å in the upper hub region and around 12-14 Å in the lower hub region, and the FSC values being 9.3 Å at $FSC^{0.2}$.

4.4 Localised Reconstruction of Hub Region

4.4.1 PPP, PPH and PHH hubs

The final post-processed maps of the three hub structures are shown in figure 4.4.1, with a colour coded schematic showing the different domains in the CLC and CHC shown in figure 4.4.1 A, and the hub maps shown in figure 4.4.1 B. The PPP hub exhibited the highest resolution of 4.7 Å.

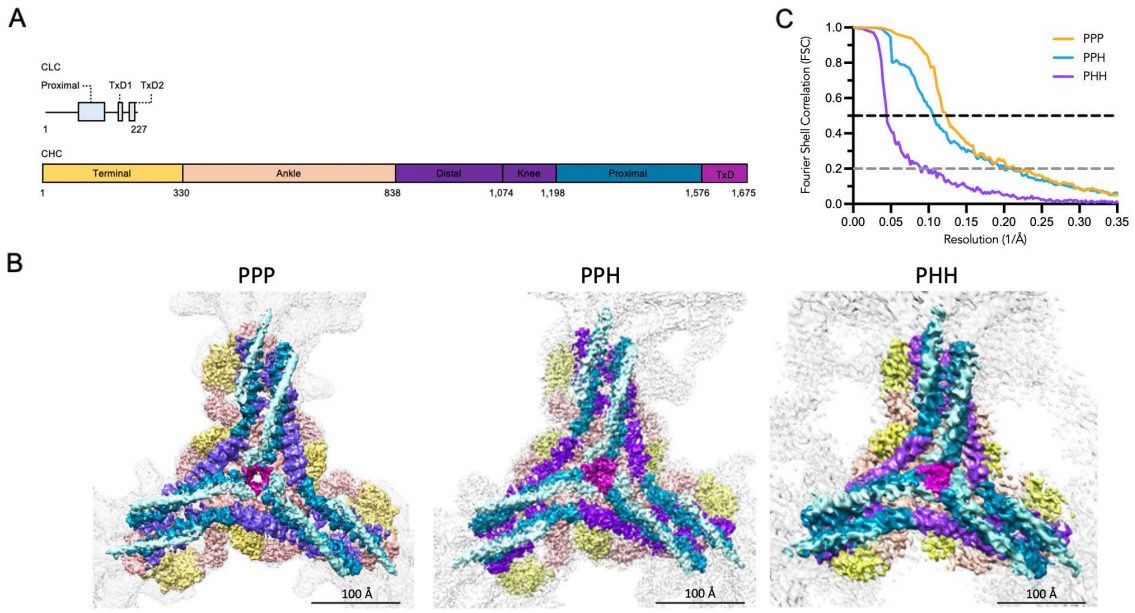

Figure 4.4.1 – Post-processed structures of different hub types

Structure and resolution information on the post-processed hub maps. A) Length and domain configuration of the CLC (top) and CHC (bottom). B) Post-processed maps of the PPP (left), PPH (middle) and PHH (right) hub structures viewed from the top. The upper hub region consisting of the CLC's and distal, knee, proximal and trimerization domains of the CHC's were set to a threshold of 0.025 (0.006 for the PHH hub). The lower hub region consisting of the ankle and terminal domains of the CHC's were set to a lower volume threshold of 0.01 (0.003 for the PHH hub). C) FSC curves of the PPP, PPH and PHH hub maps. Grey dotted line at an FSC of 0.2 indicates where the resolution value was obtained.

To ensure the terminal domain densities are not processing artefacts and to check if there is any flexibility within the ankle and terminal domain regions, 3D classification was performed with the results shown in figure 4.4.2. For the

PPP and PPH hubs, the location of the terminal domain densities did not change, and for the PHH hub more than 90 % of particles were allocated to class 5 which also showed no change. This suggests the terminal domains may adopt a default position when in the absence of adaptor proteins.

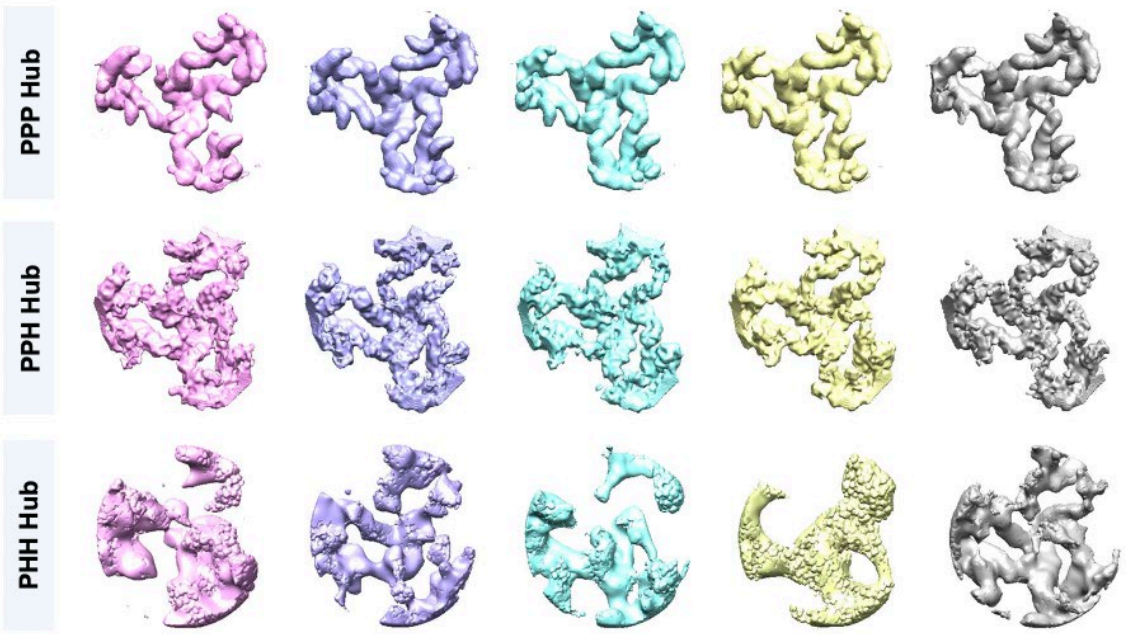

Figure 4.4.2 – 3D classification of lower hub region

3D classification of the ankle and terminal domain regions of the PPP hub (top), PPH hub (middle) and PHH hub (bottom) with no symmetry imposed.

4.4.2 Consensus hub structure

Although a resolution of 4.7 Å for the PPP hub would be sufficient for generating a model of the hub region, a higher resolution structure would be desirable to enable identification of amino acid residues within the structure. Overlaying of the hub maps showed little to no difference in hub structure up until the centre of a neighbouring hub was reached. It was therefore decided that all 28-minicoat particles would be combined to produce a consensus hub map. A box size of 270 px was used as this was the best compromise between speed of computation and retaining high resolution features displaced by CTF. The final post-processed map of the consensus hub is shown in figure 4.4.3, with a colour coded schematic

showing the different domains in the CLC and CHC shown in figure 4.4.3 A, and the map of the consensus hub shown in figure 4.4.3 C.

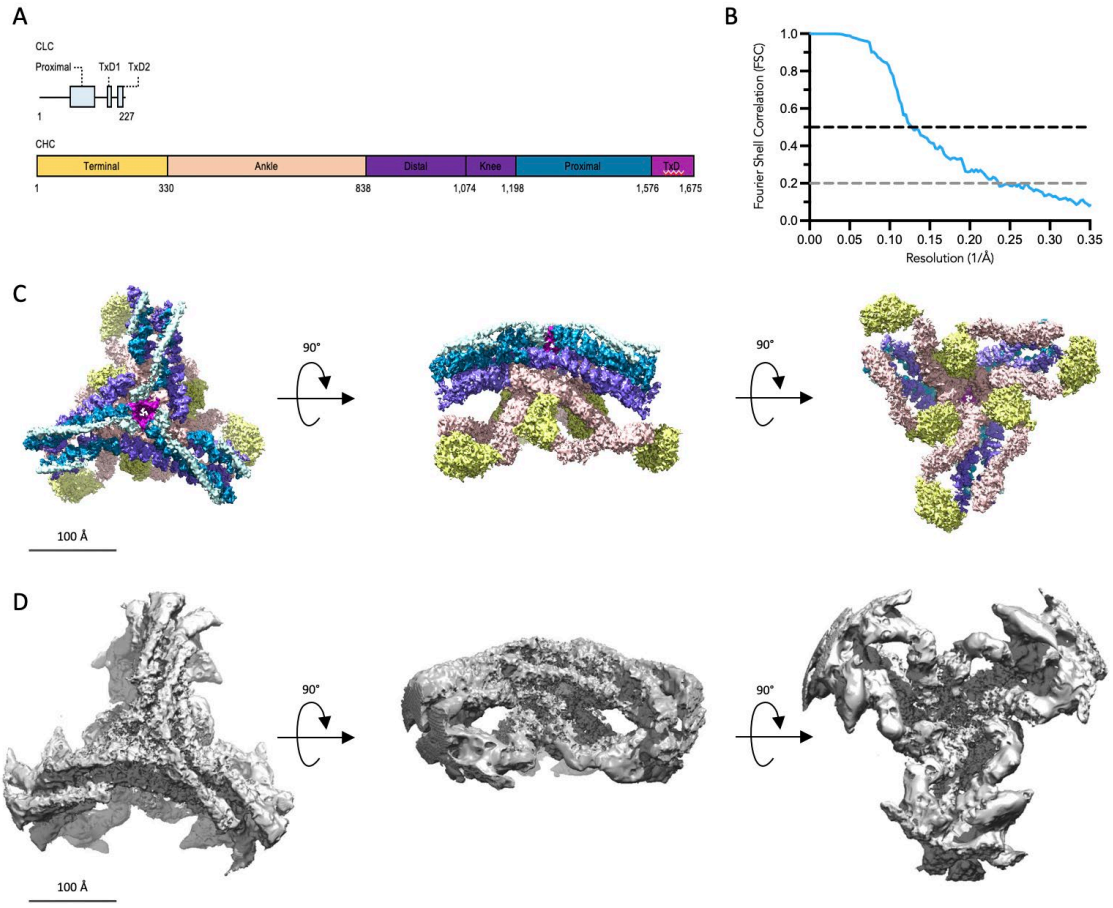

Figure 4.4.3 – Post-processed consensus hub structure

Structure and resolution information on the post-processed consensus hub map. Scale bars set to 100 Å. A) Length and domain configuration of the CLC (top) and CHC (bottom). B) Consensus hub FSC curve. Grey dotted line at an FSC of 0.2 indicates where the resolution value was obtained. C) Post-processed map of the consensus hub. The upper hub region consisting of the CLC's and distal, knee, proximal and trimerization domains of the CHC's were set to a volume threshold of 0.025. The lower hub region consisting of the ankle and terminal domains of the CHC's were set to a lower volume threshold of 0.01. D) Confidence map of the consensus hub with a noise probability of 1%.

The consensus hub was produced from 139,259 particles and has an $FSC^{0.2}$ of 4.3 Å, with the FSC curve presented in figure 4.4.3 B. The confidence map of the consensus hub volume, shown in figure 4.4.3 D, confirmed that the map volume density observed in figure 4.4.3 C was structural density as opposed to noise density. The local resolution of the consensus hub is presented in figure 4.4.4,

showing the resolution of the consensus hub is around 4-6 Å in the upper hub region and 7-9 Å in the lower hub region, in agreement with the FSC resolution value.

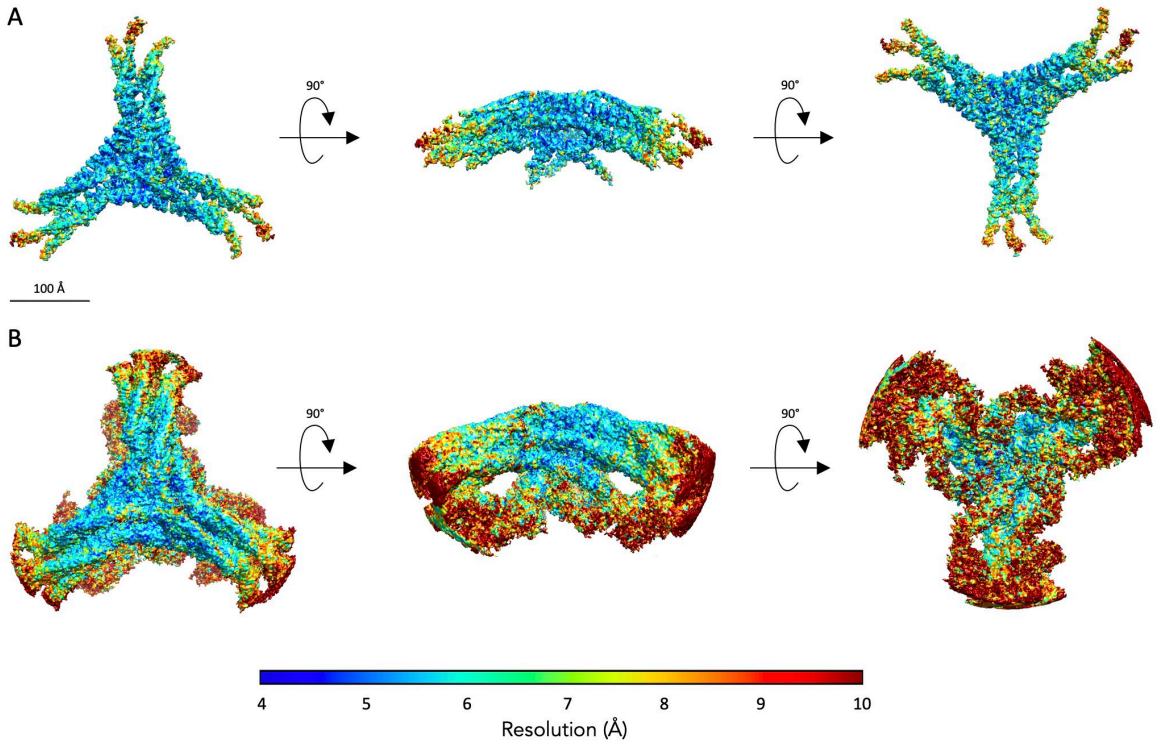

Figure 4.4.4 – Local resolution of the clathrin consensus hub

Local resolution of the clathrin consensus hub created using ResMap, with a volume threshold of A) 0.025 and B) 0.01 used. Scale bar set to 100 Å

4.4.3 Clathrin hub model generation

A new clathrin model was developed inside the consensus hub map, using the clathrin hub model (PDB: 6SCT)(35), the crystal structure of the terminal domain (PDB: 1BPO)(156), and a model of the ankle region from the clathrin triskelion model (PDB: 1XI4) (148). Fitting of the models was conducted as described in section 4.2.5. The new clathrin hub model fitted into the consensus hub map is shown in figure 4.4.5. The new model contains terminal domain and ankle domain residues that were missing from the Morris *et al.* (2019)(35)

structure, with the new terminal domain and ankle domain models fitting well into the lower hub density (see figure 4.4.5 A).

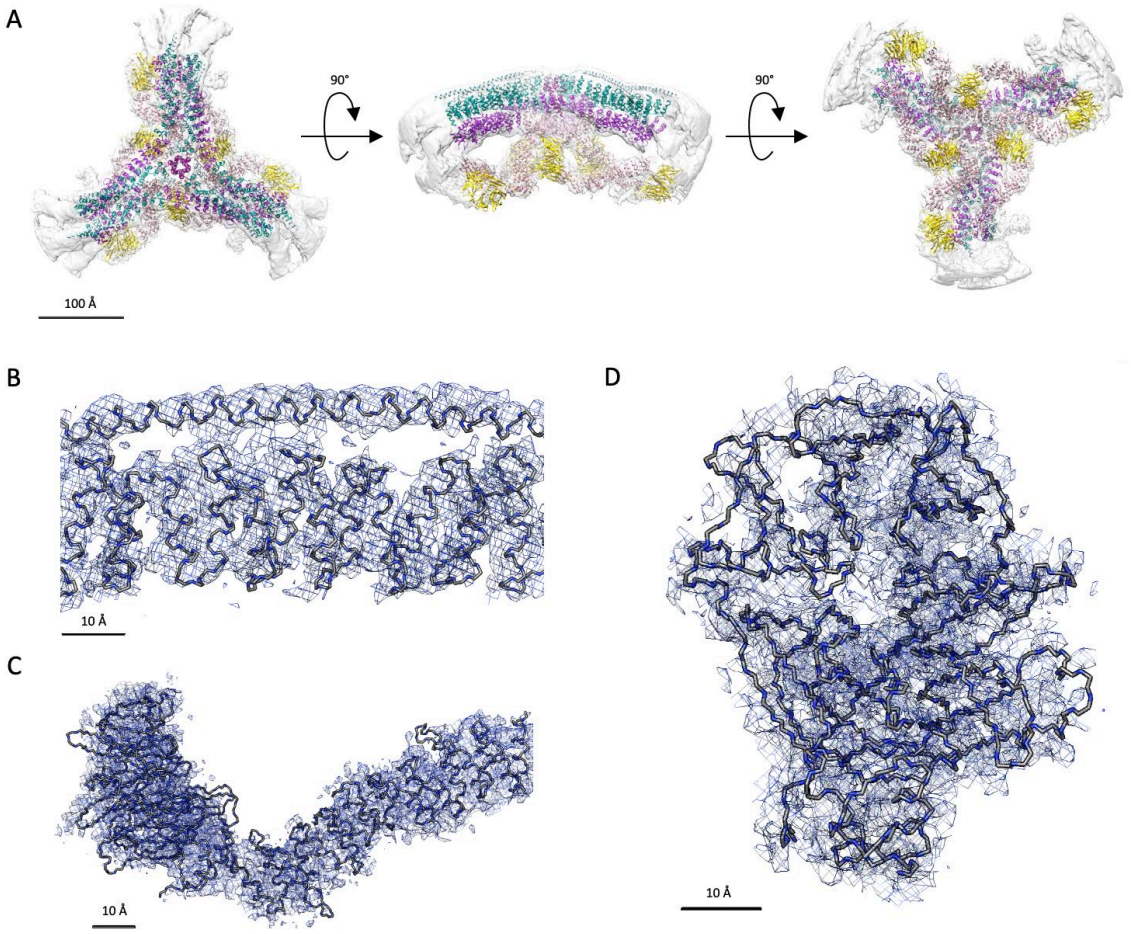

Figure 4.4.5 – New clathrin consensus hub model

New clathrin consensus hub model fitted into the consensus hub density. A) Fit of the consensus hub model in the consensus hub density. Density map presented in a transparent light grey. Scale bar set to 100 Å. B-D) Fit of the consensus hub model carbon backbone within B) proximal and light chain densities, C) terminal and ankle chain densities, and D) terminal domain β-propeller densities. Density map presented as a dark blue mesh. Scale bar set to 10 Å.

A close up view of the proximal domain and light chain residues presented in figure 4.4.5 B show the backbone residues of the model obtained from the Morris *et al.* (2019)(35) structure fit well into the proximal and light chain alpha helical densities of the consensus hub; it is not possible, however, to validate the position of amino acid side chains as the resolution of the electron density is not high enough. Close up views of the backbone residues of the terminal domain

and ankle domain residues obtained from the Ter Haar *et al.* (1998) crystal structure(156) and Fotin *et al.* (2004)(148) model respectively, as shown in figure 4.4.5 C, also show relatively good fitting into the consensus hub density, despite the lower resolution and less defined alpha helices. Fitting of the terminal domain seven-bladed β-propeller into the lower hub density, as shown in figure 4.4.5 D, highlighted structural aspects of the β-propeller observed in the density including the central hole and the location of different blades, which further validated the fitting of the model into the consensus hub density.

To assess why the terminal domain adopts a default position in clathrin cages, as suggested in section 4.4.1, Rosetta and BUDE energy scores were obtained to identify potential residue interactions between the ankle and terminal domain, with values presented in figure 4.4.6 B. Rosetta and BUDE energy scoring was performed on a relaxed version of the model, with differences in backbone and sidechain positioning presented in figure 4.4.6 A, and a Ramachandran plot of the relaxed structure shown in figure 4.4.6 E.

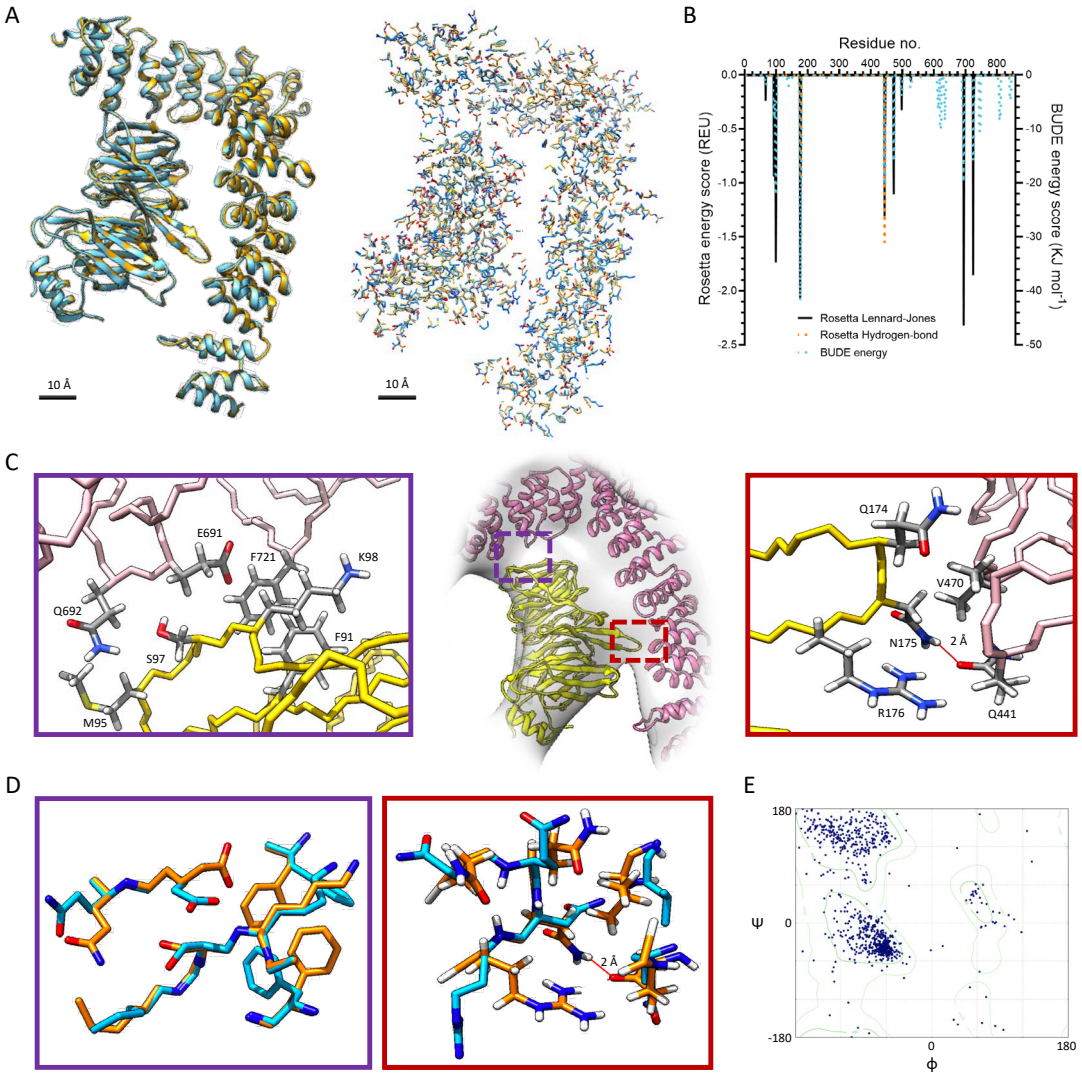

Figure 4.4.6 – Rosetta analysis of clathrin domain interactions

Intermolecular interaction energies for the CHC residues 1 – 855 as determined by Rosetta and BUDE analysis. A) Comparison of the backbone (left) and side chain (right) positions of the original (blue) and relaxed (orange) models. B) Intermolecular interaction energies for the CHC residues 1 – 855 as determined by Rosetta and BUDE analysis. C) Backbone schematic of the clathrin terminal domain (yellow) and clathrin ankle region (pink). Side chains of interacting amino acids presented in grey. D) Comparison of atom positions of the identified interacting residues within the original (blue) and relaxed (orange) models. E) Ramachandran plot of the Rosetta relaxed clathrin structure.

The location of interacting residues identified by both BUDE and Rosetta is shown in figure 4.4.6 C. Several weak interactions appear to occur at the tip of the terminal domain between residues 90 – 100, 691E, 692Q and 721F. Further weak interactions also appear to occur with terminal domain residues 174 – 176

and ankle region residues 441Q and 470V, alongside a stronger hydrogen bond between residues 175N and 441Q. These weak interactions could thus allow the terminal domain to maintain a default position in the absence of adaptors, that is somewhat flexible to allow for adaptor binding and changes in conformation. The exact positioning of the amino acid sidechains in reality could differ from the relaxed version of the model, as the difference between the positioning of side chains in the original and relaxed structure does vary (see figures 4.4.6 A and D), however, as interactions between the terminal and ankle domains have been identified we can conclude that the terminal and ankle domains form weak interactions with one another so that the terminal domain can adopt a default position when adaptor proteins are absent.

4.5 Discussion

4.5.1 Clathrin hub model

As stated previously in chapter 1.6, all published cryo-EM maps of clathrin to date have been of clathrin in the presence of CME adaptors and so, in order to verify clathrin and adaptor densities, a control map and model of clathrin was needed (35,107,123,155). It was also important to see if the resolution of a clathrin map could be improved, and if the structure and orientation of terminal domains could be resolved at a higher resolution due to the flexible nature of this domain and its location in the clathrin cage. Using the localised reconstruction technique utilised by Morris *et al.* (2019)(35,189) on clathrin cage cryo-EM images, the overall particle number was increased and a consensus hub map was developed, having a global resolution of 4.3 Å using 139,259 particles with C3 symmetry imposed. This allowed the structure of the a new consensus hub model to be developed from a clathrin sample with no adaptor proteins present, which includes the terminal and ankle domain residues, both of which were missing from the Morris *et al.* (2019)(35) model.

From the newly developed model, weak inter-molecular interactions between the terminal domain and ankle domain were identified, providing insight into clathrin-clathrin interactions in the lower hub region. From the Rosetta and BUDE analysis, residues F91, K96, and K98 were found to interact with residues from the clathrin ankle region. F91, K96, and K98 are residues from the clathrin box LϕXϕ[DE] motif binding spot, which resides on blade 2 of the 7-bladed β-propeller. The clathrin box motif is highly conserved within adaptors including the β3-appendage of AP3, amphiphysin, arrestin3 segments, and β-arrestin 1 and β-arrestin 2 (160–164). In addition, residues Q174, N175 and R176 were also found to interact with the ankle region and are found between blades 4 and 5 of the 7-bladed β-propeller near the centre of the β-propeller, which is where the W-box PWXXW motif binding spot is located (159). As the

location of interactions between the terminal domain and ankle regions aligns with predetermined binding spots for adaptor protein clathrin binding motifs, we can conclude that there are specific binding spots on the terminal domain which can interact with clathrin and adaptor proteins. The data also suggests adaptor proteins may break clathrin-clathrin interactions when binding to the PWXXW and LϕXϕ[DE], which will lead to changes in clathrin conformation. As the adaptor starts to bind to the clathrin complex, the adaptor might push or pull on the terminal domain, possibly *via* steric hindrance, with a force greater than the combined clathrin terminal-ankle interactions, thereby allowing alteration of terminal domain positioning. Gaining further insights into where and how adaptors bind, could be the key to understanding how adaptors enable clathrin coat assembly and clathrin coat disassembly.

The consensus hub map and model will also provide a control for validating adaptor protein densities bound to clathrin cages, enabling the map to be used alongside other clathrin adaptor structures for difference mapping purposes. The Fotin *et al.* (2004)(107,148) maps and models of clathrin with AP2 and clathrin with AP2 and auxilin, as well as the recent Smith *et al.* (2021)(208) map and model of clathrin bound to β2-adaptin, are examples of structures the new consensus model can be compared against, with comparisons of the hub structures and lower hub regions presented in figure 4.5.1.

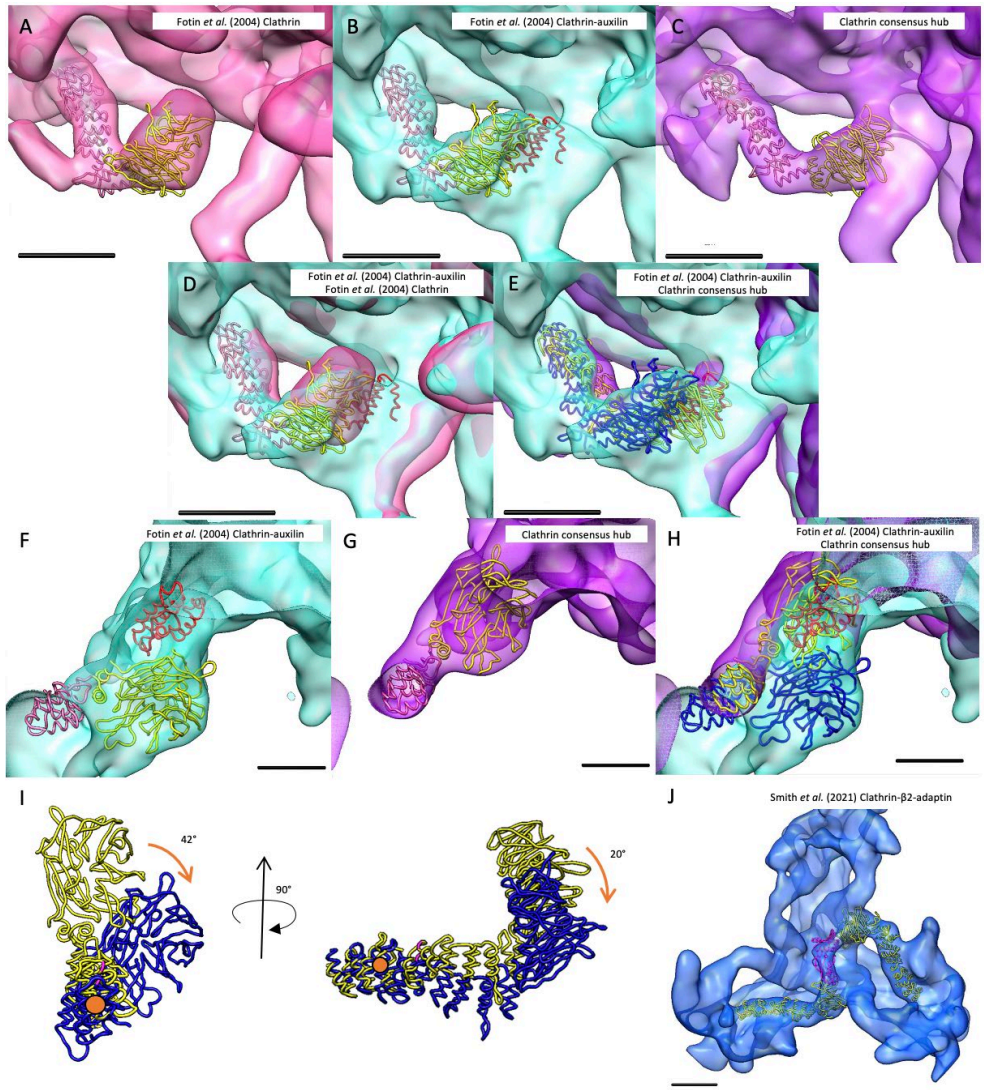

Figure 4.5.1 – Comparison of consensus hub with published clathrin structures

Comparison of the consensus hub map and model with the Fotin *et al.* (2004)(107,148) clathrin and clathrin auxilin maps and models, in addition to the fitting of the consensus hub model into Smith *et al.* (2021)(208) clathrin β_2-adaptin map. Scale bars set to 50 Å. All maps were gaussian filtered with a standard deviation (sd) of 5 Å. A-I) Fitting of the clathrin ankle (pink) and terminal domain (yellow) regions from PDB models of the consensus hub (yellow) and Fotin *et al.* (2004)(148) clathrin cage (blue) [PDB: 1XI4], and the auxilin J-domain structure from Fotin *et al.* (2004)(107) clathrin auxilin complex [PDB: 1XI5], into their respective maps (consensus: purple, clathrin cage: pink [EMDB: 5119], and clathrin auxilin: blue [EMDB: 5120]). A) Fotin *et al.* (2004) clathrin cage. B&F) Fotin *et al.* (2004) clathrin auxilin complex. C&G) Consensus hub. D) Fotin *et al.* clathrin cage transposed against the Fotin *et al.* clathrin auxilin complex. E&H) Consensus hub transposed against the Fotin *et al.* clathrin auxilin complex. I) Angular difference of the clathrin ankle and terminal domain region between the consensus hub model and the Fotin *et al.* clathrin cage model developed with AP2 present. Orange circles represent the point of rotation, and orange arrows indicate direction and amount of rotation between the two models. J) Fitting of the consensus hub model ankle and terminal domain regions (yellow), and the Owen *et al.* (2000)(209) β_2-adaptin model (pink) [PDB:1E42] into the Smith *et al.* (208) clathrin β_2-adaptin complex map (blue) [EMDB:12984].

Comparison of the consensus hub with the Fotin *et al.* clathrin and clathrin auxilin complex, as shown in figures 4.5.1 A-I, bring up several questions, such as why the terminal domain positions in the consensus and Fotin *et al.* structures differ, and whether the designated position of the auxilin J-domain in the Fotin *et al.* clathrin auxilin map is correct? The Fotin *et al.* clathrin structures were produced from clathrin cages formed in the presence of AP2, which was included to assist cage formation. The presence of AP2 appears to alter the position of the terminal domains inwards, shown in figure 4.5.1 A, when compared to the clathrin only structure, shown in figure 4.5.1 C. Figure 4.5.1 I shows that the terminal and ankle domains of the Fotin *et al.* structures appear to rotate around a point in the ankle near the 11th and 12th alpha helices, twisting 42° inwards towards the centre of the hub, and rotating 20° downwards along the z-axis, when compared to the clathrin only structure. As AP2 binds to the clathrin box binding site on the terminal domain, the rotation and position change of the terminal domain could be attributed to the strain on the 'default' clathrin structure and clathrin-clathrin interactions, caused by AP2 binding between clathrin box binding site and the clathrin ankle region.

Comparison of the Fotin *et al.* clathrin AP2 map and clathrin AP2 auxilin map, shown in figure 4.5.1 D, suggests the terminal domains in the clathrin AP2 auxilin map adopts the same position as the terminal domains in the clathrin AP2 map, with the extra density attached to the terminal domain in the clathrin AP2 auxilin map being the location of the auxilin J-domain, as presented in figure 4.5.1 B. The terminal domains between the Fotin *et al.* structures and the consensus hub, however, differ, with the location of the terminal domain in the consensus hub and the auxilin J-domain in the clathrin-auxilin complex overlapping, as presented in figure 4.5.1 E. This hints at the possibility that the position of the auxilin J-domain may instead be where the terminal domain is reported in Fotin *et al.*, as presented in figure 4.5.1 B, and the terminal domain instead positioned where the auxilin J-domain is reported. Due to the low resolution of the Fotin *et al.* clathrin-auxilin map, which was reported at 12 Å, and the overlap of the auxilin and terminal domain locations between the

clathrin only and clathrin auxilin maps, the possibility that the location of auxilin and the terminal domain may be switched around cannot be ignored. In addition, other questions are brought forward upon comparison of the consensus hub with the Fotin *et al.*, maps, including whether auxilin can alter the position of the clathrin terminal domains in the absence of AP2? How similar are the clathrin alterations caused by auxilin compared to those caused by AP2? And does auxilin saturation override alterations caused by AP2 presence? As such, there is now an alternative possible interpretation of the Fotin *et al.* clathrin-auxilin, suggesting the auxilin and terminal domain locations may be switched. It would therefore be advantageous to determine the clathrin auxilin complex structure at a higher resolution to locate the position of the auxilin J-domain and the clathrin terminal domain more accurately.

In addition to identifying new research questions on clathrin-auxilin interactions, the 9.3Å 28-minicoat map produced in this study has been utilised in the recent Smith *et al.* (2021)(208) paper as a control for difference mapping and student t-test statistical analysis. The journal paper has been attached to the end of this thesis in Appendix 2, with the difference mapping data presented in figure 3 of the paper. Fitting of the consensus hub model into the Smith *et al.* clathrin β_2-adaptin map, as shown in figure 4.5.1 J, also aided in the identification of the β_2-adaptin density, and fitting of the β_2-adaptin structure produced by Owen *et al.* (2000)(209). By fitting PDBs of the clathrin terminal domain model and the β_2-adaptin structure into the Smith *et al.* map, further statistical analysis of clathrin-adaptor interactions could be conducted. The positioning of β_2-adaptin in relation to the clathrin terminal domain shown in figure 4.5.1 J, showed binding of β_2-adaptin around the tip of the terminal domain, which is around blades 2 and 3 of the β-propeller. The clathrin box motif in β_2-adaptin was also identified in Smith *et al.* as essential for binding of β_2-adaptin to the terminal domain (208). The location of β_2-adaptin around the clathrin box binding spot provides further support for the proposed hypothesis that AP2 disrupts clathrin-clathrin interactions between the terminal domain clathrin box binding site and the clathrin ankle region, creating the

conformational changes observed in the Fotin *et al.* clathrin structure terminal domains. If the hypothesis is indeed correct, then as more information on terminal domain and adaptor protein interactions are acquired, key questions can be addressed such as how the adaptors bind to clathrin cages, how adaptor binding changes clathrin conformation, and how binding and conformational changes lead to clathrin coat assembly and disassembly.

4.5.2 Study limitations

Despite successfully producing a clathrin hub structure with the lower hub densities intact, limitations of the study will have impacted the overall result. Details of the study limitations and their potential solutions are discussed below:

4.5.2.1 Particle number

The number of micrograph images obtained is limited by equipment, project funding and computer storage space limitations. This in turn will have impacted the number of particles acquired and used for developing the clathrin structure. If more particle images were obtained, it is possible the resolution of the consensus hub structure could have been improved further. The recent installation of the Gatan K3 camera on the Titan Krios (LISCB) will improve the quantity of micrographs collected from future data collections that occur over a similar time frame, with the Gatan K3 frame rate being 1500 frames per second (fps) which is 37.5 times the speed of the Falcon III. In addition, more data collection time on the Titan Krios (LISCB) will further increase micrograph number. To store and process more micrographs and particles however, access to a larger computer storage space is required, as the storage space needed for the clathrin cage micrographs measured 14.4 TB. This could be achieved by purchasing network storage space and/or external hard drives, or by upgrading the computer with larger storage drives. Funding, however, is the largest limitation as purchase of large volumes of computer storage space and several

days of data collection on the electron microscope will currently cost several thousand British pounds. Unless the cost storage solutions and the hourly rate of electron microscopy data collection decreases, compromises are needed when using cryo-EM for structural analysis.

4.5.2.2 Pixel size

The field of view of the camera used will also impact the overall resolution possible, with a larger field of view attributed to a larger pixel size. The sensor size of the Falcon III is 16.5 megapixels, however, the recent installation of the Gatan K3 camera on the Titan Krios (LISCB) has a sensor size of 24 megapixels, nearly double the size of the Falcon III. The higher sensor size of the Gatan K3 will therefore improve the quality and pixel size of micrographs collected from future data collections.

4.5.2.3 Nyquist frequency and aliasing

The resolution of cryo-EM reconstructions is limited by the Nyquist frequency, which is half the image sampling frequency acquired from the electron detector (210). For the clathrin consensus hub a sampling pixel size of 1.39 Å px^{-1} was used, yielding a Nyquist frequency of 1/2.78 $Å^{-1}$ and Nyquist resolution limit of 2.78 Å. Aliasing also causes additional limitation of maximum resolution on top of the Nyquist frequency limits. Aliasing is where artifacts are created due to image information that has a higher spatial frequency than the Nyquist limit, causing the information to be aliased to a lower spatial frequency. When aliased signals are not easily distinguished from the background, they are perceived as noise which inevitably limits the maximum resolution further (210).

Super-resolution imaging is a possible methodology to tackle aliasing and Nyquist frequency limitations. An electron during super resolution imaging is detected by multiple adjacent pixels and can therefore be attributed to a quadrant of a pixel which in turn results in a four-fold increase in the number of image pixels to detector pixels (210–212). Super-resolution imaging therefore

can reduce aliasing effects by doubling the spatial sampling frequency (210). The recent study by Feathers *et al.* (2021)(210) was able to use super-resolution imaging on a 2-condenser lens microscope to surpass the Nyquist frequency limit, producing a 2.77 Å structure using 1.66 Å px^{-1} images (~56,000 particles) and a 3.06 Å structure using 2.1 Å px^{-1} images. Feathers was able to surpass the Nyquist frequency by re-extracting particles after an initial 3D refinement using the super-resolution pixel size as opposed to the physical pixel size, of which would be half the physical pixel size value (210). By adopting the method used by Feathers *et al.* (2021)(210), it may therefore be possible to further increase the resolution of clathrin cage and hub reconstructions closer to the Nyquist frequency by reducing the effects of aliasing. As the current resolution however is not close to Nyquist, it may be more beneficial at present to obtain more particle images and use images obtained at a larger box size, so that high resolution information at high spatial frequencies is not lost.

4.5.2.4 *In vitro* sample

Although a structure of clathrin was obtained, the sample used to obtain the structure was prepared *in vitro. In vivo,* clathrin requires assembly adaptor proteins and lipids to polymerise into clathrin coats(213), however, for the study clathrin was polymerised into cages *in vitro* by exposing high concentrations of clathrin triskelia to ionic conditions (214) as conducted by previous clathrin adaptor cryo-EM structure studies (35,107,123,148,155,173,208). The difference in the way clathrin is polymerised *in vitro* compared to *in vivo* could produce differences in clathrin conformation, and therefore impact the overall validity of the structure. To tackle this limitation, improvements in the cryo-ET methodology and equipment is required so that it is possible to produce a high-resolution structure of a CCV in *in vivo* conditions. This will allow structures of individual clathrin CCV's to be developed and compared with the structures of *in vitro* clathrin cages with and without adaptors bound, to assess the impact of *in vitro* conditions on clathrin cage structure.

4.5.3 Conclusion

Use of cryo-EM and localised reconstruction has allowed a 4.3 Å clathrin consensus hub structure and model with lower hub structure details to be obtained, enabling a greater understanding of clathrin-clathrin and clathrin-adaptor interactions, and provides a control for difference mapping, adaptor density validation, and understanding changes in clathrin conformation that occur during adaptor binding. We have identified interactions between the clathrin terminal domain and clathrin ankle regions that overlap the clathrin box motif and W-box motif binding sites and, showed how these interactions could explain the conformational changes observed in clathrin cages when AP2 is present, an adaptor known to bind to the clathrin box. The data on clathrin-clathrin interactions at terminal-ankle domain interfaces will be invaluable for understanding clathrin-adaptor interactions and adaptor effects on clathrin conformation. The developed 28-minicoat clathrin cage structure has also been used in the recent Smith *et al.* (2021)(208) to aid the identification of β_2-adaptin density, further highlighting the advantages of an adaptor-free clathrin cage map within the scientific literature for difference mapping purposes.

In addition, the new clathrin consensus hub structure has allowed potential inconsistencies in the Fotin *et al.* (2004)(107) clathrin auxilin structure to be identified which require further investigation. The possibility that the proposed binding location of the auxilin J-domain may differ from that stated in the Fotin *et al.* warrants an additional investigation to validate the location of auxilin binding. Due to the success of localised reconstruction for improving clathrin hub resolution and aiding the identification of adaptor densities, as shown from the Morris *et al.* (2019)(35), the recent Smith *et al.* (2021)(208) clathrin β_2-adaptin structure, and the consensus hub structure that has been obtained, the next chapter of this thesis will focus on the development of a clathrin auxilin structure using cryo-EM and localised reconstruction.

Chapter 5:

Cryo-EM of Clathrin with Bound Auxilin

Chapter Overview

This chapter details the determination of a clathrin auxilin complex structure using cryo-EM and localised reconstruction analysis, to produce higher resolution information on clathrin-auxilin interactions and auxilin binding locations.

5.1 Clathrin Auxilin Complex Questions

As previously discussed in section 4.5.1, due to the differences in terminal domain position between the Fotin *et al* (2004) (107,148) models and the adaptor free clathrin consensus hub model, further investigation of clathrin-auxilin interactions are required. In addition, acquiring higher resolution maps of the clathrin auxilin complex will enable interactions between auxilin and clathrin to be pinpointed more closely, allowing a greater understanding of the CME process.

As described in section 1.2.4, auxilin chaperones the adaptor protein Hsc70 to clathrin cages to trigger clathrin cage disassembly. As stated in section 1.3, mutations within auxilin and a reduction of auxilin expression within neurons are associated with Parkinson's disease. By using auxilin as a focus for the remainder of this thesis, it is hoped that a greater understanding of clathrin-auxilin interactions can be obtained which could shed light on auxilin's disassembly mechanism, and how changes to the disassembly mechanism in Parkinson's disease models for example lead to disease states. The remainder of this chapter will therefore investigate the binding location of auxilin to clathrin complexes using cryo-EM and localised reconstruction techniques.

5.2 Methods

5.2.1 Clathrin binding assays

Two samples for each of the following clathrin to adaptor concentration ratios were prepared in polymerisation buffer pH 6.4, with a final volume of 100 µl and a clathrin concentration of 3 µM: 1:1, 1:2, 1:3, 1:4, 1:5, 1:10, 1:15, 1:20, 1:30 and 1:70. Samples were incubated on ice for 1 hour, before centrifugation at 140,000 × g for 30 minutes at 4 °C. The supernatant and pellet were separated before the pellet was resuspended in 100 µl polymerisation buffer pH 6.4. SDS-PAGE samples were prepared using a 1:1 sample to loading dye ratio. SDS-PAGE was conducted to determine the level of adaptor saturation within each pellet, which were analysed using the FIJI gel analyser tool by comparing the area of SDS protein band greyscale peaks (215).

5.2.2 Cryo-EM sample preparation

The clathrin cage auxilin complex was made by reconstitution of clathrin in depolymerization buffer pH 6.4 at 4 °C, at 8 µM with a thirtyfold molar excess of auxilin for 4 hours with one buffer change, followed by dialysis overnight into polymerization buffer at pH 6.4 with one buffer change. Glow-discharged Quantifoil R 1.2/1.3 holey carbon film 300 mesh copper grids were loaded with 3 µl aliquots of clathrin-auxilin complex. Grids were single side blotted and plunge frozen in liquid ethane using a Leica Automatic Plunge Freezer EM GP2, with a single blot lasting 4 seconds and a chamber humidity of 50 %. Grids were screened on a 200 kV JEOL 2100 Plus (University of Warwick) fitted with a Gatan OneView IS camera at a nominal magnification of 20,000×. A representative micrograph image is presented in figure 5.2.1 B alongside its measured CTF (figure 5.2.1 C).

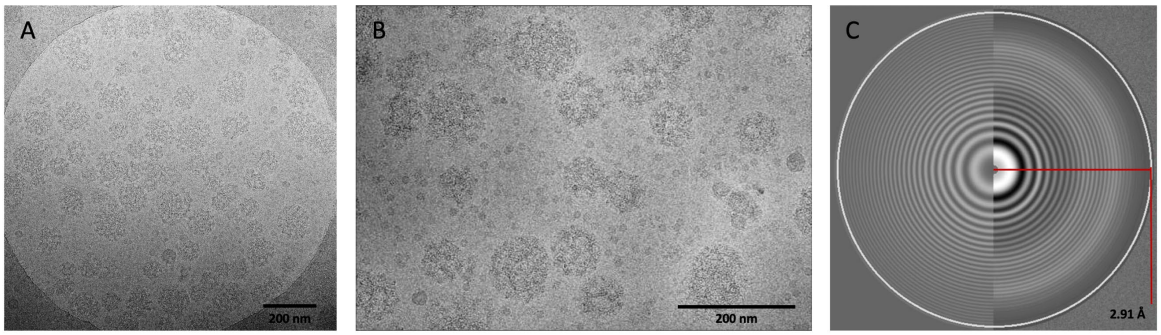

Figure 5.2.1 – Clathrin-auxilin complex cryo-EM screening and data collection

Collected EM images of clathrin cages during screening and data collection. A) Image of screened grid obtained from a 200 kV JEOL 2100 Plus. Scale bar set to 200 nm. B) Clathrin cages imaged on a 300 kV Titan Krios during data collection. Scale bar set to 200 nm. C) CTF for presented micrograph. Oscillations are detected above noise levels up to a resolution of 2.91 Å.

5.2.3 Cryo-EM data collection

Cryo-EM micrographs were collected automatically using an FEI Titan Krios G3 (LISCB) operated at 300 kV equipped with a Gatan K3 counting detector. Images were collected with a nominal magnification of 64000 and magnified pixel (px) size of 1.37 Å/px, using a 100 µm objective aperture, 50 µm C2 aperture, spot size of 5, 2.7 spherical aberration, and 1.95 µm illuminated area to ensure illumination of the carbon support with one image acquired per hole. A total dose of 41 $e^{-}/Å^{2}$ were collected over 7 s at a dose rate of 1 $e^{-}/Å^{2}$ s^{-1}. Micrographs were targeted for collection between 0.8–1.7 µm defocus with 300 nm steps. A sample micrograph is presented in figure 5.2.1 B, with the corresponding CTF

5.2.4 Cryo-EM data processing

Mrcs movie files were imported into Scipion(v3)(190) for data processing. Mrcs movie files were motion-corrected using the MotionCor2(185) plugin to produce motion-corrected summed micrographs with dose weighting. The contrast transfer function of the micrographs was estimated from the dose weighted micrographs using the gctf (v1.06)(186) plugin using the validation and EPA

functions. Clathrin-auxilin complexes were autopicked, using a 1000 box size with 1.37 Å/px, *via* the Cryolo(216) package after performing training to pick clathrin cages, selecting a total of 76,089 particles.

The remaining steps used Relion(v3.1)(191) plugins for structure refinement. Dose weighted particles were subjected to reference-free 2D classification over 25 iterations. High-resolution 2D classes were selected and used in a supervised asymmetric 3D classification into ten volume classes using a previously described cage library(35) as reference volumes. The volumes from the classification and associated particles were subjected to 3D refinement with no symmetry imposed and a low pass filter of 60 Å applied. Refined classes that produced expected cage volumes were selected for further 3D refinements with imposed symmetry, with final refinements of cages conducted with no symmetry imposed to prepare them for localized reconstruction. Masks were generated from the reconstructions at 3σ, extended and softened by 3 px and 3 px respectively, to refine the respective structures imposing symmetry whilst employing solvent flattening and a Gaussian noise background. The resolution of each reconstruction was estimated using FSC measurements, using a mask with a contour level of 3σ, expanded by 5 px and softened by 9 px. The MTF of the Gatan K3 camera operated at 300 kV was applied to the clathrin-auxilin maps, and the B factor of the map automatically calculated when the resolution exceeded 10 Å(195,196). Table 5.2.1 provides a summary of the EM map statistics for processed cages. Local resolution was calculated using ResMap(193) using a resolution range of 8-14 Å with 1.5 Å steps.

Table 5.2.1 – EM map statistics for processed clathrin-auxilin cages

	28-minicoat	32-sweet potato	36-tennis ball
Complex ordered molecular weight	17.6 MDa	20.2 MDa	22.7 MDa
Final box size (px)	700	800	800
Particle number (initial)	76,089		
Particle number (final)	39,126	2,812	12,314
Symmetry	T	D3	D2
Map resolution (FSC 0.2)	9.9 Å	18.8 Å	13.4 Å
Measured map B-factor (Å^2)	-1040	-1493	-1123

5.2.5 Localised reconstruction

The protocol for localized subparticle extraction and reconstruction was followed as previously described(35,189), to extract trimerization hub subparticles from whole cage particles. Hub domains were extracted using a 300 box size at 1.37 Å/px. All hub particles were combined and underwent a 2D classification followed by an initial 3D refinement with C3 symmetry imposed. A reference map of the lower hub was developed using the refinement volume with *volume eraser* in UCSF Chimera(176). A mask of the lower hub created from the refinement volume was created at a contour level of 1.5σ, expanded by 5 px and softened by 9 px. 3D classification was performed using the lower hub structure and mask to separate the particles into 18 classes with T set to 10, and a low pass filter of 40 Å applied. Homogenous classes were combined with 6 classes obtained in total. Each class underwent a round of 3D refinement, followed by 3D classification into 2 classes to improve hub resolution, followed by a final 3D refinement, with no symmetry or low pass filter applied. Masks were generated

from the reconstructions for the 3D refinements and classifications at 1.5σ, extended and softened by 3 and 3 px.

The resolutions of each hub reconstruction for clathrin and clathrin-auxilin complexes were estimated using the gold-standard Fourier shell correlation (FSC) measurement within a mask created from the refinement volume at a contour level of 1.5σ, expanded by 3 px and softened by 3 px. The MTF of the Gatan K3 camera operated at 300 keV and a low pass filter of 8 Å was applied to the structures, enabling the automatic calculation of map B when resolutions exceeded 10 Å(195,196). Table 5.2.2 provides a summary of the EM map statistics for processed hubs. Local resolution was calculated using ResMap(193) using a resolution range of 6 – 16 Å with 3 Å steps.

Table 5.2.2 – EM map statistics for processed clathrin-auxilin hubs

	Hub class no.					
	1	2	3	4	5	6
Complex ordered MW	1,127.6 kDa					
Final box size (px)	300					
Particle number (initial)	1,554,932					
Particle number (final)	31,334	34,225	23,037	219,146	22,814	81,449
Symmetry	C1					
Map resolution (FSC 0.5)	8.9 Å	10.5 Å	10 Å	8.6 Å	12.8 Å	8.6 Å
Map resolution (FSC 0.2)	7.4 Å	8.9 Å	8.4 Å	6.7 Å	9.3 Å	7.1 Å
Measured map B-factor (Å^2)	-15	-37.3	-28.4	-37.3	-48	-23.6

5.2.6 Difference mapping

Student's t-test was conducted using the *dimgstats* program in BSoft(v2.1.2), which uses the Milligan and Flicker programs as previously described (41,208,217–219). Three independent maps of the clathrin consensus hub and the clathrin auxilin class 4 hub were produced by splitting their respective particle stack into three sets evenly using Scipion(190), and reconstructing the volume for each particle stack subset using Relion(192). A low pass filter of 10 Å was applied to the maps during reconstruction. A mask of the clathrin auxilin class 4 hub was developed at a contour level of 2σ, expanded by 3 px and softened by 3 px, which was applied to the clathrin auxilin class 4 hub subset maps to create auxilin free versions of each map. As the clathrin consensus map has a lower sampling rate of 1.39 Å/px compared to the clathrin auxilin map (1.37 Å/px), the clathrin auxilin maps were scaled to fit the profile of the clathrin consensus maps. The independent maps were then used to calculate the average and variance of the clathrin consensus map, clathrin auxilin map, and clathrin auxilin-removed map.

5.2.7 PDB model generation

A new PDB model of the clathrin auxilin hub was generated using the auxilin J-domain from the PDB file 2QWP (residues 810 – 910) (220) and the consensus hub model developed in chapter 4, which was formed from clathrin hub PDB file 6SCT (residues 635 - 1626), the clathrin terminal domain PDB file 1BPO (residues 1 – 493), and residues 494 - 634 from the clathrin triskelion model PDB file 1XI4 (35,148,156). The consensus model was fit into each class density *via* UCSF Chimera using rigid body fitting, whilst fitting of each auxilin structure was conducted *via* manual placement within UCSF Chimera (176). Coot was utilised to rotate the ankle and terminal domain regions of the consensus hub model so that the hub model fits into the electron density maps (200).

5.2.8 Rosetta and BUDE analysis

To determine potential interactions between the terminal domain and the ankle regions of the CHC, interface energy analysis was conducted using Rosetta(v3.12) (201) on the consensus hub structure. The structure was prepared for energy scoring using the *relax* application, which alters the structure to remove any clashes between amino acids and improve its overall energy score (201,202). To ensure the structure remained similar to the original model, relaxing was conducted over 5 iterations with all atom constraints and no ramping, followed by a single iteration of backbone only constrained relaxation. The RMSD between the starting and relaxed structure was calculated using the program VMD, with the RMSD for Cα position and all atoms being 0.24 Å and 1.39 Å respectively (203). The *residue_energy_breakdown* program and ref2015 scoring function in Rosetta was used to calculate and report the interface energy scores from the relaxed structure in rosetta energy units (REU) (204,205).

BUDE(v.1.2.10)(206,207) was configured to report the theoretical free energy (ΔG kJ mol^{-1}) of binding for the Rosetta relaxed input structure using the heavy_by-atom_2016-v1.bhff forcefield, as described previously (35). The ligand file was split into five residue segments with one residue increments using a windowing operation for the BUDE analysis only.

5.3 Preparation of Cryo-EM Samples

5.3.1 Clathrin binding assays

To determine the saturation point of auxilin binding to clathrin, clathrin binding assays were performed with results shown in figure 5.3.1. Binding of auxilin to clathrin appears to saturate at a molar ratio around 30:1 auxilin to clathrin, with little to no increase in the quantity of the adaptor at 70:1 auxilin to clathrin. This is in agreement with data from Fotin *et al.* (2004) (107) who used a molar ratio of 20:1 auxilin to clathrin to generate clathrin auxilin complexes. A clathrin auxilin concentration ratio of 1:30 was therefore used for cryo-EM sample preparation.

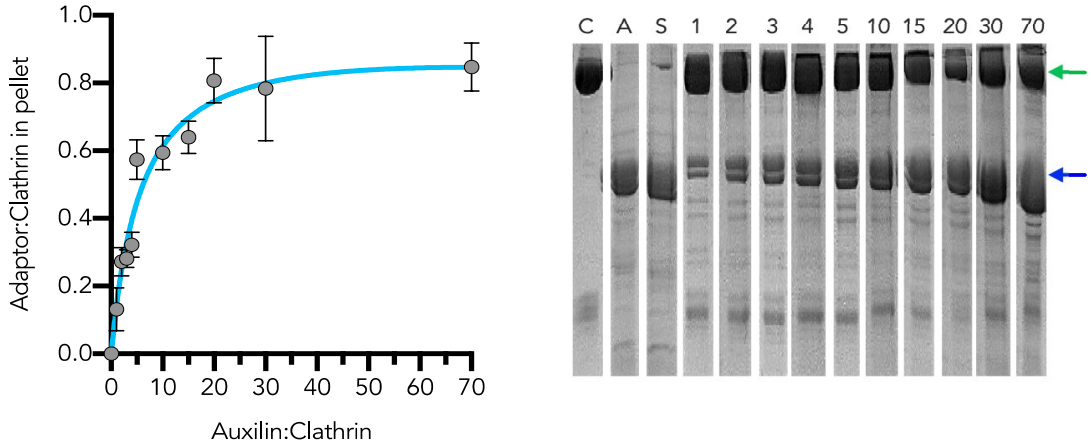

Figure 5.3.1 – Clathrin auxilin binding assay

Results of clathrin auxilin binding assay, with the total binding curve shown on the left and corresponding SDS-PAGE data shown on the right. Clathrin is indicated by the green arrow, and auxilin by the blue arrow. Error bars presented as sd.

5.3.2 Screening of clathrin adaptor grids

Initial attempts to make grids of clathrin auxilin complexes were unsuccessful, as issues arose for preparation of quantifoil grids with the glow discharger that

have yet to be resolved. Glow discharged grids remained hydrophobic causing faster blotting and uneven ice formation during the blotting and freezing process, leading to protein samples crowding the outer edges of the copper squares and empty central holes, as demonstrated in figure 5.3.2.

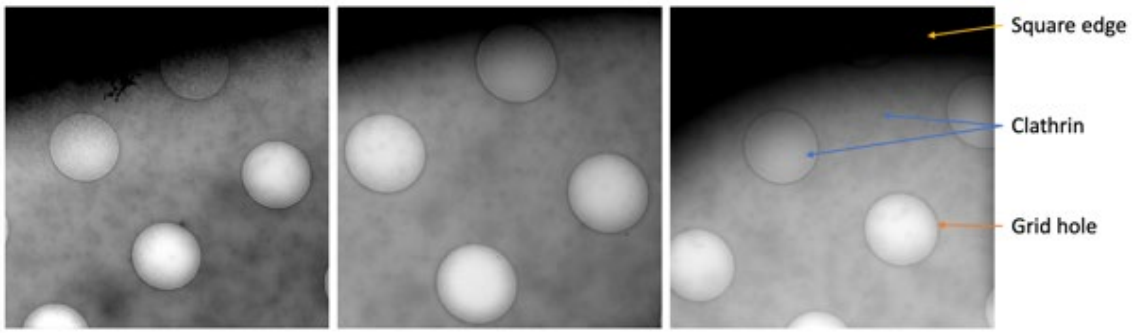

Figure 5.3.2 – Initial freezing attempts

Frozen quantifoil grid images at 8,000 × magnification, demonstrating irregular thin ice within grid holes and congregation of clathrin cages to grid square edges.

Due to the covid-19 lockdown further attempts to make grids were forced to stop, however, Dr Sarah Smith had successfully prepared clathrin auxilin complex grids prior to this which had a 30:1 auxilin to clathrin concentration ratio, with details of purification quality, binding assays and grid screening provided in figure 5.3.3. Dr Sarah Smith kindly provided so that the clathrin-auxilin cryo-EM structure project could continue. As the covid-19 lockdown impacted lab access, it was decided that attempts to produce grids of clathrin ARH complexes were to be discontinued as there would be insufficient time to develop and process the data before the end of the project.

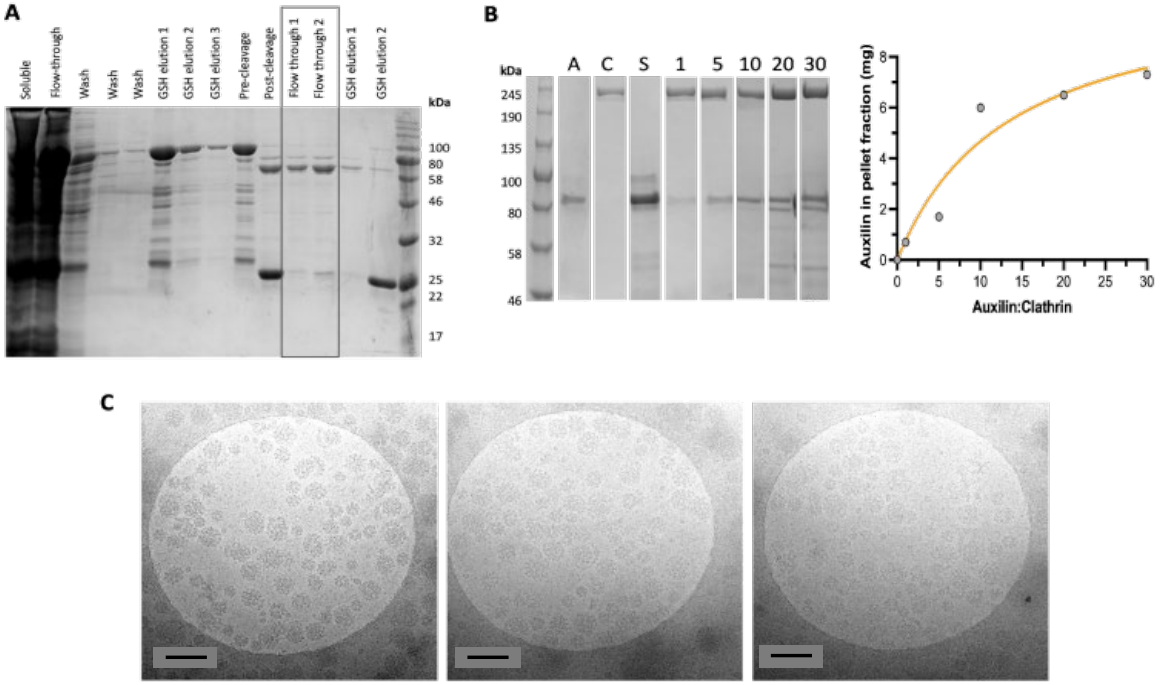

Figure 5.3.3 – Clathrin auxilin sample and grid preparation

Clathrin-auxilin complex sample and grid preparation conducted by Dr Sarah Smith. A) SDS gel of auxilin purification fractions from GST-tag chromatography steps. Black box identifies collected fractions used for binding assays and grid preparation. B) Clathrin binding assay results for auxilin binding, with the total binding curve shown on the right and corresponding SDS-PAGE data shown on the left. A = auxilin only, C = clathrin only, S = soluble fractions, 1 – 30 = pellet fractions of binding experiments with values identifying the auxilin to clathrin ratio. C) Frozen quantifoil R1.2/1.3 carbon 300 mesh copper grids containing 8 μM clathrin and 240 μM auxilin. The scale bar is set to 200 nm.

5.4 Processing of Clathrin Auxilin Complexes

5.4.1 2D and 3D classification

Particles were selected *via* automatic picking using Cryolo(216) as shown in figure 5.4.1. A defocus series was used to obtain particle images at different spatial frequencies. Multiple different cage types are present in the sample, with several large cages being present. Due to the processing abilities of the computer and the size of the clathrin cage minicoat and barrel structures we wish to use

for structural analysis, a box size of 1000 pixels was used. Overall, a total of 76,089 particles were selected from 21,576 images.

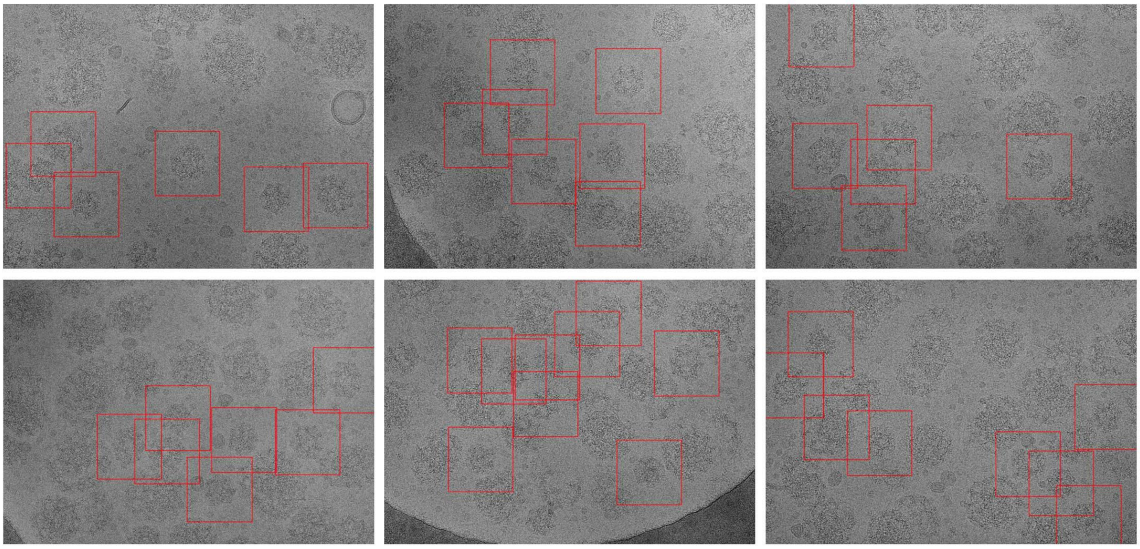

Figure 5.4.1 – Selection of clathrin auxilin particles using Cryolo

A selection of clathrin auxilin cage micrographs. Particles selected *via* Cryolo(216) are surrounded by red squares.

2D classification was conducted on the 76,089 particles selected from manual picking. Classes which looked like clathrin cages were selected for use in 3D classification, with a total of 74,379 particles selected. This step was conducted to remove 'bad' particles; this includes particles which do not match the more prevalent cage types. 3D classification was then conducted using the reference structures shown in figure 5.4.2 A, with the results demonstrated in figure 5.4.2 B. Overall the 28-minicoat structure yielded the highest number of particles with 40,507 particles.

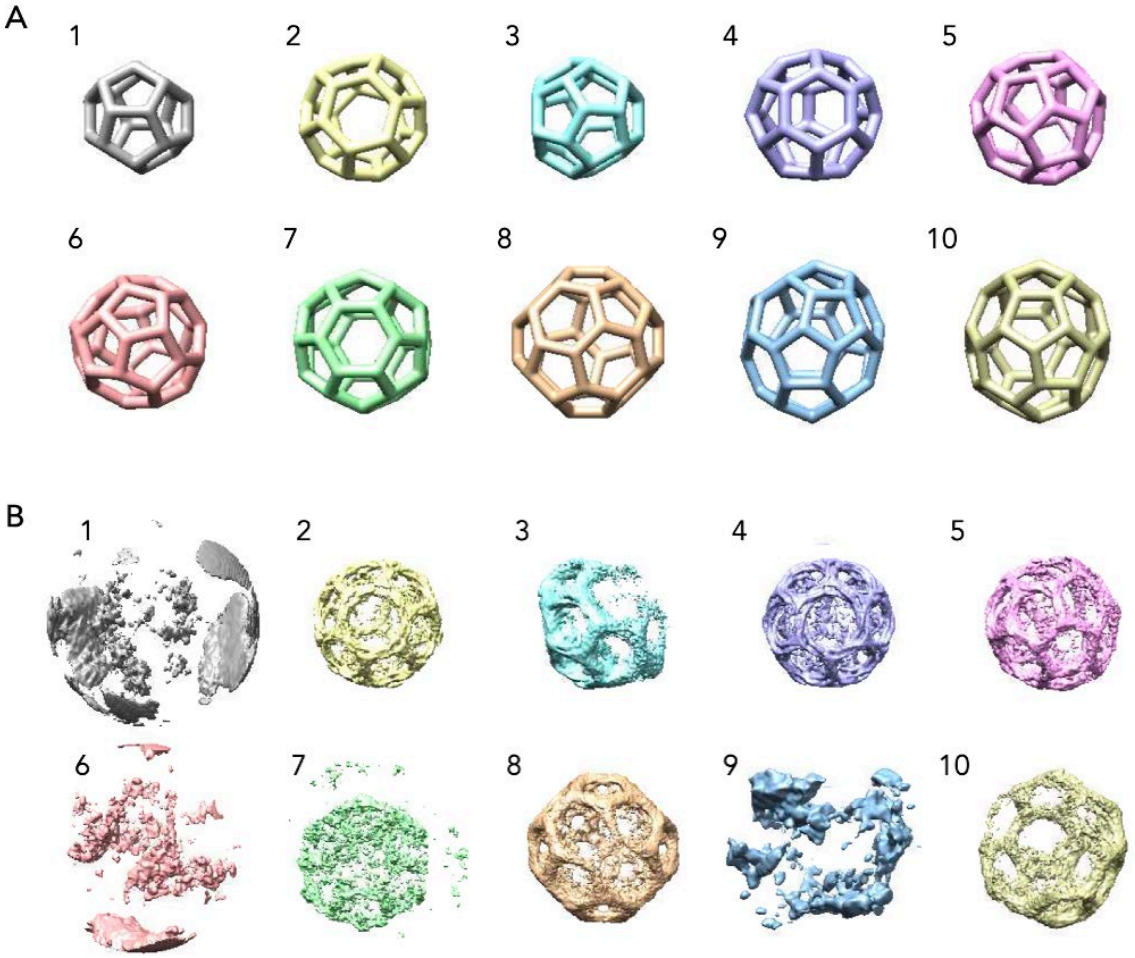

Figure 5.4.2 – 3D classification of clathrin auxilin complexes

Initial 3D classification structures of clathrin auxilin complexes. 1: 20-dodec, 2: 24-cage, 3: 26-cage, 4: 28-minicoat, 5: 32-sweet potato a, 6: 32-sweet potato b, 7: 36-barrel, 8: 36-tennis ball, 9: 38-big apple a, 10: 38-big apple b. A) Reference cage library from Springer Nature: Nature Structural & Molecular Biology, Cryo-EM of multiple cage architectures reveals a universal mode of clathrin self-assembly, Kyle L. Morris *et al.* (2019) (35). B) 3D classification results.

Another 2D classification of selected 28-minicoat, 32-sweet potato, and 36-tennis ball particles was conducted to ensure only high-quality particles are utilised during 3D refinement. Overall, 39,126 28-minicoat, 2,812 32-sweet potato, and 12,314 36-tennis ball particles were selected, with selected 2D classes shown in figure 5.4.3.

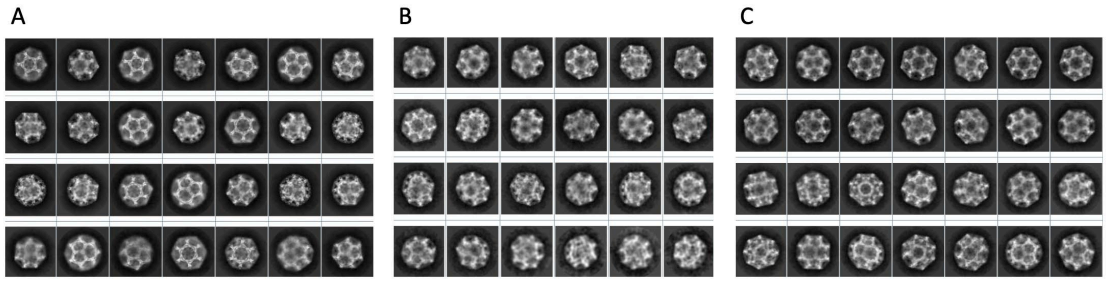

Figure 5.4.3 – Selected 2D classes of clathrin cage particles

2D classification results for 3D classified 28-minicoat, 32-sweet potato, and 36-tennis ball particles. A) Selected 2D classes for 28-minicoat structure development. B) Selected 2D classes for 32-sweet potato structure development. C) Selected 2D classes for 36-tennis ball structure development.

5.4.2 Clathrin auxilin cage structures

The final post-processed map of the 28-minicoat, 32-sweet potato and 36-tennis ball is shown in figure 5.4.4 A. The 28-minicoat structure was produced from 39,126 particles and has a resolution of 9.9 Å, the 32-sweet potato structure was produced from 2,812 particles and has a resolution of 18.8 Å, and the 36-tennis ball structure was produced from 12,314 particles and has a resolution of 13.4 Å, with the FSC curves of all three cages presented in figure 5.4.4 B.

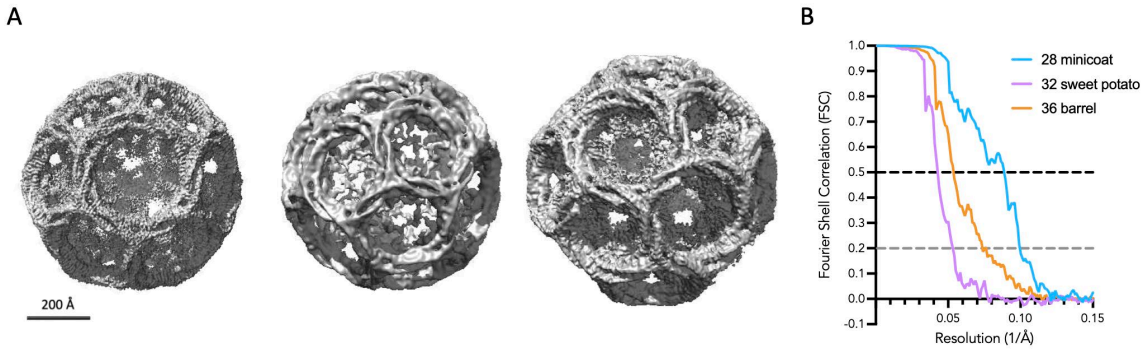

Figure 5.4.4 – Post-processed clathrin auxilin cage structures

Structure and resolution information on the post-processed cage structures. A) Structures of the 28-minicoat (left), 32-sweet potato (middle) and 36-tennis ball (right). Scale bar set to 200 Å. B) FSC curves of the 28-minicoat, 32-sweet potato and 36-tennis ball structures. Grey dotted line at an FSC of 0.2 indicates where the resolution value was obtained.

3D classification of the 28-minicoat cage lower hub region was conducted to determine if the location of auxilin could be identified from whole cages. All 3D classes presented potential auxilin densities and changes in terminal domain positioning. The 3D classes (blue) were superimposed against the 28 minicoat clathrin control (grey) obtained in chapter 4 to highlight possible differences between the structures, with results for each class presented in figures 5.4.5 A and B, and closeups of some of the possible auxilin densities and changes in terminal domain positioning shown in figures 5.4.5 C and D. From the outside facing hexagon faces shown in figure 5.4.5 A, additional densities have been located in areas previously identified by Fotin *et al.* (2004)(107), with terminal domains appearing to bind to the clathrin ankle regions closer to the N-terminal when compared with the clathrin only structure obtained in chapter 4. In addition, terminal domains also appear to rotate inwards towards the centre of hubs, as highlighted in figures 5.4.5 B and D, with additional densities connecting terminal domains together. This suggests auxilin may bind to more than one terminal domain to pull them towards the centre of the hub. Although densities can be observed within all of the 3D classes, it is possible the high level of symmetry across the whole cage causes averaging out of auxilin densities as auxilin may not be symmetrically positioned across the whole cage. For example, the 28-minicoat has 84 terminal domains that auxilin can bind to. If all cages are saturated but auxilin has 3 different states of binding for example (*i.e.*, unbound, bound orientation 1, and bound orientation 2) there will be at least 3^{84} classes, and so the likelihood of auxilin densities being averaged out during reconstruction is high. By doing localised reconstruction instead, only a single hub region will be observed which would significantly reduce the number of classes to 3^3. Conducting 3D classification on 3D refined hub regions should, therefore, aid the verification of results seen in figure 5.4.5 and produce higher resolution structures.

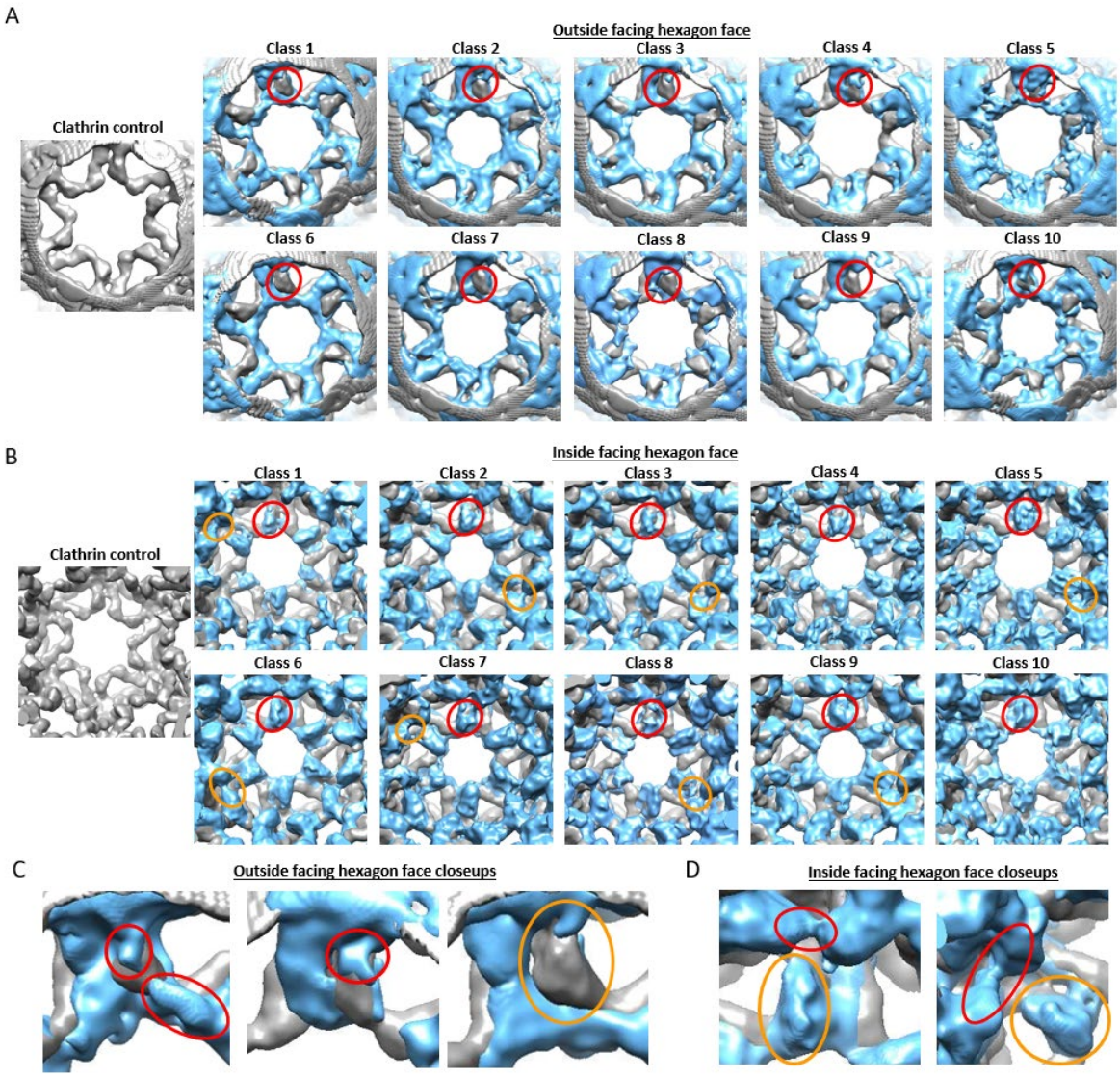

Figure 5.4.5 – 3D classification of clathrin auxilin 28-minicoat complexes

Map densities of all 3D classes from thee clathrin auxilin 28-minicoat 3D classification (blue) superimposed against the 28 minicoat clathrin control (grey) developed in chapter 4, reveals possible auxilin densities and changes in clathrin structure. Possible auxilin densities are highlighted with orange circles, and changes in terminal domain positioning are highlighted with red circles. A) Outward facing hexagon face densities of clathrin auxilin 3D classification results. B) Inward facing hexagon face densities of clathrin-auxilin 3D classification results. C&D) Closeups of possible auxilin densities and changes in terminal domain positioning from outside (C) and inside (D) facing hexagon faces.

5.5 Localised Reconstruction for Locating Auxilin

5.5.1 3D classification of clathrin auxilin hubs

The initial 3D refined clathrin auxilin hub structure is presented in figure 5.5.1 A. The clathrin terminal domains are rotated inwards towards the centre of the hub in agreement with Fotin *et al.* (2004)(107). Several densities have also been identified and pinpointed in figure 5.5.1 A where auxilin may be bound to clathrin, at the terminal domain and proximal distal region, as well as additional density around the CLC N-terminal. 3D classification was performed to further resolve the additional densities, producing six different classes presented in figure 5.5.2.

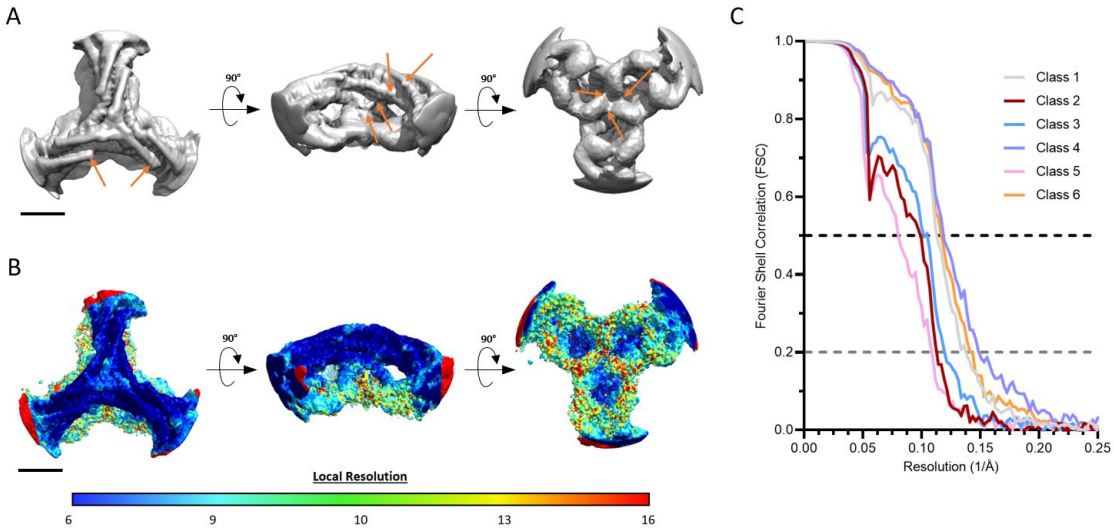

Figure 5.5.1 –Clathrin auxilin hub densities

Refined clathrin auxilin hub map and resolutions of 3D classification maps. Scale bar set to 100 Å. A) Initial clathrin auxilin hub map before 3D classification. New densities pinpointed with orange arrows. B) Local resolution map of the 3D classification class 4 map. C) FSC graph for each refined 3D class. Grey dotted line at an FSC of 0.2 indicates where the resolution value was obtained.

Figure 5.5.2 – Refined clathrin auxilin hub classes

Map volumes of each refined clathrin-auxilin hub 3D classification class in different orientations. Scale bar set to 100 Å.

The FSC curve for each refined class is shown in figure 5.5.1 C, with the local resolution of class 4 presented in figure 5.5.1 B. The resolution of each class at FSC(0.2) is between 6.7 Å – 9.3 Å, and the resolution of each class at FSC(0.5) is between 8.6 Å – 12.8 Å, as shown in table 5.2.2, which is representative of the upper and lower hub region resolution respectively when compared with the local resolution results.

5.5.2 Clathrin auxilin model generation

To confirm the location of auxilin densities within the hub structure, difference mapping was performed to highlight differences between the clathrin consensus hub and the highest resolution clathrin auxilin map, class 4, with results presented in figures 5.5.3 A-D. Due to the rotation of the terminal domains and positioning of auxilin within the clathrin auxilin map when compared to the clathrin consensus hub, it was not possible to accurately highlight the position of auxilin from the difference map. This was because some of the auxilin densities and terminal domain densities are within the same location as the terminal domain densities found in the consensus hub, as demonstrated in figures 5.5.3 A and B, and so only changes in terminal domain position were highlighted, as demonstrated in figures 5.5.3 C and D. To combat this issue, the clathrin auxilin class 4 map was masked to remove the auxilin densities around the terminal domains. The mask was based around a model of clathrin fitted to the clathrin auxilin density at a volume threshold of 0.0055, as shown in figure 5.5.3 E, with the masked clathrin auxilin map transposed against the unmasked clathrin auxilin map shown in figure 5.5.3 F. The masked map was compared with the original clathrin auxilin class 4 map, as demonstrated in figures 5.5.3 G and H. Figures 5.5.3 G and H show a clear change in the position of the clathrin terminal domains and connecting ankle region, with the change in position similar to the difference between the consensus hub and Fotin *et al.* (2004)(148) discussed and presented previously in section 4.5.1 and figure 4.5.1 I respectively.

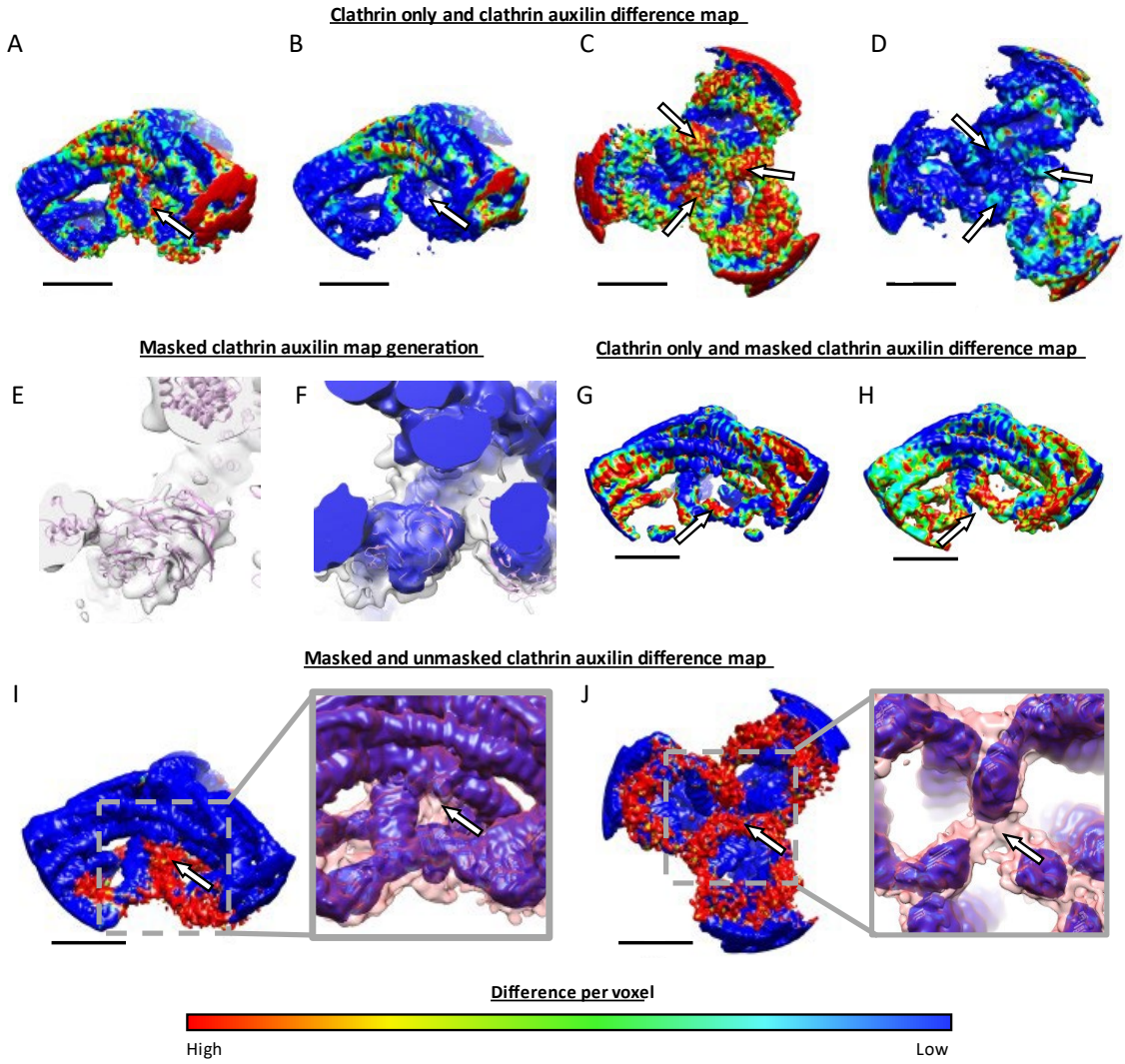

Figure 5.5.3 – Global difference analysis of the clathrin auxilin hub structure

Student t-test difference analysis of the class 4 clathrin auxilin hub map against the clathrin consensus map and masked class 4 clathrin auxilin hub map. Statistically significant differences are shown in a rainbow colour scheme, with red to green being areas of significant difference, and blue being areas of no significant difference. Scale bars set to 100 Å. A-D) Difference analysis of the clathrin auxilin class 4 map and clathrin consensus map applied to the class 4 clathrin auxilin hub (A & C) and clathrin consensus (B & D) maps. Arrows points to significant differences in terminal domain positioning. E & F) Generation of the masked clathrin auxilin map for difference analysis purposes. Clathrin hub ribbon model (pink) fitted against the clathrin auxilin class 4 map (transparent grey). E) Clathrin auxilin class 4 map volume threshold set to 0.0055 to remove lower threshold auxilin densities so a mask could be generated. F) Masked volume of the clathrin auxilin class 4 map (blue) transposed against the clathrin auxilin class 4 map with auxilin densities intact. G & H) Difference analysis of the masked clathrin auxilin class 4 map and clathrin consensus map applied to the masked clathrin auxilin class 4 map (G) and clathrin consensus map (H). Arrows points to differences in terminal domain position. I&J) Difference analysis of the masked and unmasked class 4 clathrin auxilin map applied to the unmasked class 4 clathrin auxilin map. Arrows points to possible auxilin densities. Close up views consist of transposed masked (blue) and unmasked (transparent red) clathrin auxilin class 4 maps. Grey dotted lines highlight area of closeup.

To identify auxilin densities, the clathrin auxilin class 4 map was compared with the masked clathrin auxilin class 4 map, with results shown in figures 5.5.3 I and J. Surprisingly, densities were found not only in the space between the ankle regions and terminal domains, but also between the terminal domains and around the edges of the terminal domains and ankle regions. These results support conclusions of Fotin *et al.* (2004)(107) who suggested the auxilin J-domain binds between the clathrin terminal domain and ankle region. The results also suggest the unstructured region of auxilin may play a larger role in the binding and connecting of the terminal domains to alter their overall position. The densities found around the edges of the terminal domains and ankle regions (figures 5.5.3 I & J) are likely terminal domain and ankle region density noise that forms as a result of the masking procedure, and so fitting of the unstructured auxilin region will not be possible, however, it is possible to fit the auxilin J-domain into its respective densities, with the overall fitting of the auxilin J-domains into the difference maps of each of the clathrin auxilin classes shown in figure 5.5.4. The overall fitting of the auxilin J-domain into the class 4 auxilin densities is presented in figure 5.5.5, with different views of each auxilin model fitted into auxilin densities presented in figure 5.5.5A, and selected enlarged views shown in figure 5.5.5B. Surprisingly, the positioning of the auxilin J-domain within each auxilin map density differed, with the auxilin J-domain adopting different orientations depending upon the positioning of the clathrin terminal domain, with some clathrin terminal domains seen higher up the clathrin ankle region than others which reduced the amount of space available for auxilin to occupy. Further analysis on how differences in the auxilin J-domain position impact clathrin auxilin-interactions and the positioning of Hsc70 when bound to auxilin, may shed additional light on the clathrin disassembly process.

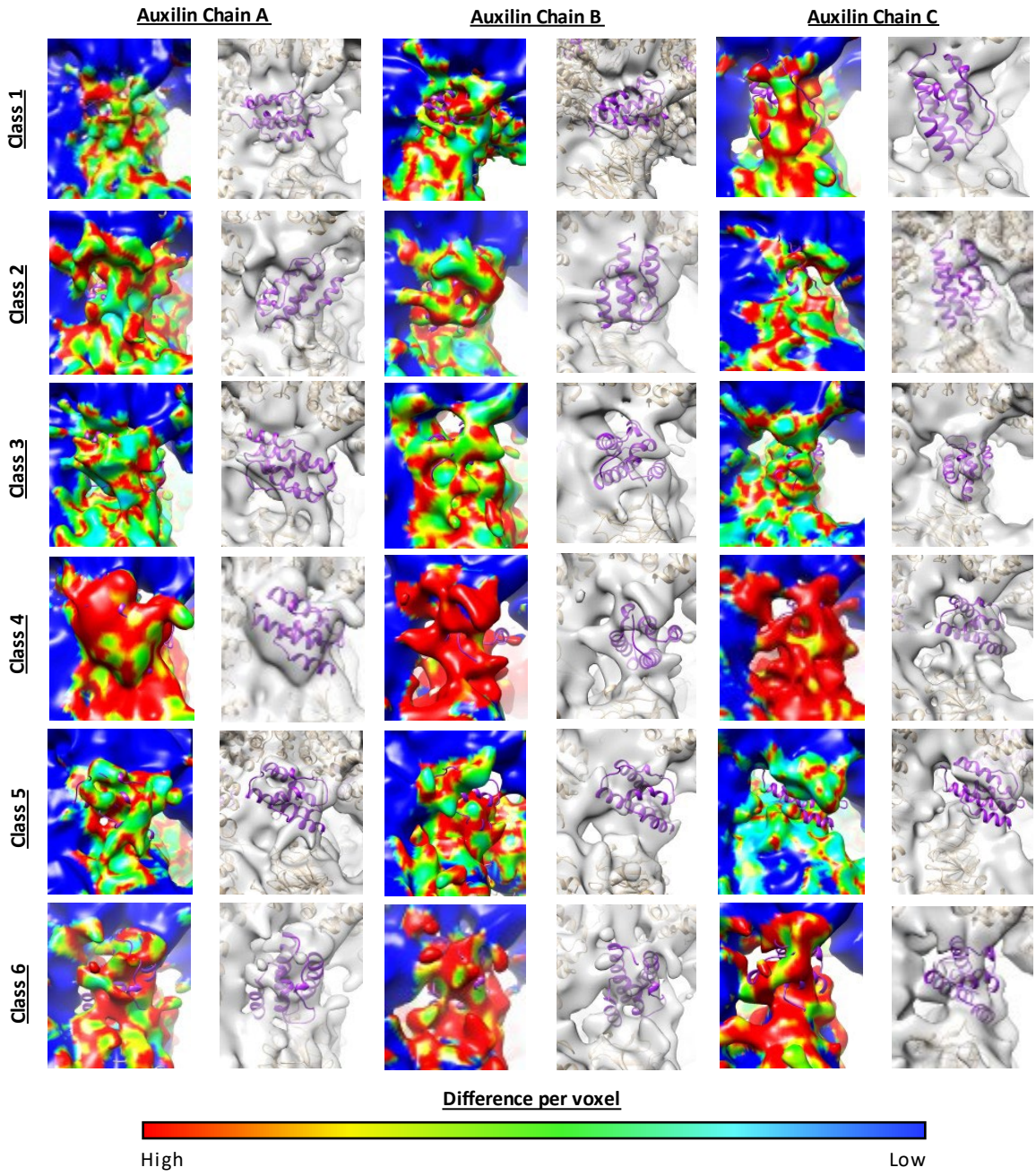

Figure 5.5.4 – Auxilin J-domain adopts different positions when bound

Fitting of residues 812 – 910 of the auxilin J-domain into the three auxilin densities identified within each refined class of the clathrin auxilin map. Ribbon diagrams of the clathrin structure and auxilin structure are coloured in gold and purple respectively. The clathrin auxilin map is coloured using difference map values determined upon comparison with the masked version of the refined class hub (left) to demonstrate where the density differences are. The clathrin auxilin map is also transparent and grey (right) to demonstrate the fitting of the auxilin J-domain within the map density.

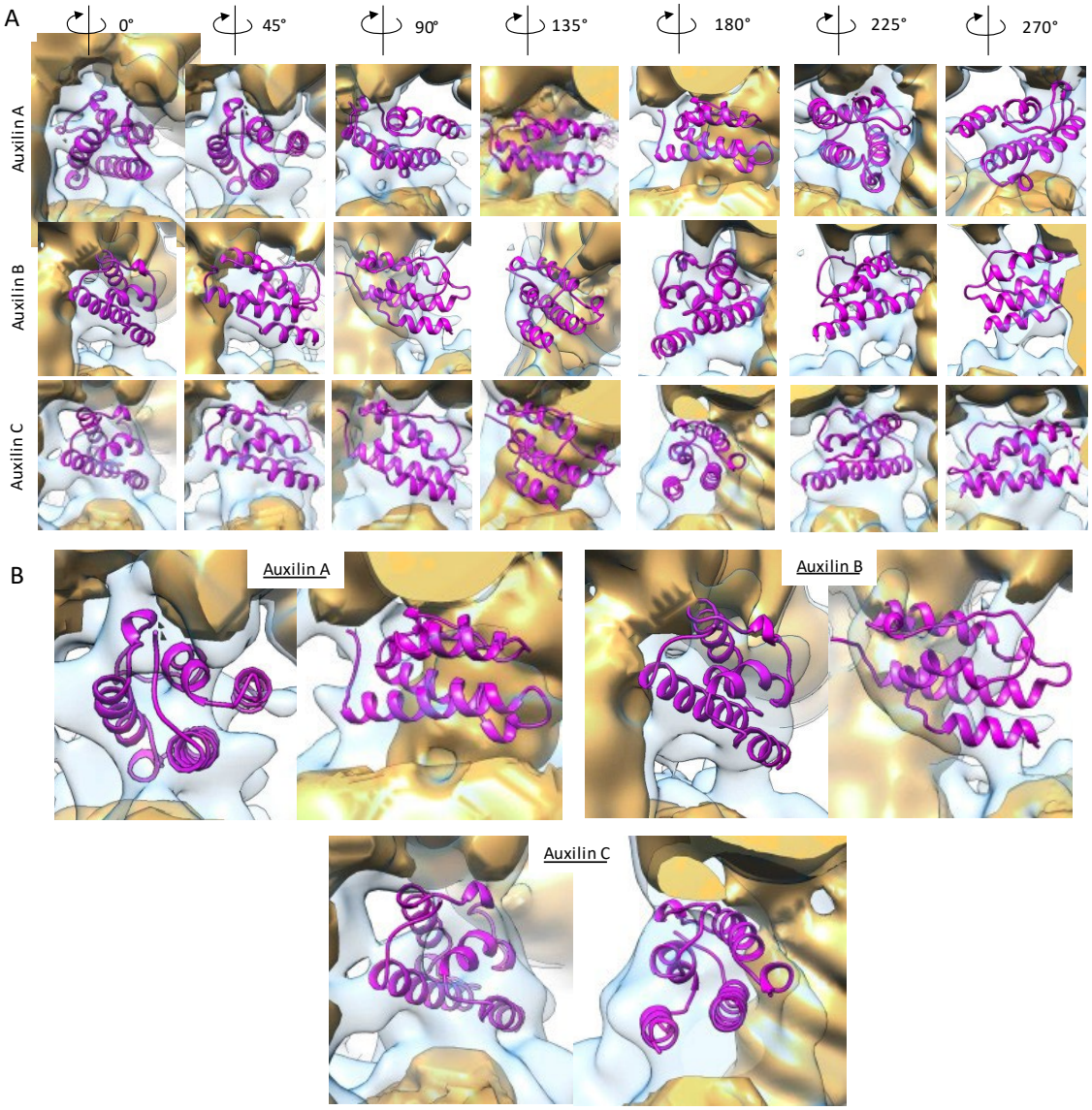

Figure 5.5.5 – Fitting of the auxilin J-domain in the class 4 auxilin densities

Fitting of residues 812 – 910 of the auxilin J-domain into the three auxilin densities identified within the class 4 clathrin auxilin map. Ribbon diagrams of auxilin are coloured in pink. The clathrin auxilin map is coloured in transparent blue, and the masked clathrin auxilin map is coloured in orange. A) Different rotational views of each auxilin J-domain model fitted into auxilin densities. B) Enlarged selected views for each auxilin model.

In addition to the auxilin J-domain density, an α-helical density was also identified at the ankle region of the hub near to where the auxilin J-domain resides (figure 5.5.6). CLCs have been found to mediate clathrin disassembly with removal of CLCs causing a reduced rate of cage disassembly (41). Auxilin has also been found to mediate phosphorylation of CLCb required for the

maturation of clathrin coated pits (221). Binding of CLCb residues near the auxilin J-domain would enable interactions between CLCb and auxilin. As all the auxilin construct α-helices had been modelled and a single α-helix needed modelling at the CLC N-terminal, the additional α-helical densities are likely to be residues 27 – 39 of CLCb,

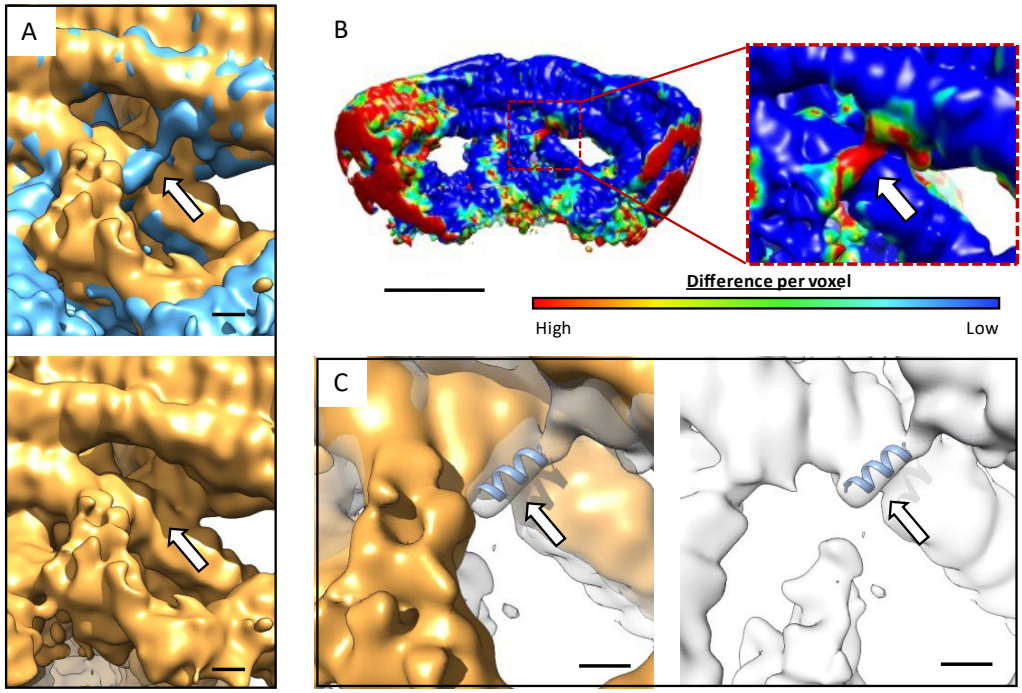

Figure 5.5.6 – CLC N-terminal α-helical density present in clathrin auxilin map

Clathrin auxilin complex map contains CLC N-terminal α-helical density that is not present in the clathrin consensus map. Arrows point to additional CLC density. A) Clathrin auxilin complex map (light blue) transposed against the clathrin consensus map (orange) (top) with a view of the clathrin consensus map shown below for comparative purposes. B) Student t-test difference map of the class 4 clathrin auxilin hub map against the clathrin consensus. Scale bar set to 100 Å. Map coloured according to the level of difference between them. C) CLC N-terminal α-helix model fitted into the clathrin auxilin complex map (transparent grey). Views with (left) and without (right) the clathrin consensus map (orange) transposed against the clathrin auxilin complex map.

5.5.3 Rosetta and BUDE analysis

Rosetta and BUDE analysis of the class 4 clathrin auxilin hub model was conducted to assess the impact of auxilin binding and positioning on clathrin-clathrin and clathrin-auxilin interactions. BUDE was conducted as a complementary analysis alongside Rosetta, as it allows calculation of interaction energies for all favorable rotamer positions. The energy-per-residue profiles from Rosetta and BUDE analysis are similar but have some differences, because Rosetta scoring is more sensitive than BUDE to uncertainties in conformation associated with a 7 Å map. Figure 5.5.7 highlights amino acid residues that could be involved in clathrin-auxilin interactions. Auxilin chains A and B showed little to no strong attractive interaction energies, whereas chain C showed several strong attractive interactions between residues 870 and 900, including hydrogen bond energies, as shown in figure 5.5.7 A. Repulsive interactions were also observed in chain A and C suggesting the fitting of the auxilin J-domain is not optimal. The non-optimal positioning of auxilin in the clathrin hub is due to difficulties associated with fitting models to low resolution map densities. As auxilin chain C showed some non-optimal positioning, any Rosetta interaction energies identified should only be viewed as possible interactions and not definitive interaction points. Residues 50 to 100 of the clathrin terminal domain (chain P), located in blade 2 of the β-propeller where the clathrin box binding site resides, were also found to have strong attractive interactions with the auxilin residues, with a visual of the interaction shown in figure 5.5.7 B.

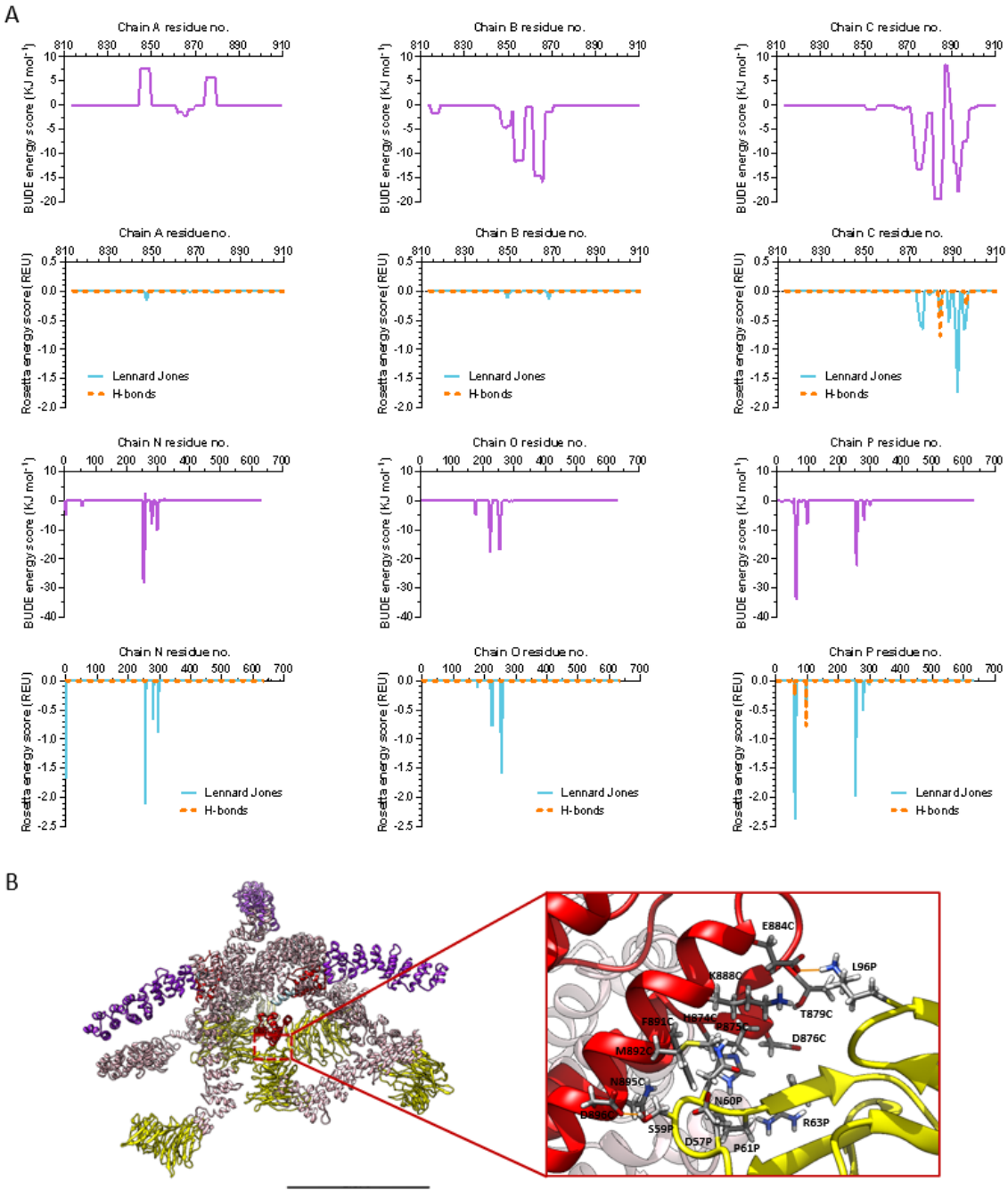

Figure 5.5.7 – Clathrin-auxilin interactions

Rosetta and BUDE energy scoring of clathrin-auxilin interactions. A) Graphs of BUDE energy scores and Rosetta Lennard Jones and hydrogen bond energy scores obtained from the class 4 clathrin auxilin PDB model. B) Atomic diagram of residue side chains with strong attractive Rosetta interaction energies, displayed against ribbon diagrams of the auxilin (chain C) and clathrin terminal domain (chain P) interface. Ribbon diagrams of clathrin terminal domains, ankle regions, distal regions and light chains are presented in yellow, pink, purple and blue respectively, with auxilin presented in red. Atoms are coloured according to their element. Hydrogen bonds are depicted by orange lines.

As only one of the three auxilin structures were found to interact with the terminal domain, this suggests most auxilin interactions with clathrin occur *via* auxilin's unstructured region, and any interactions between the clathrin terminal domain and auxilin J-domain is dependent on the positioning of auxilin with respect to the clathrin terminal domain and ankle regions. The additional interactions that occur between the auxilin J-domain and clathrin terminal domain likely enhance the stability of auxilin binding to clathrin, due to the presence of both Lennard Jones and hydrogen bond tertiary structure interactions.

Figure 5.5.8 highlights the amino acid residues involved in interactions between residues 27 to 39 of CLCb and the CHC. All CLC chains (D,R and S) showed both strong attractive interaction energies across the CHC facing side of the α-helix, as shown in figure 5.5.8 A, with residues 660 to 690 of all CHC ankle regions (chains E, F and G) also showing both BUDE and Rosetta Lennard Jones interaction energies. A visual of the interaction between CLC (chain S) and the CHC ankle region (chain E) is shown in figure 5.5.8 B. This indicates CLCb binding involves weak interactions with the CHC. As the α-helical density is not present when auxilin is not bound, binding of residues 27 to 39 of CLCb to CHC may rely on auxilin interactions to set the residues into a position which favours binding of the α-helix to the CHC ankle region.

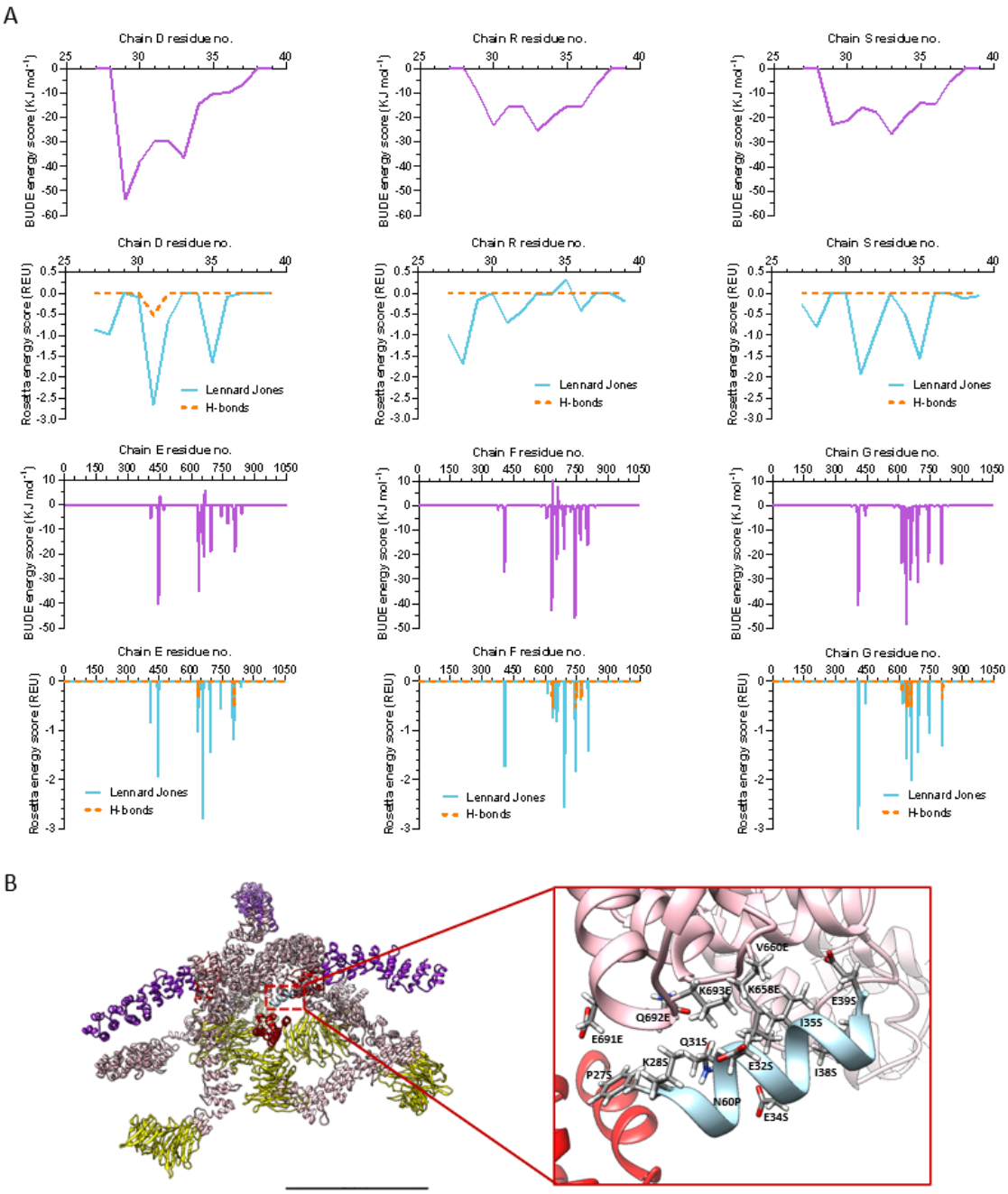

Figure 5.5.8 – Clathrin heavy and light chain interactions

Rosetta and BUDE energy scoring of CHC and CLC interactions. A) Graphs of BUDE energy scores and Rosetta Lennard Jones and hydrogen bond energy scores obtained from the class 4 clathrin auxilin PDB model. B) Atomic diagram of residue side chains with strong attractive Rosetta interaction energies, displayed against ribbon diagrams of the CLC (chain S) and clathrin ankle region (chain E) interface. Ribbon diagrams of clathrin terminal domains, ankle regions, distal regions and light chains are presented in yellow, pink, purple and blue respectively, with auxilin presented in red. Atoms are coloured according to their element.

Figure 5.5.9 highlights the amino acid residues involved in interactions between the clathrin terminal domain and ankle region. All clathrin terminal domains (chains N, O and P) showed both BUDE and Rosetta Lennard Jones interaction energies for residues 200 – 300 found inside blades 6 and 7 of the β-propeller, as shown in figure 5.5.9 A, with residues 400 – 450 of all clathrin ankle regions (chains E, F and G) also showing both BUDE and Rosetta Lennard Jones interaction energies. A visual of the interaction between the clathrin terminal domain (chain P) and ankle region (chain F) is shown in figure 5.5.9 B. In comparison to the clathrin-clathrin interactions observed within the consensus hub, which was discussed and presented in section 4.4.3 and figure 4.4.6 respectively, the clathrin terminal domain interacts with residues lower down the ankle region (*i.e.*, residues 440 – 480 for the consensus hub, compared to residues 400 – 450 for the clathrin auxilin hub), and only has one region of terminal and ankle domain interactions as opposed to two. In addition to the terminal domain and ankle region interactions, no interactions between terminal domains were observed.

As no BUDE or Rosetta interaction energies were observed that supports interactions between terminal domain, and potential auxilin densities were observed around and between the terminal domain densities as shown in figures 5.5.3 I and J, it is likely that the auxilin unstructured region is responsible for pulling the terminal domains downwards (*i.e.*, closer to the vesicle lipid membrane if a vesicle were present) and towards the centre of the hub so that the terminal domains can be linked together. Further investigations into interactions between the CHC and auxilin unstructured region are needed to uncover how the auxilin unstructured region binds to terminal domains and the key residues for these interactions.

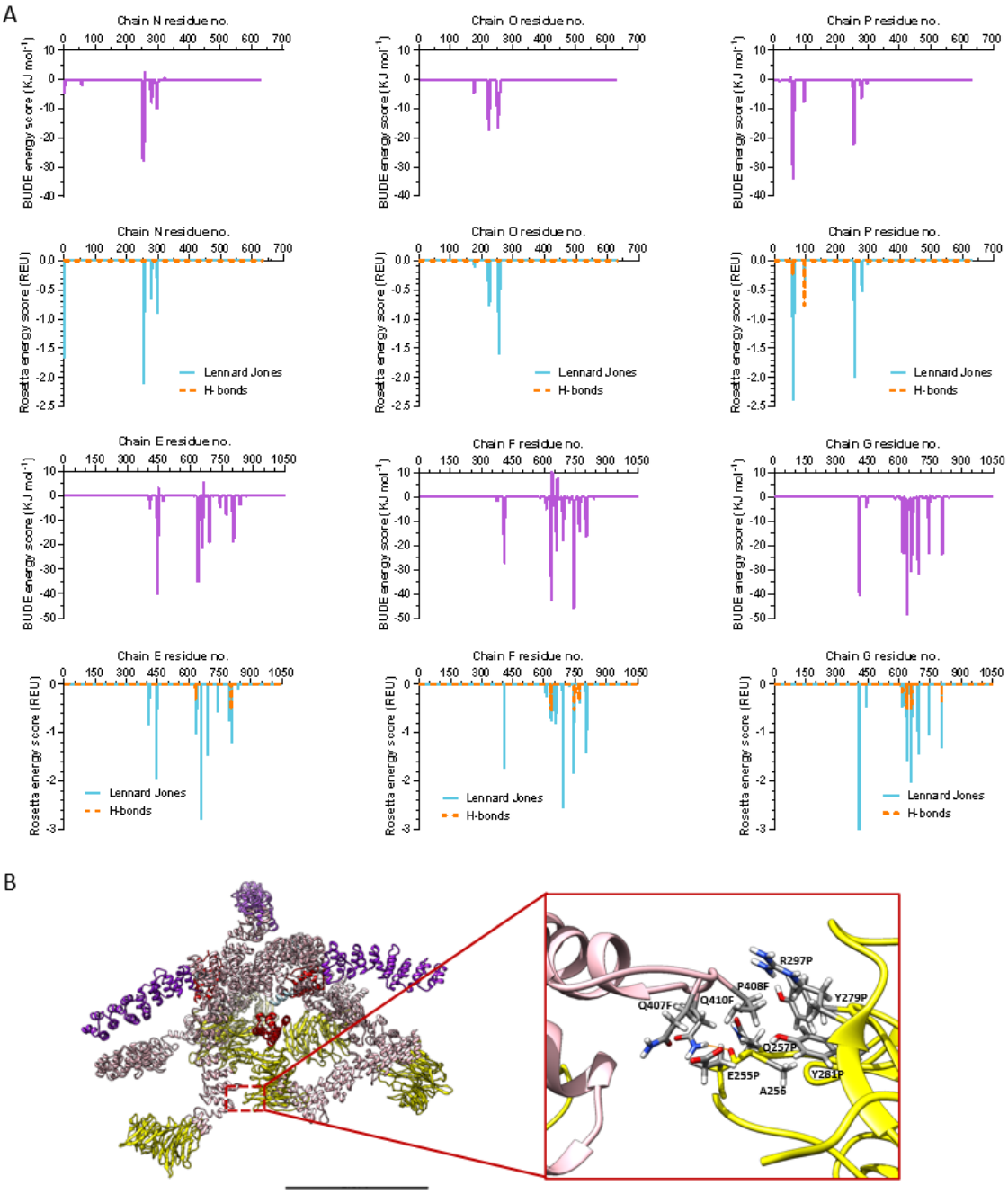

Figure 5.5.9 – Clathrin terminal and ankle domain interactions

Rosetta and BUDE energy scoring of clathrin terminal and ankle domain interactions. A) Graphs of BUDE energy scores and Rosetta Lennard Jones and hydrogen bond energy scores obtained from the class 4 clathrin auxilin PDB model. B) Atomic diagram of residue side chains with strong attractive Rosetta interaction energies, displayed against ribbon diagrams of the clathrin ankle region (chain F) and clathrin terminal domain (chain P) interface. Ribbon diagrams of clathrin terminal domains, ankle regions, distal regions and light chains are presented in yellow, pink, purple and blue respectively, with auxilin presented in red. Atoms are coloured according to their element. Hydrogen bonds are depicted by orange lines.

5.6 Discussion

5.6.1 Clathrin auxilin model

Identifying where adaptor proteins bind to clathrin and how adaptor binding impacts clathrin cage structure, will provide a greater understanding of clathrin-adaptor interactions and clathrin assembly and disassembly mechanisms. Comparison of the clathrin consensus with the Fotin *et al.* (2004)(107) clathrin-auxilin map in section 4.5.1 uncovered additional questions on the positioning of auxilin when bound to clathrin cages, and the impact auxilin may have on the clathrin cage tertiary structure. By performing cryo-EM and localised reconstruction of clathrin cages with auxilin bound, new clathrin auxilin hub models have been obtained at a higher resolution enabling the location of auxilin to be verified and further details on auxilins mechanism of action to be discerned.

Compared to the positioning of auxilin discerned by Fotin *et al.* (2004)(107) presented in figure 5.6.1 A, the positioning of auxilin within the six refined clathrin 3D classes varies, with the six common orientations presented in figure 5.6.1 B. The variable positioning of auxilins J-domain could be due to a lack of J-domain interactions with the clathrin cage, with two of three auxilin J-domains in the class 4 hub structure showing no interactions with clathrin. Previous research by Scheele *et al.* (2003)(222) identified a range of clathrin-auxilin interactions that occur within the unstructured region of auxilin, but not within the J-domain which is known to be responsible for interactions with Hsc70. Scheele *et al.,* identified the binding sites of different motifs within the unstructured region of clathrin to different regions of clathrin triskelia and AP2, with several binding to multiple locations on clathrin. The DLL motif found between residues 591 – 593 for example, can bind to the clathrin terminal domain and the clathrin distal region, and the DPF motif found between

residues 674 – 676 can bind to the clathrin terminal domain and ankle region (222).

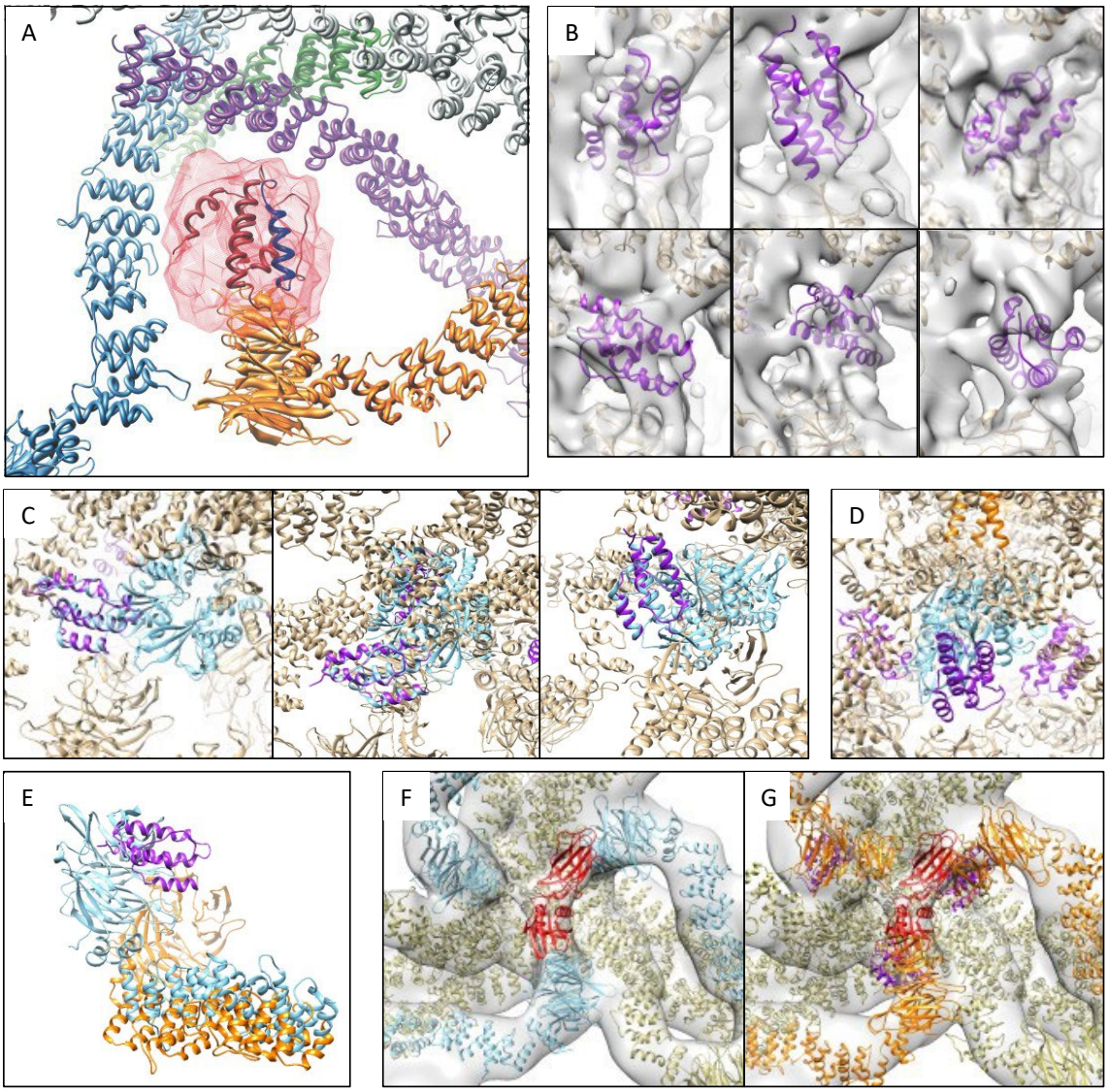

Figure 5.6.1 – Impact of variable auxilin positioning

Ribbon diagrams demonstrating the types and effects of different auxilin J-domain positioning within clathrin hubs on clathrin conformation, and the binding of Hsc70 and β_2-adaptin. A) Positioning of the auxilin J-domain (red) within the clathrin AP2 auxilin difference map (pink) developed by Fotin *et al.* (2004) (107). Reprinted by permission from Springer Nature: Fotin A., Cheng Y., Grigorieff N., Walz T., Harrison S.C., and Kirchhausen T. (2004) Structure of an auxilin-bound clathrin coat and its implications for the mechanism of uncoating. Nature, 432, 649-653 [Copyright licence number: 5177171429959]. B) The clathrin auxilin maps identify six different ways the auxilin J-domain (purple) can be positioned with respect to the clathrin terminal and ankle regions (gold). C) Auxilin (purple) positioning impacts position of bound Hsc70 (blue) on the clathrin cage (gold). Auxilin chains from the class4 PDB model and the X-ray crystallography determined structure of disulphide-bond-crosslinked *bovine* auxilin

Hsc70 complex in the ADP*Pi form [PDB: 2QWP](220) were transposed using UCSF Chimera matchmaker (176). D) The ideal auxilin J-domain (purple) position places Hsc70 (blue) at the centre of the hub between terminal domains and the upper hub region, which is located directly under the clathrin C-terminal trimerization domains (orange). E) Comparison of the clathrin terminal and ankle regions from the consensus hub (blue) and clathrin auxilin hub (orange) models, shows binding of the auxilin J-domain (purple) causes the ankle region to twist and terminal domain to point towards the centre of the hub. F&G) Fitting of ribbon models of clathrin hub models and the β_2-adaptin model (red) [PDB: 70M8] into the clathrin β_2-adaptin hub map [EMDB: 12984] developed by Smith *et al.* (2021)(208). F) Clathrin consensus hub model (blue and gold). G) Clathrin (orange and gold) auxilin (purple) hub model.

As several auxilin residues, including residues 576 – 584, 588 – 596, 633 – 641, 671 – 679, 723 – 731, and 778 – 786, found within the unstructured region (residues 401 – 910) bind to the clathrin terminal domain and other regions of the CHC, and auxilin densities were found around and between the clathrin terminal domains of the clathrin auxilin maps, the unstructured region of auxilin may be responsible for connecting and pulling the clathrin terminal domains down and towards the centre of the clathrin hub, with the difference in ankle and terminal domain conformation shown in figure 5.6.1 E (222). This in turn would allow the auxilin J-domain to be positioned between the clathrin terminal domain and ankle regions without engaging in strong binding interactions with clathrin, matching previous results from Scheele, Kalththoff and Ungewickell (2001)(223) which showed high affinity binding of auxilin fragments 547–714 and 619–738, and low affinity binding of auxilin fragment 715 – 901, to the clathrin terminal domain. Further evidence of a flexible auxilin J-domain can be seen in figure 5.6.1 C, where the matching of the auxilin J-domains from the clathrin auxilin class 4 model with the X-ray crystallography determined structure of disulphide-bond-crosslinked *bovine* auxilin Hsc70 complex in the ADP*Pi form [PDB: 2QWP](220), showed variations in the positioning of the Hsc70 structure with some auxilin J-domain orientations causing the Hsc70 to clash with the CHC. It is possible that there is an ideal position for the auxilin J-domain in the clathrin hub region, that enables placement of Hsc70 directly under the clathrin trimerization domain, with an example shown in figure 5.6.1 D, as binding of Hsc70 to the clathrin C-terminal is necessary for clathrin disassembly to occur (41,107,122–124).

The effect of auxilin binding on the tertiary conformation of clathrin lower hub region may prevent or reduce the binding of other adaptor proteins to the clathrin coat. Figures 5.6.1 F & G shows the location of clathrin terminal domains with respect to the Smith *et al.* (2021)(208) proposed binding location of β_2-adaptin for the consensus hub model and clathrin auxilin class 4 model respectively. The position of terminal domains in the clathrin auxilin model clashes with the docked β_2-adaptin, with the β_2-adaptin binding sites now located in an unfavourable position for β_2-adaptin binding. Although β_2-adaptin can bind to clathrin in other locations (224,225), one of the β_2-adaptin binding sites can link the terminal domains together as demonstrated in figure 5.6.1 F. As such, β_2-adaptin may also prevent the binding of auxilin as well as the conformational changes associated with auxilin binding by acting as a wedge of sorts that keeps the terminal domains oriented as seen in the consensus hub. As the two structures suggest potential competition between β_2-adaptin and auxilin, further studies on the effect of possible adaptor competition on adaptor binding and clathrin disassembly kinetics are required.

The positioning of auxilin within clathrin cages is also important for interactions with the CLC. The possibility of a CLC α-helix bound to the clathrin ankle region in the vicinity of the auxilin J-domain, suggests auxilin and CLC interactions at the CLC N-terminal may enable binding of the CLC N-terminal α-helix to the clathrin ankle region. When no auxilin is present, as observed in the consensus hub structure, the CLC N-terminal alpha helix is not bound to the ankle region which could potentially be a consequence of the weak interactions observed between the CHC and CLC N-terminal α-helix when auxilin is present. Interactions between auxilin and the CLC N-terminus, however, may place the CLC N-terminus alpha helix into a position where binding to the ankle region is energetically favourable. This is further backed by Böcking *et al.* (2014)(125) who showed binding of auxilin to clathrin stabilises clathrin coats, which could be due to both interactions with the CLC N-terminal and linkage of CHC N-terminals. Unfortunately, no studies to date have discussed interactions between auxilin and the CLC to date, and so further

investigation is needed to clarify these interactions. Young *et al.* (2013)(41) however has demonstrated that removal of CLC's from clathrin cages significantly reduces the rate of clathrin disassembly reactions, and binding of Hsc70 to clathrin cages cause changes in the N-terminal portion of the CHC binding region of the CLC.

If the CLC N-terminus interacts with auxilin, then binding of Hsc70 to auxilin could cause the CLC's to be pulled leading to changes in the CLC map density. One of the key roles of CLC's is to aid the stability of clathrin cages (74), and so pulling of the CLC's by auxilin and Hsc70 may have an important role in disassembly, alongside Hsc70 binding to the QLMLT motif found at the CHC C-terminal. Although Böcking *et al.* (2014)(125) found that CLC's bind equally well to wild-type and histidine mutant clathrin triskelia, leading to their conclusion that CLC's are not responsible for the increase in uncoating with the mutant clathrin coats as suggested by Young *et al.*, the histidine mutants they used would only impact binding of CLCs along the C-terminal portion of the CHC binding region, and not the N-terminal portion which has now been found to possibly interact with auxilin. As Böcking *et al.* did observe an increase in the uncoating reaction with the mutant clathrin coats, it is possible that the reduced CLC binding led to reduced stability of the coats, and upon being pulled by Hsc70 and auxilin led to a more efficient uncoating reaction, as less clathrin-clathrin interactions were needed to be broken for uncoating to occur.

5.6.2 Study limitations

Despite successfully producing maps and models of clathrin hubs with auxilin bound, several limitations of the study will have impacted the overall result. Some limitations in relation to the use of cryo-EM for the study, including particle number, pixel size, Nyquist frequency and aliasing, and use of *in vitro* samples, have already been discussed previously in section 4.5.2. Other study limitations and potential solutions associated specifically with the clathrin auxilin structure determination and analysis are discussed below:

5.6.2.1 Lower resolutions of lower hub regions

The lower hub region of the clathrin hub regions is of a significantly lower resolution in comparison to the upper hub region, reducing the level of secondary structure details available of the clathrin terminal and ankle regions, and the auxilin J-domain within the clathrin auxilin cage and clathrin auxilin hub maps. Unresolved secondary structure details of the auxilin J-domain will have an impact on the accuracy of the auxilin J-domain positioning, which if accurate would enable specific interacting residues to be elucidated between clathrin and auxilin, and enable accurate docking of Hsc70 to the model to obtain additional evidence on the clathrin disassembly mechanism. The lower resolution of the lower hub region may be caused by a higher level of protein flexibility of the lower hub region. Higher levels of flexibility would cause the positioning of residues to differ between two complexes, thereby creating noise within the electron density map.

Non-optimised defocus levels used during data acquisition will also impact the level of high-resolution spatial frequencies obtained. The lower hub region of clathrin cages is located within lower levels of vitreous ice compared to the upper hub region, and will therefore experience a higher probability of incident electrons undergoing multiple scattering events (226). To increase the overall resolution of the cages, optimisation of vitreous ice thickness would be advantageous to ensure clathrin cage complexes are frozen in the thinnest vitreous ice possible, thereby reducing multiple scattering events of incident electrons (227). To increase the resolution of the lower hub regions, however, using a larger box size during particle extraction and optimising the defocus values used during data acquisition is required, as this would the acquisition of higher resolution data by increasing the spatial frequencies that can be obtained (228).

5.6.2.2 3D classification limitations

In addition to protein flexibility reducing the resolution of the lower hub region, the overall functionality of 3D classification procedures will also limit the accuracy and overall resolution of the lower hub region of clathrin adaptor complexes. As observed in figure 5.6.1 B, the positioning of the auxilin J-domain varies, adopting a variety of different orientations between the clathrin terminal domains and ankle regions. The differences in auxilin positioning adds another layer of flexibility, and if the 3D classification procedure is unable to separate and align the different adaptor positions into suitable classes, additional noise is created within the structure that impacts the overall resolution of the bound adaptor. Advances within the field of cryo-ET may enable structures of a single clathrin adaptor complex to be determined to resolutions akin to or greater than resolutions obtained with cryo-EM SPA (229). For cryo-ET to surpass cryo-EM SPA several challenges need to be addressed including limited angular range, high electron dosage, low throughput and low data acquisition speeds (229).

5.6.3 Conclusion

Use of cryo-EM and localised reconstruction alongside 3D classification has enabled the development of six clathrin auxilin maps and models with upper and lower hub resolutions reaching between 6.7 Å – 9.3 Å and 8.6 Å – 12.8 Å respectively, with each map demonstrating the variability in auxilin J-domain positioning between the clathrin terminal domain and ankle regions. By improving the resolution of the structures and comparing the model with the clathrin consensus hub obtained in chapter 4, the positioning of the auxilin J-domains and clathrin terminal domains from the Fotin *et al.* (2004)(107) model were validated, and further insights into the effects of auxilin binding on clathrin cage conformation were identified. A new α-helical density from the CLC N-terminal was also obtained, hinting at possible CLC N-terminal interactions with auxilin that may play a role in clathrin coat stability and the clathrin cage disassembly mechanism. Finally, comparison of the clathrin

auxilin model with the clathrin β_2-adaptin model developed by Smith *et al.* (2021)(208) suggests potential competition between the two adaptor proteins for clathrin binding, as the impact the two adaptors have on clathrin conformation may prevent both adaptors from being bound at the same time. In addition, the flexibility of auxilin J-domain positioning could also allow both adaptors to bind to the terminal domain at the same time if the J-domain is able to adopt a different position to allow binding of β_2-adaptin. As new questions have surfaced on adaptor protein interactions with clathrin, as well as the involvement of CLC's in clathrin disassembly reactions, the next chapter of this thesis will look at the use of cryo-ET for the visualisation of different stages of clathrin cage disassembly.

This page is intentionally left blank

Chapter 6:

Visualising Clathrin Disassembly

Chapter Overview

This chapter details the development of disassembling clathrin cage structures using cryo-ET, to visualise how clathrin cages disassemble in the presence of auxilin, Hsc70 and ATP.

6.1 Background to Tomography

The third aim of this thesis was to investigate whether the stages of clathrin cage disassembly could be captured using cryo-ET, to uncover details on the clathrin disassembly mechanism. Cryo-ET sample preparation follows the same process discussed and presented in section 4.1.2 and figure 4.1.1 respectively, but during the imaging process the grid is tilted at a variety of angles allowing a single clathrin cage molecule to be imaged from multiple angles (230), as presented in figure 6.1.1 A. The tilt images are used to create 3D model of the clathrin cage molecule by aligning the tilt images according to their tilt angle (230), as shown in figure 6.1.1 B, and then applying a weighted back projection to the aligned tilt images. Alignment of the tilt images is made possible by aligning gold fiducials in the images that are added to the sample during grid preparation (230).

The first cryo-ET clathrin coated vesicle map was obtained by Cheng *et al.* (2007)(152) and is presented in figure 6.1.1 C. Despite the low resolution of the Cheng *et al.* map, subtomogram averaging of cryo-ET maps have enabled the production of higher resolution clathrin coat structures, with the most recent being the Kovtun *et al.* (2020)(225) map of clathrin coated vesicles with AP2 bound. The higher resolution of the Kovtun *et al.* map enabled the identification of β_2-adaptin densities, as shown in figure 6.1.1 D, which provided insight into how the AP2 β_2-adaptin appendage interacts with the clathrin terminal domain. By using cryo-ET it is therefore hoped that the separation of individual triskelia from clathrin cages can be visualised during clathrin disassembly, which would provide additional details on the clathrin uncoating mechanism. The remainder of this chapter shall discuss the acquisition of higher resolution tomograms of disassembling clathrin cages, and an assessment of how sufficient resolution could be obtained to visualise disassembly in detail. The results of this chapter are of an initial study, which was conducted to determine the parameters required and resolutions attainable using cryo-ET for the visualisation of clathrin disassembly.

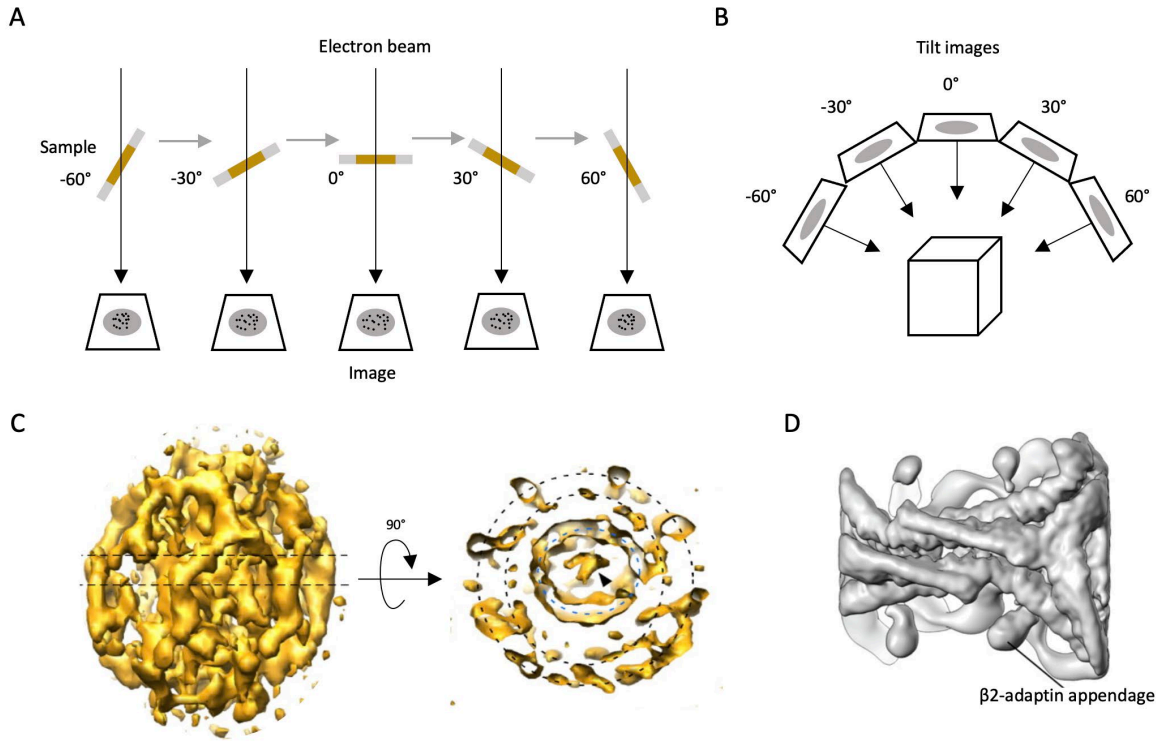

Figure 6.1.1 – Acquisition of clathrin structures using cryo-ET

Schematics and models demonstrating the cryo-ET process and cryo-ET clathrin models. A) Grid (gold) is rotated in a TEM to produce images of sample particles in different orientations. B) Tilt images of a particle that were taken at different angles are combined to produce a 3D model. C) First model of a clathrin coated vesicle structure produced by cryo-ET. Reprinted from Journal of Molecular Biology, 365/3, Yifan Cheng, Werner Boll, Tomas Kirchhausen, Stephen C. Harrison, Thomas Walz, Cryo-electron Tomography of Clathrin-coated Vesicles: Structural Implications for Coat Assembly, 892-899 (2007)(152), with permission from Elsevier. D) Cryo-ET clathrin coat model with AP2 bound. From Science Advances, 6/30, Oleksiy Kovtun, Veronica K Dickson, Bernard T. Kelly, David J. Owen, and John A.G. Briggs, Architecture of the AP2/clathrin coat on the membranes of clathrin-coated vesicles, eaba8381 (2020)(225). Reprinted with permission from AAAS.

6.2 Methods

6.2.1 Clathrin disassembly assays

Disassembly assays were performed at 25 ºC on a FP-6500 fluorimeter (JASCO) *via* perpendicular light scattering (PLS), using 390 nm excitation and emission wavelength, 3 nm bandwidth, 485 PMT voltage, 0.5 s response time, and 1 s data pitch. Disassembly reactions consisted of 500 μM ATP with varying quantities of clathrin, auxilin and Hsc70 in Buffer C as previously described(118). Disassembly was initiated upon addition of 3 μl Hsc70.

6.2.2 Cryo-ET sample preparation

Glow-discharged lacey carbon supported 200 mesh copper grids were loaded with 3 μl aliquots of a clathrin disassembly reactions, containing of 10% 10 nm gold nanoparticles, 10 μM clathrin cages, 1 mM ATP, 10 μM auxilin and 20 μM Hsc70 in Buffer C. Clathrin disassembly reactions were proceeded for 80 s before single side blotting for 3 s at 50% chamber humidity, and plunge freezing in liquid ethane using a Leica Automatic Plunge Freezer EM GP2. Grids were screened on a 200 kV JEOL 2100 Plus (University of Warwick) fitted with a Gatan OneView IS camera at a nominal magnification of 20,000×.

6.2.3 Cryo-ET data collection

Cryo-grids were loaded into a JEOL 2200FS transmission electron microscope operated at 200 kV equipped with a Gatan K2 counting detector with a 30 eV energy slit in zero-loss mode. Tomographic tilt series between −50° and +50° were collected using SerialEM(231) in a dose-symmetric scheme with 3° angular increment. Images were collected at a nominal magnification of 20,000× and magnified pixel size of 1.9 Å/px, using a 2 μm C2 aperture. An electron dose of

2.1 e^{-} A^{-2} sec^{-2} per tilt image was applied resulting in a cumulative dose of 71.4 e^{-} A^{-2} sec^{-2} over the whole tilt series.

6.2.4 Tomography data processing

Tilt images were aligned and reconstructed using Etomo from IMOD(v.4.11)(232). Frames underwent automatic x-ray replacement using CCD eraser and coarse alignment with Tiltxcorr. Fiducial model generation was conducted using Beadtracker before frames underwent fine alignment. Tilt series with less than two trackable gold fiducials were discarded. No CTF and dose-weighting was conducted as this was a preliminary study. Tomograms were generated with 2x binning and a z thickness of 1500. Visualisation of frames and tomogram slices was conducted using 3dmod from IMOD(v.4.11)(232). Visualisation of cryo-ET maps was conducted in UCSF Chimera(176), with a gaussian filter of 30 and -1 scale applied.

6.3 Results

6.3.1 Sample preparation

PLS of clathrin disassembly was conducted to determine the most appropriate adaptor protein ratio and blot timings for the preparation of cryo-ET grids, with PLS traces for different adaptor quantities presented in figure 6.3.1 A. Overall a 1:1:2 ratio of clathrin, auxilin and Hsc70 and an 80 s reaction time were determined to be the ideal conditions for freezing disassembling clathrin cages for an initial attempt of Cryo-ET, as the ratio produced a disassembly speed that was deemed potentially fast enough to visualise disassembling clathrin cages, but not too fast so that there was enough time to freeze the samples. Carbon lacey grids were used for grid preparation due to continued problems associated with the quantifoil grids, which was previously discussed in section 5.3.2. The quality of grid ice thickness and sample quality is presented in figure 6.3.1 B and C respectively.

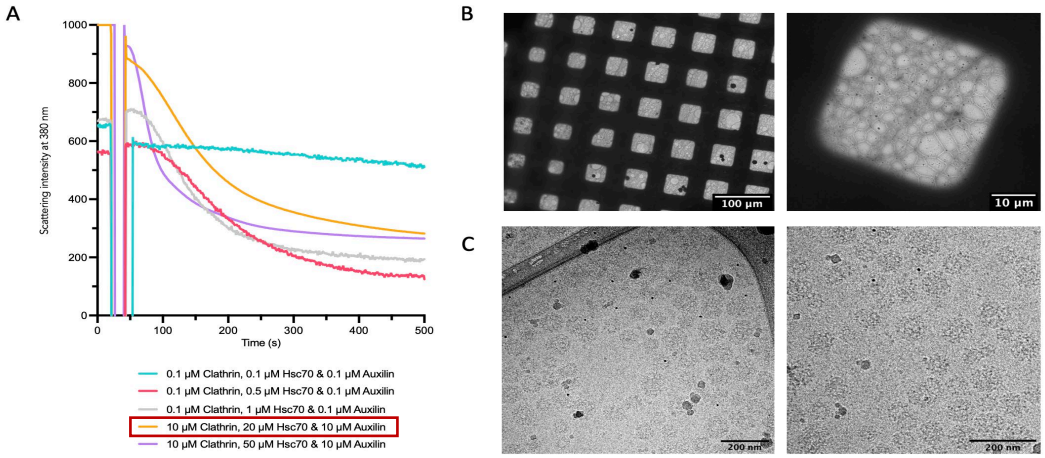

Figure 6.3.1 – Preparation of cryo-ET grids with disassembling clathrin cages

Preparation of cryo-ET grids of disassembling clathrin cages. A) PLS clathrin disassembly assay with different ratios of clathrin, auxilin and Hsc70. Red box highlights selected condition. B) Ice thickness variation across super-cooled lacey carbon supported 200 mesh copper grids containing clathrin, auxilin, Hsc70 and ATP. C) Presence of clathrin cages within super-cooled lacey carbon supported 200 mesh copper grids.

6.3.2 Tomogram generation and processing

A selection of tilt images taken between -50 and 50 degrees is shown in figure 6.3.2. These tilt series were taken forward for processing if there were more than two gold fiducials present in each tilt image. From these images we can see a wide variety of clathrin cages, and so it was hoped that generating 3D maps of these cages will reveal different states of clathrin disassembly. The gold fiducials that were selected for fine alignment of each tilt series is shown in figure 6.3.3. Upon completion of alignment, 3D tomogram maps were generated using back projection of tilt images, with slices for each tomogram shown in figure 6.3.4. From the tomogram slices we can see a range of clathrin cage sizes, with pentagon and hexagon arrangements being clear at the top and bottom of cages along the z axis. The contrast of these images is quite poor, however, which would make it very difficult to conduct map segmentation for each clathrin cage. It was therefore decided that extraction of a cage from each tomogram will be conducted to determine the overall quality of the cryo-ET 3D maps, with the selected cages identified in figure 6.3.5.

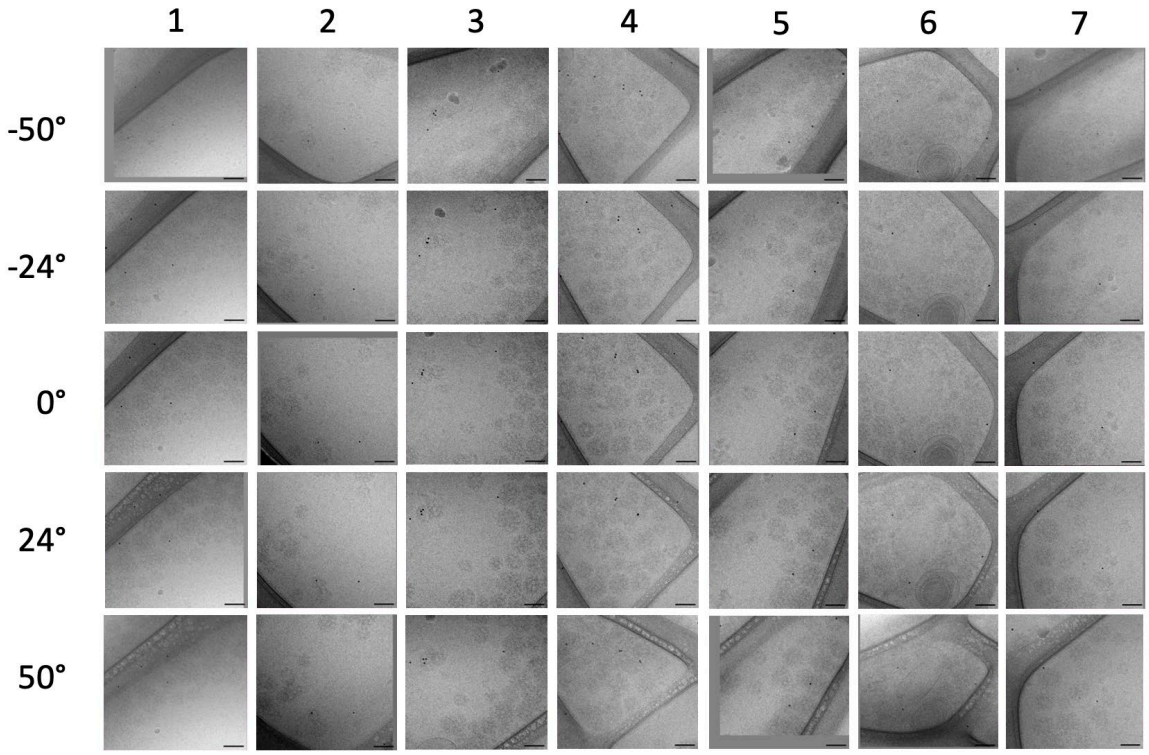

Figure 6.3.2 – Images taken at different angles for each tilt series

Images of selected tilt series taken at -50°, -24°, 0°, 24° and 50°. Scale bar set to 100 nm.

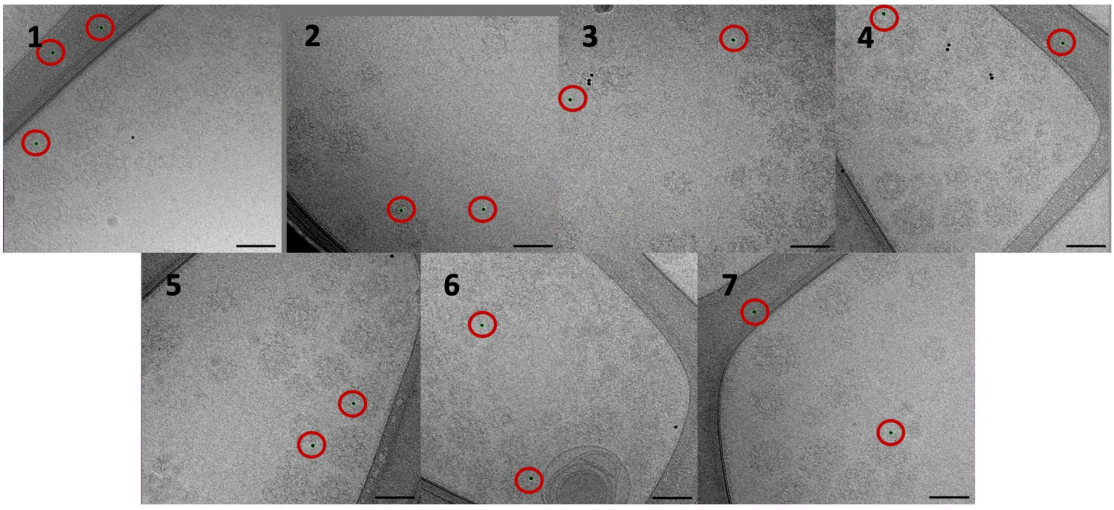

Figure 6.3.3 – Selected fiducials for tilt series alignment

Location of fiducials (circled in red) used for alignment. Scale bar set to 100 nm.

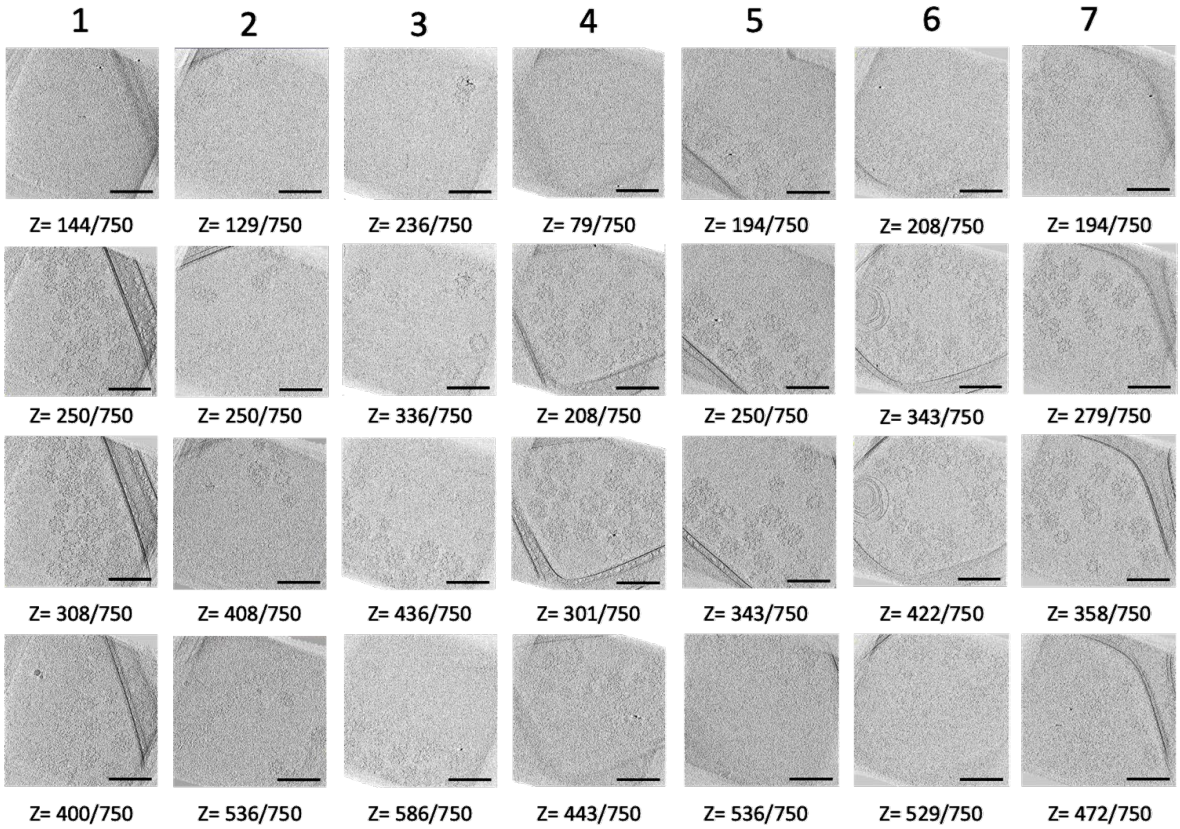

Figure 6.3.4 – Tomogram slices

Z-slices of processed tomograms with a box size of 750. Scale bar set to 200 nm.

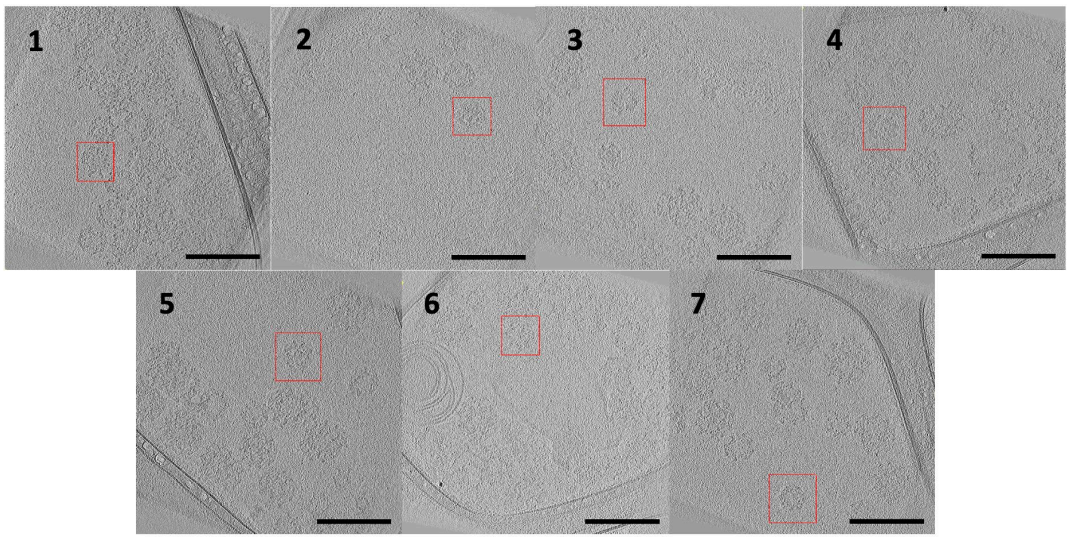

Figure 6.3.5 – Extracted cage from each tomogram

Extracted cages from each tomogram with a box size of 750. Scale bar set to 200 nm. Red squares denote positioning of extraction box in x and y for each tomogram. Extraction box size varied depending on the size of the extracted clathrin cage.

The extracted clathrin cage maps, shown in figure 6.3.6, unfortunately were poorly defined and noisy, with little structural information observed at the high angles; it was therefore not possible to determine any states of clathrin disassembly.

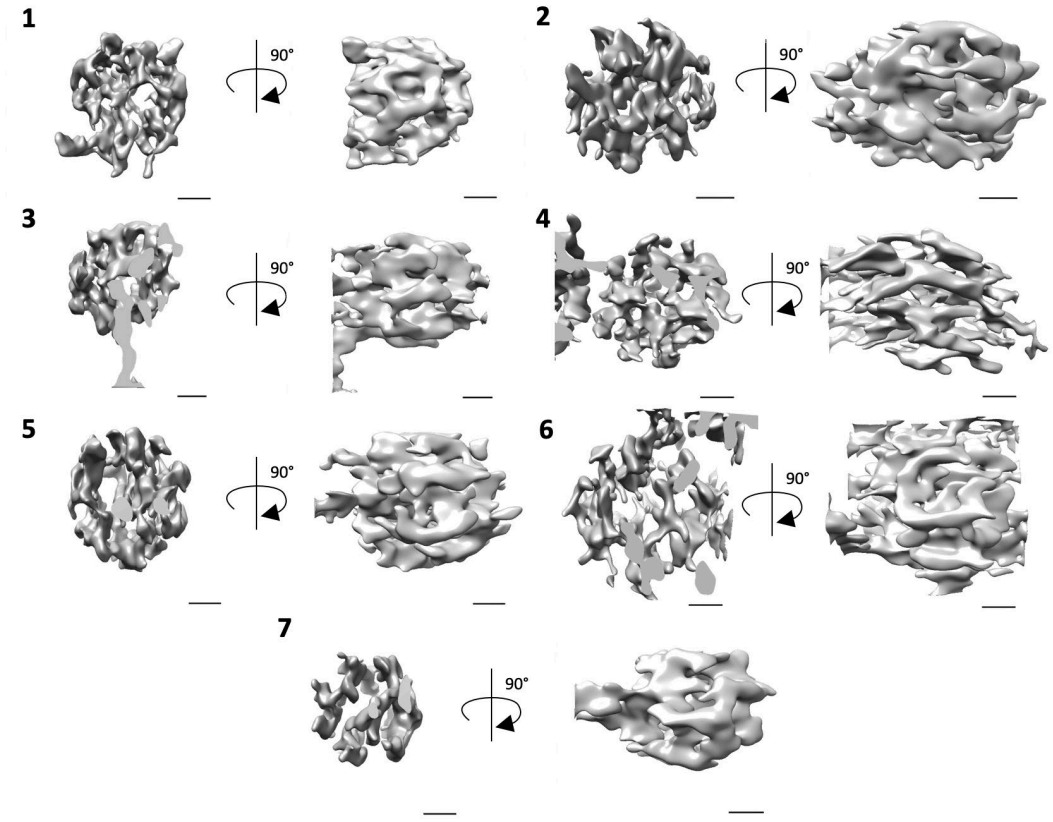

Figure 6.3.6 – 3D maps of cryo-ET clathrin cages

Front and side views of a clathrin cage map obtained from each tomogram. A gaussian filter of 30 Å was applied to each cage to reduce noise. Scale bars set to 200 Å.

6.4 Discussion

6.4.1 Study limitations and possible solutions

The aim of this chapter was to conduct an initial study to assess the ideal cryo-ET parameters required for obtaining high resolution maps of different clathrin cage disassembly states, however, the maps that were obtained were noisy and anisotropic and therefore hard to interpret, meaning no structural information on the different states of clathrin disassembly could be obtained at this time. Several issues and limitations will have led to these results, however, due to the success of other cryo-ET project like Kovtun *et al.* (2020)(225), an alternative approach when using cryo-ET may yield more favourable results. More time is therefore required in order to reach resolutions obtained by Kovtun *et al.* and others. Understanding the limitations and identifying areas for improvement is important for increasing the probability of success of future attempts of using cryo-ET for studying clathrin disassembly. Details of the study limitations and potential solutions are discussed below:

6.4.1.1 Tilt series

The range of angles used for the tilt series was between -50° and 50° rather than -60° and 60°, due to technical limitations associated with using 300 mesh grids. The reduced range of angles however resulted in poor structure reconstruction for areas of clathrin cages viewed at the high tilt angles (i.e., side views), limited structural information for these regions were obtained. To further improve the reconstruction of clathrin cages from tomograms, a higher range of angles is therefore needed so that more structural information can be obtained at the high tilts (233). Most tomography studies have used an angle range of -60° to 60°, as this is the maximum tilt limit for the majority of TEMs (233). In addition to the range of angles, the tilt increment value should also be addressed. Having a larger tilt increment of 3° throughout the tilt series as opposed to a smaller tilt

increment means there are less images taken overall per tomogram, but the speed of data acquisition increases as less images need to be taken for a tomogram. By decreasing the tilt increment to 2° or 1° the number of images taken per tomogram will increase by 2 or 3 times respectively, thereby allowing higher resolution tomograms to be obtained as more images can be used to reconstruct the 3D structure of clathrin cages (233). By increasing the range to -60° and 60°, and by reducing the angle increment to 1° or 2°, it is therefore hoped that upon reconducting and processing clathrin disassembly tomograms, the 3D structures produced will be of a high enough resolution that separation of clathrin triskelia from clathrin cages can be identified.

6.4.1.2 High electron dosage

A high electron dose was used during data collection to improve the contrast of tilt images, however, the electron dosage was too high causing burning of the sample, as can be seen in figure 6.3.2 from the presence of white bubbling along the carbon film once the midpoint of data collection was reached. Radiation damage of samples tend to occur at an accumulated dose of 120-160 $e^-/Å^2$ (233,234). To prevent burning of the sample in future, the total electron dose applied to the entire tomogram should be reduced, as burning of the sample appeared to occur after half of the tomogram was imaged. If the suggested advice for the tilt series range and increments is applied (*i.e.*, -60° and 60° with 2° increments to produce 61 tilt images), the electron dose per image should therefore not exceed 1.9 $e^-/Å^2$. Although a lower electron dose will reduce the contrast of images, preventing the burning of samples is more important as burning leads to loss of high resolution features, such as through decarboxylation of side chains for example (235). In addition to altering the dose applied per tomogram, acquiring accurate dose information for electron dose weighting during data processing is also required. By conducting the initial study, several technical limitations and solutions have therefore been identified to help tackle issues associated with high electron dosage. To further ensure accurate dose weighting of tomograms during data processing in future

attempts of visualising clathrin disassembly with cryo-ET, dose weighting files should be obtained during tomogram collection so that an accurate dose weighting can be applied for each tilt image during data processing in Etomo (232).

6.4.1.3 CTF measurements

CTF correction was not applied to tomograms as the CTF is not uniform across tilt images, except for the 0° tilt image, as the defocus value will change along the tilt axis (233). CTF correction, however, is important for extracting high-resolution information from TEM images. To overcome this challenge, Etomo contains a CTF plotter function that requires a stack of noise images to determine the CTF values across a tilt image (232,236). Future attempts to acquire clathrin cage disassembly tomograms should therefore ensure a stack of noise files are acquired during collection, so that CTF plotter can be used during the processing of tomograms, thereby enabling high resolution information to be extracted. These noise files could be obtained from taking a tomogram in an area with empty ice (*i.e.,* no clathrin cages or contaminations present).

6.4.1.4 Low number of fiducials

To ensure accurate alignment of tilt images, the presence of more than 2 fiducials within all tilt images is required (233). By having more than two gold fiducials present in the tomogram, there are more references within the sample to ensure an accurate alignment of the tilt images, enabling accurate 3D reconstructions of each gold fiducial and the clathrin cages present within the tomogram. If there are fewer gold fiducials present within the sample, then there will be more error in the angular assignments of each tilt image, resulting in lower resolution 3D structures. Although the tomograms that were taken had few gold fiducials present, some areas of the sample grid had an abundance of gold fiducials. By ensuring sufficient mixing of the sample before applying to grids during grid preparation, it is hoped that the spread of gold fiducials across

the grid will be more even, and thereby ensure more tomogram areas are present that contain more than two gold fiducials.

6.4.1.5 Producing interpretable reconstructions

The maps that were obtained from the cryo-ET study were noisy and anisotropic and therefore hard to interpret. As there are only a limited number of tilt images that can be obtained per tomogram, obtaining high resolution maps is very difficult. One method to increase the resolution of tomograms is by using subtomogram averaging. Subtomogram averaging employs a similar method to SPA but instead of combining particle images, tomograms are combined to increase the global resolution (225). As the disassembling clathrin cage sample would be very heterogenous however, not only due to the presence of different sized cages but also due to an unknown number of intermediate states of disassembling cages, subtomogram averaging would not be suitable. As such, other methods capable of improving the interpretability of the reconstructions by reducing noise would be required, such as employing binning and filtering. Binning enables a reduction of noise within the tomograms by combining adjacent pixels to improved signal to noise ratios, however, this is at the expense of a reduced spatial resolution (260). Filtering can further improve the signal to noise ratio, however, this is at the expense of blurring particle features (260). Future attempts should therefore try a range of filtering techniques such as standard linear filtering and anisotropic nonlinear diffusion filtering, to determine the most suitable filtering technique for improving the interpretability of reconstructions (260).

6.4.2 Conclusion

Despite being ultimately unsuccessful in the production of high-resolution 3D maps of clathrin disassembly states using cryo-ET, the project enabled additional knowledge on and gave useful insights into the application of cryo-ET for characterisation of clathrin disassembly, including information on CTF

plotter, the desired number of fiducials per image, and the ideal angle range, angle increment, and electron dosage applied during data collection. Time and budget did not permit further pursuit of the project, however, the work described in this chapter demonstrates the potential for use of cryo-ET in elucidating disassembling clathrin cages. This new knowledge will be key for future clathrin cryo-ET projects, as it will increase the possibility of success in obtaining high quality tilt images during data collection and will aid the data processing step to ensure CTF correction and electron dosage are accounted for.

This page is intentionally left blank

Chapter 7:

Interactions Between Clathrin and Adaptors

Chapter Overview

This chapter details the development and functionality of fluorescently labelled disassembly adaptor protein for measuring the kinetics of clathrin-adaptor interactions *via* fluorescence anisotropy (FA) and perpendicular light scattering (PLS).

7.1 Background to Fluorescence Anisotropy

Although the attempt to visualise how clathrin cages disassemble using cryo-ET was unsuccessful, alternative methods can be utilised to acquire information on clathrin-adaptor interactions which may shed light on mechanisms of action. The fourth aim of this thesis is to assess the kinetics of clathrin-adaptor interactions, and the impact other adaptors may have on clathrin-adaptor interactions, using FA and PLS. The remainder of section 7.1 will go into further detail on what FA is, how FA works, and why anisotropy is an ideal technique for measuring clathrin-adaptor interactions.

7.1.1 How does fluorescence anisotropy work?

FA uses polarised light and fluorescently labelled probes to acquire information on probe motion, dynamics, and diffusion from the rotational correlation time (237,238). In the FA technique, a pulse of linearly polarised light irradiates fluorescent probe molecules in solution, causing them to become excited and emit fluorescence with the same dipole orientation as the polarised light (237–240). The fluorescence passes through a polarisation filter oriented either parallel or perpendicular to the incident polarised light, before hitting the detector, allowing the intensity of fluorescence emission parallel to the vertically polarised light ($I_{\parallel}$) and perpendicular to the vertically polarised light ($I_{\perp}$) to be measured (238–240). Steady-state anisotropy (r) is therefore defined as the difference between the vertical ($I_{\parallel}$) and horizontal ($I_{\perp}$) polarised fluorescence emission divided by the total fluorescence emission, with the anisotropy equation defined in formula 1 (237,238,240).

(1) $$r = \frac{I_{\parallel} - I_{\perp}}{I_{\parallel} + 2I_{\perp}}$$

As FA and polarisation are interrelated the equations for calculating the two are very similar, with the equation for determining polarisation (p) presented in formula 2 (238–240).

(2) $$p = \frac{I_{\parallel} - I_{\perp}}{I_{\parallel} + I_{\perp}}$$

Over time the fluorescent probe molecules will shift by rotational diffusion and brownian motion, causing the fluorophore dipole to rotate (see figure 7.1.1) (237,238,240). As stated in the Perrin equation and Stokes-Einstein-Debye equation, defined in formulas 3 and 4 respectively, FA, therefore, is directly related to the rotational correlation time (θ_{rot}) of the fluorophore, which is in turn related to the hydrodynamic volume (V) of the fluorescent probe molecule (238–240).

(3) $$\frac{r_0}{r} = 1 + \frac{\tau}{\theta_{rot}} = 1 + 6D_{\tau}$$

(4) $$\theta_{rot} = \frac{\eta V}{k_B T}$$

Key
θ_{rot} = Rotational correlation time
r = Anisotropy
r_0 = Fundamental anisotropy
V = Molecular volume
η = Viscosity
τ = Fluorescence lifetime
D = Diffusion constant
k_B = Boltzmann's constant
T = Temperature

FA thus provides a value between 0 and 1 in relation to the motion dynamics of the fluorescent probe molecule, where 1 is a completely static molecule, and 0 is a completely mobile molecule (237,238,240). If the labelled molecule (*e.g.*, a labelled CME adaptor) increases in size due to ligand binding (*e.g.,* binding to unlabelled clathrin cages), the total anisotropy value will increase as the level of rotational diffusion will decrease due to an increase in volume and resistance (238–240). The presence of unlabelled molecules (*e.g.,* clathrin) would not impact the FA value unless binding occurred, as the unlabelled molecules would not produce polarised fluorescence emission.

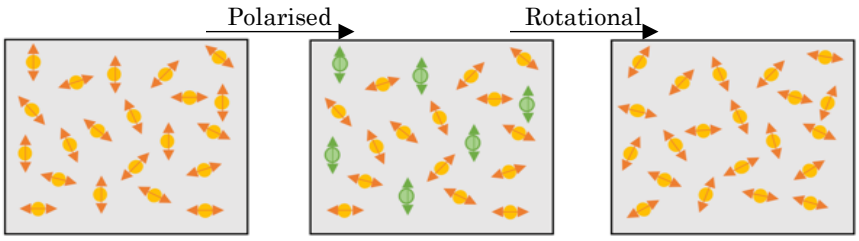

Figure 7.1.1 – Photoselective excitation of fluorophores by polarised light

Fluorophores are indicated by spheres, with their dipole transition moment indicated by double ended arrows. Fluorophores emitting vertical polarised emission are coloured in green. Figure adapted from Lakowicz (2006) (241).

Differences in the data collection efficiency of anisotropy equipment, however, cause errors in steady-state anisotropy (237). By using time-dependent measurements of anisotropy, as defined in formula 5, the anisotropy measurement can consider the fundamental (r_0) and limiting (r_∞) anisotropy values, as well as the rotational correlation time (θ), reducing the error in anisotropy values and preventing a non-zero anisotropy value from occurring if the angular motion of the fluorescent probe is hindered (237,240).

(5) $$r(t) = \sum_j r_{0_j} e^{(-t/\theta_j)+r_\infty}$$

When measuring either steady-state or time-resolved anisotropy it is important to consider the lifetime of the fluorophore (τ) (237,239). If the fluorescence lifetime is too short then the fluorophore will be unable to rotate sufficiently between absorption and emission, causing the r value to be high and approach fundamental anisotropy (239). On the other hand, if the fluorescence lifetime is much longer than the rotational time, where $\tau \gg \theta_{rot}$, then r will end up low as depolarisation will occur before emission ends (239). Ideally the fluorescence lifetime will equal the rotational time, where $\tau = \theta_{rot}$, for the best sensitivity and correct r value (239). Other factors can also impact the r values including the shape of the fluorophore, linker length and flexibility, fluorophore brightness, light scattering, spectral range, temperature, polarity, pH, and ionic strength (239).

7.1.2 Biologic MOS-450 anisotropy measurements

In addition to the section 7.1.1 method, there is another alternative method for measuring anisotropy which is used for the Biologic MOS-450 instrument (242,243). In conventional fluorescence anisotropy measurements, two photomultiplier tubes are placed perpendicular to one another which simultaneously measure the parallel ($I_{\parallel}$) and perpendicular ($I_{\perp}$) emitted fluorescence light in relation to the polarised excitation beam (244). Anisotropy is therefore measured by fluorimeters using formula 6:

(6) $$r = (I_{\parallel} - G \times I_{\perp})/(I_{\parallel} + 2 \times G \times I_{\perp})$$

A factor of 2 is applied within the formulae as once there has been vertically polarised excitation, there are two equivalent orthogonal horizontal directions in existence (242). A correction factor (G) is also applied to the formulae to account for differences in detection sensitivity of the two photomultipliers for each polarising direction (242). The correction factor is calculated using formula 7 where the excitation polariser is placed into a horizontal position, however, the correction factor can potentially introduce other errors into measurements, which occurs from the displacement of excitation beam during polariser rotation (242,243).

(7) $$G = I_{\perp}/I_{=}$$

The modified procedure used by Biologic does not require a correction factor, as it uses a simpler detection system with only one photomultiplier tube without a polariser (242,243). Instead, a photoelastic modulator alters the polarised light between vertical and horizontal, with both polarisers detected simultaneously on the emissions side (242,243). The anisotropy can therefore be measured using formula 8, which does not include a correction factor:

(8) $$r = (I_{\parallel} - I_{\perp})/(I_{\parallel} + 2 \times I_{\perp})$$

7.1.3 Measuring the dissociation constant using anisotropy

Because anisotropy is influenced by mobility of the fluorophore, we can often use it to monitor binding interactions. By conducting binding assays through measuring changes in the r value of fluorescently labelled adaptors while varying clathrin, it is possible to measure the interactions between adaptors and clathrin, and how the presence of other adaptors can impact these interactions. Formula 9 defines a basic reversible biomolecular binding reaction between two molecules (A & B), where collision of molecule A and molecule B leads to the production of a complex (AB) (245).

(9) $$A + B \leftrightarrows AB$$

The simplest biological reactions have a 1:1 stoichiometry between the reactant molecules, and so because there are two reactants involved in the formation of complex AB, the reaction should be a second order reaction (245). As there is a binding spot for auxilin on the clathrin terminal domain and there is one terminal domain per clathrin heavy chain, it is likely auxilin and clathrin binding follows a 1:1 stoichiometry. The 1:1 auxilin to clathrin binding stoichiometry is further backed by the presence of one auxilin per terminal domain on the clathrin auxilin map obtained in chapter 4. Formula 10 defines how the rate of a second order reaction is determined using the association rate constant (k_a), with units of $M^{-1} \cdot s^{-1}$, and the reactant concentrations (245).

(10) $$Rate = k_a[A][B]$$

For the reverse reaction of equation 10, the reaction should be a first order reaction as there will be only one reactant. Formula 11 defines how the first order rate is determined from the dissociation rate constant (k_d), with units of s^{-1}, and the concentration of AB (245).

(11) $$Rate = k_d[AB]$$

The association and dissociation rate constants can be used to determine the probability that the complex will assemble or disassemble respectively in a unit of time (245). A reaction may be considered to have reached equilibrium when the rate constants are equal. (245,246). The equilibrium constant (K_{eq}) can be determined from formula 12 and has the units of M^{-1} (245).

(12) $$K_{eq} = \frac{k_a}{k_d} = \frac{[AB_{eq}]}{[A_{eq}][B_{eq}]}$$

The larger the value of the K_{eq} the greater the proportion of associated complexes (245). Formula 13 is the reciprocal of equation 12 and describes the dissociation equilibrium constant (K_d), which has the units of M (238,245,246).

(13) $$K_d = \frac{k_d}{k_a} = \frac{[A_{eq}][B_{eq}]}{[AB_{eq}]}$$

As the K_d is the reciprocal of the K_{eq}, a smaller K_d value denotes a stronger binding reaction with a greater proportion of associated complexes (245,246). For binding experiments, the K_d can be determined from the equation for specific binding (B), shown in formula 14, which is determined from the ligand concentration ($[L]$), and maximum specific binding (B_{max}) (247).

(14) $$B = \frac{B_{max} \times [L]}{K_d + [L]}$$

By using FA and formula 14, it is therefore possible to measure clathrin-adaptor interactions, by measuring the anisotropy value of fluorescently labelled adaptor with varying clathrin cage concentrations to determine the K_d value.

7.1.4 Why anisotropy as opposed to other methods?

There are a variety of methods that can be used to study molecular interaction including dialysis, nitrocellulose filter binding, gel electrophoresis, capillary electrophoresis, high performance liquid chromatography, fluorescence intensity, FA, UV-vis absorption, circular dichroism, surface plasmon resonance, and isothermal titration calorimetry (248). FA's main strengths over other techniques include high sensitivity and reproducibility of measurements with small sample volumes, and simple and rapid operation allowing for a high throughput of measurements (238,249,250). Due to FA only requiring relatively small sample volumes, and as there is a limited quantity of clathrin and adaptors obtained from purification (purifications shown in chapter 3), it was decided that FA would be an ideal method for measuring clathrin-adaptor interaction kinetics.

By using FA to measure the anisotropy of fluorescently labelled adaptors, addition of clathrin cages should cause an increase in anisotropy due to the larger size of clathrin auxilin complexes compared to auxilin. Changes in anisotropy can be measured to determine the K_d of labelled adaptors binding to clathrin, allowing a greater understanding of the strength of clathrin-adaptor interactions, and allowing measurement of clathrin disassembly rates, providing a better understanding of both reaction mechanisms and the order of adaptor binding. In addition, anisotropy may also be used to determine whether adaptors compete with one another for clathrin binding sites by comparing the K_d of adaptors binding to clathrin, or the rate of clathrin disassembly, in the presence and absence of other adaptor proteins. The remainder of this chapter shall therefore look at whether FA is a functional method for measuring clathrin-adaptor interactions and clathrin disassembly kinetics, and if FA can be used to measure possible competition between adaptors.

7.2 Methods

7.2.1 PLS

Clathrin disassembly assays were performed at 25 °C on an FP-6500 fluorimeter (JASCO), using an excitation and emission wavelength of 390 nm. A band width of 3 nm for both excitation and emission was used alongside a PMT voltage of 485 V, with a response time of 0.5 seconds and a data pitch of 1 second. Buffer C pH 7 used as a blank. Measurements were conducted for a maximum of 1800 seconds to ensure the disassembly reaction had completed. The disassembly reaction consisted of 0.09 μM clathrin cages, 500 μM ATP, 0.1 μM auxilin and 2 μM Hsc70 in 200 μl Buffer C pH 7 (118). Two controls were performed to ensure both Hsc70 and auxilin were required for clathrin cage disassembly to occur, which consisted of a premixed solution of clathrin cages with ATP, followed by addition of either auxilin or Hsc70 with the other adaptor added later. The remaining disassembly reactions were performed using a premixed solution of clathrin cages, ATP and auxilin with a final volume of 197 μl, followed by addition of 3 μl Hsc70 once a baseline was reached.

7.2.2 DLS

Dynamic light scattering (DLS) analysis was performed alongside PLS analysis to confirm clathrin cages had disassembled by determining the particle size distribution by number. DLS analysis was performed on a Malvern Nano-series DLS system using a nano series ultra-micro quartz cell with 45 μl volume capacity. Measurements were conducted over 10 minutes at 25 ºC. Three controls were performed which consisted of a 0.09 μM clathrin cage sample, a 0.1 μM auxilin, 2 μM Hsc70 and 500 μM ATP sample, and a 0.09 μM clathrin cage, 0.1 μM auxilin and 2 μM Hsc70 sample, all of which were in 50 μl Buffer C pH 7. The disassembly reaction consisted of 0.09 μM clathrin cages, 500 μM ATP, 0.1 μM auxilin and 2 μM Hsc70 in 100 μl Buffer C pH 7.

7.2.3 Fluorescent labelling of cysteine residues

Cysteine mutants of auxilin were prepared previously by Dr Michael Baker before the start of the project. Each cysteine mutant was formed from an auxilin construct with cysteine to serine mutations, followed by a single serine to cysteine (SC) mutation. The mutants available had a single cysteine remaining at sites 427, 438, 835 and 899. To selectively label auxilin mutants SC427, SC438, SC835, and SC899, 1mM Alexa Fluor 488 C_5 maleimide (AF488) (Thermofisher Scientific) was added. The mixture was incubated for 1 hour on ice and protected from light. Excess label was removed *via* gel filtration using Zeba spin desalting columns (Thermofisher Scientific) washed with Buffer C. Sodium dodecyl sulfate polyacrylamide gel electrophoresis (SDS-PAGE) gels were conducted to confirm Alexa Fluor 488 labelling of adaptors.

7.2.4 Anisotropy

Anisotropy measurements were performed at 25 ºC on a FP-6500 fluorimeter (JASCO), using 500 nm excitation and 520 nm emission wavelength, 5 nm bandwidth, 570 PMT voltage, 0.1 s response time, and 0.5 s data pitch. Reactions consisted of 0 - 2 μM clathrin cages, 500 μM ATP, and 0.2 μM AF488-labelled auxilin in Buffer C pH 6.0, in the presence or absence of 0.2 μM of either epsin 1, ARH, ap180 or β_2-adaptin. Measurements were averaged over 60s.

7.2.5 Stopped flow PLS

Stopped flow PLS was performed using a Biologic MOS-450 fitted with an SFM-400. The SFM-400 was set up with four 10 ml syringes, with syringe A containing 4 μM clathrin and 8 mM ATP, B containing 0.8 μM wild type (WT) auxilin and 8 μM Hsc70, C containing either Buffer C pH7 only or 0.8 μM of either AP180, epsin, β_2-adaptin or ARH, and D containing Buffer C pH 7. Injection of 50 μl per syringe at 1 ml/s into an FC-15 cuvette with a 1.5 mm light

path was conducted to initiate the clathrin disassembly reaction, with a final reaction volume of 200 µl, total flow rate of 4 ml/s, and estimated dead time of 9.2 ms. The final disassembly reaction consisted of 1 µM clathrin cages, 2 mM ATP, 0.2 µM auxilin and 2 µM Hsc70 in Buffer C pH 7, either in the presence or absence of 0.2 µM of another adaptor (*i.e.*, AP180, ARH, β_2-adaptin or epsin). PLS of clathrin disassembly assays was measured at room temperature with an excitation wavelength of 390 nm and 2 mm slit width, using a PMS-450 detector set to 90° from the light path with a PMT voltage of 700 V. Measurements were conducted over 800 seconds, with a data acquisition of 50 ms between 0 – 200 s and 500 ms between 200 – 800 s. Data acquisition was started at 10ms before the stop.

7.2.6 Stopped flow anisotropy

Stopped flow anisotropy was performed using a Biologic MOS-450 fitted with an SFM-400. The SFM-400 was set up with four 10 ml syringes, with syringe A containing 4 µM clathrin and 8 mM ATP, B containing 0.8 µM AF488 SC247 auxilin and 8 µM Hsc70, and C and D containing Buffer C pH 7. Injection of 50 µl per syringe at 1 ml/s into an FC-15 cuvette with a 1.5 mm light path was conducted to initiate the clathrin disassembly reaction, with a final reaction volume of 200 µl, total flow rate of 4 ml/s, and estimated dead time of 9.2 ms. The final disassembly reaction consisted of 1 µM clathrin cages, 2 mM ATP, 0.2 µM auxilin and 2 µM Hsc70 in Buffer C pH 7. Anisotropy of clathrin disassembly assays were measured at room temperature with an excitation wavelength of 500 nm and slit width of 2 mm, using a PMS-450 detector set to 90° from the light path with a PMT voltage of 500 V. Measurements were conducted over 800 seconds, with a data acquisition of 500 µs between 0 – 3 s and 500 ms between 200 – 800 s. Data acquisition was started at 10ms before the stop.

7.3 Confirming the Activity of Hsc70 and Auxilin

7.3.1 Clathrin disassembly assays

Clathrin disassembly assays were conducted using PLS, with changes in scattering intensity over time shown in figure 7.3.1. As clathrin cages disassemble the scattering intensity decreases since clathrin cages scatter more light in comparison to clathrin triskelia, triskelia having a smaller molecular size. The disassembly controls in figure 7.3.1 A showed addition of both Hsc70 and auxilin alongside ATP was required for the clathrin cages to disassemble into triskelia, as was expected based on previously published results (75,76,106–115,118). The fast rate of disassembly was causing the start of disassembly reactions to be missed. Stopped flow capabilities would be beneficial to use in future studies to capture the start of the disassembly reactions. As the aim was to see if auxilin mutants were functional, no alternative conditions were used for this experiment.

Disassembly assays of WT and cysteine mutant combinations of Hsc70 and auxilin were tested to ensure the mutations did not impact clathrin disassembly activity. The rate of disassembly did not appear to change when the mutants were used in comparison to the WT versions of Hsc70 and auxilin, based on results presented in figure 7.3.1 B, as all reactions went from the max to min signal within a similar timescale. Disassembly of cages was further backed by DLS analysis of clathrin cages after the disassembly reaction had completed, as shown in figure 7.3.2. DLS analysis of particles by number showed a drop in particle size from 100 nm to around 10 nm only when clathrin cages were in the presence of auxilin, Hsc70 and ATP, which matches the clathrin cage disassembly results from PLS. Thus, we can conclude that the cysteine mutations of auxilin and Hsc70 have little to no impact on the ability of the mutants to disassemble clathrin cages into triskelia.

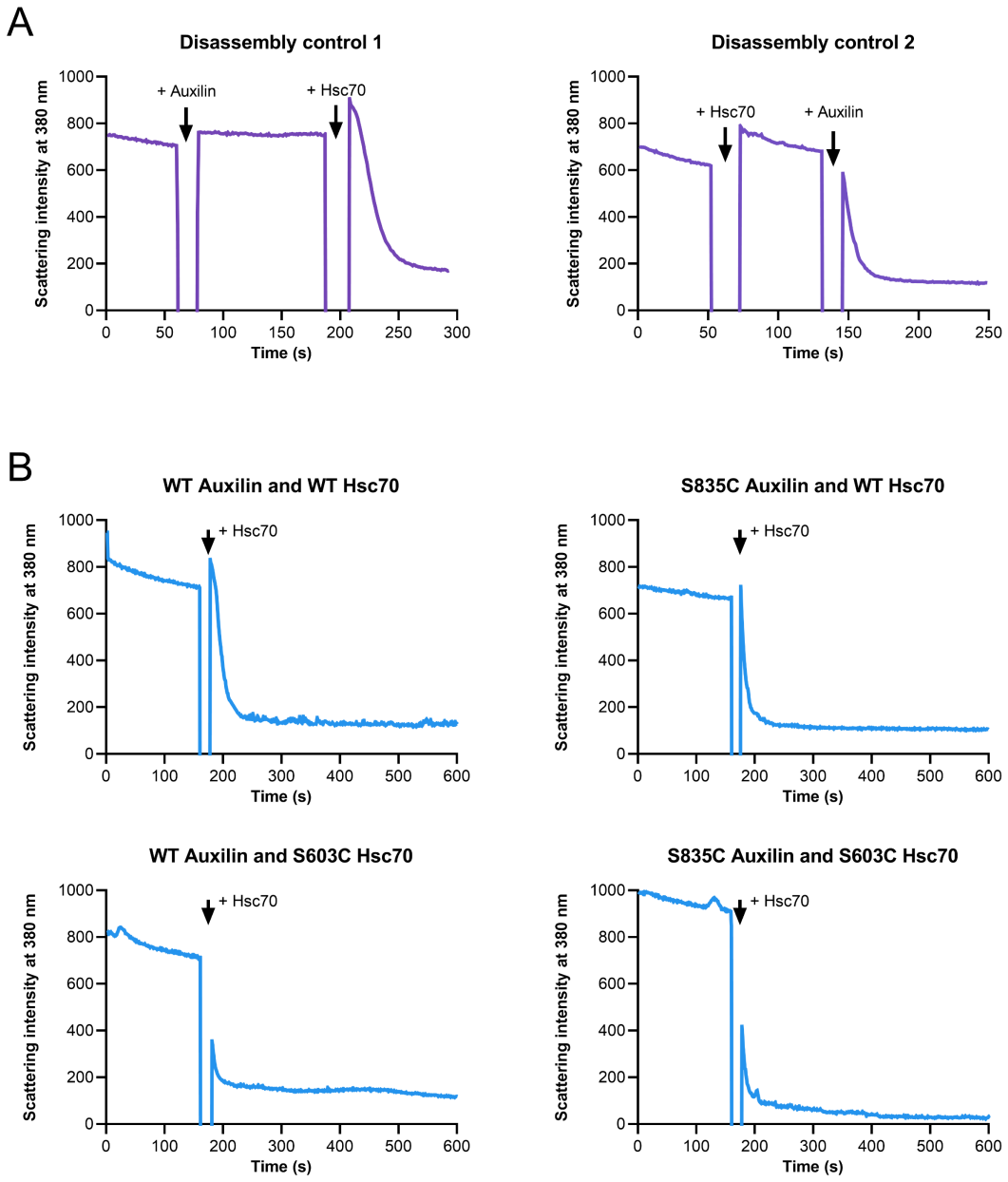

Figure 7.3.1 – Clathrin disassembly analysed *via* perpendicular light scattering

The scattering intensity of clathrin cages using perpendicular light scattering at 380 nm. These are initial experiments to confirm the functionality of auxilin and hsc70, therefore, repeats for these experiments were unrequired. Disassembly reactions consisted of 0.09 µM clathrin cages, 500 µM ATP, 0.1 µM auxilin and 2 µM Hsc70 in 200 µl Buffer C pH 7 at 25 °C. A) Disassembly controls showing that both auxilin and Hsc70 are required for clathrin cage disassembly. B) Clathrin disassembly reactions using different auxilin and Hsc70 combinations. Scattering of clathrin cages mixed with ATP and auxilin (197 µl) was measured before addition of 3 µl Hsc70, indicated by a black arrow.

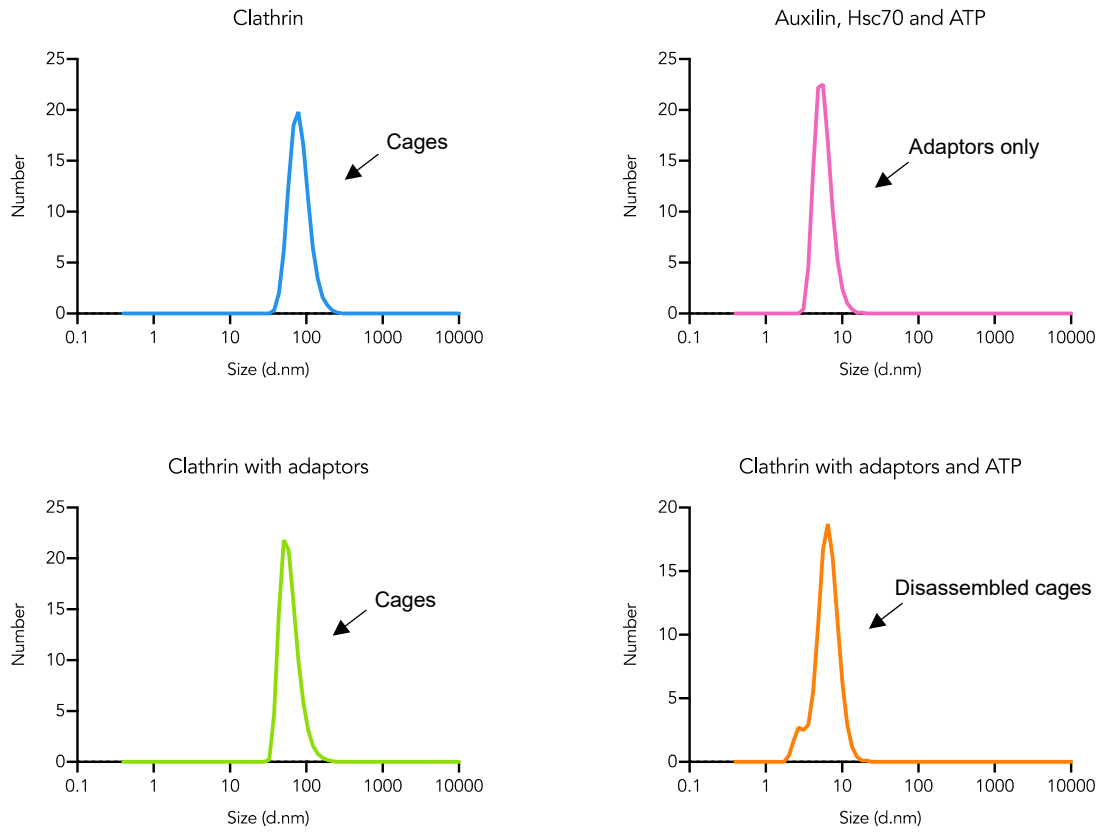

Figure 7.3.2 – Clathrin disassembly analysed *via* dynamic light scattering

DLS size distribution analysis of clathrin mixed with Hsc70 and auxilin. Graphs represent the size distributions of particles by number. Three controls were performed shown at the top of the figure to confirm the size distribution of clathrin cages and adaptor proteins before disassembly, and the requirement for ATP in the disassembly process. Measurements were conducted over 10 minutes at 25 °C. Clathrin sample consisted of 50 µl of 0.09 µM clathrin cages in Buffer C pH 7. Auxilin, Hsc70 and ATP sample consisted of 50 µl of 0.1 µM auxilin, 2 µM Hsc70 and 500 µM ATP in Buffer C pH 7. Clathrin with adaptors sample consisted of 50 µl of 0.09 µM clathrin cage, 0.1 µM auxilin and 2 µM Hsc70 in Buffer C pH 7.Clathrin with adaptors and ATP sample consisted of 0.09 µM clathrin cages, 500 µM ATP, 0.1 µM auxilin and 2 µM Hsc70 in 100 µl Buffer C pH 7. These are initial experiments to confirm the functionality of auxilin and hsc70, therefore, repeats for these experiments were unrequired.

7.3.2 Fluorescent labelling of constructs

To enable anisotropy measurements to be performed, SC835 auxilin and SC603 Hsc70 mutants were labelled with Alexa Fluor 488 C_5-maleimide (AF488), with SDS-page gels presented in figure 7.3.3.

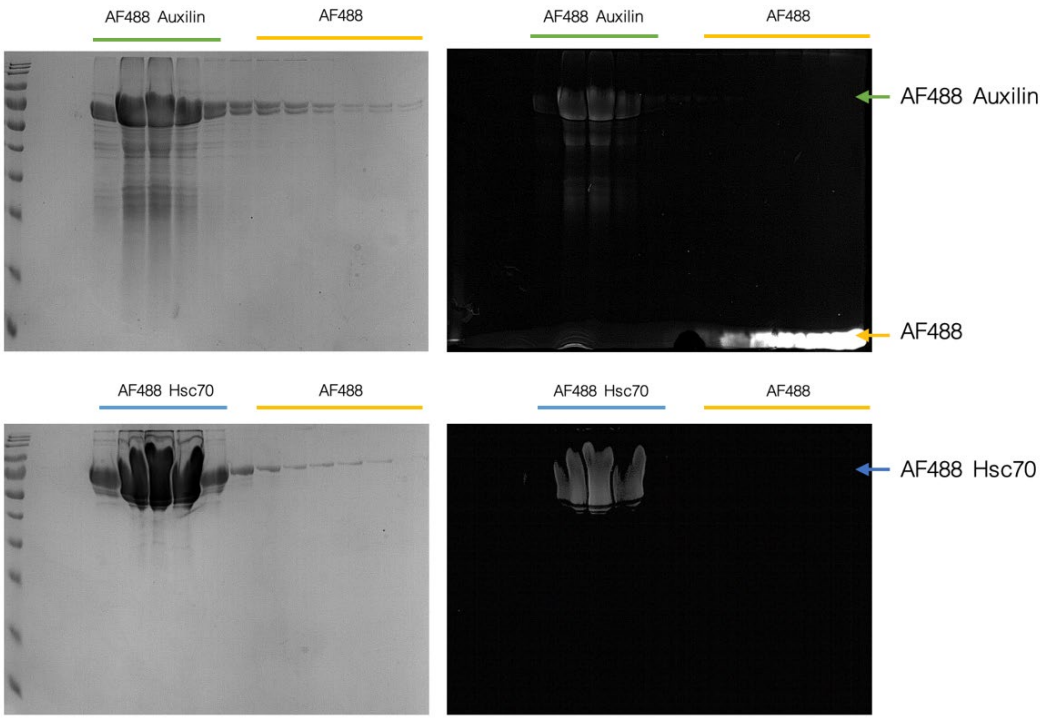

Figure 7.3.3 – SDS gels of AF488 labelled S835C auxilin and S603C Hsc70

SDS gels of AF488 labelled S835C auxilin (top) and AF488 labelled S603C Hsc70 (bottom) imaged with white light (left) and UV light (right). The green, blue and yellow arrows indicate labelled auxilin, labelled Hsc70 and excess AF488 C5-maleimide respectively.

PLS of clathrin disassembly using the labelled components, AF488 SC835 auxilin or AF488 SC603 Hsc70, showed that labelled mutants are capable of disassembling clathrin cages (see figure 7.3.4 A), however, AF488 SC835 auxilin showed a reduced rate of clathrin cage disassembly. PLS of clathrin disassembly was thus conducted for auxilin mutants and compared to WT auxilin to determine if cysteine labelling affected auxilin functionality, as shown in figure 7.3.4 C. Only AF488 SC835 auxilin showed reduced functionality, with AF488 labelled SC427, SC438, and SC899 showing similar initial disassembly rates to WT auxilin.

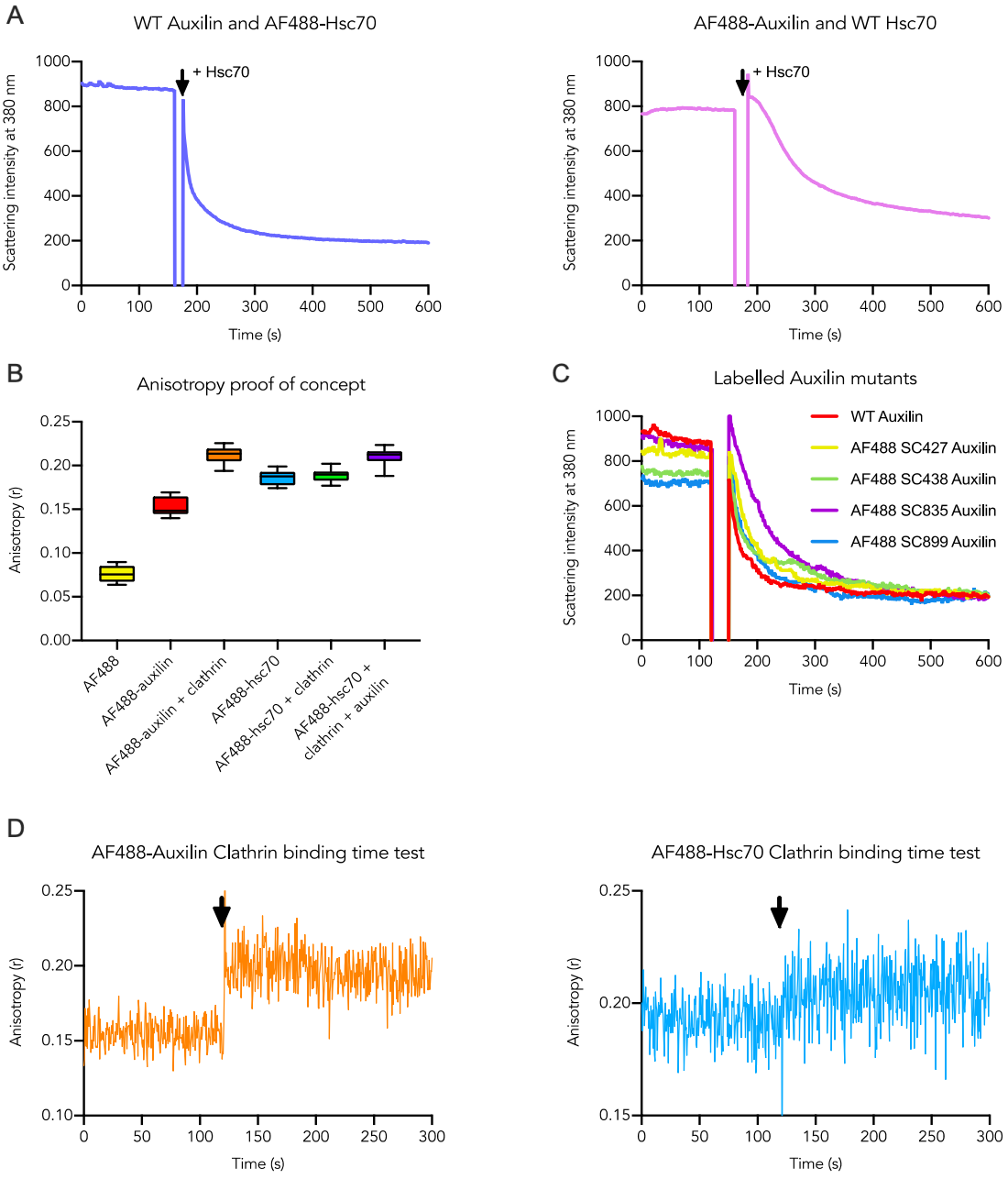

Figure 7.3.4 – Assessing the use of AF488 labelled adaptors for anisotropy

Different experimental assessments used to confirm the suitability of AF488 labelled auxilin and Hsc70 for use in anisotropy experiments of clathrin disassembly and clathrin binding. All samples contained ATP. These are initial experiments to confirm the functionality of labelled auxilin and hsc70 for anisotropy of disassembling clathrin cages, therefore repeats for these experiments were unrequired. A) Clathrin disassembly experiments showing scattering intensity changes over time when clathrin is in the presence of either WT auxilin and AF488 S603C Hsc70 (left) or AF488 S835C auxilin and WT Hsc70. Black arrow indicates addition of Hsc70. Disassembly reactions consisted of 0.09 µM clathrin cages, 500 µM ATP, 0.1 µM auxilin and 2 µM Hsc70 in 200 µl Buffer C pH 7 at 25 °C. B) Box plot showing the anisotropy reading of AF488, AF488 labelled auxilin in the presence and absence of clathrin, and AF488 labelled Hsc70 in the presence and absence of clathrin and auxilin. Error bars represent sd. Reactions consisted of 0.2 µM AF488-labelled adaptor and 500 µM ATP in Buffer C pH 6 at 25 °C. 2 µM

clathrin cages were included in AF488-adaptor + clathrin samples only. C) Clathrin disassembly experiments showing the change in scattering intensity over time when clathrin is in the presence of either WT auxilin or the AF488 labelled auxilin mutants S427C, S438C, S835C, and S899C. Disassembly reactions consisted of 0.09 µM clathrin cages, 500 µM ATP, 0.1 µM AF488-labelled auxilin and 2 µM Hsc70 in 200 µl Buffer C pH 7 at 25 °C. D) Anisotropy value of AF488 S427C auxilin (left) and AF488 S603C hsc70 (right) over time. Black arrow indicates addition of clathrin cages. Reactions consisted of 0.2 µM AF488-labelled adaptor and 500 µM ATP in Buffer C pH 6 at 25 °C. 2 µM clathrin cages were injected into the samples at 120s.

We then performed fluorescence anisotropy analysis of labelled auxilin and Hsc70 in the presence and absence of clathrin cages, as shown in figure 7.3.4 B, to determine if the anisotropy output values were of a suitable distance to allow for binding analysis of adaptors to clathrin cages using both single point measurements and time-course measurements. AF488 auxilin exhibited a median anisotropy value of 0.148 and range of 0.138 - 0.168, which rose to a median anisotropy value of 0.212 and range of 0.194 – 0.224 when in the presence of 1 µM clathrin cages, with the rise in anisotropy value clearly visible during time-course measurements, shown in figure 7.3.4 D, upon injection of clathrin cages at 120 s. AF488 Hsc70, however, exhibited a median anisotropy value of 0.185 and range of 0.172 - 0.199, which rose only to a median anisotropy value of 0.211 and range of 0.187 – 0.223 when in the presence of WT auxilin and 1 µM clathrin cages, with the rise in anisotropy value being difficult to visualise during time-course measurements, shown in figure 7.3.4 D, upon injection of clathrin cages at 120 s. We therefore concluded that further anisotropy measurements should be conducted using AF488 labelled mutants only, with scope for testing and production of other cysteine hsc70 mutants in the future.

7.4 Measuring Binding with Anisotropy

7.4.1 Equilibrium binding of auxilin to clathrin cages

We conducted equilibrium binding analysis of addition of clathrin cages to AF488 auxilin mutants to determine the quality of anisotropy measurements for analysing clathrin-adaptor interactions (see figure 7.4.1 A), with measured Bmax and K_d values presented in figure 7.4.1 B.

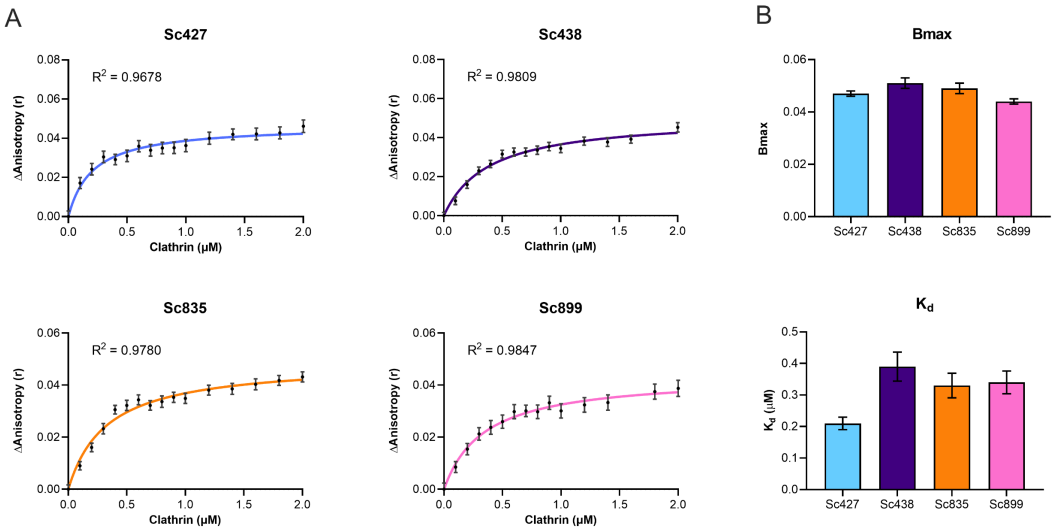

Figure 7.4.1 – Equilibrium binding of clathrin to AF488 labelled auxilin mutants

Equilibrium binding measured from changes in anisotropy value upon varying clathrin concentration. Reactions consisted of 0 - 2 µM clathrin cages, 500 µM ATP, and 0.2 µM AF488-labelled auxilin in Buffer C pH 6.0 at 25 °C. Three measurements were taken per point, and each measurement was averaged over 60s. A) Binding curves obtained using AF488 labelled auxilin mutants S427C, S438C, S835C, and S899C. Error bars presented as 95% confidence intervals. B) Bar charts presenting the different Bmax and K_d values of clathrin binding to AF488 labelled auxilin mutants S427C, S438C, S835C, and S899C. Error bars presented as SEM.

Saturation binding curves were used to analyse the data as the saturation binding curve equation describes the equilibrium binding of clathrin to auxilin as a function of increasing clathrin concentration. Of the four mutants, AF488

SC427 auxilin presented the smallest K_d value of 0.21 ± 0.02 μM. Bmax values for all auxilin mutants were very similar between 0.044 – 0.051. Overall, we were able to successfully measure binding of clathrin cages to AF488 auxilin.

7.4.2 Determining competition between adaptors

As the SC427 auxilin mutant presented the lowest K_d value, we conducted equilibrium binding analysis of addition of clathrin cages to AF488 SC427 auxilin in the presence of other CME adaptor proteins (figure 7.4.2 A), with measured Bmax and K_d values presented in figure 7.4.2 B. The R^2 values of the models for ARH, epsin and β_2-adaptin are smaller compared to the R^2 value for SC427 auxilin, which will lead to higher error values in Bmax and K_d values, however, the R^2 values are greater than 0.9 indicating a high level of confidence within the Bmax and K_d values. Epsin, β_2-adaptin and ARH overall caused a small increase in the Bmax value (0.054 ± 0.005, 0.056 ± 0.001, and 0.066 ± 0.005 respectively), and AP180 caused a large increase in Bmax (0.118 ± 0.007) when compared to SC427 auxilin alone (0.047 ± 0.001). Epsin, β_2-adaptin and ARH also caused a small increase in K_d (0.67 ± 0.17 μM, 0.48 ± 0.03 μM, and 0.75 ± 0.12 μM respectively), and AP180 caused a large increase in K_d (2.81 ± 0.29 μM) compared to SC427 auxilin alone (0.21 ± 0.02 μM). This suggests all adaptors are competitive inhibitors of clathrin-auxilin interactions. How competition between auxilin and other CME adaptors impacts the rate of clathrin disassembly, however, still needs to be assessed. The increase in maximum anisotropy also suggests either an increase in size of the complex or an increase in fluorophore rigidity in the presence of the other adaptor proteins. An increase in the size of the complex could potentially be due to binding of the competitive adaptors, which may cause conformational changes in the clathrin complex causing it to expand. Additional experiments using labelled versions of AP180, M1 ARH, epsin and β_2-adaptin would enable further validation of the anisotropy maximum increase and may also provide additional details on the cause of this increase.

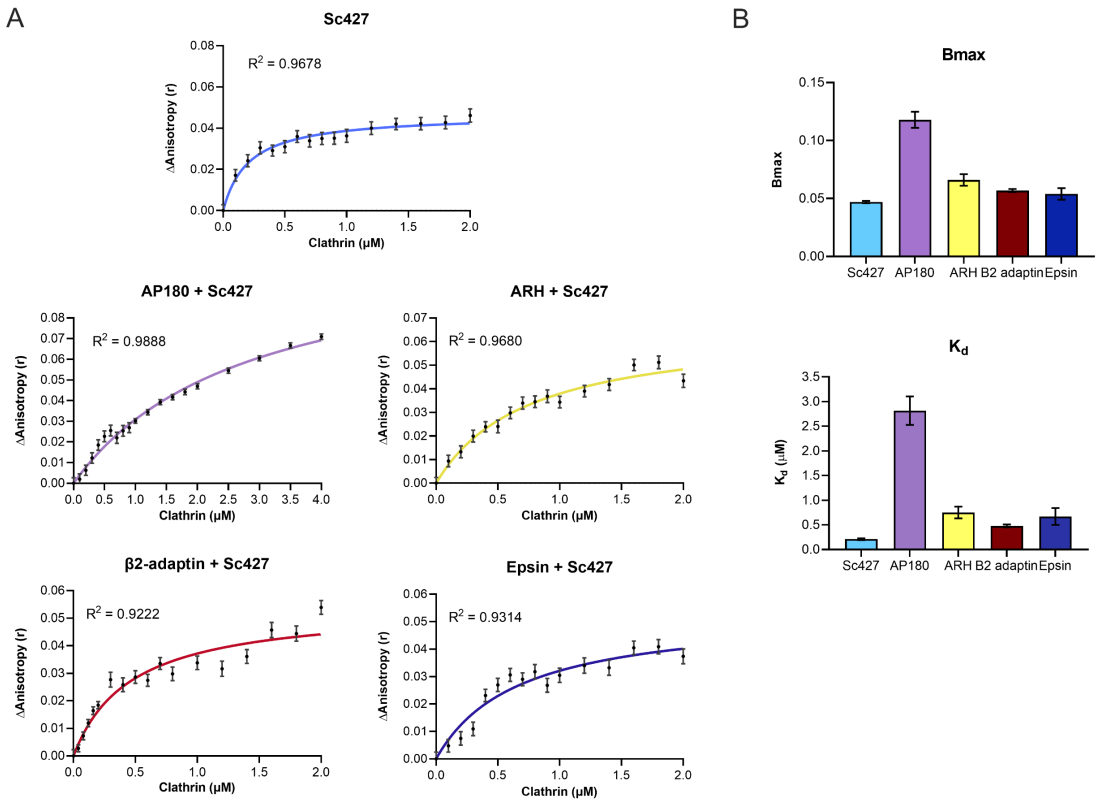

Figure 7.4.2 – Competition between different adaptors for clathrin binding

Equilibrium binding measured from measuring changes in the anisotropy value of AF488 labelled S427C auxilin upon varying clathrin concentration. Reactions consisted of 0 - 2 μM clathrin cages, 500 μM ATP, and 0.2 μM AF488-labelled auxilin in Buffer C pH 6.0, in the presence or absence of 0.2 μM of either epsin 1, ARH, ap180 or b2-adaptin, at 25 ºC. Three measurements were taken per point, and each measurement was averaged over 60s. A) Binding curves obtained using auxilin on its own or in the presence of either AP180, ARH, β_2-adaptin or epsin, with an auxilin to adaptor concentration ratio of 1:1. Error bars presented as 95% confidence intervals. B) Bar charts presenting the different Bmax and K_d values of clathrin binding to AF488 labelled S427C auxilin either on its own or in the presence of either AP180, ARH, β_2-adaptin or epsin. Error bars presented as SEM.

7.4.3 Stopped flow PLS studies

To acquire the rate of disassembly from the point of sample mixing, use of a fluorimeter with stopped flow capabilities is required to ensure data is captured immediately upon mixing of components. PLS measurements of clathrin disassembly, shown in figure 7.4.3, were obtained to assess the impact of competitive adaptor presence on WT auxilin binding and clathrin disassembly.

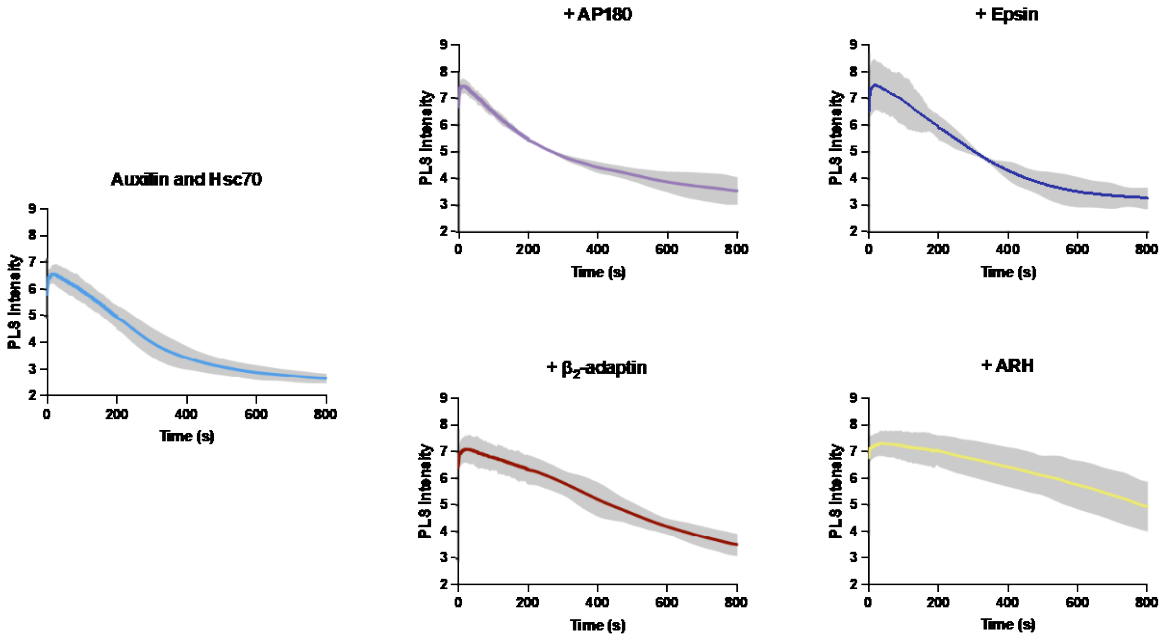

Figure 7.4.3 – PLS of clathrin cage disassembly with competitive adaptors

PLS stopped flow measurement intensities of clathrin cage disassembly over time in the presence and absence of competitive adaptors. Errors are reported as 95% CI in grey. Disassembly reactions consisted of 1 µM clathrin cages, 2 mM ATP, 0.2 µM auxilin and 2 µM Hsc70 in Buffer C pH 7, either in the presence or absence of 0.2 µM of another adaptor (i.e., AP180, ARH, b2-adaptin or epsin), at 25 ºC. N=3.

For all traces, an initial rise in PLS intensity is seen which may indicate the adaptors binding to clathrin cages. When a competitive adaptor is present the PLS intensity during the initial rise and at the end of the disassembly reaction is higher compared to the control reaction. Whether the higher level in PLS intensity is due to any leftover clathrin cages unable to disassemble because of the competitive adaptor, or from the presence of a competitive adaptor in the sample, will need to be verified. The initial maximum rate of clathrin disassembly can be measured from the PLS data despite the higher PLS intensity levels for the competitive adaptor containing experiments, by fitting a linear regression line against the initial downward slope of the PLS curve (see figure 7.4.4). Comparison of the rates of disassembly show both expected and conflicting results when considering the K_d measurements presented previously in figure 7.4.2. The initial maximum rate of clathrin disassembly in the presence of β_2-adaptin and ARH decreased from 9.4×10^{-3} to 2.6×10^{-3} and 4.2×10^{-3}

respectively, which is expected if β_2-adaptin and ARH are affecting auxilin binding, as predicted by the higher K_d values. Epsin, however, caused no significant change (from 9.4×10^{-3} to 9×10^{-3}) to the initial maximum rate of clathrin disassembly despite causing a higher K_d value, and AP180 caused the initial maximum rate of disassembly to increase from 9.4×10^{-3} to 11.6×10^{-3} despite also increasing the K_d. This conflicting data suggests other CME adaptors can possibly both promote or inhibit clathrin disassembly. How CME adaptors switch between promoting and inhibiting clathrin disassembly could be due to local adaptor concentrations, and so further experiments should look at how CME adaptor concentrations impact the initial maximum clathrin disassembly rate and the K_d of auxilin clathrin interactions.

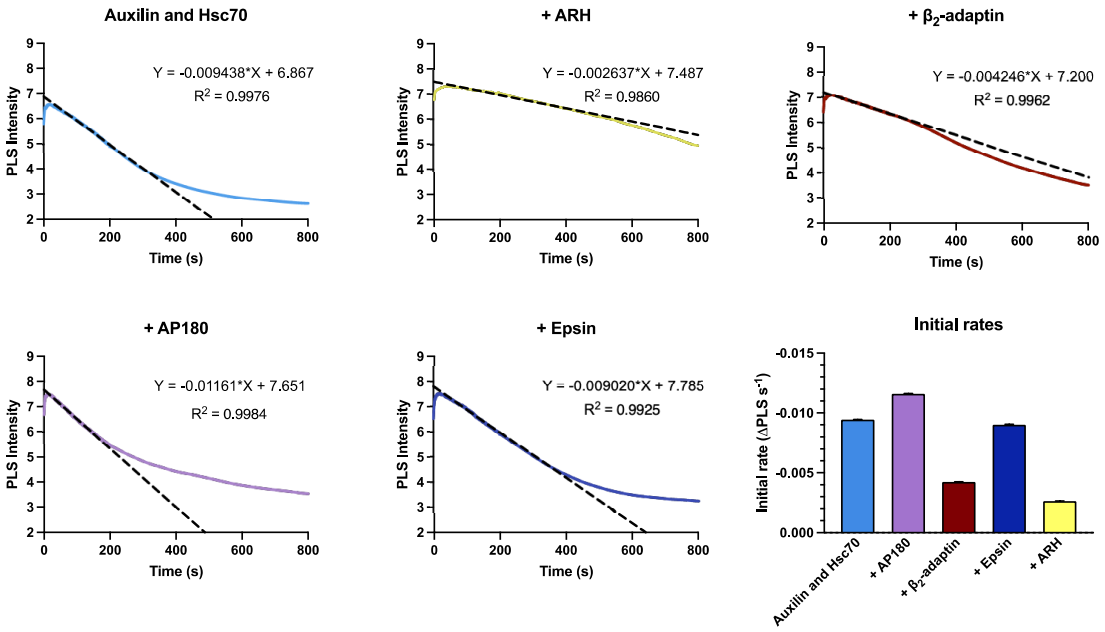

Figure 7.4.4 – Competitive adaptors reduce maximum clathrin disassembly rate

Fitting of linear regression lines (dashed black lines) against PLS curves for clathrin disassembly in the presence and absence of competitive adaptors, to determine the initial rates of clathrin disassembly. Comparison of determined initial rates presented as a bar chart on the bottom right, with error bars reported as se. Disassembly reactions consisted of 1 µM clathrin cages, 2 mM ATP, 0.2 µM auxilin and 2 µM Hsc70 in Buffer C pH 7, either in the presence or absence of 0.2 µM of another adaptor (i.e., AP180, ARH, b2-adaptin or epsin), at 25 °C. N=3.

7.4.4 Stopped flow anisotropy studies

In addition to PLS, use of stopped flow anisotropy (r) measurements is another possibility for determining clathrin disassembly rates, and allows visualisation of adaptors binding to and dissociating from clathrin cages. Characterisation of anisotropy with stopped flow controls for measuring clathrin disassembly was conducted, with results presented in figure 7.4.5. The traces obtained from anisotropy measurements (see figure 7.4.5 A) were consistent and produced an inverse sigmoidal curve. The maximum rate of auxilin dissociation was measured by fitting a linear regression line against the slope (see figure 7.4.5 B), with the rate of auxilin dissociation determined to be 0.37×10^{-3} r s^{-1}. In addition to measuring the maximum dissociation rate, binding of auxilin to clathrin cages was also captured allowing the rate of auxilin association to be determined also by fitting a linear regression line against the starting slope (see figure 7.4.5 C), with the association rate of auxilin to clathrin cages determined to be 1.58 r s^{-1}.

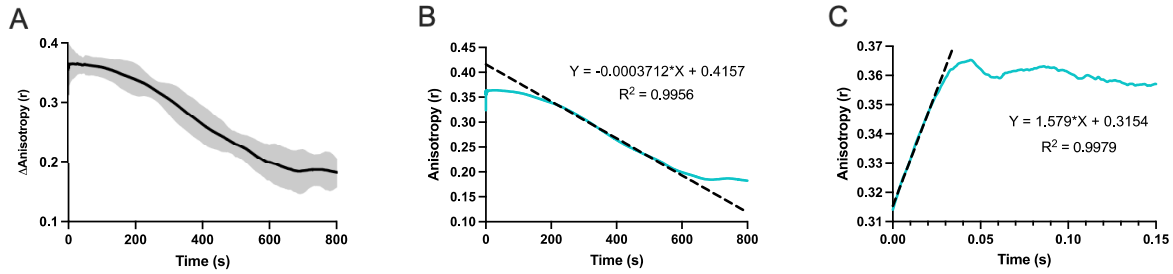

Figure 7.4.5 – Characterising anisotropy for measuring clathrin disassembly

Characterisation of anisotropy for measuring clathrin disassembly rates and identifying timings of clathrin-adaptor interactions. Disassembly reactions consisted of 1 µM clathrin cages, 2 mM ATP, 0.2 µM auxilin and 2 µM Hsc70 in Buffer C pH 7 at 25 °C. N=3. A) Change in anisotropy of AF488 SC427 auxilin over time during clathrin cage disassembly, with stopped flow mechanics used for sample preparation. Errors reported as 95% CI in grey. B) Fitting of a linear regression line (dashed black line) against the anisotropy curve (blue line) where the rate of clathrin cage disassembly reaches maximum. C) Fitting of a linear regression line (dashed black line) against the anisotropy curve (blue line) data obtained between 0 – 25 ms after sample injection, identifying the potential rate of auxilin binding to clathrin cages.

7.5 Discussion

7.5.1 Anisotropy for studying clathrin-adaptor interactions

Several key research questions have yet to be answered on the kinetics of clathrin-adaptor interactions and clathrin disassembly, and whether adaptors compete with one another for clathrin binding sites (1,118). Comparison and use of AF-488 labelled auxilin constructs for clathrin disassembly enabled the evaluation of FA as a functional method for determining equilibrium binding of adaptors to clathrin cages, with the AF488 labelled SC427 auxilin construct maintaining clathrin disassembly functionality when in the presence of clathrin cages, ATP and Hsc70.

Literature on clathrin-adaptor interactions has yet to measure binding affinity and clathrin disassembly and assembly rates, with only the affinity of Hsc70 for ATP measured so far by Rothnie *et al.* (2011)(118). Use of FA for measuring equilibrium binding will thus allow the possibility of measuring the strength of clathrin-adaptor interactions, the rate of clathrin assembly and disassembly reactions, and allow competition between adaptors to be evaluated. In addition, the effect of adaptor mutations on binding affinity and clathrin assembly and disassembly rates can also now be measured and compared with WT adaptors, allowing the importance of residues for clathrin-adaptor interactions to be measured. By having more details on clathrin-adaptor interactions and adaptor competition for clathrin binding within the scientific literature, there will be a greater understanding of the mechanisms of clathrin coat assembly and disassembly, which will be beneficial for understanding why changes in adaptor protein expression levels or mutations within adaptors lead to disease states (see section 1.3 for examples).

FA was used to measure the K_d of clathrin binding to auxilin, as well as for determining competition between auxilin and AP180, epsin, β_2-adaptin, and ARH, *via* comparison of K_d measurements. Comparison of K_d measurements showed AP180, epsin, β_2-adaptin, and ARH reduced the strength of auxilin binding to clathrin cages, with AP180 having the greatest effect, indicating that AP180, epsin, β_2-adaptin, and ARH are competitive inhibitors of clathrin-auxilin interactions. PLS was used to measure clathrin disassembly rates in the presence and absence of the competitive adaptors as an additional method of measuring competition between AP180, epsin, β_2-adaptin, and ARH with auxilin, using the same adaptor concentrations used for K_d measurements. The results obtained from PLS, however, are not consistent with the results obtained from the binding assays. Although ARH and β_2-adaptin caused a decrease in the rate of clathrin disassembly, as was expected, the rate of clathrin disassembly in the presence of AP180 and epsin was not reduced when compared to clathrin disassembly with auxilin, Hsc70 and ATP only. The effect of AP180 was the most surprising as AP180 caused the greatest increase in K_d but also produced an increase in the rate of clathrin cage disassembly. As AP180 also caused a significant increase in Bmax it is possible that binding of AP180 causes changes in clathrin cage conformation that not only causes the cage to expand, but also reduces the energy requirements needed for disassembly. Further investigation is therefore required to clarify the effects of the four competitive adaptor proteins on clathrin-auxilin interactions and clathrin disassembly. As the K_d experiments were performed on different days to the PLS experiments, repeating the experiments so they are performed on the same day would add additional reliability to the results.

The results for β_2-adaptin do however align with results from the literature, as both auxilin and β_2-adaptin contain a clathrin box motif which binds to the clathrin box on the terminal. Recent papers from Smith *et al.* (2021)(208), Paraan *et al.* (2020)(224) and Kovtun *et al.* (2020)(225), have also identified three different binding modes of β_2-adaptin to the clathrin terminal domain, with some causing similar changes to the terminal domain and ankle domain

positioning as observed in the clathrin auxilin structures developed and presented in chapter 5 and Fotin *et al.* (2004)(107), when compared to the clathrin hub structure developed and presented in chapter 4. In addition, the location of β_2-adaptin in the Smith *et al.* and Kovtun *et al.* models overlap the positioning of auxilin in both the Fotin *et al.* model and the developed clathrin auxilin model shown in chapter 5. It is therefore expected that further analysis of β_2-adaptin effects on clathrin disassembly will find that β_2-adaptin is a competitive inhibitor of clathrin-auxilin interactions.

Investigations assessing the effect of varying concentrations of the competitive adaptors on the rate of clathrin disassembly and the K_d of clathrin auxilin binding, will not only confirm the results we have seen so far, but also provide greater insight into competitive adaptor interactions with clathrin cages. It may also be beneficial to utilize FA for measuring the rates of clathrin disassembly in the presence of competitive to see whether using this method will provide results consistent with the PLS results. Although PLS allows measurements of initial rates of clathrin cage disassembly, the measurements also show the lag phase of clathrin disassembly caused by the binding of Hsc70 to clathrin, which is represented as an initial increase in intensity before intensity decreases as a consequence of clathrin disassembly. Due to Hsc70 scattering interference from PLS measurements, it can be difficult to determine when clathrin cage disassembly begins.

Conducting stopped flow kinetics with FA could be another suitable alternative for measuring the disassembly rate of clathrin cages, as FA will only measure labelled auxilin binding to clathrin. A decrease in FA will therefore show dissociation of auxilin from clathrin as clathrin cages are disassembled. The rate of clathrin disassembly determined by FA compared with the initial rate of clathrin disassembly measured by PLS were very similar, measuring 2×10^{-3} s^{-1} and 2.4×10^{-3} s^{-1} respectively. In addition, the FA measurements produced a sigmoidal curve as opposed to the exponential decay curve produced from PLS measurements, allowing a more accurate measurement of the

disassembly rate to be acquired by using linear regression on the FA sigmoidal curve slope. On top of the benefits of FA stopped flow kinetic measurements for clathrin disassembly, FA was also able to identify the rate of auxilin binding to clathrin cages. Being able to visualise the binding of adaptor proteins to clathrin cages would be beneficial for understanding mechanisms of action, as it would allow determination of the order and speed of adaptor protein binding to clathrin cages.

7.5.2 Study limitations

Despite successfully developing a FA method for measuring the K_d of clathrin-adaptor interactions and clathrin disassembly rates, limitations of the study will have impacted the overall result. Details of the study limitations and their potential solutions are discussed below.

7.5.2.1 Fluorescent labelling

Labelling adaptor proteins so that only one fluorescent probe is attached per protein molecule provides one of the greater challenges and limitations of the FA project. Not only does the fluorophore need to be bright so that it can be detected, but the fluorophore also needs to have a fluorescence lifetime long enough to allow changes in FA to be measured (251). These requirements therefore caused a limitation on what fluorophores could be used; the chosen fluorophore was AF488 C_5-maleimide which has a fluorescence lifetime of 4.1 ns and an excitation and emission max of 494 nm and 520 nm respectively (252,253). Other maleimide fluorescent probes that could have been used that also fit the criteria included AF555 C_2-maleimide with a fluorescence lifetime of 4 ns and an excitation and emission max of 554 nm and 570 nm respectively (253,254), Fluorescein-5-maleimide with a fluorescence lifetime of 4 ns and an excitation and emission max of 495 nm and 517 nm respectively (253,255), BODIPY® TMR C_5-maleimide with a fluorescence lifetime of 5.4 ns and an excitation and emission max of 544 nm and 570 nm respectively (253,256).

AF488 was used over the other fluorescent probes due to its substantial difference in the excitation and emission max. It would be interesting to see if the type of fluorescent probe used had an impact on clathrin-adaptor interaction measurements, due to the different sizes and chemistry of the fluorescent probes (252,254–256). An experiment comparing the K_d or clathrin disassembly rate measurements of mixtures containing AF488 labelled adaptors with Fluorescein, AF546, and BODIPY TMR labelled adaptors would also be beneficial for determining whether other probes would be more suitable for future FA experiments.

In addition to the limitations regarding the types of fluorescent probes available, the labelling of adaptors could also impact the study due to the need for cysteine to serine mutations within the adaptor protein. Mutations to adaptor protein can have an impact on their structure and functionality, which can be further impaired upon labelling with a fluorescent probe (251). This can be observed in figure 7.3.4 C, where the SC835 auxilin mutant was found to have reduced clathrin disassembly functionality upon labelling, suggesting the fluorescent label inhibited and weakened the binding of auxilin to clathrin cages. The reduction in disassembly rate with SC835 auxilin also highlights auxilin residue 835 as important for clathrin or Hsc70 binding. Understanding the structure of the adaptor proteins and the location of key clathrin interaction sequences will be beneficial for aiding the decision of where mutations should be placed within adaptors, however, several versions of single cysteine adaptor mutants will still need to be created and compared before the reliability of FA clathrin-adaptor interaction measurements can be justified (251).

7.5.2.2 Limited library of adaptor constructs

Due to the success of using FA for measuring clathrin-auxilin interactions and adaptor competition, it would be advantageous to develop constructs of all clathrin interacting adaptor proteins in their WT state and with different cysteine mutations so additional clathrin interaction studies using FA can be

performed. To develop the adaptor library 33 adaptors would need to be cloned by reverse transcriptase polymerase chain reaction (PCR), as the adaptors are produced from post-spliced mRNA within eukaryotic cell, which is mRNA that has had the intron sequences removed. The PCR template would therefore need to be developed by reverse transcription of mRNA, which produces a complementary DNA strand. The PCR product would then need to be inserted into a suitable vector so that the protein can be expressed upon transformation into *E. coli* cells. Mutagenesis of each construct would then be required to remove each cysteine from the construct and add a single cysteine into the desired location, with some adaptors having more than 10 cysteines within their structure.

On top of the PCR and mutagenesis, testing of protein overexpression, protein purification optimisation, and functionality testing of each construct would also need to be conducted before clathrin interaction studies using FA could be performed. This work falls outside of the scope/remit of this thesis and will need to be completed by another funded researcher in the future if further investigation of clathrin-adaptor interactions with FA is desired.

7.5.3 Conclusion

Development and use of FA has provided greater insight of clathrin-adaptor interactions and competition between adaptors, by enabling the measurement of K_d of adaptor binding to clathrin cages, as well as the effect of adaptors on the rate of clathrin disassembly. We have identified β_2-adaptin and ARH as potential competitive inhibitors of clathrin-auxilin interactions and clathrin disassembly, suggesting their interactions with clathrin overlap with auxilin's interactions with clathrin. The competitive nature of β_2-adaptin can be seen from recent literature produced by Smith *et al.* (2021)(208), Paraan *et al.* (2020)(224) and Kovtun *et al.* (2020)(225), where they show that the binding location of β_2-adaptin overlaps with the auxilin binding site identified by the

new clathrin auxilin hub model in chapter 5 and the Fotin *et al.* (2004)(107) clathrin auxilin cage model.

We also identified AP180 and epsin as competitive inhibitors of clathrin-auxilin interactions but not clathrin disassembly rates, suggesting further experimentation is required to confirm whether AP180 and epsin are indeed competitive inhibitors. If results of further experiments produce the same results, it is possible that AP180 and epsin occupy some binding sites on clathrin cages that overlap with auxilin binding sites, but the overlap is not sufficient to prevent auxilin binding thereby inhibit clathrin cage disassembly. Overall, results produced from FA of clathrin-adaptor interactions not only shed light on the strength of adaptor binding, but also the relationship between and mechanisms of action for different adaptor proteins.

Chapter 8:

Overall Conclusions

Chapter Overview

The final chapter of this thesis will summarise and discuss the impact of the project outcomes and suggest further research opportunities that can be conducted.

8.1 Overview

The current understanding of clathrin-adaptor interactions is limited to low-resolution cryo-EM structures and crystal structures of the clathrin terminal domain with bound peptides derived from adaptor proteins, despite the wealth of data on the role of adaptor proteins within endocytosis. There are also still many questions with regards to how multiple adaptor proteins interact and bind to clathrin cages to enable controlled clathrin coat assembly and disassembly. This project aimed to gain a greater understanding of how adaptor proteins interact with clathrin, and the impact these interactions have clathrin cage disassembly.

The initial focus was placed on using cryo-EM to determine the structure of a clathrin cage hub with no adaptor proteins bound and terminal domains resolved, providing new insights into clathrin-clathrin interactions between the terminal domain and ankle region in the absence of adaptor proteins. This was followed by cryo-EM of clathrin cages with auxilin bound to acquire higher resolution details on auxilin binding to clathrin cages, which revealed a more complex and varied mode of binding in comparison to the Fotin *et al.* (2004)(107) structure. Finally, effects of clathrin-adaptor interactions on clathrin disassembly were further analysed using fluorescence anisotropy (FA), providing insights into adaptor competition for clathrin binding. In this chapter the implications of cryo-EM and FA analysis results will be discussed, including whether the questions and aims outlined in chapter 1.6 were achieved, how the results impact the current understanding of the CME process, and what further research could be conducted considering the results.

8.2 Impact of Research

8.2.1 Updating the model for clathrin disassembly

The variable orientation of the auxilin J-domain when bound to clathrin cages, the changes in terminal domain position caused by auxilin binding, and the possible interactions between auxilin and CLC's, provide additional clues into how the clathrin uncoating reaction may occur. As previously discussed in section 1.2.4, there are two main proposed models for clathrin coat disassembly called the steric wedge/Brownian ratchet model and the entropic pulling model/collision pressure (1). In the steric wedge/Brownian ratchet model, binding of auxilin and Hsc70 on the inner face of the clathrin coat increases the excluded volume below clathrin coat vertices, producing a strained clathrin coat conformation (107,123). Upon ATP hydrolysis, Hsc70's Brownian motion will increase causing collisions with the clathrin coat to further weaken clathrin-clathrin interactions (79,107,123). As chapter 5 showed that binding of auxilin caused the terminal domains to shift and link together through auxilin interactions, and Hsc70 likely binds in the space between the terminal domains and the QLMLT motif in the trimerisation domains, it is unlikely that binding of Hsc70 increases the excluded volume under the clathrin vertices to a point that strains clathrin-clathrin interactions. Further evidence against the steric wedge/Brownian ratchet model is provided by Sousa *et al.* (2016)(79), where they showed persistence of clathrin disassembly even when Hsc70 has been displaced to relieve direct steric clashes. It is still possible however for Brownian motion to weaken clathrin-clathrin interactions, as the Hsc70 would be trapped in the space between the terminal domains and clathrin vertices, thereby increasing the possibility of Hsc70 collisions with clathrin.

In the entropic pulling/collision pressure model ATP hydrolysis by Hsc70 dissociates auxilin from clathrin and tightens Hsc70 binding to clathrin, which in turn restricts Hsc70 movement (127–129). Now that Hsc70 is bound to the

unstructured and flexible clathrin C-terminus, it can move away from clathrin vertices to increase entropy and freedom of movement, creating a directional force that pulls on the clathrin carboxy domain to break clathrin proximal-distal interactions (127–129). The likely positioning of Hsc70 under the clathrin vertices as observed in figure 5.6.1 D, provides support for the entropic pulling/collision pressure model. Additional evidence from Sousa *et al.* (2016)(79) shows Hsc70 binding increases the rigidity of cages and increases the likelihood of cages experiencing catastrophic deformations. Figure 8.2.1 developed by Sousa *et al.,* demonstrates the steps of the entropic pulling/collision pressure model for clathrin coat disassembly.

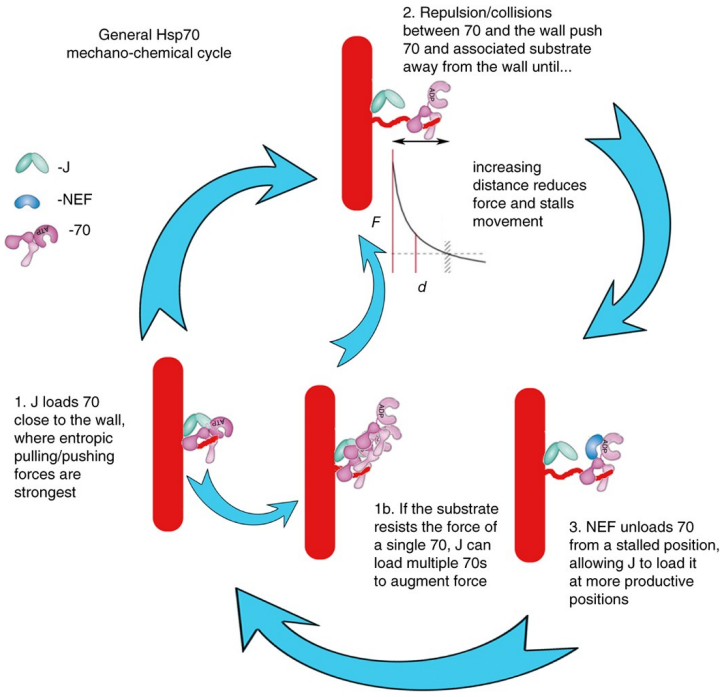

Figure 8.2.1 – Entropic pulling/collision pressure model

The entropic pulling/collision pressure model developed by Sousa *et al.* (2016)(79). 1) Auxilin loads Hsc70 onto the clathrin QLMLT motif where there are strong entropic pulling and pushing forces. 1b) If clathrin resists the forces, then more Hsc70 will be loaded by auxilin. 2) Hsc70 collides with and repels against the clathrin cage, causing Hsc70 to move away from the clathrin cage in order to increase entropy, pulling the clathrin c-terminus in the process. Movement however will stall with increasing distance due to reduced collisions and forces. 3) Hsp110 removes Hsc70 from clathrin, allowing auxilin to load another Hsc70 closer to the clathrin cage vertex so that the cycle can repeat until the cage disassembles. Reprinted by permission from Springer Nature: Nature Structural and Molecular Biology. Sousa R, Liao HS, Cuéllar J, Jin S, Valpuesta JM, Jin AJ, Lafer EM. Clathrin-coat disassembly illuminates the mechanisms of Hsp70 force generation. Nat Struct Mol Biol. 2016;23(9):821–9. DOI: 10.1038/nsmb.3272 (79). Copyright licence number: 5193050468761.

The initial stage of the model, however, is likely to be more complex than the model shown in figures 1.2.3 and 8.2.1 as CLCs are likely to play a role in the uncoating reaction. The presence of potential clathrin-auxilin interactions observed in chapter 5, and the results from published literature showing a reduction in the rate of clathrin disassembly when CLC's are missing (41,125), suggests CLC's play an important role in the clathrin disassembly process that has yet to be identified. A new model hypothesis of the entropic pulling model has therefore been developed suggesting how CLC's could be involved within the clathrin disassembly process if CLC's do interact with auxilin via the CLC N-terminus.

The schematic of the entropic pulling model hypothesis is presented in figure 8.2.2. In this model, binding of auxilin to clathrin cages causes changes in clathrin cage structure to increase cage stability, including rotation and binding of the terminal domains *via* auxilin interactions to provide space underneath clathrin vertices for Hsc70 binding, and binding of the CLC to the CHC ankle region caused by auxilin interactions to further increase cage stability. Binding of ATP bound Hsc70 to auxilin may cause auxilin to pull on the CLC if interactions do indeed occur between them, thereby breaking CLC and CHC interactions. ATP hydrolysis by Hsc70 then leads to binding of Hsc70 to the QLMLT motif in the clathrin trimerisation domain, and dissociation of auxilin from the clathrin coat and Hsc70. Dissociation of auxilin from the complex will provide more space for Hsc70 under the clathrin vertex, promoting entropic pulling of the clathrin C terminus via Hsc70. ATP hydrolysis also causes a change in Hsc70 conformation that causes pulling of the CHC trimerisation domain *via* entropic pulling, reducing the stability of the clathrin cage leading to coat disassembly. Further investigations looking into CLC and auxilin interactions and their effect on clathrin disassembly are required to further validate the proposed model, of which will be discussed in section 8.4.2.

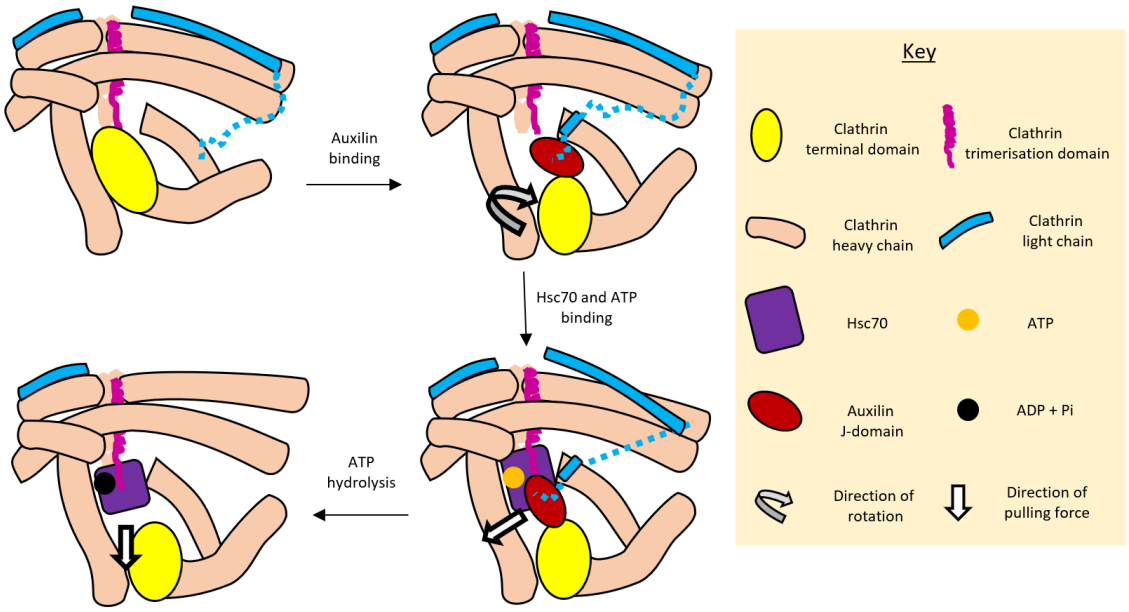

Figure 8.2.2 – Proposed model for initial clathrin uncoating steps

Schematic of proposed model for the initial clathrin uncoating steps developed from the chapter 5 results and published literature on the entropic pulling/collision pressure model (1,127–129). Diagram is not to scale.

8.2.2 CME adaptors are competitive by nature

The presence of competition between different adaptor proteins suggests regulation of adaptor protein concentrations at sites of CME may be vital for ensuring a functional CME process. Several disease states are associated with changes in CME adaptor protein expression levels. Parkinson's disease models show a reduction in auxilin expression levels produce Parkinson's disease symptoms (136). A depletion of PICALM in the brain has been found to reduce levels of intracellular amyloid precursor protein, which could be beneficial for slowing or preventing Alzheimer's disease (141). In addition to neurological diseases, overexpression of HIP1 and epsin, and loss of Dab2 is associated with a variety of cancers (257).

As competitive inhibition of clathrin disassembly was observed in chapter 7, and changes in adaptor protein expression levels lead to disease states, it is likely that regulation of adaptor protein expression and local concentrations during

CME causes shifts in the adaptor protein equilibrium to enable different stages of CME to occur. The shift in adaptor protein concentrations could prevent clathrin coats from assembling or disassembling by blocking the binding of adaptor proteins required for the next CME stage, thereby preventing the import of proteins and molecules into cells. As interactions between auxilin, clathrin and Hsc70 are vital for clathrin disassembly to occur, as indicated in figure 8.2.2, binding of competitive adaptors to clathrin could prevent auxilin and hsc70 from establishing the necessary interactions with clathrin required for disassembly to take place. In addition, binding of adaptors like AP180 for instance which increase the K_d of auxilin binding to clathrin but also increase the rate of disassembly, could cause changes in the structure of clathrin coats to aid the disassembly process, possibly by reducing clathrin-clathrin interactions. Further experiments assessing how adaptors interact with clathrin and the level of competition between adaptors, will enable a greater understanding of the effects of altered adaptor expression levels within cells.

8.3 Future Research Prospects

The outputs of the project have not only enhanced the understanding of the CME process but have also created additional questions and hypotheses. Possible further research prospects will now be discussed.

8.3.1 Further clathrin adaptor complex structures

After successfully producing maps and models of clathrin auxilin complexes that revealed different modes of auxilin binding and provided further information on auxilin effects on clathrin conformation and clathrin-clathrin interactions, it would be beneficial to produce other clathrin adaptor complex structures using cryo-EM to gain insights into how other adaptors bind to clathrin and the effects they have on clathrin structure. To date, only structures of the clathrin auxilin complex and the clathrin β_2-adaptin structure have been produced to a high enough resolution to accurately determine the location and modes of adaptor binding (107,208,224,225), with the mode of Hsc70 binding in the clathrin auxilin Hsc70 complex still under debate (123,258). It would therefore not only be beneficial to produce cryo-EM maps of clathrin auxilin Hsc70 complexes, but also of clathrin complexed with other known clathrin interacting adaptors such as epsin, AP180, Dab2, ARH, β-arrestin, OCRL1, amphiphysin, CALM, GAK, Hip1, Hip1R, AAK1, Hrb, connecdenn, and Ack (20). In addition, it would also be beneficial to acquire structures of clathrin complexes with multiple adaptors bound to simulate the structure of clathrin at different stages of CME, which would provide further structural insight into CME mechanisms and how adaptors may work together to either assemble or disassemble clathrin coats.

8.3.2 Assessing interactions between auxilin and CLC

The possibility of CLC N-terminal interactions with auxilin warrants additional investigation, particularly due to mounting evidence suggesting CLC auxilin

interactions impact the uncoating and stability of clathrin coats. By performing GST pull down experiments of CLC N-terminal mutants with GST-labelled auxilin, and CLC with GST-labelled auxilin J-domain mutants, the location of residues important for auxilin CLC interactions can be identified. As binding of CLC to labelled auxilin will likely produce minimal differences in FA due to the small size of CLCs in comparison to clathrin cages, isothermal titration calorimetry could be used instead to obtain accurate measurements of K_d, reaction stoichiometry, enthalpy and entropy (248). In addition to measuring binding interactions between CLC and auxilin, if clathrin cages can be developed that have mutant CLCs bound FA can be conducted to measure the effects of mutations in auxilin and CLCs to verify which interactions are valuable for clathrin coat stability and uncoating reactions.

8.3.3 Anisotropy for assessing competition and interactions

Further studies of clathrin-adaptor interactions are needed to fully understand the kinetics of clathrin-adaptor interactions and the level of competition between adaptor proteins. This would require the development of a library of adaptor proteins using PCR, with both WT and cysteine mutant versions of the adaptors for use in FA. By using FA, the K_d for clathrin adaptor binding could be measured for all clathrin interacting proteins including auxilin, hsc70, epsin, AP180, β_2-adaptin, Dab2, ARH, β-arrestin, OCRL1, amphiphysin, CALM, GAK, Hip1, Hip1R, AAK1, Hrb, connecdenn, and Ack (20). By using combinations of adaptors of varying quantities, the competitiveness between adaptor proteins and the effects of competition on clathrin assembly and disassembly can be determined. In addition, by inserting point mutations into adaptor protein constructs it will be possible to measure the importance of adaptor protein residues for clathrin binding, as well as the importance of adaptor protein residues for adaptor mechanisms of action. By uncovering information of adaptor protein competition and interactions, a greater insight into the role of

adaptor proteins in CME and how adaptors cause or contribute to clathrin coat assembly and disassembly will be obtained. This will be invaluable information for understanding why changes in adaptor protein expression levels in different disease states, like Alzheimer's and Parkinson's disease, lead to a disruption of CME in cells and may also pave the way for the development of new treatments for these diseases.

8.3.4 Production of clathrin cages from *E. coli*

Although native full length clathrin triskelia can be obtained from source (*i.e.,* pig brains), it is not possible to acquire mutants of clathrin using this method. To further analyse clathrin-adaptor and clathrin-clathrin interactions, it would be beneficial to obtain plasmids of CHC and CLCb that can be expressed and purified from *E. coli* to form clathrin cages. A previous study by Rapoport *et al.* (2008)(122) successfully expressed full length CHC and CLCb in insect cells, however, due to the large CHC gene size, studies using *E. coli* for expression have so far only expressed partial length versions of CHC (156,259). By generating plasmids that can successfully express functional CHC and CLCb in *E. coli,* it will be possible to generate mutants of clathrin to allow the importance of specific clathrin residues for both clathrin-clathrin and clathrin-adaptor interactions to be measured. Assessment of the impact of mutations could be conducted by measuring clathrin assembly and/or disassembly rate using FA or PLS analysis, K_d measurements using FA analysis, and cage structure using negative staining and cryo-EM or cryo-ET analysis. By locating the key residues important for clathrin-adaptor interactions and clathrin-clathrin interactions, the residues can be aligned with structural data to shed light on how adaptor proteins bind to clathrin cages.

8.4 Final Remarks

Overall, structures of the clathrin cage complex and the clathrin auxilin complex have been successfully produced which not only validate previous studies, but also provide information on how auxilin interacts with clathrin during clathrin disassembly, enabling further development of the entropic pulling model for clathrin coat disassembly. The FA technique has been developed and assessed as a suitable method for measuring clathrin-adaptor interactions and clathrin disassembly rates, which enabled competition between adaptor proteins auxilin, AP180, epsin, ARH and β_2-adaptin to be identified. These results have opened new opportunities for further research including the potential for other clathrin adaptor structures, and the identification of key residues for clathrin-adaptor interactions using FA, which will be of benefit for understanding adaptor protein mechanisms of action during CME, and how mutations and change in expression levels cause or contribute to disease states.

This page is intentionally left blank

References

1. Wood KM, Smith CJ. Clathrin - The Molecular Shapeshifter. Biochem J. 2021;478(16):3099–123. DOI: 10.1042/bcj20200740.
2. Doherty GJ, McMahon HT. Mechanisms of Endocytosis. Annu Rev Biochem. 2009;78(1):857–902. DOI: 10.1146/annurev.biochem.78.081307.110540.
3. Baranov M V, Olea RA, van den Bogaart G. Chasing Uptake: Super-Resolution Microscopy in Endocytosis and Phagocytosis. Trends Cell Biol. 2019;29(9):727–39. DOI: 10.1016/j.tcb.2019.05.006.
4. Hoeller D, Volarevic S, Dikic I. Compartmentalization of growth factor receptor signalling [Internet]. Vol. 17, Current Opinion in Cell Biology. 2005. p. 107–11. DOI: 10.1016/j.ceb.2005.01.001.
5. Cossart P, Helenius A. Endocytosis of viruses and bacteria. Cold Spring Harb Perspect Biol. 2014;6(8):a016972. DOI: 10.1101/cshperspect.a016972.
6. Marsh M, Helenius A. Virus entry: Open sesame [Internet]. Vol. 124, Cell. 2006. p. 729–40. DOI: 10.1016/j.cell.2006.02.007.
7. Lavoie PM, Levy O. Mononuclear Phagocyte System. In: Fetal and Neonatal Physiology. Elsevier; 2017. p. 1208-1216.e3. DOI: 10.1016/b978-0-323-35214-7.00125-6.
8. Stillwell W. Membrane Transport. In: An Introduction to Biological Membranes. Elsevier; 2016. p. 423–51. DOI: 10.1016/b978-0-444-63772-7.00019-1.
9. Garrett WS, Mellman I. Studies of endocytosis. In: Lotze MT, Thomson AW, editors. Dendritic Cells. 2nd editio. Academic Press; 2001. p. 213–29. DOI: 10.1016/b978-012455851-9/50055-9.
10. Bitsikas V, Corrêa IR, Nichols BJ. Clathrin-independent pathways do

not contribute significantly to endocytic flux. Elife. 2014;2014(3):1–26. DOI: 10.7554/elife.03970.

11. Ho H-C. Clathrin-Coated Vesicles Leaving the Caudal Margin of the Developing Acrosome Facilitate Acrosomal Shaping During Mouse Spermiogenesis. Biol Reprod. 2008;78(Suppl_1):218–218. DOI: 10.1093/biolreprod/78.s1.218b.

12. Sochacki KA, Taraska JW. From Flat to Curved Clathrin: Controlling a Plastic Ratchet [Internet]. Vol. 29, Trends in Cell Biology. 2019. p. 241–56. DOI: 10.1016/j.tcb.2018.12.002.

13. Wecker L. Receptor Regulation. In: xPharm: The Comprehensive Pharmacology Reference. Elsevier; 2007. p. 1–5. DOI: 10.1016/b978-008055232-3.60004-2.

14. Royle SJ, Bright NA, Lagnado L. Clathrin is required for the function of the mitotic spindle. Nature. 2005;434(7037):1152–7. DOI: 10.1038/nature03502.

15. Roth TF, Porter KR. Yolk protein uptake in the oocyte of the Mosquito Aedes Aegypti. L. J Cell Biol. 1964;20(2):313–32. DOI: 10.1083/jcb.20.2.313.

16. Pearse BMF. Coated vesicles from pig brain: Purification and biochemical characterization. J Mol Biol. 1975;97(1):93–8. DOI: 10.1016/s0022-2836(75)80024-6.

17. Kaksonen M, Roux A. Mechanisms of clathrin-mediated endocytosis [Internet]. Vol. 19, Nature Reviews Molecular Cell Biology. Nature Publishing Group; 2018. p. 313–26. DOI: 10.1038/nrm.2017.132.

18. Zhang B, Koh YH, Beckstead RB, Budnik V, Ganetzky B, Bellen HJ. Synaptic Vesicle Size and Number Are Regulated by a Clathrin Adaptor Protein Required for Endocytosis. Neuron. 1998;21(6):1465–75. DOI: 10.1016/s0896-6273(00)80664-9.

19. Miller SE, Mathiasen S, Bright NA, Pierre F, Kelly BT, Kladt N, Schauss

A, Merrifield CJ, Stamou D, Höning S, Owen DJ. CALM Regulates Clathrin-Coated Vesicle Size and Maturation by Directly Sensing and Driving Membrane Curvature. Dev Cell. 2015;33(2):163–75. DOI: 10.1016/j.devcel.2015.03.002.

20. Traub LM. Regarding the amazing choreography of clathrin coats. PLoS Biol. 2011;9(3):e1001037. DOI: 10.1371/journal.pbio.1001037.

21. Mettlen M, Chen P-H, Srinivasan S, Danuser G, Schmid SL. Regulation of Clathrin-Mediated Endocytosis. Annu Rev Biochem. 2018;87(1):871–96. DOI: 10.1146/annurev-biochem-062917-012644.

22. Merrifield CJ, Feldman ME, Wan L, Almers W. Imaging actin and dynamin recruitment during invagination of single clathrin-coated pits. Nat Cell Biol. 2002;4(9):691–8. DOI: 10.1038/ncb837.

23. Taylor MJ, Perrais D, Merrifield CJ. A high precision survey of the molecular dynamics of mammalian clathrin-mediated endocytosis. Schmid SL, editor. PLoS Biol. 2011;9(3):e1000604. DOI: 10.1371/journal.pbio.1000604.

24. Tonikian R, Xin X, Toret CP, Gfeller D, Landgraf C, Panni S, et al. Bayesian modeling of the yeast SH3 domain interactome predicts spatiotemporal dynamics of endocytosis proteins. Walhout M, editor. PLoS Biol. 2009;7(10):e1000218. DOI: 10.1371/journal.pbio.1000218.

25. Kadlecova Z, Spielman SJ, Loerke D, Mohanakrishnan A, Reed DK, Schmid SL. Regulation of clathrin-mediated endocytosis by hierarchical allosteric activation of AP2. J Cell Biol. 2017;216(1):167–79. DOI: 10.1083/jcb.201608071.

26. Maldonado-Báez L, Wendland B. Endocytic adaptors: recruiters, coordinators and regulators [Internet]. Vol. 16, Trends in Cell Biology. 2006. p. 505–13. DOI: 10.1016/j.tcb.2006.08.001.

27. Smith SM, Baker M, Halebian M, Smith CJ. Weak molecular interactions in clathrin-mediated endocytosis. Front Mol Biosci. 2017;4(72). DOI: 10.3389/fmolb.2017.00072.

28. Baschieri F, Porshneva K, Montagnac G. Frustrated clathrin-mediated endocytosis – causes and possible functions. J Cell Sci. 2020;133(11). DOI: 10.1242/jcs.240861.

29. Stabley DR, Jurchenko C, Marshall SS, Salaita KS. Visualizing mechanical tension across membrane receptors with a fluorescent sensor. Nat Methods. 2012;9(1):64–7. DOI: 10.1038/nmeth.1747.

30. Haucke V, Kozlov MM. Membrane remodeling in clathrin-mediated endocytosis. J Cell Sci. 2018;131(17):jcs216812. DOI: 10.1242/jcs.216812.

31. Henne WM, Boucrot E, Meinecke M, Evergren E, Vallis Y, Mittal R, McMahon HT. FCHo proteins are nucleators of Clathrin-Mediated endocytosis. Science (80-). 2010;328(5983):1281–4. DOI: 10.1126/science.1188462.

32. Cocucci E, Aguet F, Boulant S, Kirchhausen T. The first five seconds in the life of a clathrin-coated pit. Cell. 2012;150(3):495–507. DOI: 10.1016/j.cell.2012.05.047.

33. Antonescu CN, Aguet F, Danuser G, Schmid SL. Phosphatidylinositol-(4,5)-bisphosphate regulates clathrin-coated pit initiation, stabilization, and size. Gruenberg JE, editor. Mol Biol Cell. 2011;22(14):2588–600. DOI: 10.1091/mbc.e11-04-0362.

34. Zoncu R, Perera RM, Sebastian R, Nakatsu F, Chen H, Balla T, Ayala G, Toomre D, De Camilli P V. Loss of endocytic clathrin-coated pits upon acute depletion of phosphatidylinositol 4,5-bisphosphate. Proc Natl Acad Sci U S A. 2007;104(10):3793–8. DOI: 10.1073/pnas.0611733104.

35. Morris KL, Jones JR, Halebian M, Wu S, Baker M, Armache J-P, Avila Ibarra A, Sessions RB, Cameron AD, Cheng Y, Smith CJ. Cryo-EM of multiple cage architectures reveals a universal mode of clathrin self-assembly. Nat Struct Mol Biol. 2019;26(10):890–8. DOI: 10.1038/s41594-019-0292-0.

36. Frost A, Perera R, Roux A, Spasov K, Destaing O, Egelman EH, De Camilli P, Unger VM. Structural Basis of Membrane Invagination by F-

BAR Domains. Cell. 2008;132(5):807–17. DOI: 10.1016/j.cell.2007.12.041.

37. Habermann B. The BAR-domain family of proteins: A case of bending and binding? EMBO Rep. 2004;5(3):250–5. DOI: 10.1038/sj.embor.7400105.

38. Mim C, Cui H, Gawronski-Salerno JA, Frost A, Lyman E, Voth GA, Unger VM. Structural basis of membrane bending by the N-BAR protein endophilin. Cell. 2012;149(1):137–45. DOI: 10.1016/j.cell.2012.01.048.

39. Antonny B, Burd C, De Camilli P, Chen E, Daumke O, Faelber K, et al. Membrane fission by dynamin: what we know and what we need to know. EMBO J. 2016;35(21):2270–84. DOI: 10.15252/embj.201694613.

40. Barouch W, Prasad K, Greene L, Eisenberg E. Auxilin-Induced Interaction of the Molecular Chaperone Hsc70 with Clathrin Baskets. Biochemistry. 1997;36(14):4303–8. DOI: 10.1021/bi962727z.

41. Young A, Stoilova-McPhie S, Rothnie A, Vallis Y, Harvey-Smith P, Ranson N, Kent H, Brodsky FM, Pearse BMF, Roseman A, Smith CJ. Hsc70-induced Changes in Clathrin-Auxilin Cage Structure Suggest a Role for Clathrin Light Chains in Cage Disassembly. Traffic. 2013;14(9):987–96. DOI: 10.1111/tra.12085.

42. Packschies L, Theyssen H, Buchberger A, Bukau B, Goody R, Reinstein J. GrpE accelerates nucleotide exchange of the molecular chaperone DnaK with an associative displacement mechanism. Biochemistry. 1997;36(12):3417–22. DOI: 10.1021/bi962835l.

43. McCarty JS, Buchberger A, Reinstein J, Bukau B. The Role of ATP in the Functional Cycle of the DnaK Chaperone System. J Mol Biol. 1995;249(1):126–37. DOI: 10.1006/jmbi.1995.0284.

44. Takeda S, McKay DB. Kinetics of Peptide Binding to the Bovine 70 kDa Heat Shock Cognate Protein, a Molecular Chaperone †. Biochemistry. 1996;35(14):4636–44. DOI: 10.1021/bi952903o.

45. Theyssen H, Schuster H-P, Packschies L, Bukau B, Reinstein J. The

Second Step of ATP Binding to DnaK Induces Peptide Release. J Mol Biol. 1996;263(5):657–70. DOI: 10.1006/jmbi.1996.0606.

46. Morgan JR, Jiang J, Oliphint PA, Jin S, Gimenez LE, Busch DJ, Foldes AE, Zhuo Y, Sousa R, Lafer EM. A Role for an Hsp70 Nucleotide Exchange Factor in the Regulation of Synaptic Vesicle Endocytosis. J Neurosci. 2013;33(18):8009. DOI: 10.1523/jneurosci.4505-12.2013.

47. Ma L, Umasankar PK, Wrobel AG, Lymar A, McCoy AJ, Holkar SS, Jha A, Pradhan-Sundd T, Watkins SC, Owen DJ, Traub LM. Transient Fcho1/2·Eps15/R·AP-2 Nanoclusters Prime the AP-2 Clathrin Adaptor for Cargo Binding. Dev Cell. 2015;37(5):428–43. DOI: 10.1016/j.devcel.2016.05.003.

48. Umasankar PK, Sanker S, Thieman JR, Chakraborty S, Wendland B, Tsang M, Traub LM. Distinct and separable activities of the endocytic clathrin-coat components Fcho1/2 and AP-2 in developmental patterning. Nat Cell Biol. 2012;14(5):488–501. DOI: 10.1038/ncb2473.

49. Stimpson HEM, Toret CP, Cheng AT, Pauly BS, Drubin DG. Early-arriving Syp1p and Ede1p function in endocytic site placement and formation in budding yeast. Schmid SL, editor. Mol Biol Cell. 2009;20(22):4640–51. DOI: 10.1091/mbc.e09-05-0429.

50. Brach T, Godlee C, Moeller-Hansen I, Boeke D, Kaksonen M. The initiation of clathrin-mediated endocytosis is mechanistically highly flexible. Curr Biol. 2014;24(5):548–54. DOI: 10.1016/j.cub.2014.01.048.

51. Twyman RM. Clathrin and Clathrin-Adaptors. Encycl Neurosci. 2009;1013–7. DOI: 10.1016/b978-008045046-9.01364-4.

52. Ehrlich M, Boll W, Van Oijen A, Hariharan R, Chandran K, Nibert ML, Kirchhausen T. Endocytosis by random initiation and stabilization of clathrin-coated pits. Cell. 2004;118(5):591–605. DOI: 10.1016/j.cell.2004.08.017.

53. Owen DJ, Collins BM, Evans PR. ADAPTORS FOR CLATHRIN COATS: Structure and Function. Annu Rev Cell Dev Biol. 2004;20(1):153–91.

DOI: 10.1146/annurev.cellbio.20.010403.104543.

54. Brown MS, Goldstein JL. Receptor-mediated endocytosis: insights from the lipoprotein receptor system. Proc Natl Acad Sci. 1979;76(7):3330–7. DOI: 10.1073/pnas.76.7.3330.

55. Traub LM. Tickets to ride: Selecting cargo for clathrin-regulated internalization [Internet]. Vol. 10, Nature Reviews Molecular Cell Biology. Nature Publishing Group; 2009. p. 583–96. DOI: 10.1038/nrm2751.

56. Liu AP, Aguet F, Danuser G, Schmid SL. Local clustering of transferrin receptors promotes clathrin-coated pit initiation. J Cell Biol. 2010;191(7):1381–93. DOI: 10.1083/jcb.201008117.

57. Kibbey RG, Rizo J, Gierasch LM, Anderson RG. The LDL receptor clustering motif interacts with the clathrin terminal domain in a reverse turn conformation. J Cell Biol. 1998;142(1):59–67. DOI: 10.1083/jcb.142.1.59.

58. Henry AG, Hislop JN, Grove J, Thorn K, Marsh M, von Zastrow M. Regulation of Endocytic Clathrin Dynamics by Cargo Ubiquitination. Dev Cell. 2012;23(3):519–32. DOI: 10.1016/j.devcel.2012.08.003.

59. Nunez D, Antonescu C, Mettlen M, Liu A, Schmid SL, Loerke D, Danuser G. Hotspots Organize Clathrin-Mediated Endocytosis by Efficient Recruitment and Retention of Nucleating Resources. Traffic. 2011;12(12):1868–78. DOI: 10.1111/j.1600-0854.2011.01273.x.

60. Merrifield CJ, Perrais D, Zenisek D. Coupling between clathrin-coated-pit invagination, cortactin recruitment, and membrane scission observed in live cells. Cell. 2005;121(4):593–606. DOI: 10.1016/j.cell.2005.03.015.

61. Layton AT, Savage NS, Howell AS, Carroll SY, Drubin DG, Lew DJ. Modeling vesicle traffic reveals unexpected consequences for Cdc42p-mediated polarity establishment. Curr Biol. 2011;21(3):184–94. DOI: 10.1016/j.cub.2011.01.012.

62. Loerke D, Mettlen M, Yarar D, Jaqaman K, Jaqaman H, Danuser G, Schmid SL. Cargo and dynamin regulate clathrin-coated pit maturation. Hughson F, editor. PLoS Biol. 2009;7(3):0628–39. DOI: 10.1371/journal.pbio.1000057.

63. Carroll SY, Stimpson HEM, Weinberg J, Toret CP, Sun Y, Drubin DG. Analysis of yeast endocytic site formation and maturation through a regulatory transition point. Schmid SL, editor. Mol Biol Cell. 2012;23(4):657–68. DOI: 10.1091/mbc.e11-02-0108.

64. Mettlen M, Loerke D, Yarar D, Danuser G, Schmid SL. Cargo- and adaptor-specific mechanisms regulate clathrin-mediated endocytosis. J Cell Biol. 2010;188(6):919–33. DOI: 10.1083/jcb.200908078.

65. Mettlen M, Stoeber M, Loerke D, Antonescu CN, Danuser G, Schmid SL. Endocytic accessory proteins are functionally distinguished by their differential effects on the maturation of clathrin-coated pits. Lemmon S, editor. Mol Biol Cell. 2009;20(14):3251–60. DOI: 10.1091/mbc.e09-03-0256.

66. Sochacki KA, Dickey AM, Strub MP, Taraska JW. Endocytic proteins are partitioned at the edge of the clathrin lattice in mammalian cells. Nat Cell Biol. 2017;19(4):352–61. DOI: 10.1038/ncb3498.

67. Nossal R. Energetics of clathrin basket assembly. Traffic. 2001;2(2):138–47. DOI: 10.1034/j.1600-0854.2001.020208.x.

68. Kirchhausen T. Coated pits and coated vesicles - sorting it all out. Curr Opin Struct Biol. 1993;3(2):182–8. DOI: 10.1016/s0959-440x(05)80150-2.

69. Heuser J, Evans L. Three-dimensional visualization of coated vesicle formation in fibroblasts. J Cell Biol. 1980;84(3):560–83. DOI: 10.1083/jcb.84.3.560.

70. Avinoam O, Schorb M, Beese CJ, Briggs JAG, Kaksonen M. Endocytic sites mature by continuous bending and remodeling of the clathrin coat. Science (80-). 2015;348(6241):1369–72. DOI: 10.1126/science.aaa9555.

71. Saleem M, Morlot S, Hohendahl A, Manzi J, Lenz M, Roux A. A balance between membrane elasticity and polymerization energy sets the shape of spherical clathrin coats. Nat Commun. 2015;6(6249). DOI: 10.1038/ncomms7249.

72. Boulant S, Kural C, Zeeh JC, Ubelmann F, Kirchhausen T. Actin dynamics counteract membrane tension during clathrin-mediated endocytosis. Nat Cell Biol. 2011;13(9):1124–32. DOI: 10.1038/ncb2307.

73. Ford MGJ, Mills IG, Peter BJ, Vallis Y, Praefcke GJK, Evans PR, McMahon HT. Curvature of clathrin-coated pits driven by epsin. Nature. 2002;419(6905):361–6. DOI: 10.1038/nature01020.

74. Dannhauser PN, Platen M, Böning H, Ungewickell H, Schaap IAT, Ungewickell EJ. Effect of Clathrin Light Chains on the Stiffness of Clathrin Lattices and Membrane Budding. Traffic. 2015;16(5):519–33. DOI: 10.1111/tra.12263.

75. Massol RH, Boll W, Griffin AM, Kirchhausen T. A burst of auxilin recruitment determines the onset of clathrin-coated vesicle uncoating. Proc Natl Acad Sci U S A. 2006;103(27):10265–70. DOI: 10.1073/pnas.0603369103.

76. Schlossman DM, Schmid SL, Braell WA, Rothman JE. An enzyme that removes clathrin coats: Purification of an uncoating ATPase. J Cell Biol. 1984;99(2):723–33. DOI: 10.1083/jcb.99.2.723.

77. Wu X, Zhao X, Baylor L, Kaushal S, Eisenberg E, Greene LE. Clathrin exchange during clathrin-mediated endocytosis. J Cell Biol. 2001;155(2):291–300. DOI: 10.1083/jcb.200104085.

78. Loerke D, Wienisch M, Kochubey O, Klingauf J. Differential control of clathrin subunit dynamics measured with EW-FRAP microscopy. Traffic. 2005;6(10):918–29. DOI: 10.1111/j.1600-0854.2005.00329.x.

79. Sousa R, Liao HS, Cuéllar J, Jin S, Valpuesta JM, Jin AJ, Lafer EM. Clathrin-coat disassembly illuminates the mechanisms of Hsp70 force generation. Nat Struct Mol Biol. 2016;23(9):821–9. DOI:

10.1038/nsmb.3272.

80. Ayscough KR, Stryker J, Pokala N, Sanders M, Crews P, Drubin DG. High rates of actin filament turnover in budding yeast and roles for actin in establishment and maintenance of cell polarity revealed using the actin inhibitor latrunculin-A. J Cell Biol. 1997;137(2):399–416. DOI: 10.1083/jcb.137.2.399.

81. Fujimoto LM, Roth R, Heuser JE, Schmid SL. Actin Assembly Plays a Variable, but not Obligatory Role in Receptor-Mediated Endocytosis. Traffic. 2000;1(2):161–71. DOI: 10.1034/j.1600-0854.2000.010208.x.

82. Lamaze C, Fujimoto LM, Yin HL, Schmid SL. The actin cytoskeleton is required for receptor-mediated endocytosis in mammalian cells. J Biol Chem. 1997;272(33):20332–5. DOI: 10.1074/jbc.272.33.20332.

83. Grassart A, Cheng AT, Hong SH, Zhang F, Zenzer N, Feng Y, Briner DM, Davis GD, Malkov D, Drubin DG. Actin and dynamin2 dynamics and interplay during clathrin-mediated endocytosis. J Cell Biol. 2014;205(5):721–35. DOI: 10.1083/jcb.201403041.

84. Li D, Shao L, Chen B-C, Zhang X, Zhang M, Moses B, Milkie DE, Beach JR, Hammer JA, Pasham M, Kirchhausen T, Baird MA, Davidson MW, Xu P, Betzig E. Extended-resolution structured illumination imaging of endocytic and cytoskeletal dynamics. Science. 2015;349(6251):aab3500. DOI: 10.1126/science.aab3500.

85. Picco A, Mund M, Ries J, Nédélec F, Kaksonen M. Visualizing the functional architecture of the endocytic machinery. Elife. 2015;4:e04535. DOI: 10.7554/elife.04535.

86. Collins A, Warrington A, Taylor KA, Svitkina T. Structural organization of the actin cytoskeleton at sites of clathrin-mediated endocytosis. Curr Biol. 2011;21(14):1167–75. DOI: 10.1016/j.cub.2011.05.048.

87. Goode BL, Eskin JA, Wendland B. Actin and endocytosis in budding yeast. Genetics. 2014;199(2):315–58. DOI: 10.1534/genetics.112.145540.

88. Engqvist-Goldstein ÅEY, Zhang CX, Carreno S, Barroso C, Heuser JE, Drubin DG. RNAi-mediated Hip1R Silencing Results in Stable Association between the Endocytic Machinery and the Actin Assembly Machinery. Mol Biol Cell. 2004;15(4):1666–79. DOI: 10.1091/mbc.e03-09-0639.

89. Messa M, Fernández-Busnadiego R, Sun EW, Chen H, Czapla H, Wrasman K, Wu Y, Ko G, Ross T, Wendland B, De Camilli P. Epsin deficiency impairs endocytosis by stalling the actin-dependent invagination of endocytic clathrin-coated pits. Elife. 2014;3:e03311. DOI: 10.7554/elife.03311.

90. Skruzny M, Brach T, Ciuffa R, Rybina S, Wachsmuth M, Kaksonen M. Molecular basis for coupling the plasma membrane to the actin cytoskeleton during clathrin-mediated endocytosis. Proc Natl Acad Sci U S A. 2012;109(38):E2533-42. DOI: 10.1073/pnas.1207011109.

91. Skruzny M, Desfosses A, Prinz S, Dodonova SO, Gieras A, Uetrecht C, Jakobi AJ, Abella M, Hagen WJH, Schulz J, Meijers R, Rybin V, Briggs JAG, Sachse C, Kaksonen M. An Organized Co-assembly of Clathrin Adaptors Is Essential for Endocytosis. Dev Cell. 2015;33(2):150–62. DOI: 10.1016/j.devcel.2015.02.023.

92. Carlsson AE, Bayly P V. Force generation by endocytic actin patches in budding yeast. Biophys J. 2014;106(8):1596–606. DOI: 10.1016/j.bpj.2014.02.035.

93. Dmitrieff S, Nédélec F. Membrane Mechanics of Endocytosis in Cells with Turgor. Ewers H, editor. PLoS Comput Biol. 2015;11(10):e1004538. DOI: 10.1371/journal.pcbi.1004538.

94. Wilbur JD, Chen C-Y, Manalo V, Hwang PK, Fletterick RJ, Brodsky FM. Actin Binding by Hip1 (Huntingtin-interacting Protein 1) and Hip1R (Hip1-related Protein) Is Regulated by Clathrin Light Chain. J Biol Chem. 2008;283(47):32870–9. DOI: 10.1074/jbc.m802863200.

95. Bashkirov P V, Akimov SA, Evseev AI, Schmid SL, Zimmerberg J, Frolov

VA. GTPase Cycle of Dynamin Is Coupled to Membrane Squeeze and Release, Leading to Spontaneous Fission. Cell. 2008;135(7):1276–86. DOI: 10.1016/j.cell.2008.11.028.

96. Daumke O, Roux A, Haucke V. BAR domain scaffolds in dynamin-mediated membrane fission [Internet]. Vol. 156, Cell. Elsevier; 2014. p. 882–92. DOI: 10.1016/j.cell.2014.02.017.

97. Pucadyil TJ, Schmid SL. Real-Time Visualization of Dynamin-Catalyzed Membrane Fission and Vesicle Release. Cell. 2008;135(7):1263–75. DOI: 10.1016/j.cell.2008.11.020.

98. Morlot S, Roux A. Mechanics of dynamin-mediated membrane fission. Annu Rev Biophys. 2013;42:629–49. DOI: 10.1146/annurev-biophys-050511-102247.

99. Ingerman E, Perkins EM, Marino M, Mears JA, McCaffery JM, Hinshaw JE, Nunnari J. Dnm1 forms spirals that are structurally tailored to fit mitochondria. J Cell Biol. 2005;170(7):1021–7. DOI: 10.1083/jcb.200506078.

100. Miserey-Lenkei S, Chalancon G, Bardin S, Formstecher E, Goud B, Echard A. Rab and actomyosin-dependent fission of transport vesicles at the Golgi complex. Nat Cell Biol. 2010;12(7):645–54. DOI: 10.1038/ncb2067.

101. Slepnev VI, De Camilli P. Accessory factors in clathrin-dependent synaptic vesicle endocytosis. Nat Rev Neurosci. 2000;1(3):161–72. DOI: 10.1038/35044540.

102. Itoh T, Erdmann KS, Roux A, Habermann B, Werner H, De Camilli P. Dynamin and the actin cytoskeleton cooperatively regulate plasma membrane invagination by BAR and F-BAR proteins. Dev Cell. 2005;9(6):791–804. DOI: 10.1016/j.devcel.2005.11.005.

103. Meinecke M, Boucrot E, Camdere G, Hon W-C, Mittal R, McMahon HT. Cooperative recruitment of dynamin and BIN/amphiphysin/Rvs (BAR) domain-containing proteins leads to GTP-dependent membrane scission.

J Biol Chem. 2013;288(9):6651–61. DOI: 10.1074/jbc.m112.444869.

104. Schöneberg J, Lehmann M, Ullrich A, Posor Y, Lo WT, Lichtner G, Schmoranzer J, Haucke V, Noé F. Lipid-mediated PX-BAR domain recruitment couples local membrane constriction to endocytic vesicle fission. Nat Commun. 2017;8(1):15873. DOI: 10.1038/ncomms15873.

105. Wu M, Huang B, Graham M, Raimondi A, Heuser JE, Zhuang X, De Camilli P. Coupling between clathrin-dependent endocytic budding and F-BAR-dependent tubulation in a cell-free system. Nat Cell Biol. 2010;12(9):902–8. DOI: 10.1038/ncb2094.

106. Nández R, Balkin DM, Messa M, Liang L, Paradise S, Czapla H, Hein MY, Duncan JS, Mann M, De Camilli P. A role of OCRL in clathrin-coated pit dynamics and uncoating revealed by studies of Lowe syndrome cells. Elife. 2014;3:e02975. DOI: 10.7554/elife.02975.

107. Fotin A, Cheng Y, Grigorieff N, Walz T, Harrison SC, Kirchhausen T. Structure of an auxilin-bound clathrin coat and its implications for the mechanism of uncoating. Nature. 2004;432(7017):649–53. DOI: 10.1038/nature03078.

108. Ahle S, Ungewickell E. Auxilin, a newly identified clathrin-associated protein in coated vesicles from bovine brain. J Cell Biol. 1990;111(1):19–29. DOI: 10.1083/jcb.111.1.19.

109. Schroder S, Morris SA, Knorr R, Plessmann U, Weber K, Vinh NG, Ungewickell E. Primary Structure of the Neuronal Clathrin-Associated Protein Auxilin and its Expression in Bacteria. Eur J Biochem. 1995;228(2):297–304. DOI: 10.1111/j.1432-1033.1995.0297n.x.

110. Ungewickell E, Ungewickell H, Holstein SEH, Lindner R, Prasad K, Barouch W, Martini B, Greene LE, Eisenberg E. Role of auxilin in uncoating clathrin-coated vesicles. Nature. 1995;378(6557):632–5. DOI: 10.1038/378632a0.

111. Holstein SE, Ungewickell H, Ungewickell E. Mechanism of clathrin basket dissociation: separate functions of protein domains of the DnaJ

homologue auxilin. J Cell Biol. 1996;135(4):925–37. DOI: 10.1083/jcb.135.4.925.

112. Ungewickell E. The 70-kd mammalian heat shock proteins are structurally and functionally related to the uncoating protein that releases clathrin triskelia from coated vesicles. EMBO J. 1985;4(13A):3385–91. DOI: 10.1002/j.1460-2075.1985.tb04094.x.

113. Braell WA, Schlossman DM, Schmid SL, Rothman JE. Dissociation of clathrin coats coupled to the hydrolysis of ATP: Role of an uncoating ATPase. J Cell Biol. 1984;99(2):735–41. DOI: 10.1083/jcb.99.2.734.

114. McPherson PS, Garcia EP, Slepnev VI, David C, Zhang X, Grabs D, Sossin WS, Bauerfeind R, Nemoto Y, De Camilli P. A presynaptic inositol-5-phosphatase. Nature. 1996;379(6563):353–7. DOI: 10.1038/379353a0.

115. Cremona O, Di Paolo G, Wenk MR, Lüthi A, Kim WT, Takei K, Daniell L, Nemoto Y, Shears SB, Flavell RA, McCormick DA, De Camilli P. Essential role of phosphoinositide metabolism in synaptic vesicle recycling. Cell. 1999;99(2):179–88. DOI: 10.1016/s0092-8674(00)81649-9.

116. Kalli AC, Morgan G, Sansom MSP. Interactions of the Auxilin-1 PTEN-like Domain with Model Membranes Result in Nanoclustering of Phosphatidyl Inositol Phosphates. Biophys J. 2013;105(1):137–45. DOI: 10.1016/j.bpj.2013.05.012.

117. Park B-C, Yim Y-I, Zhao X, Olszewski MB, Eisenberg E, Greene LE. The clathrin-binding and J-domains of GAK support the uncoating and chaperoning of clathrin by Hsc70 in the brain. J Cell Sci. 2015;128(20):3811–21. DOI: 10.1242/jcs.171058.

118. Rothnie A, Clarke AR, Kuzmic P, Cameron A, Smith CJ. A sequential mechanism for clathrin cage disassembly by 70-kDa heat-shock cognate protein (Hsc70) and auxilin. Proc Natl Acad Sci U S A. 2011;108(17):6927–32. DOI: 10.1073/pnas.1018845108.

119. Barouch W, Prasad K, Greene LE, Eisenberg E. ATPase activity

associated with the uncoating of clathrin baskets by Hsp70. J Biol Chem. 1994;269(46):28563–8.

120. Greene MK, Maskos K, Landry SJ. Role of the J-domain in the cooperation of Hsp40 with Hsp70. Proc Natl Acad Sci. 1998;95(11):6108–13. DOI: 10.1073/pnas.95.11.6108.

121. Xue Y-L, Zhou L, Sun Y, Li H, Jones GW, Song Y. Steered molecular dynamics simulation of the binding of the bovine auxilin J domain to the Hsc70 nucleotide-binding domain. J Mol Model. 2017;23(320). DOI: 10.1007/s00894-017-3453-2.

122. Rapoport I, Boll W, Yu A, Böcking T, Kirchhausen T. A Motif in the Clathrin Heavy Chain Required for the Hsc70/Auxilin Uncoating Reaction. Mol Biol Cell. 2008;19(1):405–13. DOI: 10.1091/mbc.e07-09-0870.

123. Xing Y, Böcking T, Wolf M, Grigorieff N, Kirchhausen T, Harrison SC. Structure of clathrin coat with bound Hsc70 and auxilin: mechanism of Hsc70-facilitated disassembly. EMBO J. 2010;29(3):655–65. DOI: 10.1038/emboj.2009.383.

124. Sousa R, Lafer EM. The role of molecular chaperones in clathrin mediated vesicular trafficking. Front Mol Biosci. 2015;2(26). DOI: 10.3389/fmolb.2015.00026.

125. Böcking T, Aguet F, Rapoport I, Banzhaf M, Yu A, Zeeh JC, Kirchhausen T. Key Interactions for Clathrin Coat Stability. Structure. 2014;22(6):819–29. DOI: 10.1016/j.str.2014.04.002.

126. Sousa R. Structural mechanisms of chaperone mediated protein disaggregation. Front Mol Biosci. 2014;1(12). DOI: 10.3389/fmolb.2014.00012.

127. Sousa R, Lafer EM. The Physics of Entropic Pulling: A Novel Model for the Hsp70 Motor Mechanism. Int J Mol Sci. 2019;20(9). DOI: 10.3390/ijms20092334.

128. Goloubinoff P, Rios PDL. The mechanism of Hsp70 chaperones: (entropic) pulling the models together. Trends Biochem Sci. 2007;32(8):372–80. DOI: 10.1016/j.tibs.2007.06.008.

129. Rios PDL, Ben-Zvi A, Slutsky O, Azem A, Goloubinoff P. Hsp70 chaperones accelerate protein translocation and the unfolding of stable protein aggregates by entropic pulling. Proc Natl Acad Sci. 2006;103(16):6166–71. DOI: 10.1073/pnas.0510496103.

130. Böcking T, Aguet F, Harrison SC, Kirchhausen T. Single-molecule analysis of a molecular disassemblase reveals the mechanism of Hsc70-driven clathrin uncoating. Nat Struct Mol Biol. 2011;18(3):295–301. DOI: 10.1038/nsmb.1985.

131. Ferreira F, Foley M, Cooke A, Cunningham M, Smith G, Woolley R, Henderson G, Kelly E, Mundell S, Smythe E. Endocytosis of G Protein-Coupled Receptors Is Regulated by Clathrin Light Chain Phosphorylation. Curr Biol. 2012;22(15):1361–70. DOI: 10.1016/j.cub.2012.05.034.

132. He K, Song E, Upadhyayula S, Dang S, Gaudin R, Skillern W, Bu K, Capraro BR, Rapoport I, Kusters I, Ma M, Kirchhausen T. Dynamics of Auxilin 1 and GAK in clathrin-mediated traffic. J Cell Biol. 2020;219(3). DOI: 10.1083/jcb.201908142.

133. Krantz KC, Puchalla J, Thapa R, Kobayashi C, Bisher M, Viehweg J, Carr CM, Rye HS. Clathrin Coat Disassembly by the Yeast Hsc70/Ssa1p and Auxilin/Swa2p Proteins Observed by Single-particle Burst Analysis Spectroscopy. J Biol Chem. 2013;288(37):26721. DOI: 10.1074/jbc.m113.491753.

134. Edvardson S, Cinnamon Y, Ta-Shma A, Shaag A, Yim YI, Zenvirt S, Jalas C, Lesage S, Brice A, Taraboulos A, Kaestner KH, Greene LE, Elpeleg O. A deleterious mutation in DNAJC6 encoding the neuronal-specific clathrin-uncoating Co-chaperone auxilin, is associated with juvenile parkinsonism. Wider C, editor. PLoS One. 2012;7(5):e36458.

DOI: 10.1371/journal.pone.0036458.

135. Vilariño-Güell C, Rajput A, Milnerwood AJ, Shah B, Szu-Tu C, Trinh J, et al. DNAJC13 mutations in Parkinson disease. Hum Mol Genet. 2014;23(7):1794–801. DOI: 10.1093/hmg/ddt570.

136. Song L, He Y, Ou J, Zhao Y, Li R, Cheng J, Lin CH, Ho MS. Auxilin Underlies Progressive Locomotor Deficits and Dopaminergic Neuron Loss in a Drosophila Model of Parkinson's Disease. Cell Rep. 2017;18(5):1132–43. DOI: 10.1016/j.celrep.2017.01.005.

137. Nguyen M, Krainc D. LRRK2 phosphorylation of auxilin mediates synaptic defects in dopaminergic neurons from patients with Parkinson's disease. Proc Natl Acad Sci U S A. 2018;115(21):5576–81. DOI: 10.1073/pnas.1717590115.

138. Cao M, Wu Y, Ashrafi G, McCartney AJ, Wheeler H, Bushong EA, Boassa D, Ellisman MH, Ryan TA, De Camilli P. Parkinson Sac Domain Mutation in Synaptojanin 1 Impairs Clathrin Uncoating at Synapses and Triggers Dystrophic Changes in Dopaminergic Axons. Neuron. 2017;93(4):882-896.e5. DOI: 10.1016/j.neuron.2017.01.019.

139. Chen XQ, Mobley WC. Alzheimer disease pathogenesis: Insights from molecular and cellular biology studies of oligomeric Aß and tau species [Internet]. Vol. 13, Frontiers in Neuroscience. 2019. p. 659. DOI: 10.3389/fnins.2019.00659.

140. Ponomareva N V., Andreeva T V., Protasova MA, Filippova Y V., Kolesnikova EP, Fokin VF, Illarioshkin SN, Rogaev EI. Genetic Association between Alzheimer's Disease Risk Variant of the PICALM Gene and Auditory Event-Related Potentials in Aging. Biochem. 2018;83(9):1075–82. DOI: 10.1134/s0006297918090092.

141. Thomas RS, Henson A, Gerrish A, Jones L, Williams J, Kidd EJ. Decreasing the expression of PICALM reduces endocytosis and the activity of ß-secretase: Implications for Alzheimer's disease. BMC Neurosci. 2016;17(1):50. DOI: 10.1186/s12868-016-0288-1.

142. Kanatsu K, Hori Y, Takatori S, Watanabe T, Iwatsubo T, Tomita T. Partial loss of CALM function reduces Aβ42 production and amyloid deposition in vivo. Hum Mol Genet. 2016;25(18):3988–97. DOI: 10.1093/hmg/ddw239.

143. Soutar AK, Naoumova RP. Autosomal recessive hypercholesterolemia. Semin Vasc Med. 2004;4(3):241–8. DOI: 10.1055/s-2004-861491.

144. Wei J, Fu ZY, Li PS, Miao HH, Li BL, Ma YT, Song BL. The clathrin adaptor proteins ARH, Dab2, and numb play distinct roles in Niemann-Pick C1-Like 1 versus low density lipoprotein receptor-mediated cholesterol uptake. J Biol Chem. 2014;289(48):33689–700. DOI: 10.1074/jbc.m114.593764.

145. Nahorski MS, Al-Gazali L, Hertecant J, Owen DJ, Borner GHH, Chen Y-C, Benn CL, Carvalho OP, Shaikh SS, Phelan A, Robinson MS, Royle SJ, Woods CG. A novel disorder reveals clathrin heavy chain-22 is essential for human pain and touch development. Brain. 2015;138(8):2147–60. DOI: 10.1093/brain/awv149.

146. Kirchhausen T, Harrison SC. Protein organization in clathrin trimers. Cell. 1981;23(3):755–61. DOI: 10.1016/0092-8674(81)90439-6.

147. Ungewickell E, Branton D. Assembly units of clathrin coats. Nature. 1981;289(5796):420–2. DOI: 10.1038/289420a0.

148. Fotin A, Cheng Y, Sliz P, Grigorieff N, Harrison SC, Kirchhausen T, Walz T. Molecular model for a complete clathrin lattice from electron cryomicroscopy. Nature. 2004;432(7017):573–9. DOI: 10.1038/nature03079.

149. Chen CY, Reese ML, Hwang PK, Ota N, Agard D, Brodsky FM. Clathrin light and heavy chain interface: α-helix binding superhelix loops via critical tryptophans. EMBO J. 2002;21(22):6072–82. DOI: 10.1093/emboj/cdf594.

150. Kirchhausen T, Scarmato P, Harrison SC, Monroe JJ, Chow EP, Mattaliano RJ, Ramachandran KL, Smart JE, Ahn AH, Brosius J.

Clathrin light chains LCA and LCB are similar, polymorphic, and share repeated heptad motifs. Science (80-). 1987;236(4799):320–4. DOI: 10.1126/science.3563513.

151. Kirchhausen T, Toyoda T. Immunoelectron microscopic evidence for the extended conformation of light chains in clathrin trimers. J Biol Chem. 1993;268(14):10268–73.

152. Cheng Y, Boll W, Kirchhausen T, Harrison SC, Walz T. Cryo-electron Tomography of Clathrin-coated Vesicles: Structural Implications for Coat Assembly. J Mol Biol. 2007;365(3):892–9. DOI: 10.1016/j.jmb.2006.10.036.

153. Heymann JB, Winkler DC, Yim Y-I, Eisenberg E, Greene LE, Steven AC. Clathrin-coated vesicles from brain have small payloads: a cryo-electron tomographic study. J Struct Biol. 2013;184(1):43–51. DOI: 10.1016/j.jsb.2013.05.006.

154. Turkewitz AP, Harrison SC. Concentration of transferrin receptor in human placental coated vesicles. J Cell Biol. 1989;108(6):2127–35. DOI: 10.1083/jcb.108.6.2127.

155. Smith CJ, Grigorieff N, Pearse BMF. Clathrin coats at 21 Å resolution: A cellular assembly designed to recycle multiple membrane receptors. EMBO J. 1998;17(17):4943–53. DOI: 10.1093/emboj/17.17.4943.

156. Ter Haar E, Musacchio A, Harrison SC, Kirchhausen T. Atomic structure of clathrin: A β propeller terminal domain joins an α zigzag linker. Cell. 1998;95(4):563–73. DOI: 10.1016/s0092-8674(00)81623-2.

157. Muenzner J, Traub LM, Kelly BT, Graham SC. Cellular and viral peptides bind multiple sites on the N-terminal domain of clathrin. Traffic. 2017;18(1):44–57. DOI: 10.1111/tra.12457.

158. Kang DS, Kern RC, Puthenveedu MA, von Zastrow M, Williams JC, Benovic JL. Structure of an arrestin2-clathrin complex reveals a novel clathrin binding domain that modulates receptor trafficking. J Biol Chem. 2009;284(43):29860–72. DOI: 10.1074/jbc.m109.023366.

159. Miele AE, Watson PJ, Evans PR, Traub LM, Owen DJ. Two distinct interaction motifs in amphiphysin bind two independent sites on the clathrin terminal domain β-propeller. Nat Struct Mol Biol. 2004;11(3):242–8. DOI: 10.1038/nsmb736.

160. Shih W, Gallusser A, Kirchhausen T. A clathrin-binding site in the hinge of the β2 chain of mammalian AP-2 complexes. J Biol Chem. 1995;270(52):31083–90. DOI: 10.1074/jbc.270.52.31083.

161. Ramjaun AR, McPherson PS. Multiple Amphiphysin II Splice Variants Display Differential Clathrin Binding: Identification of Two Distinct Clathrin-Binding Sites. J Neurochem. 2002;70(6):2369–76. DOI: 10.1046/j.1471-4159.1998.70062369.x.

162. Krupnick JG, Goodman OB, Keen JH, Benovic JL. Arrestin/clathrin interaction. Localization of the clathrin binding domain of nonvisual arrestins to the carboxyl terminus. J Biol Chem. 1997;272(23):15011–6. DOI: 10.1074/jbc.272.23.15011.

163. Dell'Angelica EC, Klumperman J, Stoorvogel W, Bonifacino JS. Association of the AP-3 adaptor complex with clathrin. Science (80-). 1998;280(5362):431–4. DOI: 10.1126/science.280.5362.431.

164. Drake MT, Traub LM. Interaction of Two Structurally Distinct Sequence Types with the Clathrin Terminal Domain β-Propeller. J Biol Chem. 2001;276(31):28700–9. DOI: 10.1074/jbc.m104226200.

165. Ter Haar E, Harrison SC, Kirchhausen T. Peptide-in-groove interactions link target proteins to the beta -propeller of Peptide-in-groove interactions link target proteins to the ␣-propeller of clathrin. Proc Natl Acad Sci U S A. 1999;97(3):1096–100. DOI: 10.1073/pnas.97.3.1096.

166. Willox AK, Sahraoui YME, Royle SJ. Non-specificity of Pitstop 2 in clathrin-mediated endocytosis. Biol Open. 2014;3(5):326–31. DOI: 10.1242/bio.20147955.

167. Zhuo Y, Ilangovan U, Schirf V, Demeler B, Sousa R, Hinck AP, Lafer

EM. Dynamic Interactions between Clathrin and Locally Structured Elements in a Disordered Protein Mediate Clathrin Lattice Assembly. J Mol Biol. 2010;404(2):274–90. DOI: 10.1016/j.jmb.2010.09.044.

168. Schlosshauer M, Baker D. Realistic protein-protein association rates from a simple diffusional model neglecting long-range interactions, free energy barriers, and landscape ruggedness. Protein Sci. 2004;13(6):1660–9. DOI: 10.1110/ps.03517304.

169. Zhuo Y, Cano KE, Wang L, Ilangovan U, Hinck AP, Sousa R, Lafer EM. Nuclear magnetic resonance structural mapping reveals promiscuous interactions between clathrin-box motif sequences and the N-terminal domain of the clathrin heavy chain. Biochemistry. 2015;54(16):2571–80. DOI: 10.1021/acs.biochem.5b00065.

170. Drake MT, Downs MA, Traub LM. Epsin binds to clathrin by associating directly with the clathrin- terminal domain. Evidence for cooperative binding through two discrete sites. J Biol Chem. 2000;275(9):6479–89. DOI: 10.1074/jbc.275.9.6479.

171. Gijsbers A, Nishigaki T, Sánchez-Puig N. Fluorescence Anisotropy as a Tool to Study Protein-protein Interactions. J Vis Exp. 2016;(116). DOI: 10.3791/54640.

172. Helmerhorst E, Chandler DJ, Nussio M, Mamotte CD. Real-time and Label-free Bio-sensing of Molecular Interactions by Surface Plasmon Resonance: A Laboratory Medicine Perspective. Clin Biochem Rev. 2012;33(4):161–73.

173. Smith CJ, Dafforn TR, Kent H, Sims CA, Khubchandani-Aswani K, Zhang L, Saibil HR, Pearse BMF. Location of Auxilin Within a Clathrin Cage. J Mol Biol. 2004;336(2):461–71. DOI: 10.1016/j.jmb.2003.12.006.

174. Kalthoff C, Groos S, Kohl R, Mahrhold S, Ungewickell EJ. Clint: a novel clathrin-binding ENTH-domain protein at the Golgi. Mol Biol Cell. 2002;13(11):4060–73. DOI: 10.1091/mbc.e02-03-0171.

175. Hood FE, Williams SJ, Burgess SG, Richards MW, Roth D, Straube A,

Pfuhl M, Bayliss R, Royle SJ. Coordination of adjacent domains mediates TACC3–ch-TOG–clathrin assembly and mitotic spindle binding. J Cell Biol. 2013;202(3):463–78. DOI: 10.1083/jcb.201211127.

176. Pettersen EF, Goddard TD, Huang CC, Couch GS, Greenblatt DM, Meng EC, Ferrin TE. UCSF Chimera - A visualization system for exploratory research and analysis. J Comput Chem. 2004;25(13):1605–12. DOI: 10.1002/jcc.20084.

177. Nogales E. The development of cryo-EM into a mainstream structural biology technique. Nat Methods. 2016;13(1):24–7. DOI: 10.1038/nmeth.3694.

178. Lyumkis D. Challenges and opportunities in cryo-EM single-particle analysis. J Biol Chem. 2019;294(13):5181–97. DOI: 10.1074/jbc.rev118.005602.

179. Carroni M, Saibil HR. Cryo electron microscopy to determine the structure of macromolecular complexes. Methods. 2016;95:78. DOI: 10.1016/j.ymeth.2015.11.023.

180. Merk A, Bartesaghi A, Banerjee S, Falconieri V, Rao P, Davis MI, Pragani R, Boxer MB, Earl LA, Milne JLS, Subramaniam S. Breaking Cryo-EM Resolution Barriers to Facilitate Drug Discovery. Cell. 2016;165(7):1698–707. DOI: 10.1016/j.cell.2016.05.040.

181. Dubochet J, Adrian M, Chang J-J, Homo J-C, Lepault J, McDowall AW, Schultz P. Cryo-electron microscopy of vitrified specimens. Q Rev Biophys. 1988;21(2):129–228. DOI: 10.1017/s0033583500004297.

182. Kuntsche J, Horst JC, Bunjes H. Cryogenic transmission electron microscopy (cryo-TEM) for studying the morphology of colloidal drug delivery systems. Int J Pharm. 2011;417(1–2):120–37. DOI: 10.1016/j.ijpharm.2011.02.001.

183. Frank J (Joachim). Three-dimensional electron microscopy of macromolecular assemblies. Academic Press; 1996. 342 p.

184. Glaeser RM. Retrospective: Radiation damage and its associated "Information Limitations." J Struct Biol. 2008;163(3):271–6. DOI: 10.1016/j.jsb.2008.06.001.

185. Zheng SQ, Palovcak E, Armache JP, Verba KA, Cheng Y, Agard DA. MotionCor2: Anisotropic correction of beam-induced motion for improved cryo-electron microscopy [Internet]. Vol. 14, Nature Methods. NIH Public Access; 2017. p. 331–2. DOI: 10.1038/nmeth.4193.

186. Zhang K. Gctf: Real-time CTF determination and correction. J Struct Biol. 2016;193(1):1–12. DOI: 10.1016/j.jsb.2015.11.003.

187. Punjani A. Single-particle CryoEM: Data Processing Techniques for Obtaining Optimal Results. Microsc Microanal. 2018;24(S1):2328–9. DOI: 10.1017/s1431927618012126.

188. Fernández JJ, Luque D, Castón JR, Carrascosa JL. Sharpening high resolution information in single particle electron cryomicroscopy. J Struct Biol. 2008;164(1):170–5. DOI: 10.1016/j.jsb.2008.05.010.

189. Ilca SL, Kotecha A, Sun X, Poranen MM, Stuart DI, Huiskonen JT. Localized reconstruction of subunits from electron cryomicroscopy images of macromolecular complexes. Nat Commun. 2015;6(1):8843. DOI: 10.1038/ncomms9843.

190. de la Rosa-Trevín JM, Quintana A, del Cano L, Zaldívar A, Foche I, Gutiérrez J, et al. Scipion: A software framework toward integration, reproducibility and validation in 3D electron microscopy. J Struct Biol. 2016;195(1):93–9. DOI: 10.1016/j.jsb.2016.04.010.

191. Zivanov J, Nakane T, Forsberg BO, Kimanius D, Hagen WJ, Lindahl E, Scheres SH. New tools for automated high-resolution cryo-EM structure determination in RELION-3. Elife. 2018;7. DOI: 10.7554/elife.42166.

192. Fernandez-Leiro R, Scheres SHW. A pipeline approach to single-particle processing in RELION. In: Acta Crystallographica Section D: Structural Biology. International Union of Crystallography; 2017. p. 496–502. DOI: 10.1107/s2059798316019276.

193. Kucukelbir A, Sigworth FJ, Tagare HD. Quantifying the local resolution of cryo-EM density maps. Nat Methods. 2014;11(1):63–5. DOI: 10.1038/nmeth.2727.

194. Scheres SHW. RELION: Implementation of a Bayesian approach to cryo-EM structure determination. J Struct Biol. 2012;180(3):519–30. DOI: 10.1016/j.jsb.2012.09.006.

195. Chen S, McMullan G, Faruqi AR, Murshudov GN, Short JM, Scheres SHW, Henderson R. High-resolution noise substitution to measure overfitting and validate resolution in 3D structure determination by single particle electron cryomicroscopy. Ultramicroscopy. 2013;135:24–35. DOI: 10.1016/j.ultramic.2013.06.004.

196. Rosenthal PB, Henderson R. Optimal determination of particle orientation, absolute hand, and contrast loss in single-particle electron cryomicroscopy. J Mol Biol. 2003;333(4):721–45. DOI: 10.1016/j.jmb.2003.07.013.

197. Beckers M, Sachse C. Permutation testing of Fourier shell correlation for resolution estimation of cryo-EM maps. J Struct Biol. 2020;212(1):107579. DOI: 10.1016/j.jsb.2020.107579.

198. Beckers M, Jakobi AJ, Sachse C. Thresholding of cryo-EM density maps by false discovery rate control. IUCrJ. 2019;6(1):18–33. DOI: 10.1107/s2052252518014434.

199. RStudio Team. RStudio: Integrated Development for R [Internet]. Boston, MA: RStudio, Inc; 2015.

200. Emsley P, Lohkamp B, Scott WG, Cowtan K. Features and development of Coot. Acta Crystallogr D Biol Crystallogr. 2010;66(Pt 4):486–501. DOI: 10.1107/s0907444910007493.

201. Park H, Bradley P, Greisen P, Liu Y, Mulligan VK, Kim DE, Baker D, DiMaio F, DiMaio F. Simultaneous Optimization of Biomolecular Energy Functions on Features from Small Molecules and Macromolecules. J Chem Theory Comput. 2016;12(12):6201–12. DOI:

10.1021/acs.jctc.6b00819.

202. Alford RF, Leaver-Fay A, Jeliazkov JR, O'Meara MJ, DiMaio FP, Park H, et al. The Rosetta All-Atom Energy Function for Macromolecular Modeling and Design. J Chem Theory Comput. 2017;13(6):3031–48. DOI: 10.1021/acs.jctc.7b00125.

203. Humphrey W, Dalke A, Schulten K. VMD: Visual molecular dynamics. J Mol Graph. 1996;14(1):33–8. DOI: 10.1016/0263-7855(96)00018-5.

204. Nivón LG, Moretti R, Baker D. A Pareto-optimal refinement method for protein design scaffolds. PLoS One. 2013;8(4):e59004. DOI: 10.1371/journal.pone.0059004.

205. Conway P, Tyka MD, DiMaio F, Konerding DE, Baker D. Relaxation of backbone bond geometry improves protein energy landscape modeling. Protein Sci. 2014;23(1):47–55. DOI: 10.1002/pro.2389.

206. McIntosh-Smith S, Wilson T, Ibarra AA, Crisp J, Sessions RB. Benchmarking Energy Efficiency, Power Costs and Carbon Emissions on Heterogeneous Systems. Comput J. 2012;55(2):192–205. DOI: 10.1093/comjnl/bxr091.

207. Wood CW, Bruning M, Ibarra AÁ, Bartlett GJ, Thomson AR, Sessions RB, Brady RL, Woolfson DN. CCBuilder: an interactive web-based tool for building, designing and assessing coiled-coil protein assemblies. Bioinformatics. 2014;30(21):3029–35. DOI: 10.1093/bioinformatics/btu502.

208. Smith SM, Larocque G, Wood KM, Morris KL, Roseman AM, Sessions RB, Royle SJ, Smith CJ. Multi-modal adaptor-clathrin contacts drive coated vesicle assembly. EMBO J. 2021;40:e108795. DOI: 10.15252/embj.2021108795.

209. Owen DJ, Vallis Y, Pearse BM, McMahon HT, Evans PR. The structure and function of the beta 2-adaptin appendage domain. EMBO J. 2000;19(16):4216–27. DOI: 10.1093/emboj/19.16.4216.

210. Feathers JR, Spoth KA, Fromme JC. Experimental evaluation of super-resolution imaging and magnification choice in single-particle cryo-EM. J Struct Biol X. 2021;5:100047. DOI: 10.1016/j.yjsbx.2021.100047.

211. Li X, Zheng SQ, Egami K, Agard DA, Cheng Y. Influence of electron dose rate on electron counting images recorded with the K2 camera. J Struct Biol. 2013;184(2):251–60. DOI: 10.1016/j.jsb.2013.08.005.

212. Booth C. K2: A Super-Resolution Electron Counting Direct Detection Camera for Cryo-EM. Microsc Microanal. 2012;18(S2):78–9. DOI: 10.1017/s1431927612002243.

213. Smythe E, Carter LL, Schmid SL. Cytosol- and clathrin-dependent stimulation of endocytosis in vitro by purified adaptors. J Cell Biol. 1992;119(5):1163–71. DOI: 10.1083/jcb.119.5.1163.

214. Crowther RA, Pearse BM. Assembly and packing of clathrin into coats. J Cell Biol. 1981;91(3):790–7. DOI: 10.1083/jcb.91.3.790.

215. Schindelin J, Arganda-Carreras I, Frise E, Kaynig V, Longair M, Pietzsch T, Preibisch S, Rueden C, Saalfeld S, Schmid B, Tinevez J-Y, White DJ, Hartenstein V, Eliceiri K, Tomancak P, Cardona A. Fiji: an open-source platform for biological-image analysis. Nat Methods. 2012;9(7):676–82. DOI: 10.1038/nmeth.2019.

216. Wagner T, Raunser S. The evolution of SPHIRE-crYOLO particle picking and its application in automated cryo-EM processing workflows. Commun Biol. 2020;3(1):61. DOI: 10.1038/s42003-020-0790-y.

217. Frank J, Radermacher M, Penczek P, Zhu J, Li Y, Ladjadj M, Leith A. SPIDER and WEB: Processing and Visualization of Images in 3D Electron Microscopy and Related Fields. J Struct Biol. 1996;116(1):190–9. DOI: 10.1006/jsbi.1996.0030.

218. Milligan RA, Flicker PF. Structural relationships of actin, myosin, and tropomyosin revealed by cryo-electron microscopy. J Cell Biol. 1987;105(1):29–39. DOI: 10.1083/jcb.105.1.29.

219. Heymann JB. Bsoft: Image and Molecular Processing in Electron Microscopy. J Struct Biol. 2001;133(2–3):156–69. DOI: 10.1006/jsbi.2001.4339.

220. Jiang J, Maes EG, Taylor AB, Wang L, Hinck AP, Lafer EM, Sousa R. Structural basis of J cochaperone binding and regulation of Hsp70. Mol Cell. 2007;28(3):422–33. DOI: 10.1016/j.molcel.2007.08.022.

221. Maib H, Ferreira F, Vassilopoulos S, Smythe E. Cargo regulates clathrin-coated pit invagination via clathrin light chain phosphorylation. J Cell Biol. 2018;217(12):4253–66. DOI: 10.1083/jcb.201805005.

222. Scheele U, Alves J, Frank R, Duwel M, Kalthoff C, Ungewickell E. Molecular and functional characterization of clathrin- and AP-2-binding determinants within a disordered domain of auxilin. J Biol Chem. 2003;278(28):25357–68. DOI: 10.1074/jbc.m303738200.

223. Scheele U, Kalthoff C, Ungewickell E. Multiple interactions of auxilin 1 with clathrin and the AP-2 adaptor complex. J Biol Chem. 2001;276(39):36131–8. DOI: 10.1074/jbc.m106511200.

224. Paraan M, Mendez J, Sharum S, Kurtin D, He H, Stagg SM. The structures of natively assembled clathrin-coated vesicles. Sci Adv. 2020;6(30):eaba8397. DOI: 10.1126/sciadv.aba8397.

225. Kovtun O, Dickson VK, Kelly BT, Owen DJ, Briggs JAG. Architecture of the AP2/clathrin coat on the membranes of clathrin-coated vesicles. Sci Adv. 2020;6(30):eaba8381. DOI: 10.1126/sciadv.aba8381.

226. Bhella D. Cryo-electron microscopy: an introduction to the technique, and considerations when working to establish a national facility. Biophys Rev 2019 114. 2019;11(4):515–9. DOI: 10.1007/s12551-019-00571-w.

227. Drulyte I, Johnson RM, Hesketh EL, Hurdiss DL, Scarff CA, Porav SA, Ranson NA, Muench SP, Thompson RF. Approaches to altering particle distributions in cryo-electron microscopy sample preparation. Acta Crystallogr Sect D, Struct Biol. 2018;74(Pt 6):560–71. DOI: 10.1107/s2059798318006496.

228. Danev R, Iijima H, Matsuzaki M, Motoki S. Fast and accurate defocus modulation for improved tunability of cryo-EM experiments. IUCrJ. 2020;7(3):566–74. DOI: 10.1107/s205225252000408x.

229. Turk M, Baumeister W. The promise and the challenges of cryo-electron tomography. FEBS Lett. 2020;594(20):3243–61. DOI: 10.1002/1873-3468.13948.

230. Pyle E, Zanetti G. Current data processing strategies for cryo-electron tomography and subtomogram averaging. Biochem J. 2021;478(10):1827–45. DOI: 10.1042/bcj20200715.

231. Mastronarde DN. Automated electron microscope tomography using robust prediction of specimen movements. J Struct Biol. 2005;152(1):36–51. DOI: 10.1016/j.jsb.2005.07.007.

232. Kremer JR, Mastronarde DN, McIntosh JR. Computer Visualization of Three-Dimensional Image Data Using IMOD. J Struct Biol. 1996;116(1):71–6. DOI: 10.1006/jsbi.1996.0013.

233. Wang Z, Zhang Q, Mim C. Coming of Age: Cryo-Electron Tomography as a Versatile Tool to Generate High-Resolution Structures at Cellular/Biological Interfaces. Int J Mol Sci. 2021;22(12). DOI: 10.3390/ijms22126177.

234. Glaeser RM. Specimen Behavior in the Electron Beam. Methods Enzymol. 2016;579:19–50. DOI: 10.1016/bs.mie.2016.04.010.

235. Hattne J, Shi D, Glynn C, Zee C-T, Gallagher-Jones M, Martynowycz MW, Rodriguez JA, Gonen T. Analysis of Global and Site-Specific Radiation Damage in Cryo-EM. Structure. 2018;26(5):759-766.e4. DOI: 10.1016/j.str.2018.03.021.

236. Xiong Q, Morphew MK, Schwartz CL, Hoenger AH, Mastronarde DN. CTF determination and correction for low dose tomographic tilt series. J Struct Biol. 2009;168(3):378–87. DOI: 10.1016/j.jsb.2009.08.016.

237. Yengo CM, Berger CL. Fluorescence anisotropy and resonance energy

transfer: powerful tools for measuring real time protein dynamics in a physiological environment. Curr Opin Pharmacol. 2010;10(6):731–7. DOI: 10.1016/j.coph.2010.09.013.

238. Zhao Q, Tao J, Feng W, Uppal JS, Peng H, Le XC. Aptamer binding assays and molecular interaction studies using fluorescence anisotropy - A review. Anal Chim Acta. 2020;1125:267–78. DOI: 10.1016/j.aca.2020.05.061.

239. Zhang H, Wu Q, Berezin MY. Fluorescence anisotropy (polarization): from drug screening to precision medicine. Expert Opin Drug Discov. 2015;10(11):1145–61. DOI: 10.1517/17460441.2015.1075001.

240. Vinegoni C, Feruglio PF, Gryczynski I, Mazitschek R, Weissleder R. Fluorescence anisotropy imaging in drug discovery. Adv Drug Deliv Rev. 2019;151–152:262–88. DOI: 10.1016/j.addr.2018.01.019.

241. Lakowicz J.R. Fluorescence Anisotropy. In: Principles of Fluorescence Spectroscopy. Boston, MA: Springer US; 2006. p. 353–82. DOI: 10.1007/978-0-387-46312-4_10.

242. Lakowicz JR. Principles of Fluorescence Spectroscopy [Internet]. Boston, MA: Springer US; 1999. DOI: 10.1007/978-1-4757-3061-6.

243. Canet D, Doering K, Dobson CM, Dupont Y. High-Sensitivity Fluorescence Anisotropy Detection of Protein-Folding Events: Application to α-Lactalbumin. Biophys J. 2001;80(4):1996–2003. DOI: 10.1016/s0006-3495(01)76169-3.

244. Otto MR, Lillo MP, Beechem JM. Resolution of multiphasic reactions by the combination of fluorescence total-intensity and anisotropy stopped-flow kinetic experiments. Biophys J. 1994;67(6):2511–21. DOI: 10.1016/s0006-3495(94)80741-6.

245. Pollard TD. A guide to simple and informative binding assays. Mol Biol Cell. 2010;21(23):4061–7. DOI: 10.1091/mbc.e10-08-0683.

246. Jarmoskaite I, AlSadhan I, Vaidyanathan PP, Herschlag D. How to

measure and evaluate binding affinities. Elife. 2020;9. DOI: 10.7554/elife.57264.

247. Motulsky HJ, Neubig RR. Analyzing Binding Data. Curr Protoc Neurosci. 2010;52(1):7.5.1-7.5.65. DOI: 10.1002/0471142301.ns0705s52.

248. Jing M, Bowser MT. Methods for measuring aptamer-protein equilibria: A review. Anal Chim Acta. 2011;686(1–2):9–18. DOI: 10.1016/j.aca.2010.10.032.

249. Checovich WJ, Bolger RE, Burke T. Fluorescence polarization — a new tool for cell and molecular biology. Nature. 1995;375(6528):254–6. DOI: 10.1038/375254a0.

250. Jameson DM, Ross JA. Fluorescence Polarization/Anisotropy in Diagnostics and Imaging. Chem Rev. 2010;110(5):2685–708. DOI: 10.1021/cr900267p.

251. Toseland CP. Fluorescent labeling and modification of proteins. J Chem Biol. 2013;6(3):85–95. DOI: 10.1007/s12154-013-0094-5.

252. ThermoFisher Scientific. Alexa Fluor™ 488 C_5 Maleimide [Internet]. Available from: https://www.thermofisher.com/order/catalog/product/A10254#/A10254

253. ISS. ISS Data Tables | Lifetime Data of Selected Fluorophores [Internet]. Available from: http://www.iss.com/resources/reference/data_tables/LifetimeDataFluorophores.html

254. ThermoFisher Scientific. Alexa Fluor™ 555 C_2 Maleimide [Internet]. Available from: https://www.thermofisher.com/order/catalog/product/A20346#/A20346

255. ThermoFisher Scientific. Fluorescein-5-Maleimide [Internet]. Available from: https://www.thermofisher.com/order/catalog/product/F150?SID=srch-srp-F150#/F150?SID=srch-srp-F150

256. ThermoFisher Scientific. BODIPY™ TMR C_5-Maleimide [Internet]. Available from: https://www.thermofisher.com/order/catalog/product/B30466#/B30466

257. Azarnia Tehran D, López-Hernández T, Maritzen T. Endocytic Adaptor Proteins in Health and Disease: Lessons from Model Organisms and Human Mutations. Cells. 2019;8(11). DOI: 10.3390/cells8111345.

258. Gruschus JM, Greene LE, Eisenberg E, Ferretti JA. Experimentally biased model structure of the Hsc70/auxilin complex: Substrate transfer and interdomain structural change. Protein Sci. 2004;13(8):2029–44. DOI: 10.1110/ps.03390504.

259. Ohmori K, Endo Y, Yoshida Y, Ohata H, Taya Y, Enari M. Monomeric but not trimeric clathrin heavy chain regulates p53-mediated transcription. Oncogene. 2008;27(15):2215–27. DOI: 10.1038/sj.onc.1210854.

260. Fernandez J. TOMOBFLOW: feature-preserving noise filtering for electron tomography. BMC Bioinformatics. 2009;10(178). DOI: 10.1186/1471-2105-10-178.

Appendix – Publications

1. Wood, K. M., & Smith, C. J. (2021). Clathrin - The Molecular Shapeshifter. *Biochemical Journal*, *478*(16), 3099–3123. https://doi.org/10.1042/BCJ20200740

2. Smith, S. M., Larocque, G., Wood, K. M., Morris, K. L., Roseman, A. M., Sessions, R. B., Royle, S. J., & Smith, C. J. (2021). Multi-modal adaptor-clathrin contacts drive coated vesicle assembly. *EMBO Journal*, *40*, e108795. https://doi.org/10.15252/embj.2021108795

Biochemical Journal (2021) **478** 3099–3123
https://doi.org/10.1042/BCJ20200740

Review Article

Clathrin: the molecular shape shifter

Katherine M. Wood[1] **and Corinne J. Smith**[2]

[1]Warwick Medical School, University of Warwick, Coventry, U.K.; [2]School of Life Sciences, University of Warwick, Coventry, U.K.

Correspondence: Corinne J. Smith (corinne.smith@warwick.ac.uk)

Clathrin is best known for its contribution to clathrin-mediated endocytosis yet it also participates to a diverse range of cellular functions. Key to this is clathrin's ability to assemble into polyhedral lattices that include curved football or basket shapes, flat lattices or even tubular structures. In this review, we discuss clathrin structure and coated vesicle formation, how clathrin is utilised within different cellular processes including synaptic vesicle recycling, hormone desensitisation, spermiogenesis, cell migration and mitosis, and how clathrin's remarkable 'shapeshifting' ability to form diverse lattice structures might contribute to its multiple cellular functions.

Introduction

Eukaryotic cells use endocytosis to internalise cargo from their extracellular environment, in which invagination of the plasma membrane creates a vesicle or tubule that is cleaved off and released into the cytoplasm of the cell [1–4]. In receptor mediated endocytosis (RME) receptors on cell surfaces target specific cargo for import, which when internalised is transported to endosomes. The cargo may then be recycled back to the cell membrane, transported intracellularly or delivered to lysosomes for degradation [5–7]. Clathrin mediated endocytosis (CME) is the most studied form of RME and is believed to be the major endocytic process in cells [8]. CME is named after the clathrin coated vesicles (CCV) of ∼60 nm to 135 nm in diameter that form from cell membranes in order to achieve this. The clathrin coat is formed from the scaffold protein clathrin and other CME adaptor proteins [9–13]. Clathrin is highly evolutionarily conserved within eukaryotes and is involved in multiple cellular processes including mitosis, spermiogenesis, hormone desensitisation, cell migration, synaptic vesicle (SV) recycling, and intracellular trafficking [14–19]. Figure 1 illustrates the variety of different processes in which clathrin is involved. Defects within CME are associated with several pathological conditions, including Parkinson's disease, Alzheimer's disease, HIV/AIDs, and autosomal recessive hypercholesterolemia [20–27].

For CME to occur clathrin is required to form a coat bound to the cell membrane, but clathrin cannot directly interact with cell membrane lipids and proteins and thus relies on CME adaptor proteins to form these connections [20,28]. Once a clathrin coat starts to form, invagination can begin, as the formation of the clathrin coat and the presence of CME adaptors such as BAR-domain proteins and epsin alter the balance of forces stabilising the cell membrane to allow membrane bending to occur [1,29–31]. For invagination to occur, the CME adaptors need to contribute forces of the order of picoNewtons so that factors that make bending the membrane challenging, such as high membrane tension, internal hydrostatic pressure, and cargo properties, can be overcome [1,11,32,33]. These picoNewton forces could be provided via the consequences of actin polymerisation and crosslinking, involving hydrolysis of ATP, interactions of BAR domain proteins with the membrane and one another, molecular crowding or clathrin assembly [34]. Despite our understanding of the challenges of membrane invagination, there is still ongoing debate over how clathrin coats assemble, the role and nature of clathrin lattice rearrangement, how CME adaptors interact and cooperate to produce CCVs and clathrin coated pits (CCP), and how the CME process is regulated to ensure the successful formation of vesicles containing appropriate cargo. In this review, we will discuss current knowledge of

Received: 2 April 2021
Revised: 19 July 2021
Accepted: 4 August 2021

Version of Record published:
26 August 2021

Biochemical Journal (2021) **478** 3099–3123
https://doi.org/10.1042/BCJ20200740

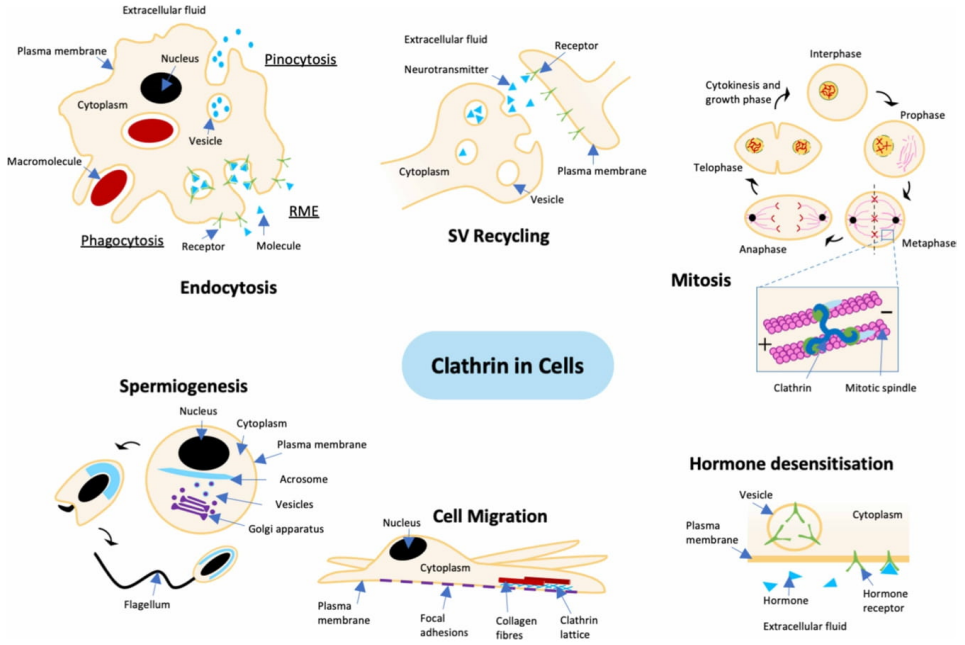

Figure 1. Clathrin-mediated endocytosis in cellular processes.

Schematic diagram demonstrating the variety of cellular processes in which clathrin is used, including but not limited to endocytosis, spermiogenesis, cell migration, hormone desensitisation, mitosis, and SV recycling [1–4,14–19]. Diagram is not to scale.

clathrin structure and how this contributes to the molecular mechanism of CME, how clathrin is utilised during different cellular processes, and how clathrin's remarkable 'shapeshifting' ability to form diverse lattice structures might contribute to its multiple cellular functions.

Clathrin structure

Clathrin forms a three-legged structure called a triskelion composed of three clathrin heavy chains (CHC) ~190 kDa in size, and three clathrin light chains (CLC) ~25 kDa in size [35,36]. CHC consists of five domains called the trimerization domain, proximal domain, distal domain, ankle domain, and terminal domain, as shown in Figure 2A [37]. The trimerization domain consists of a ~45-residue carboxy-terminal segment responsible for binding to other CHC carboxy-terminal regions to create a protein complex in the form of a triskelion structure. The next region consists of 42 zig-zagging alpha-helices that form the proximal, distal and ankle domains, which are responsible for the curved legs of the clathrin triskelion that create its tripod-like structure. The final region, the terminal domain, consists of a seven-bladed WD40 repeat beta-propeller at the amino-terminal responsible for interactions between clathrin and other CME adaptor proteins. The structure of a CLC consists of a long alpha-helix in the centre of its structure responsible for interactions with the CHC proximal domain, disordered terminal regions whose interaction with CHC is unclear, and a folded helical region close to the C-terminus that is embedded in and stabilises the CHC trimerization domain [37–40]. The structure of a bovine clathrin triskelion and the location of CLCs, CHCs and CHC domains is shown in Figure 2B.

Clathrin triskelia interact with each other to form clathrin cages *in vitro*, and clathrin lattices, CCPs and CCVs *in vivo*. The size and shape of clathrin coats and lattices varies and this allows vesicles to accommodate the required size and quantity of cargo being imported. For example, bovine brain CCVs have smaller

Biochemical Journal (2021) **478** 3099–3123
https://doi.org/10.1042/BCJ20200740

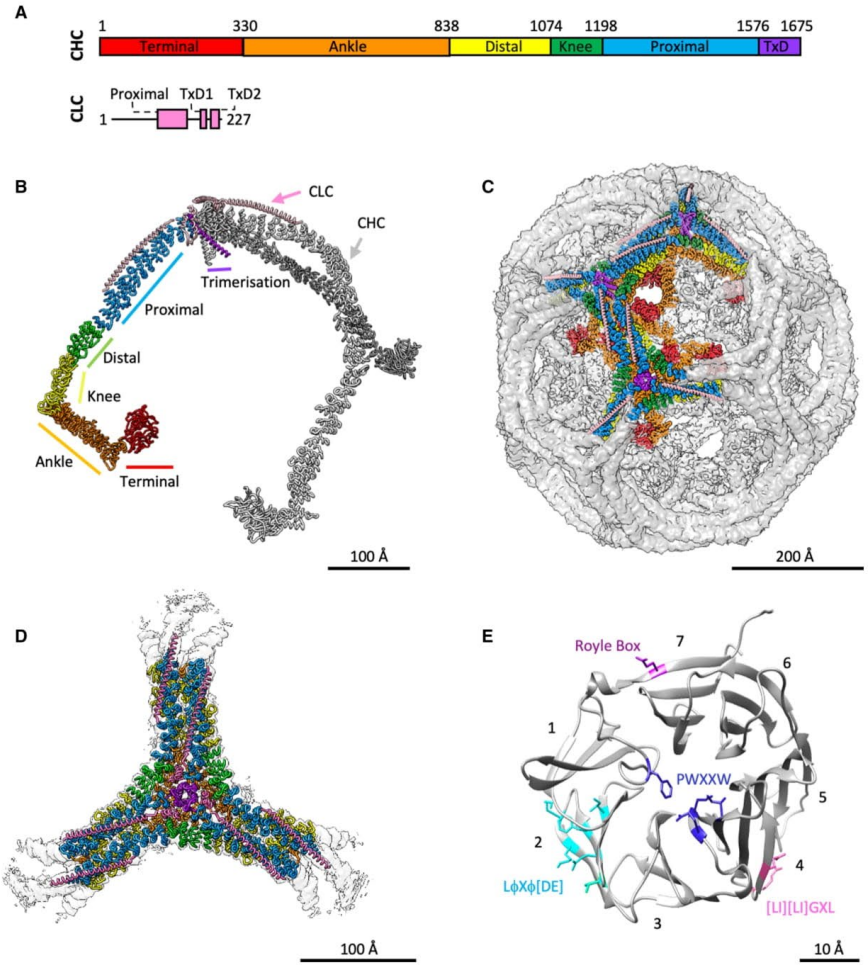

Figure 2. Clathrin structure.

(**A**) Domain organisation within CLC and CHC [41]. (**B**) Model of a clathrin triskelion including the bovine CHC model (Protein Data Bank (PDB): 3IYV) [37] informed by fitting the high resolution X-ray structure (PDB: 1B89) [42] into cryo-EM density maps and the porcine CLC model produced from cryo-EM density maps (PDB: 6SCT) [41]. (**C**) Model of a bovine clathrin cage (EMD: 5119) with fitted clathrin triskelion model produced from cryo-EM density maps (PDB: 1XI5) [37]. (**D**) Recent 4.7 Å porcine clathrin hub structure with fitted PDB model (PDB: 6SCT) produced from cryo-EM density maps (EMD: 0126) [41]. (**E**) Model of a rat CHC terminal domain produced from X-ray diffraction density (PDB: 1BPO), with location of binding sites for different motifs highlighted [43]. All structure visualization was performed with UCSF Chimera [44].

diameters of 60–80 nm compared with human placenta CCVs that produce larger CCVs of 100–135 nm [10,45,46]. This size variability is possible due to clathrin's ability to assemble into different configurations, including pentagon and hexagon arrangements, and, less frequently, heptagons and squares [10,41]. Clathrin

Biochemical Journal (2021) **478** 3099–3123
https://doi.org/10.1042/BCJ20200740

assembles into empty coat structures *in vitro*, also known as clathrin cages or baskets, if placed in a buffer at pH 6.5 or less with magnesium and calcium ions present [35]. Formation of clathrin cages *in vitro* has allowed cryo-electron microscopy analysis of these large multi-protein complexes at high resolution, which led to the production of the 7.8 Å D6 dihedral symmetry clathrin coat structure shown in Figure 2C, and the more recent 4.7 Å clathrin consensus hub substructure demonstrated in Figure 2D [37,41,47,48]. Within each of these structures, a clathrin triskelion is centred at each hub or lattice point, with the triskelion legs interacting with other triskelia and causing the legs to bend inwards. The degree of bending of the triskelion leg varies depending upon the clathrin cage or lattice configuration, indicating some flexibility most likely due to the arrangement of paired alpha-helices oriented perpendicular to the long leg axis in the proximal, distal and ankle domains, which would be able to change conformation to produce a variety of different leg configurations [37,41].

The clathrin terminal domain

The clathrin terminal domain is the primary interaction point between clathrin and CME adaptors. It consists of a seven-bladed β-propeller at the CHC amino-terminal joined to short α-helices that connect to the ankle region of the CHC. X-ray crystallography has been used to determine the terminal domain's structure to 2.6 Å, shown in Figure 2E [43]. Additional analysis of terminal domain interactions with CME adaptors has identified four binding sites within the seven-bladed β-propeller called the clathrin box, the W-box, the arrestin box and the Royle box, indicated in Figure 2E [20]. The clathrin box is located in a groove between blades one and two of the β-propeller and binds to the highly conserved clathrin box motif which comprises acidic and bulky hydrophobic residues L(L, I)(D, E, N)(L, F)(D, E) (LϕXϕ[DE]) [49]. The clathrin box motif has been found in several adaptors including the β3-appendage of AP3, amphiphysin, arrestin3 segments, and β-arrestin 1 and β-arrestin 2 [50–54]. The arrestin box is located between blades four and five of the β-propeller and binds to the arrestin box motif, which is found in arrestin proteins and consists of residues [LI][LI]GXL [55]. The W-box is located towards the centre of the β-propeller rather than on the blades' outskirts (where other binding sites are found) and binds to the W-box motif, which consists of residues PWXXW. Amphiphysin 1 is one CME adaptor that contains a W-box motif which binds to the W-box with a compact helical structure as determined at 2.3 Å via X-ray crystallography [56]. The final binding site, called the Royle box, is found on the seventh blade of the β-propeller. The nature of the motif required to bind to the Royle box is currently unknown [57] but Muenzner et al. [58] present crystal structures showing three different peptides bound to the Royle box which facilitated further definition of this site. This study together with work from Zhou et al. [59] also suggests there is a degree of degeneracy in the sequence of motifs interacting with different terminal domain sites, enabling some motifs to bind to more than one site on the clathrin terminal domain.

Other motifs, called DLL and DLF motifs have been identified in a number of clathrin adaptors, including assembly protein 180 kDa (AP180), which can also bind to the clathrin terminal domain via weak interactions with a K_d value of the order of $\sim 2 \times 10^{-4}$ M [60,61]. Since there are multiple such motifs within the AP180 sequence their combined effect, or avidity, could potentially facilitate stable interactions. As individual DLL and DLF motifs only associate with clathrin via weak interactions, this allows for rapid association and dissociation between CME adaptors and clathrin, which could be vital for AP180 to capture clathrin whilst allowing a clathrin lattice to form [20,62].

Clathrin mediated endocytosis

CME involves the coordination of ∼50 different adaptor or accessory proteins, which can interact with clathrin and or each other to complete different stages of CME. Each adaptor has a different role and may be involved in one or several stages, which have so far been described as nucleation and assembly, stabilisation and maturation, neck constriction and scission, and clathrin uncoating [11,63,64]. A visual representation of each CME stage is presented in Figure 3. During CME, adaptor proteins may arrive at CME sites at different times, resulting in fluctuations of local concentrations of adaptor proteins depending on the stage clathrin assembly has reached [63,65–68].

Nucleation and assembly

Initiation of CME occurs upon the formation of an 'interaction nucleus', which is required for recruiting adaptors and forming a clathrin coat. How this nucleus develops is under debate, as it could be due to interactions between multiple accessory proteins including Fer/Cip4 homology domain-only proteins 1 and 2 (FCHo1/2), adaptor protein 2 (AP2), epidermal growth factor receptor substrate 15 (Eps15), Eps15 receptor (Eps15R),

Biochemical Journal (2021) **478** 3099–3123
https://doi.org/10.1042/BCJ20200740

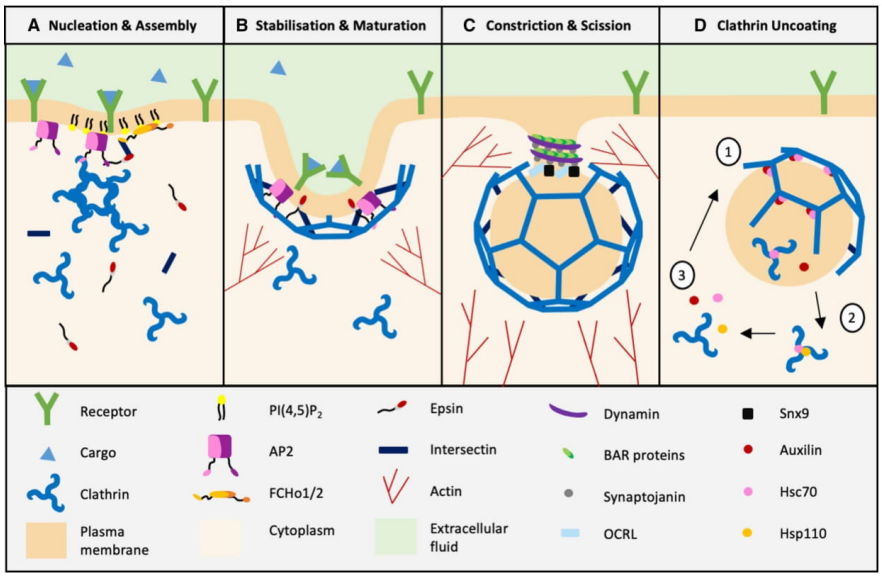

Figure 3. Stages in clathrin mediated endocytosis.

Schematic diagram illustrating different stages in CME, including (**A**) nucleation and assembly, followed by (**B**) stabilisation and maturation, followed by (**C**) constriction and scission, followed by (**D**) clathrin uncoating. Figure is not to scale.

intersectins 1/2, and potentially other adaptors that have yet to be identified [29,66,69]. However, evidence from several groups indicates that the FCHo1/2 complex and the AP2 complex could be the primary initiators for the formation of the CME nucleus [29,69–73]. Once the CME nucleus has formed, adaptor proteins can recruit cargo to the site through interactions with the cytosolic regions of transmembrane cargo or transmembrane cargo receptors, allowing the import of cargo and associated lipids into the cell [74–77]. Some of the known cargo adaptors include AP2, FCHo1, Eps15, and clathrin-assembly lymphoid myeloid leukaemia protein (CALM) [78,79]. As these four adaptors are associated with initiation, it seems possible that cargo can play a role in recruiting adaptor proteins to form a nucleation point and thereby initiate CME [80–82].

Despite the large surface area of cell membranes, CME nucleation tends to occur at spatially distinct sites, for example as in neuronal synapses [83]. The location of CME nucleation may be due to differing levels of availability of CME adaptors across the cell, such as AP2 and phosphatidylinositol 4,5-bisphosphate (PI(4,5)P_2), and the local formation of cortical actin [84]. PI(4,5)P_2 is necessary for nucleation site formation since depletion of PI(4,5)P_2 prevents the formation of CCPs, and many CME adaptors bind to PI(4,5)P_2 at the cell membrane [85,86]. It is possible that different local concentrations of PI(4,5)P_2 and CME adaptors may explain why CME occurs at spatially distinct sites [85,86]. Nucleation can occur randomly at positions in the cell membrane where endocytosis does not usually occur, possibly due to stochastic collisions between CME adaptors, however, the majority of nucleation sites are formed at spatially distinct locations [70,76].

For CME to occur at spatially distinct sites, there must be some level of organisation, potentially through the use of nucleation factors and organisers such as FCHo1/2 and Sorting Nexin 9 (SNX9). Changes in the expression levels of FCHo1/2 and SNX9 have been found to impact the quantity of CCP formation and spatial clustering of CCPs, respectively [29,84]. FCHo1/2 is responsible for engaging with AP2 and the scaffold proteins eps15 and intersectin to sculpt the nucleation site to create a CCP. Thus by having high local concentrations of FCHo1/2, cells can ensure high quantities of CCPs are formed which is of great functional value for, for example, neuron synapses which require localised synaptic vesicle recycling [29,70].

Biochemical Journal (2021) **478** 3099–3123
https://doi.org/10.1042/BCJ20200740

Quality control in CME is critical to ensure that productive vesicles are developed that contain sufficient cargo. CCP intermediates are frequently aborted, as observations of nucleation events have shown weak or short-lived CCPs in cells, but multiple checkpoints may determine the level of CME turnover [76]. Checkpoints may include the presence or quantity of cargo in CCPs, the ubiquitination of cargo adaptors, or other factors [4,76,82,87,88]. If CCPs are incapable of clearing the checkpoint, then CCP formation can be delayed or aborted. The recruitment of dynamin could also be viewed as a checkpoint controlling the level of CME turnover, as dynamin is responsible for the final stage of CME, scission [89].

Stabilisation and maturation

Once a CCP has formed, the CCP undergoes stabilisation and maturation so that it develops a vesicle-like structure filled with cargo. Several proteins that have either direct roles in membrane bending or act indirectly by influencing clathrin assembly are recruited to the CCP, including epsin, CALM, clathrin, heat shock cognate 71 kDa protein (Hsc70), Cyclin G-associated kinase (GAK), auxilin and actin. Clathrin's ability to form lattices and polyhedral cages consisting predominantly of hexagonal and pentagonal arrangements helps stabilise and potentially induce curvature in cell membranes [10,41]. When bound to clathrin, the amphipathic helices found within epsin and CALM can wedge into the cell membrane to bend and curve the membrane in the area [13,90,91]. CLCs help to stabilise the developed membrane curvature through their interaction with CHCs in clathrin lattices which causes clathrin lattices to become more rigid [92,93]. Hsc70, GAK and auxilin, the adaptors responsible for clathrin uncoating, have also been proposed to be involved in reorganising the clathrin lattice as the CCP develops [94–99].

The actin cytoskeleton helps to further stabilise the CCP by assembling around CCP sites, particularly around clathrin coats and the base of CCPs, potentially acting as a scaffold that can generate and transmit a force to promote membrane curvature [100–103]. The presence of the actin cytoskeleton helps support CME during periods of high membrane tension, as live cell imaging studies have shown that perturbations in the actin cytoskeleton can inhibit CME [65,83,104–110]. For actin to stabilise or contribute to membrane bending it needs to couple with the clathrin coat. This is thought to occur via epsin and Huntington-interacting protein 1-related protein (HIP1R), both of which are known to bind to actin, clathrin and $PI(4,5)P_2$ [111–115].

Neck constriction and scission

Once the CCP has formed, Bin/Amphiphysin/Rvs (BAR) domain proteins bind to the CCP and, when recruited in high densities, can tubulate the membrane to constrict the CCP neck [116–118]. The level of membrane curvature has been shown to influence recruitment of BAR domain proteins, with F-BAR domain and N-BAR domain proteins being preferentially recruited to low and high membrane curvature respectively [119,120]. Once the neck of the CCP has constricted, and the vesicle is ready to be released into the cell, BAR domain proteins recruit the GTPase dynamin to conduct the scission process [119,121,122]. Dynamin assembles around the neck of the vesicle as tight oligomers ∼20 nm in diameter, which upon GTP binding and hydrolysis, constrict to stimulate membrane fission [123]. However, it should be noted that scission cannot occur by dynamin constriction alone, as the scission process requires the presence of several dynamin partners to ensure that preconditions for scission are met, such as control of membrane tension and/or remodelling by actin, synaptojanin and endophilin [124–128]. How the scission process occurs *in vivo* is thus still under debate.

Clathrin uncoating

Upon the CCV being released from the membrane and into the cell, the clathrin coat is disassembled. Removal of the clathrin coat allows the vesicle to be trafficked to the early endosome and CME adaptors associated with the clathrin coat to be recycled. Synaptojanin and Oculocerebrorenal syndrome of Lowe inositol polyphosphate 5-phosphatase (OCRL1) have been implicated in the uncoating of clathrin-coated vesicles and have been proposed to act via dephosphorylation of $PI(4,5)P_2$ to PI(4)P [24,129–134]. Loss of $PI(4,5)P_2$ from the CCV is thought to weaken binding of coated vesicle adaptors such as AP-2, AP180 and epsin [134–136], and has been proposed to stimulate recruitment of the chaperone auxilin [94,137–141], which in turn recruits the ATPase Hsc70 and adenosine triphosphate (ATP) via its J-domain to enable clathrin disassembly [95,142]. The phosphatase and tensin homolog deleted on chromosome ten (PTEN) domain within auxilin is important for auxilin to bind to the CCV membrane, via interactions with negatively charged lipids such as $PI(4,5)P_2$ [132,133,143]. The PTEN domain is not essential for clathrin uncoating but does increase auxilin's functional

Biochemical Journal (2021) **478** 3099–3123
https://doi.org/10.1042/BCJ20200740

efficiency, potentially by allowing auxilin to be positioned in a suitable orientation for efficient clathrin uncoating [140,143–145]. The J-domain in auxilin, however, is vital for clathrin coat disassembly due to its role in recruiting Hsc70 bound to ATP to assembled clathrin. Auxilin has been shown to act catalytically, enabling recruitment of multiple Hsc70 molecules to CCVs for clathrin disassembly. [139,146–149].

The binding of Hsc70 to auxilin's J-domain occurs predominantly via electrostatic interactions, with auxilin surface residues Tyr866, Arg867, Lys868, His874, Asp876 and Lys877 being involved in crucial interactions with Hsc70 [150,151]. Upon recruitment to a CCV, the Hsc70-ATP complex binds to the QLMLT motif at the CHC carboxy-terminus. The three copies of the QLMLT motif available per triskelion provide Hsc70 with the opportunity to bind to up to three sites per clathrin vertex [141,147,152–154]. *In vitro* studies have shown that, when bound to auxilin and clathrin, the ATPase activity of Hsc70 is enhanced, which in cells would likely promote vesicle uncoating [148]. Upon ATP hydrolysis, Hsc70 binds stably to clathrin, and the J-domain is released, setting in train events leading to clathrin disassembly [153,155,156]. The stability of the clathrin coat will impact the level of structural perturbation required to break triskelion interactions and thus will influence the rate of uncoating and the number of Hsc70 molecules required for coat disassembly [155]. As few as one Hsc70 molecule for every two clathrin trimers has been observed to be required for initiating clathrin coat disassembly, but this stoichiometric value depends on pH [154,155,157]. CLCs help regulate the interaction between auxilin and clathrin to control clathrin coat stabilisation and control auxilin's ability to perform catalytically [147]. Regulation of auxilin is achieved via phosphorylation of CLCs which promote auxilin dissociation from clathrin [147,158].

As clathrin coats are disassembled, triskelia have been observed in yeast to separate from the CCV as partially uncoated intermediates consisting of two or more triskelia which will continue to depolymerise in the cytosol [159]. The depolymerised clathrin triskelia remain bound to Hsc70 and adenosine diphosphate (ADP), but auxilin dissociates [140]. *In vitro* experiments show that Hsc70 and ADP remain bound to dissociated triskelia, leading the clathrin coat disassembly reaction to follow burst kinetics, where the addition of a limited quantity of Hsc70 causes an initial burst of rapid uncoating followed by a slower steady-state rate where most of the Hsc70 remains bound to the dissociated triskelia [148,154,160]. The Hsc70-ADP complex can be released from clathrin by the nucleotide exchange factor heat shock protein 110 (Hsp110) which allows ADP to dissociate from Hsc70 and ATP to bind, thus allowing Hsc70 and clathrin to be recycled for additional rounds of endocytosis [161–165].

In vitro studies of clathrin cage disassembly have shown that a ratio of one auxilin molecule per clathrin triskelion is sufficient for clathrin to disassemble at the maximum rate, although up to three auxilins can be bound per vertex in cages [160]. In cells, auxilin appears to bind to CCVs in transient bursts immediately after scission of CCPs occurs, with only a small number of auxilin molecules observed, ranging from 2 to 20, bound to CCVs of 36 and 100 clathrin trimers in size [94,132,166]. However, both in cells and in *in vitro* studies, auxilin has been shown to act catalytically, with one auxilin molecule capable of recruiting multiple Hsc70 molecules in sequential order and potentially moving to different clathrin vertices upon dissociation from clathrin after ATP hydrolysis [132,154,160]. While maximal rates of disassembly *in vitro* have been shown to require Hsc70 to be present in excess compared with clathrin and auxilin [160], the situation in cells is more complex. It has been inferred from studies in a human cell line that CCVs formed of ∼60 clathrin trimers have less than 10 Hsc70 molecules bound at a time during uncoating [132]. This difference could be due to the presence of nucleotide exchange factors in cells that would facilitate recycling of Hsc70 and to the possibility that disassembly at the maximum rate is not utilised under cellular conditions.

The mechanics by which Hsc70 and auxilin disassemble clathrin coats is intriguing because of the intricate shape of clathrin assemblies and the comparatively small size of the Hsc70 and auxilin molecules that achieve disassembly. Discussion has so far centred around two main models: the steric wedge/Brownian ratchet model, and the entropic pulling or wrecking ball model. A schematic representation of each model is presented in Figure 4. The steric wedge model proposes that when auxilin recruits Hsc70, this results in an increase in the excluded volume below the clathrin coat vertices that stabilises a locally strained conformation. Disassembly is favoured by an accumulation of these distortions caused as further Hsc70 molecules bind favours disassembly [141,153].

Following ATP hydrolysis, Hsc70 no longer binds to the auxilin J domain and becomes tightly associated with the flexible clathrin carboxy-terminal domain, with the potential to move freely, as if a ball on a string, unless sterically hindered by the surrounding structures of the clathrin vertex. The entropic pulling model suggests that the increase in entropy occasioned by increased freedom of movement when Hsc70 moves away from

Biochemical Journal (2021) **478** 3099–3123
https://doi.org/10.1042/BCJ20200740

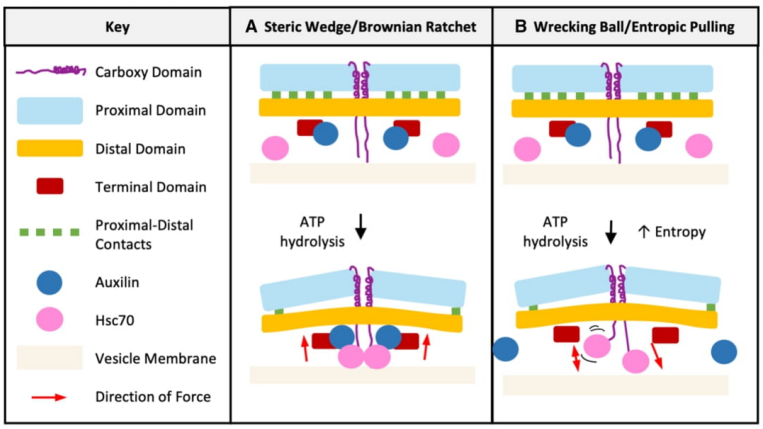

Figure 4. Models for clathrin cage disassembly.

Schematic diagram demonstrating two different models for hsc70 driven disassembly of clathrin cages, including (**A**) the steric wedge/Brownian ratchet model, and (**B**) the wrecking ball/entropic pulling model. Diagram is not to scale.

the constraints of the clathrin vertex creates a directional force that pulls on the clathrin carboxy-terminal domain and ultimately disrupts clathrin proximal-distal interactions [99,167–169].

By showing that attachment of Fab fragments bound to clathrin at the Hsc70 binding site could cause cage disassembly, Sousa et al. [167] elegantly demonstrated that the energy of ATP hydrolysis was not required to disassemble clathrin *per se*. When the Fab fragment binding site was moved away from the clathrin vertex, clathrin disassembly continued, suggesting that physical leverage of Hsc70 against the clathrin vertex was not critical for clathrin disassembly. However, disassembly became progressively slower as the distance of the Fab/Hsc70 binding site from the clathrin vertex was increased and was consistent with the effect on rate predicted by the calculations of De los Rios and Goloubinoff, lending weight to the proposal that the driving force for disassembly lay with an entropic pulling/collision pressure model [168].

Diversity of clathrin function in cells

The import of molecules into cells via clathrin-mediated endocytosis has been well-studied over many years and comprehensively reviewed [20,170,171]. However, clathrin plays more diverse cellular roles that go beyond internalisation of cargo. Here we discuss the diversity of roles CME, and elements of CME machinery, in synaptic vesicle recycling, hormone desensitisation and spermiogenesis, and how clathrin participates in creating other structures, such as tubules and bridges, to aid with cellular migration and mitosis (See Figure 5).

Synaptic vesicle recycling

Clathrin is essential for SV recycling during neurotransmission. Neurotransmission is the process of transmitting a signal from one nerve cell to another through synapses, allowing the sensory and nervous systems to communicate with one another. For neurotransmission to occur, an action potential is generated: a short-lived rise and fall of a membrane's electrical potential caused by Na^+ and K^+ transport across the membrane. Upon the action potential reaching a synapse, calcium will flood into the pre-synaptic terminal and prompt SV's to fuse with the plasma membrane and release the neurotransmitters found within them, allowing the neurotransmitter to bind to receptors on the post-synaptic terminal to initiate an action potential in the adjacent neuron. SV recycling is critical for maintaining the population of SV's in neurons, with defects in SV recycling causing neurodegeneration and impaired neuronal function [176].

Endophilin is a membrane binding protein that senses and generates curvature in cellular membranes [66,122,177–179]. It interacts with clathrin and other CME adaptors including synaptojanin and dynamin,

Biochemical Journal (2021) **478** 3099–3123
https://doi.org/10.1042/BCJ20200740

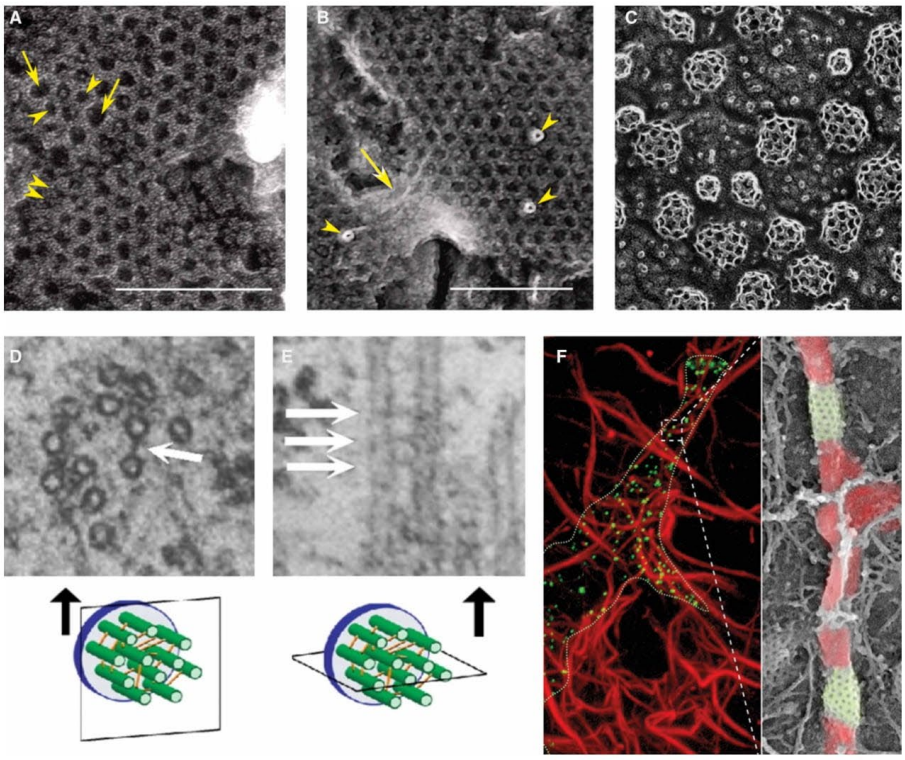

Figure 5. Clathrin structures in cells.

EM images reproduced from published works demonstrating the different shapes clathrin complexes can make. (**A**) Flat clathrin lattice formed primarily of hexagonal arrangements. Yellow arrows highlight other arrangements including pentagonal (arrowheads) and heptagonal (arrows). (**B**) Flat clathrin lattices with a distorted or incomplete connecting lattice between the two, indicated by a yellow arrow, as well as possible attached remnants of cytoskeletal filaments, indicated by yellow arrowheads. **A** and **B** are reprinted from Akisaka et al. [172] with permission from Elsevier. Scale bar represents 0.2 μm. (**C**) Clathrin coated vesicles formed primarily in a pentagonal arrangement. Reproduced and adapted with permission from the Heuser lab. (**D** and **E**) Orthogonal (**D**) and longitudinal (**E**) slices of kinetochore fibres, with bridges indicated by white arrows. It has been suggested that clathrin contributes to the composition of these bridges. Images are from Royle et al. [173], reproduced and adapted with permission from The Company of Biologists Ltd. Original EM images from ©1970 Rockefeller University Press. Originally published in Hepler et al. [174]. (**F**) Collagen fibres (red) with clathrin lattices (green) forming tubular structures around the fibers. From Elkhatib et al. [175]. Reproduced and adapted with permission from AAAS. Panels **C**–**F**: No scale bars were available from original publication.

contributing both to clathrin-mediated endocytosis and a newly identified form of endocytosis called fast endophilin-mediated endocytosis (FEME). While clathrin is essential for synaptic vesicle regeneration, its precise role has been re-examined in light of developments such as the identification of FEME and activity-dependent bulk endocytosis (ADBE), reviewed in Chanaday et al. [180]. CCV uncoating has long been identified as an essential component of synaptic vesicle regeneration [178,181–183] but further light has been shed on this by a report from Farsi et al. [184] that reacidification of synaptic vesicles occurs rapidly following Hsc70-driven removal of clathrin coats. Farsi et al. propose a model whereby steric hindrance by the assembled clathrin scaffold inhibits vATPase activity. This intriguing possibility further highlights the versatility of clathrin in different functional contexts.

Biochemical Journal (2021) **478** 3099–3123
https://doi.org/10.1042/BCJ20200740

Hormone desensitisation

Hormone desensitisation is essential for controlling the cellular response to hormones in the environment. Desensitisation follows sustained stimulation of receptors, leading them to lose their ability to respond to the hormone. Clathrin-mediated endocytosis has been shown to facilitate desensitisation through the internalisation of a wide range of receptors, including the parathyroid hormone receptor, β2-adrenergic receptor, and delta-opioid receptor [185–187]. In the case of G-protein-coupled receptors (GPCR) [188,189], desensitisation is mediated through phosphorylation of the GPCRs, which often occurs within their C-terminal tail. This stimulates arrestins (such as beta-arrestin) to bind to the GPCR, which prevents activation of the associated G-protein and targets the GPCR for internalisation via CME through the interaction of arrestin with the clathrin terminal domain and AP2 [190–194]. It is now understood that there are multiple routes for GPCR internalisation that employ both clathrin-independent endocytic pathways and clathrin and AP-2 dependent, but arrestin-independent, routes [195].

Spermiogenesis

Spermiogenesis must be performed to create functional sperm cells, which is the process of forming matured elongated spermatids. CME is vital during spermiogenesis as it ensures germ cells take up the proteins and molecules required to create components for the flagellum and acrosome [196]. For example, the spreading and shaping of the acrosome over the nucleus and establishing distinct regions in the acrosome have been attributed to coated vesicle formation at the acrosome posterior and the trafficking of vesicles between the Golgi apparatus and acrosome [197].

CME adaptors may also have other roles besides enabling CME during spermiogenesis. Stromal membrane-associated protein 2 (SMAP2) is an ADP ribosylation factor (Arf) GTPase-activating protein that interacts with CALM and clathrin. During spermiogenesis, SMAP2 deficiency impairs acrosome formation and nucleus reorganisation, and causes the trans-Golgi network structure to be distorted and produce larger proacrosomal vesicles, as CALM is not recruited to the trans-Golgi network. This suggests that CALM regulation of proacrosomal vesicle size at the trans-Golgi network is vital for acrosome formation [198]. Another example involves endophilin. The endophilin III N-terminal BAR domain protein called endophilin A3 has been found to interact with the protein DPY30 domain-containing protein 1 (DYDC1), which is exclusively expressed in the brain and testis and accumulates around the acrosome during the late stages of spermiogenesis. Knockdown of DYDC1 negatively impacts acrosome formation, suggesting that endophilin A3 and DYDC1 are required for acrosome formation [199]. Endophilin A3 has also been found to form a complex with activated epidermal growth factor receptor and interact with Synaptojanin I, with endophilin A3, clathrin and synaptojanin being colocalised in elongated spermatids [196]. This evidence suggests that the CME adaptors endophilin A3, Synaptojanin I, CALM, and clathrin are necessary for acrosome development during spermatogenesis.

Collagen and cell migration

Clathrin's shape shifting ability is further illustrated in the context of cell migration. Regulation of integrin endocytosis is required for adhesion disassembly and cell movement, which is achieved through the recruitment of clathrin coated structures (CCS) to focal adhesions [200,201]. Focal adhesions form contacts between intracellular actin bundles and extracellular substrates and are mostly observed at the extremities of elongated cells during cell migration [202].

During cell migration, CCS's will also interact with collagen fibres. In comparison with other areas of the cell, CCS's are found to nucleate preferentially along collagen fibres, and when in contact with collagen fibres, CCS's are longer lived [175]. As CCSs that interact with integrin can form tight contacts with planar substrates [203,204], CCSs bound to collagen fibres allow cells to anchor cellular protrusions to collagen fibres by forming tight contacts with integrin-containing focal adhesions. Pinching of collagen fibres by CCSs may also create friction to help cells produce long protrusions for cell migration [175]. The clathrin-coated structures identified by Elkhatib et al. [175] showed previously unseen clathrin lattices with a cylindrical shape, further emphasising the versatility of clathrin assemblies (See Figure 5).

Elkhatib et al. [175] also showed that the endocytic adaptors Disabled-2 (Dab2) and AP2 were essential for cellular migration [175]. Dab2 is required for recruiting integrins. Silencing of Dab2 inhibits the clustering of integrins on CCS's, leading to reduced CCS lifetimes on collagen fibres. This suggested that Dab2 and integrin are required for balancing out budding forces created by CCS's on collagen fibres. Silencing of Dab2 and AP2

Biochemical Journal (2021) **478** 3099–3123
https://doi.org/10.1042/BCJ20200740

also caused a more pronounced retraction of cellular protrusions, further supporting the idea that CCSs stabilise cellular protrusions by anchoring collagen fibres to focal adhesions, allowing cells to sustain high tension and form long protrusions during cell migration [175].

Mitosis

Perhaps one of the more unusual roles clathrin adopts in cells is in mitosis, since here its function does not appear to be associated with the formation of the curved or planar lattices that have become a hallmark of clathrin function in other contexts. In mitosis, a cell divides into two identical daughter cells. To carry this out, mitotic spindles attach to the kinetochore complex on chromosomes and bring the chromosomes together. The chromosomes are then aligned during the metaphase stage and segregated towards the poles of the cell during the anaphase stage. Clathrin has been found to colocalise alongside tubulin at mitotic spindles [18,173,205–207]. The mitotic spindle requires the presence of clathrin triskelia which have been shown to stabilise kinetochore fibres [18,208–210]. The N-terminal domains of clathrin are responsible for interactions between clathrin and microtubules within the mitotic spindle. The bridge hypothesis suggests that clathrin increases kinetochore stability by bracing between two to three microtubules within a kinetochore fibre, which is possible due to its trimeric structure. Experiments using clathrin constructs with altered trimeric structural properties have shown that the native structure of clathrin triskelia is vital for its stabilising function during metaphase and anaphase [209]. CHC acts with transforming acidic coiled-coil containing protein 3 (TACC3) and colonic hepatic tumour overexpressed gene (ch-TOG; also known as cytoskeleton-associated protein 5, CKAP5) in performing this function. Depletion of CHC has been found to stop TACC3 relocation to the mitotic spindle, which causes disorganised spindles and chromosome misalignment [211]. Recent work by Rondelet et al. [212] has identified an additional protein in this complex, GTSE1, which binds to clathrin via the N-terminal domain and inhibits the microtubule depolymerase MCAK. This discovery directly links clathrin-adaptor interactions classically associated with endocytosis, with stabilisation of microtubules during mitosis.

Interestingly, the clathrin light chain subunit, CLCa, also interacts with mitosis adaptors, such as mitotic arrest deficient 2-like protein 2 (MAD2B). MAD2B binds to the proteins cell division cycle protein 20 homolog (CDC20) and/or cadherin-1 to inhibit the anaphase promoting complex, and colocalise at the mitotic spindle. Depletion of MAD2B stops CLCa from being concentrated at the mitotic spindle, which inevitably leads to an increase in misaligned chromosomes [208]. The precise structures that clathrin adopts when associated with kinetochores have not yet been determined. However, the current morphological information available suggests that any structure adopted by clathrin is likely to differ from the classical polyhedral arrays seen in clathrin-coated vesicles and flat lattices, since such structures have not been observed in mitotic spindles [213].

Pathogen entry into cells facilitated by clathrin

One more dramatic form of shape-shifting performed by clathrin is in engulfment of large cargoes, and particularly microorganisms. Early studies showed that large areas of the plasma membrane surrounding vesicular stomatitis virus exhibited a clathrin coat as demonstrated in Figure 6A,B, and that internalisation depended on clathrin [214–217]. Since then, many viruses have been shown to enter cells by endocytosis, many through clathrin-dependent pathways [218]. Viruses present a sizeable cargo, but in 2005 it was shown that clathrin was essential for the internalisation of an even larger cargo, the bacterium *Listeria monocytgenes*, which can reach lengths of 2–6 μm long [219–222]. This led to further discoveries of a requirement for clathrin in internalisation of other bacteria including S. *aureus* and Enteropathogenic *E. coli* (EPEC), and the fungal pathogen *Candida albicans* [220,221,223–226].

Bonazzi et al. [221] investigated the mechanism by which clathrin might be employed to engulf cargo of such a size. Observations from electron microscopy images of cells undergoing infection by either *Listeria* or enteropathogenic *E. coli* (EPEC) showed that complete clathrin-coated vesicles were not observed in the vicinity of the bacterium. Rather clathrin-coated pits, of a size and shape similar to those observed in uninfected cells, were seen in the membrane surrounding the bacterium, as seen in Figure 6C,D. Immunolabelling of clathrin in HeLa cells infected with *L. monocytogenes* showed that it was always associated with curved invaginations, and was not seen in areas where the membrane was flat. In the case of EPEC-infected cells, clathrin in the vicinity of EPEC-induced actin pedestals also appeared in the form of coated pits rather than complete vesicles. Further investigations by Bonazzi et al. [221] showed that coated pit formation required the adaptor Dab2 and this in turn facilitated recruitment of actin via Hip1R and the clathrin light chain. Actin recruitment depended on tyrosine phosphorylation of the clathrin heavy chain. Once assembled, this machinery was then able to recruit

Biochemical Journal (2021) **478** 3099–3123
https://doi.org/10.1042/BCJ20200740

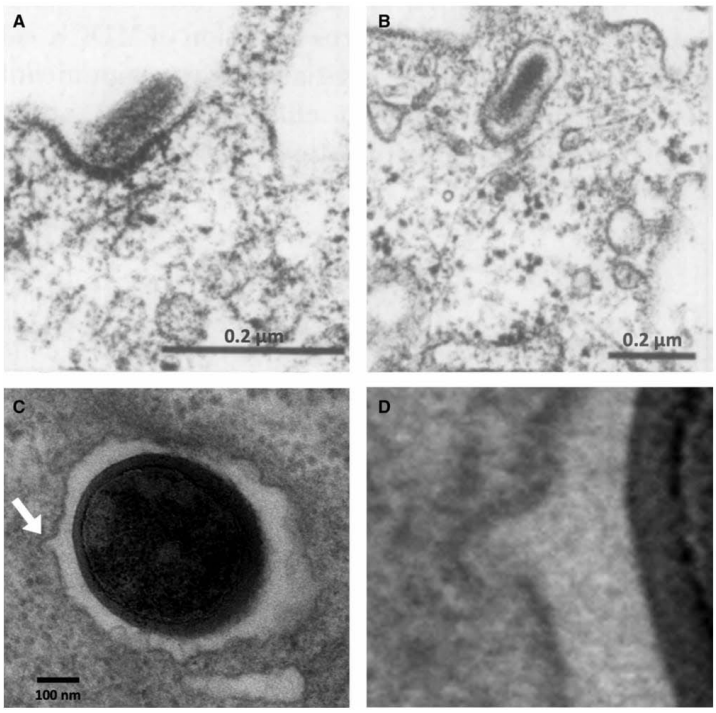

Figure 6. Early images of viral entry into cells.

TEM images of CME during viral entry. (**A** and **B**) CME of vesicular stomatitis virus in MDCK cells. (**A**) CCV formation around virus. (**B**) Partially coated CCV around internalised virus. **A** and **B** reprinted from Matlin et al. [217] with permission from Elsevier. (**C** and **D**) Formation of clathrin-coated structures during infection of Jeg3 cells by L. monocytogenes. The arrow points to a clathrin-coated structure close to the internalised bacterium. This is shown as an enlarged view in **D**. Image was provided by M. Bonazzi and P. Cossart and adapted by permission.

the motor protein Myosin VI which could provide a pulling force. Thus, in an alternative form of shape-shifting, the invading bacterium triggers clathrin and its associated machinery to organise actin to generate structures that facilitate uptake of a cargo far exceeding the size of a CCV.

GLUT4 trafficking and the role of CHC22

So far we have discussed the action of clathrin that in humans is encoded by the gene CLTC on chromosome 17 and is termed CHC17. However, in jawed vertebrates there is a second form of clathrin, CHC22, encoded by the gene CLTCL1 on chromosome 22 [227,228]. This form of clathrin is expressed most highly in muscle and adipose tissue and has been shown to play a key role in transport of insulin-regulated glucose transporter 4 (GLUT4). GLUT4 is a glucose transporter found in adipocyte and muscle cells which is transported to the cells plasma membrane upon insulin signalling [229,230]. This is achieved through sorting of GLUT4 into insulin-responsive vesicles for selective transport [230]. CHC22 interacts with GLUT4 as well as the ER-to-Golgi intermediate compartment (ERGIC) tether p115, sortilin, IRAP, and GGA2 to sort GLUT4 in the GLUT4 storage compartment in cells [229,231]. Unlike CHC17 which is involved in CME and other cellular pathways like mitosis and cell migration, CHC22 is limited to retrograde sorting as it does not support vesicle formation at

Biochemical Journal (2021) **478** 3099–3123
https://doi.org/10.1042/BCJ20200740

the plasma membrane in the presence or absence of CHC17, and also forms a more stable coat which cannot be removed by the same disassembly complex used to remove CHC17 [229,232]. CHC22 is also restricted in its tissue and species expression, in contrast to CHC17 [229]. Several studies however have suggested another role for CHC22 besides sorting GLUT4 involving the initiation of GLUT4 sequestration upon an insulin response. Down-regulation of either p115 or CHC22 reduces trafficking of GLUT4 to the plasma membrane, suggesting CHC22 initiates GLUT4 sequestration from the ERGIC in humans and conducts retrograde sorting of GLUT4 [231]. Additionally, functional studies of different CHC22 allotypes identified differences in GLUT4 transport in response to insulin; these results suggested that changes in diet (i.e. a shift from eating mostly meat to more plant-based foods) have impacted the allotype of CHC22 selected in humans, causing an alteration in the effectiveness of CHC22's role in insulin-regulated GLUT4 transport [227]. Further studies on the mechanism by which CHC22 sorts and transports GLUT4, as well as structural studies on a CHC22 coat that might explain its additional stability are needed to determine how this different form of clathrin CHC contributes to its more specialised function [227,229–232].

Clathrin shapeshifting

Clathrin exchange and the dynamic coat assembly model

Clathrin is remarkable for its ability to form both planar and curved lattice structures within its diverse cellular roles. This has led to debate about how, or whether, these clathrin lattice structures might shapeshift to form planar or curved arrangements. High energy costs have been predicted for remodelling of a planar clathrin lattice to a curved CCP due to the structural rearrangements between triskelion leg contacts that would be required [233,234]. Two models have emerged within this debate [235]. The first has been termed the 'constant curvature' model, in which clathrin assembles into a curved lattice as the membrane invaginates to form a CCP [19,236]. In the second 'dynamic coat' or 'constant area' model, the area of membrane coated by the clathrin lattice remains constant during budding while curvature increases [19,233,234,237–239]. These two models of CCV formation are illustrated in Figure 7A.

One means proposed by which a planar clathrin lattice could transform into a curved lattice involves dynamic exchange of clathrin between the invaginating membrane and a soluble pool of clathrin triskelia [96,240]. The mechanism by which this exchange could take place may utilise the coated vesicle uncoating apparatus of ATP-dependent clathrin disassembly by Hsc70, recruited to the vesicle by auxilin/GAK, and there is experimental evidence supporting this [139,241–243]. Exchange of clathrin in a 'wrong' conformation for new clathrin able to adopt a 'right' conformation that is fuelled by an existing ATP-driven system for clathrin disassembly neatly addresses the question of how established planar lattices could be remodelled to produce a curved coated pit [98,238,241,244]. However, arguing against this is the observation that in genome-edited cells, endogenously labelled auxilin and GAK could not be detected during the early stages of vesicle development [132].

A planar lattice is not, however, the only route to CCV formation. Clathrin-coated structures have been observed in a number of systems [108,246–248] to have formed independently, suggesting that a planar lattice is not a prerequisite for generation of curvature. Indeed, curved clathrin lattices have been shown to form spontaneously both *in vitro* and in unroofed cells [31,245] suggesting that lattice remodelling may not be essential in coated vesicle formation.

Evidence in support or otherwise of mechanisms for achieving clathrin modelling has been carefully discussed in several reviews [16,19,235] but as some authors point out [19,235] it seems likely that there are multiple routes to curvature. Such alternative routes may be influenced by the need to regulate import of cargo, as shown by Maib et al. [249]. In this study, the import of the GPCR P2Y12 into neuronal cells differed from that of transferrin in requiring clathrin rearrangement dependent on phosphorylation of CLCb and the presence of auxilin. This suggested that different modes of lattice formation may be required for certain cargos, which in turn could provide additional layers of control for their uptake.

Interestingly, recent work from Sochacki et al. [245] presents a comprehensive analysis of the morphology of clathrin lattices seen in eight different mammalian cell lines. As a result of this analysis the authors propose a new model for CCV formation whereby the potential to form curved structures is 'pre-programmed' within a planar lattice. This model is based on new structural detail obtained using cryo-electron tomography that has revealed irregular structures within planar lattices showing the potential for curved structures to form upon release of constraints holding the planar lattice in place [245]. This is in contrast with previous assumptions

Biochemical Journal (2021) **478** 3099–3123
https://doi.org/10.1042/BCJ20200740

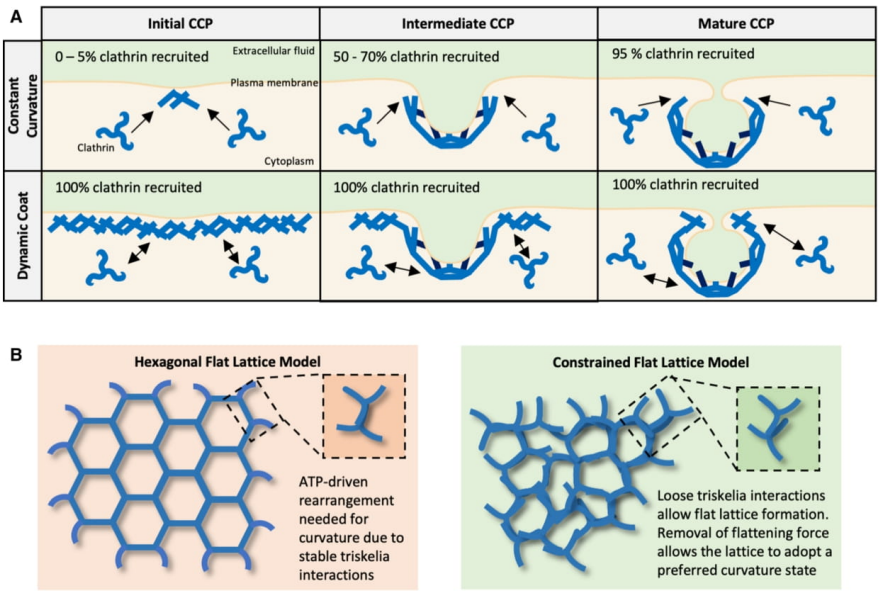

Figure 7. Models for CCV and flat lattice formation.

Schematic diagrams demonstrating models for CCV and flat lattice formation. (**A**) Two models for CCV formation, including the constant curvature model where no clathrin exchange occurs, and the dynamic coat model where all clathrin is recruited into a lattice prior to membrane bending and requires clathrin exchange for curvature formation. (**B**) Comparison of the hexagonal flat lattice model with the constrained flat lattice model proposed by Sochaki et al. [245].

that such lattices would be fully formed hexagonal arrays, upon which energetic calculations for changes in morphology had been based [233,234]. Figure 7B demonstrates the differences between the old and new models. This model suggests a new way to see clathrin shape-shifting — as the outcome of the balance achieved between opposing forces generated through interactions between membrane, adaptors and clathrin, membrane tension and the mechanical properties of these components.

A structural basis for clathrin shape-shifting

This review has so far focussed on the way that clathrin participates in cellular processes and in the involvement of binding partners in formation of multiple clathrin lattices. But clathrin is able to adopt different shapes in the absence of other cellular components, as shown in early studies [35,36,250–253] where multiple cage arrangements similar to those observed in coated vesicles could be induced using only purified protein [254]. Later studies showed that clathrin could also adopt more unusual conformations such as cube arrangements (see Figure 8) and tetrahedral cages [255,256]. On the other hand, formation of biochemically generated flat lattices seemed to require involvement of additional support such as stabilisation of clathrin association with a flat surface or membrane through use of an adaptor protein [31,92,257]. Thus, in this final section we discuss how the structural properties of clathrin itself lead to formation of multiple distinct lattice arrangements.

The mechanical properties of clathrin are determined by the tertiary structure of the CHC legs which are composed of pairs of short, stacked alpha helices, and the strong association of the CLC long helix which acts as a brace, giving strength and rigidity to the triskelion leg [92,233,234,258–261]. The trimerization domain, strengthened by additional helices contributed by the light chain C terminus, joins three CHC subunits together via a highly stable interaction to form the triskelion structure that serves as clathrin's smallest functional

Biochemical Journal (2021) **478** 3099–3123
https://doi.org/10.1042/BCJ20200740

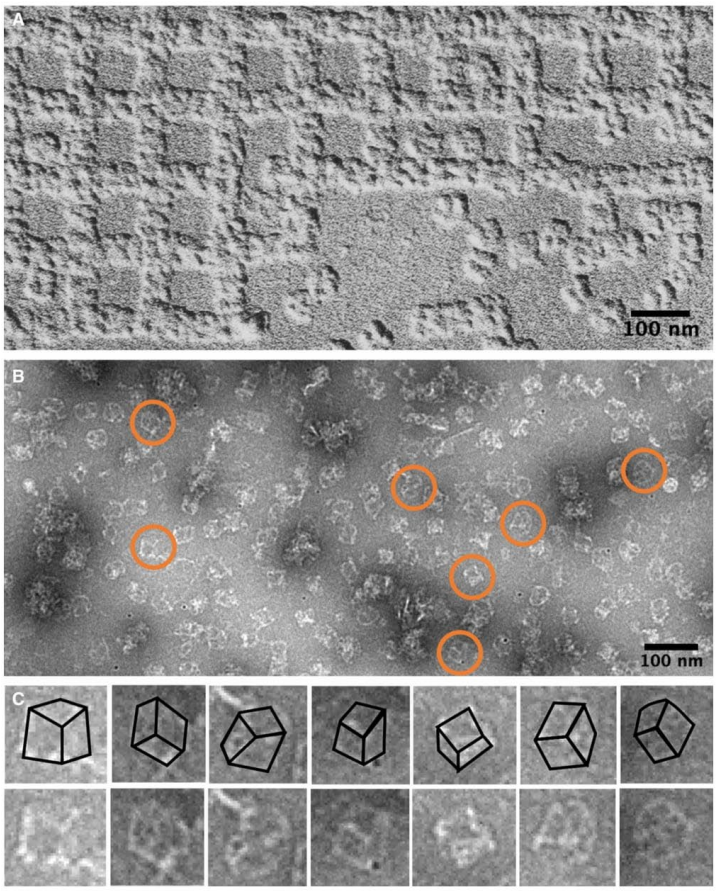

Figure 8. Cube lattice structures formed by clathrin *in vitro*.
Unusual structures formed from clathrin triskelia *in vitro*. (**A**) Electron micrograph of clathrin cubes that have formed into an open square-packed array. Image provided by R. A. Crowther. (**B** and **C**) Clathrin cube structures imaged by negative stain electron microscopy. Circled cubes in **B** have been enlarged and presented in **C** alongside fitted schematics of clathrin cubes to the images. Image provided by and adapted with permission from M. Halebian (Smith lab).

structural unit in classical clathrin lattices [260–263]. The arrangement of alpha helices in stacked pairs within the CHC leg seems to confer flexibility to the leg, as with the coils in a spring, that is then braced where the CLC binds. This is supported by structural studies showing that in conformations adopted by triskelion legs within a cage, most flexibility is seen beyond the reach of the bound light chain [41,264]. Furthermore, the mode of binding of the CLCs has been shown to influence CHC conformation [261] and a recent study has demonstrated a role for the light chain in controlling how clathrin deforms lipid membrane. Redlinghofer et al. [93] showed that the quality of clathrin lattices and the size and shape of clathrin-coated buds varied according to the composition of CLC isoforms a and b, and their neuronal splice variants, suggesting a means by which lattice size and shape could be controlled to meet the needs of the cell.

Biochemical Journal (2021) **478** 3099–3123
https://doi.org/10.1042/BCJ20200740

The relationship between leg conformation and lattice structure was explored by Morris et al. [41] who determined cryo-EM structures for five different types of cage arrangement, with three of these at sufficient resolution to support further analysis. Superimposition of the paths adopted by triskelion legs in several different cage forms showed that the leg shapes varied most through changes in the angle between the CHC distal joint and distal domain, ranging between 7° and 17°. Furthermore, the shapes of legs from similar types of local structure (e.g. a hexagonal or pentagonal face) could not always be superimposed, and no pattern between the leg angles adopted and the type of local structure formed could be seen. This suggested there were multiple ways in which legs could come together to arrive at the same overall cage structure. In contrast, however, no significant differences in intermolecular contact patterns were observed at the resolutions obtained, regardless of the type of local structure formed. This suggested that clathrin triskelia adopt a universal mode of assembly, and that multiple combinations of particular leg conformations can lead to structures with the same lattice geometry through adaptation of the shape of one leg to that of another [41]. Thus, assuming the energetic requirements of rearranging contacts could be met, clathrin seems to be uniquely adapted to being able to transition from planar to curved lattices simply through making relatively small changes in the leg angles adopted by clathrin triskelia. This in turn allows clathrin molecules to accommodate varying curvature and differing local geometric environments.

Conclusions

Clathrin's unusual structure and capacity to assemble into multiple lattice types gives it a remarkable 'shape-shifting' ability. In addition to forming lattices, clathrin is also able to bind multiple partners via its terminal domains. Lattice assembly together with coordination of multiple protein-protein interactions fits clathrin for multiple roles within cells. The best-known function is the formation of clathrin-coated vesicles which are employed in a variety of contexts including absorption of nutrients and other required molecules at the plasma membrane, receptor down-regulation, intracellular trafficking, synaptic vesicle recycling and spermiogenesis. The precise nature of the shape shifting required to achieve coated vesicle formation is still debated, but advances in cryo-electron tomography and correlative light and electron microscopy techniques, large scale statistical analyses and single molecule light microscopy are revealing these processes in increasing detail [48,132,245,265,266], and recent developments in time-resolved cryo-electron microscopy may enable the capture of conformational changes in clathrin and its assemblies on a millisecond timescale [267].

Alongside formation of clathrin-coated vesicles, clathrin forms other structures with different roles. The prevalence of flat clathrin lattices, or plaques, in cells has recently been termed 'frustrated endocytosis' [1]. Roles in signal transduction, cell migration and cell adhesion have been proposed and recently tubular clathrin structures have been observed around collagen fibres. These lattices appear to lend a stabilising force in situations where the cell makes contact with a surface, a large potential cargo, or neighbouring cells. These examples illustrate the versatility of the clathrin structure for different cellular roles and in these cases clathrin is seen to form different lattice morphologies. However, in the case of mitosis the situation appears to be different. Clathrin has been shown to stabilise the kinetochore within the mitotic spindle but so far none of the commonly observed clathrin lattices have been observed, suggesting that the shape adopted by clathrin in this role is unlike the classic polyhedral lattices we commonly see.

In conclusion, we see clathrin able to form a remarkable range of lattice structures in cells, and within different functions. At the core of this lies the ability of clathrin molecules to flexibly adapt to the shape of a neighbouring triskelion leg, whilst maintaining a universal mode of assembly. Discussion continues as to how these structures are formed but comprehensive studies of different cell types combined with high resolution structural analysis show promise in addressing the many questions such structural arrangements pose.

Data Availability

Molecular models 1B89, 1XI5, 6SCT, 1BPO, 3IYV used in the production of Figure 2 can be found at Protein Data Bank in Europe (PDBe) at https://www.ebi.ac.uk/pdbe/. E.M. maps EMD-5119 and EMD-0126 used in the production of Figure 2 can be found at the Electron Microscopy Data Bank (EMDB) at PDBe: https://www.ebi.ac.uk/pdbe/emdb/index.html.

Competing Interests

The authors declare that there are no competing interests associated with the manuscript.

Acknowledgements
K.M.W. is funded by MRC Doctoral Training Partnership grant MR/N014294/1. C.J.S. thanks BBSRC [grant no. BB/N008391/1] for support and the Royal Society and Leverhulme Trust for a Senior Research Leave Fellowship. We thank S J Royle for helpful comments on the manuscript.

Abbreviations
ADBE, Activity-dependent bulk endocytosis; ADP, Adenosine diphosphate; AP1, Adaptor protein 1; AP180, Assembly protein 180 kDa; AP2, Adaptor protein 2; Arf, ADP ribosylation factor; ATP, Adenosine triphosphate; BAR, Bin/Amphiphysin/Rvs; CALM, Clathrin-assembly lymphoid myeloid leukaemia protein; CCP, Clathrin coated pit; CCS, Clathrin coated structure; CCV, Clathrin coated vesicle; CDC20, Cell division cycle protein 20 homolog; CHC, Clathrin heavy chain; ch-TOG, Colonic hepatic tumour overexpressed gene; CKAP5, Cytoskeleton-associated protein 5; CLC, Clathrin light chain; CME, Clathrin mediated endocytosis; Dab2, Disabled-2; DYDC1, DPY30 domain-containing protein 1; Eps15, Epidermal growth factor receptor substrate 15; Eps15R, Epidermal growth factor receptor substrate 15 receptor; FBXO32, F-Box Protein 32; FCHo1/2, Fer/Cip4 homology domain-only proteins 1 and 2; FEME, Fast endophilin-mediated endocytosis; FRAP, Fluorescence recovery after photobleaching; GAK, Cyclin G-associated kinase; GHSR-1a, GH secretagogue receptor subtype 1a; GPCR, G-protein coupled receptor; HIP1R, Huntington-interacting protein 1-related protein; Hsc70, Heat shock cognate 71 kDa protein; Hsp110, Heat shock protein 110; LϕXϕ[DE], L(L, I)(D, E, N)(L, F)(D, E); MAD2B, Mitotic arrest deficient 2-like protein 2; OCRL1, Oculocerebrorenal syndrome of Lowe protein 1; PDB, Protein Data Bank; PI(4,5)P2, Phosphatidylinositol 4,5-bisphosphate; PTEN, Phosphatase and tensin homolog deleted on chromosome ten; RME, Receptor mediated endocytosis; SMAP2, Stromal membrane-associated protein 2; SNX9, Sorting Nexin 9; SV, Synaptic vesicle; TACC3, Transforming acidic coiled-coil containing protein 3; TIRF, Total internal reflection fluorescence.

References

1 Baschieri, F., Porshneva, K. and Montagnac, G. (2020) Frustrated clathrin-mediated endocytosis: causes and possible functions. *J. Cell Sci.* **133**, jcs240861 https://doi.org/10.1242/jcs.240861
2 Doherty, G.J. and McMahon, H.T. (2009) Mechanisms of endocytosis. *Annu. Rev. Biochem.* **78**, 857–902 https://doi.org/10.1146/annurev.biochem.78.081307.110540
3 Mayor, S., Parton, R.G. and Donaldson, J.G. (2014) Clathrin-independent pathways of endocytosis. *Cold Spring Harb. Perspect. Biol.* **6**, a016758 https://doi.org/10.1101/cshperspect.a016758
4 Mettlen, M., Loerke, D., Yarar, D., Danuser, G. and Schmid, S.L. (2010) Cargo- and adaptor-specific mechanisms regulate clathrin-mediated endocytosis. *J. Cell Biol.* **188**, 919–933 https://doi.org/10.1083/jcb.200908078
5 Garrett, W.S. and Mellman, I. (2001) Studies of endocytosis. In *Dendritic Cells*, 2nd ed (Lotze, M.T. and Thomson, A.W., eds), pp. 213–229, Academic Press
6 Stillwell, W. (2016) Membrane Transport. In *An Introduction to Biological Membranes*, 2nd edition, pp. 423–451, Elsevier https://doi.org/10.1016/B978-0-444-63772-7.00019-1
7 Cullen, P.J. and Steinberg, F. (2018) To degrade or not to degrade: mechanisms and significance of endocytic recycling. *Nat. Rev. Mol. Cell Biol.* **19**, 679–696 https://doi.org/10.1038/s41580-018-0053-7
8 Bitsikas, V., Corrêa, I.R. and Nichols, B.J. (2014) Clathrin-independent pathways do not contribute significantly to endocytic flux. *eLife* **3**, e03970 https://doi.org/10.7554/elife.03970
9 Roth, T.F. and Porter, K.R. (1964) Yolk protein uptake in the oocyte of the mosquito *Aedes aegypti*. L. *J. Cell Biol.* **20**, 313–332 https://doi.org/10.1083/jcb.20.2.313
10 Pearse, B.M.F. (1975) Coated vesicles from pig brain: purification and biochemical characterization. *J. Mol. Biol.* **97**, 93–98 https://doi.org/10.1016/s0022-2836(75)80024-6
11 Kaksonen, M. and Roux, A. (2018) Mechanisms of clathrin-mediated endocytosis. *Nat. Rev. Mol. Cell Biol.* **19:**, 313–326 https://doi.org/10.1038/nrm.2017.132
12 Zhang, B., Koh, Y.H., Beckstead, R.B., Budnik, V., Ganetzky, B. and Bellen, H.J. (1998) Synaptic vesicle size and number are regulated by a clathrin adaptor protein required for endocytosis. *Neuron* **21**, 1465–1475 https://doi.org/10.1016/s0896-6273(00)80664-9
13 Miller, S.E., Mathiasen, S., Bright, N.A., Pierre, F., Kelly, B.T., Kladt, N. et al. (2015) CALM regulates clathrin-coated vesicle size and maturation by directly sensing and driving membrane curvature. *Dev. Cell* **33**, 163–175 https://doi.org/10.1016/j.devcel.2015.03.002
14 Wideman, J.G., Leung, K.F., Field, M.C. and Dacks, J.B. (2014) The cell biology of the endocytic system from an evolutionary perspective. *Cold Spring Harb. Perspect. Biol.* **6**, a016998 https://doi.org/10.1101/cshperspect.a016998
15 Ho, H.-C. (2008) Clathrin-coated vesicles leaving the caudal margin of the developing acrosome facilitate acrosomal shaping during mouse spermiogenesis. *Biol. Reprod.* **78**, 218 https://doi.org/10.1093/biolreprod/78.s1.218b
16 Sochacki, K.A. and Taraska, J.W. (2019) From flat to curved clathrin: controlling a plastic ratchet. *Trends Cell Biol.* **29**, 241–256 https://doi.org/10.1016/j.tcb.2018.12.002
17 Wecker, L. (2007) Receptor Regulation. In *xPharm: the Comprehensive Pharmacology Reference* (Enna, S.J. and David B. Bylund, eds.), pp. 1–5, Elsevier https://doi.org/10.1016/B978-008055232-3.60004-2

Biochemical Journal (2021) **478** 3099–3123
https://doi.org/10.1042/BCJ20200740

18 Royle, S.J., Bright, N.A. and Lagnado, L. (2005) Clathrin is required for the function of the mitotic spindle. *Nature* **434**, 1152–1157 https://doi.org/10.1038/nature03502
19 Briant, K., Redlingshöfer, L. and Brodsky, F.M. (2020) Clathrin's life beyond 40: connecting biochemistry with physiology and disease. *Curr. Opin. Cell Biol.* **65**, 141–149 https://doi.org/10.1016/j.ceb.2020.06.004
20 Smith, S.M., Baker, M., Halebian, M. and Smith, C.J. (2017) Weak molecular interactions in clathrin-mediated endocytosis. *Front. Mol. Biosci.* **4**, 72 https://doi.org/10.3389/fmolb.2017.00072
21 Goldstein, J.L., Brown, M.S., Anderson, R.G.W., Russell, D.W. and Schneider, W.J. (1985) Receptor-mediated endocytosis: concepts emerging from the LDL receptor system. *Annu. Rev. Cell Biol.* **1**, 1–39 https://doi.org/10.1146/annurev.cb.01.110185.000245
22 McMahon, H.T. and Boucrot, E. (2011) Molecular mechanism and physiological functions of clathrin-mediated endocytosis. *Nat. Rev. Mol. Cell Biol.* **12**, 517–533 https://doi.org/10.1038/nrm3151
23 Zhang, F., Zang, T., Wilson, S.J., Johnson, M.C. and Bieniasz, P.D. (2011) Clathrin facilitates the morphogenesis of retrovirus particles. *PLoS Pathog.* **7**, e1002119 https://doi.org/10.1371/journal.ppat.1002119
24 Song, L., He, Y., Ou, J., Zhao, Y., Li, R., Cheng, J. et al. (2017) Auxilin underlies progressive locomotor deficits and dopaminergic neuron loss in a drosophila model of Parkinson's disease. *Cell Rep.* **18**, 1132–1143 https://doi.org/10.1016/j.celrep.2017.01.005
25 Nguyen, M. and Krainc, D. (2018) LRRK2 phosphorylation of auxilin mediates synaptic defects in dopaminergic neurons from patients with Parkinson's disease. *Proc. Natl Acad. Sci. U.S.A.* **115**, 5576–5581 https://doi.org/10.1073/pnas.1717590115
26 Thomas, R.S., Henson, A., Gerrish, A., Jones, L., Williams, J. and Kidd, E.J. (2016) Decreasing the expression of PICALM reduces endocytosis and the activity of β-secretase: implications for Alzheimer's disease. *BMC Neurosci.* **17**, 50 https://doi.org/10.1186/s12868-016-0288-1
27 Soutar, A.K. and Naoumova, R.P. (2004) Autosomal recessive hypercholesterolemia. *Semin. Vasc. Med.* **4**, 241–248 https://doi.org/10.1055/s-2004-861491
28 Maldonado-Báez, L. and Wendland, B. (2006) Endocytic adaptors: recruiters, coordinators and regulators. *Trends Cell Biol.* **16**, 505–513 https://doi.org/10.1016/j.tcb.2006.08.001
29 Henne, W.M., Boucrot, E., Meinecke, M., Evergren, E., Vallis, Y., Mittal, R. et al. (2010) FCHo proteins are nucleators of clathrin-mediated endocytosis. *Science* **328**, 1281–1284 https://doi.org/10.1126/science.1188462
30 Boucrot, E., Pick, A., Çamdere, G., Liska, N., Evergren, E., McMahon, H.T. et al. (2012) Membrane fission is promoted by insertion of amphipathic helices and is restricted by crescent BAR domains. *Cell* **149**, 124–136 https://doi.org/10.1016/j.cell.2012.01.047
31 Dannhauser, P.N. and Ungewickell, E.J. (2012) Reconstitution of clathrin-coated bud and vesicle formation with minimal components. *Nat. Cell Biol.* **14**, 634–639 https://doi.org/10.1038/ncb2478
32 Stabley, D.R., Jurchenko, C., Marshall, S.S. and Salaita, K.S. (2012) Visualizing mechanical tension across membrane receptors with a fluorescent sensor. *Nat. Methods* **9**, 64–67 https://doi.org/10.1038/nmeth.1747
33 Haucke, V. and Kozlov, M.M. (2018) Membrane remodeling in clathrin-mediated endocytosis. *J. Cell Sci.* **131**, jcs216812 https://doi.org/10.1242/jcs.216812
34 Lacy, M.M., Ma, R., Ravindra, N.G. and Berro, J. (2018) Molecular mechanisms of force production in clathrin-mediated endocytosis. *FEBS Lett.* **592**, 3586–3605 https://doi.org/10.1002/1873-3468.13192
35 Kirchhausen, T. and Harrison, S.C. (1981) Protein organization in clathrin trimers. *Cell* **23**, 755–761 https://doi.org/10.1016/0092-8674(81)90439-6
36 Ungewickell, E. and Branton, D. (1981) Assembly units of clathrin coats. *Nature* **289**, 420–422 https://doi.org/10.1038/289420a0
37 Fotin, A., Cheng, Y., Sliz, P., Grigorieff, N., Harrison, S.C., Kirchhausen, T. et al. (2004) Molecular model for a complete clathrin lattice from electron cryomicroscopy. *Nature* **432**, 573–579 https://doi.org/10.1038/nature03079
38 Chen, C.Y., Reese, M.L., Hwang, P.K., Ota, N., Agard, D. and Brodsky, F.M. (2002) Clathrin light and heavy chain interface: α-helix binding superhelix loops via critical tryptophans. *EMBO J.* **21**, 6072–6082 https://doi.org/10.1093/emboj/cdf594
39 Kirchhausen, T., Scarmato, P., Harrison, S.C., Monroe, J.J., Chow, E.P., Mattaliano, R.J. et al. (1987) Clathrin light chains LCA and LCB are similar, polymorphic, and share repeated heptad motifs. *Science* **236**, 320–324 https://doi.org/10.1126/science.3563513
40 Kirchhausen, T. and Toyoda, T. (1993) Immunoelectron microscopic evidence for the extended conformation of light chains in clathrin trimers. *J. Biol. Chem.* **268**, 10268–10273 PMID:7683673
41 Morris, K.L., Jones, J.R., Halebian, M., Wu, S., Baker, M., Armache, J.-P. et al. (2019) Cryo-EM of multiple cage architectures reveals a universal mode of clathrin self-assembly. *Nat. Struct. Mol. Biol.* **26**, 890–898 https://doi.org/10.1038/s41594-019-0292-0
42 Ybe, J.A., Brodsky, F.M., Hofmann, K., Lin, K., Liu, S.-H., Chen, L. et al. (1999) Clathrin self-assembly is mediated by a tandemly repeated superhelix. *Nature* **399**, 371–375 https://doi.org/10.1038/20708
43 Haar E, T., Musacchio, A., Harrison, S.C. and Kirchhausen, T. (1998) Atomic structure of clathrin: a β propeller terminal domain joins an α zigzag linker. *Cell* **95**, 563–573 https://doi.org/10.1016/s0092-8674(00)81623-2
44 Pettersen, E.F., Goddard, T.D., Huang, C.C., Couch, G.S., Greenblatt, D.M., Meng, E.C. et al. (2004) UCSF chimera: a visualization system for exploratory research and analysis. *J. Comput. Chem.* **25**, 1605–1612 https://doi.org/10.1002/jcc.20084
45 Cheng, Y., Boll, W., Kirchhausen, T., Harrison, S.C. and Walz, T. (2007) Cryo-electron tomography of clathrin-coated vesicles: structural implications for coat assembly. *J. Mol. Biol.* **365**, 892–899 https://doi.org/10.1016/j.jmb.2006.10.036
46 Heymann, J.B., Winkler, D.C., Yim, Y.-I., Eisenberg, E., Greene, L.E. and Steven, A.C. (2013) Clathrin-coated vesicles from brain have small payloads: a cryo-electron tomographic study. *J. Struct. Biol.* **184**, 43–51 https://doi.org/10.1016/j.jsb.2013.05.006
47 Smith, C.J., Grigorieff, N. and Pearse, B.M.F. (1998) Clathrin coats at 21 Å resolution: a cellular assembly designed to recycle multiple membrane receptors. *EMBO J.* **17**, 4943–4953 https://doi.org/10.1093/emboj/17.17.4943
48 Paraan, M., Mendez, J., Sharum, S., Kurtin, D., He, H. and Stagg, S.M. (2020) The structures of natively assembled clathrin-coated vesicles. *Sci. Adv.* **6**, eaba8397 https://doi.org/10.1126/sciadv.aba8397
49 Haar E, T., Harrison, S.C. and Kirchhausen, T. (1999) Peptide-in-groove interactions link target proteins to the beta-propeller of clathrin. *Proc. Natl Acad. Sci. U.S.A.* **97**, 1096–1100 https://doi.org/10.1073/pnas.97.3.1096
50 Shih, W., Gallusser, A. and Kirchhausen, T. (1995) A clathrin-binding site in the hinge of the β2 chain of mammalian AP-2 complexes. *J. Biol. Chem.* **270**, 31083–31090 https://doi.org/10.1074/jbc.270.52.31083

51 Ramjaun, A.R. and McPherson, P.S. (2002) Multiple amphiphysin II splice variants display differential clathrin binding: identification of two distinct clathrin-binding sites. *J. Neurochem.* **70**, 2369–2376 https://doi.org/10.1046/j.1471-4159.1998.70062369.x
52 Krupnick, J.G., Goodman, O.B., Keen, J.H. and Benovic, J.L. (1997) Arrestin/clathrin interaction. localization of the clathrin binding domain of nonvisual arrestins to the carboxyl terminus. *J. Biol. Chem.* **272**, 15011–6 https://doi.org/10.1074/jbc.272.23.15011
53 Dell'Angelica, E.C., Klumperman, J., Stoorvogel, W. and Bonifacino, J.S. (1998) Association of the AP-3 adaptor complex with clathrin. *Science* **280**, 431–434 https://doi.org/10.1126/science.280.5362.431
54 Drake, M.T. and Traub, L.M. (2001) Interaction of two structurally distinct sequence types with the clathrin terminal domain β-Propeller. *J. Biol. Chem.* **276**, 28700–9 https://doi.org/10.1074/jbc.m104226200
55 Kang, D.S., Kern, R.C., Puthenveedu, M.A., von Zastrow, M., Williams, J.C. and Benovic, J.L. (2009) Structure of an arrestin2-clathrin complex reveals a novel clathrin binding domain that modulates receptor trafficking. *J. Biol. Chem.* **284**, 29860–29872 https://doi.org/10.1074/jbc.m109.023366
56 Miele, A.E., Watson, P.J., Evans, P.R., Traub, L.M. and Owen, D.J. (2004) Two distinct interaction motifs in amphiphysin bind two independent sites on the clathrin terminal domain β-propeller. *Nat. Struct. Mol. Biol.* **11**, 242–248 https://doi.org/10.1038/nsmb736
57 Willox, A.K., Sahraoui, Y.M.E. and Royle, S.J. (2014) Non-specificity of pitstop 2 in clathrin-mediated endocytosis. *Biol. Open* **3**, 326–331 https://doi.org/10.1242/bio.20147955
58 Muenzner, J., Traub, L.M., Kelly, B.T. and Graham, S.C. (2017) Cellular and viral peptides bind multiple sites on the N-terminal domain of clathrin. *Traffic* **18**, 44–57 https://doi.org/10.1111/tra.12457
59 Zhuo, Y., Cano, K.E., Wang, L., Ilangovan, U., Hinck, A.P., Sousa, R. et al. (2015) Nuclear magnetic resonance structural mapping reveals promiscuous interactions between clathrin-box motif sequences and the N-terminal domain of the clathrin heavy chain. *Biochemistry* **54**, 2571–2580 https://doi.org/10.1021/acs.biochem.5b00065
60 Smith, C.J., Dafforn, T.R., Kent, H., Sims, C.A., Khubchandani-Aswani, K., Zhang, L. et al. (2004) Location of auxilin within a clathrin cage. *J. Mol. Biol.* **336**, 461–471 https://doi.org/10.1016/j.jmb.2003.12.006
61 Zhuo, Y., Ilangovan, U., Schirf, V., Demeler, B., Sousa, R., Hinck, A.P. et al. (2010) Dynamic interactions between clathrin and locally structured elements in a disordered protein mediate clathrin lattice assembly. *J. Mol. Biol.* **404**, 274–290 https://doi.org/10.1016/j.jmb.2010.09.044
62 Schlosshauer, M. and Baker, D. (2004) Realistic protein-protein association rates from a simple diffusional model neglecting long-range interactions, free energy barriers, and landscape ruggedness. *Protein Sci.* **13**, 1660–1669 https://doi.org/10.1110/ps.03517304
63 Mettlen, M., Chen, P.-H., Srinivasan, S., Danuser, G. and Schmid, S.L. (2018) Regulation of clathrin-mediated endocytosis. *Annu. Rev. Biochem.* **87**, 871–896 https://doi.org/10.1146/annurev-biochem-062917-012644
64 Traub, L.M. (2011) Regarding the amazing choreography of clathrin coats. *PLoS Biol.* **9**, e1001037 https://doi.org/10.1371/journal.pbio.1001037
65 Merrifield, C.J., Feldman, M.E., Wan, L. and Almers, W. (2002) Imaging actin and dynamin recruitment during invagination of single clathrin-coated pits. *Nat. Cell Biol.* **4**, 691–698 https://doi.org/10.1038/ncb837
66 Taylor, M.J., Perrais, D. and Merrifield, C.J. (2011) A high precision survey of the molecular dynamics of mammalian clathrin-mediated endocytosis. *PLoS Biol.* **9**, e1000604 https://doi.org/10.1371/journal.pbio.1000604
67 Tonikian, R., Xin, X., Toret, C.P., Gfeller, D., Landgraf, C., Panni, S. et al. (2009) Bayesian modeling of the yeast SH3 domain interactome predicts spatiotemporal dynamics of endocytosis proteins. *PLoS Biol.* **7**, e1000218 https://doi.org/10.1371/journal.pbio.1000218
68 Kadlecova, Z., Spielman, S.J., Loerke, D., Mohanakrishnan, A., Reed, D.K. and Schmid, S.L. (2017) Regulation of clathrin-mediated endocytosis by hierarchical allosteric activation of AP2. *J. Cell Biol.* **216**, 167–179 https://doi.org/10.1083/jcb.201608071
69 Umasankar, P.K., Sanker, S., Thieman, J.R., Chakraborty, S., Wendland, B., Tsang, M. et al. (2012) Distinct and separable activities of the endocytic clathrin-coat components Fcho1/2 and AP-2 in developmental patterning. *Nat. Cell Biol.* **14**, 488–501 https://doi.org/10.1038/ncb2473
70 Cocucci, E., Aguet, F., Boulant, S. and Kirchhausen, T. (2012) The first five seconds in the life of a clathrin-coated pit. *Cell* **150**, 495–507 https://doi.org/10.1016/j.cell.2012.05.047
71 Ma, L., Umasankar, P.K., Wrobel, A.G., Lymar, A., McCoy, A.J., Holkar, S.S. et al. (2015) Transient Fcho1/2·Eps15/R-AP-2 nanoclusters prime the AP-2 clathrin adaptor for cargo binding. *Dev. Cell* **37**, 428–443 https://doi.org/10.1016/j.devcel.2016.05.003
72 Stimpson, H.E.M., Toret, C.P., Cheng, A.T., Pauly, B.S. and Drubin, D.G. (2009) Early-arriving Syp1p and Ede1p function in endocytic site placement and formation in budding yeast. *Mol. Biol. Cell* **20**, 4640–4651 https://doi.org/10.1091/mbc.e09-05-0429
73 Brach, T., Godlee, C., Moeller-Hansen, I., Boeke, D. and Kaksonen, M. (2014) The initiation of clathrin-mediated endocytosis is mechanistically highly flexible. *Curr. Biol.* **24**, 548–554 https://doi.org/10.1016/j.cub.2014.01.048
74 Brown, M.S. and Goldstein, J.L. (1979) Receptor-mediated endocytosis: insights from the lipoprotein receptor system. *Proc. Natl Acad. Sci. U.S.A.* **76**, 3330–3337 https://doi.org/10.1073/pnas.76.7.3330
75 Twyman, R.M. (2009) Clathrin and clathrin-Adaptors. In *Encyclopedia of Neuroscience* (Larry R. Squire, ed.), Academic Press, 1013–1017 https://doi.org/10.1016/b978-008045046-9.01364-4
76 Ehrlich, M., Boll, W., Van Oijen, A., Hariharan, R., Chandran, K., Nibert, M.L. et al. (2004) Endocytosis by random initiation and stabilization of clathrin-coated pits. *Cell* **118**, 591–605 https://doi.org/10.1016/j.cell.2004.08.017
77 Owen, D.J., Collins, B.M. and Evans, P.R. (2004) Adaptors for clathrin coats: structure and function. *Annu. Rev. Cell Dev. Biol.* **20**, 153–191 https://doi.org/10.1146/annurev.cellbio.20.010403.104543
78 Traub, L.M. (2009) Tickets to ride: selecting cargo for clathrin-regulated internalization. *Nat. Rev. Mol. Cell Biol.* **10**, 583–596 https://doi.org/10.1038/nrm2751
79 Koo, S.J., Markovic, S., Puchkov, D., Mahrenholz, C.C., Beceren-Braun, F., Maritzen, T. et al. (2011) SNARE motif-mediated sorting of synaptobrevin by the endocytic adaptors clathrin assembly lymphoid myeloid leukemia (CALM) and AP180 at synapses. *Proc. Natl Acad. Sci. U.S.A.* **108**, 13540–5 https://doi.org/10.1073/pnas.1107067108
80 Liu, A.P., Aguet, F., Danuser, G. and Schmid, S.L. (2010) Local clustering of transferrin receptors promotes clathrin-coated pit initiation. *J. Cell Biol.* **191**, 1381–1393 https://doi.org/10.1083/jcb.201008117
81 Kibbey, R.G., Rizo, J., Gierasch, L.M. and Anderson, R.G. (1998) The LDL receptor clustering motif interacts with the clathrin terminal domain in a reverse turn conformation. *J. Cell Biol.* **142**, 59–67 https://doi.org/10.1083/jcb.142.1.59

Biochemical Journal (2021) **478** 3099–3123
https://doi.org/10.1042/BCJ20200740

82 Henry, A.G., Hislop, J.N., Grove, J., Thorn, K., Marsh, M. and von Zastrow, M. (2012) Regulation of endocytic clathrin dynamics by cargo ubiquitination. *Dev. Cell* **23**, 519–532 https://doi.org/10.1016/j.devcel.2012.08.003
83 Merrifield, C.J., Perrais, D. and Zenisek, D. (2005) Coupling between clathrin-coated-pit invagination, cortactin recruitment, and membrane scission observed in live cells. *Cell* **121**, 593–606 https://doi.org/10.1016/j.cell.2005.03.015
84 Nunez, D., Antonescu, C., Mettlen, M., Liu, A., Schmid, S.L., Loerke, D. et al. (2011) Hotspots organize clathrin-mediated endocytosis by efficient recruitment and retention of nucleating resources. *Traffic* **12**, 1868–1878 https://doi.org/10.1111/j.1600-0854.2011.01273.x
85 Antonescu, C.N., Aguet, F., Danuser, G. and Schmid, S.L. (2011) Phosphatidylinositol-(4,5)-bisphosphate regulates clathrin-coated pit initiation, stabilization, and size. *Mol. Biol. Cell* **22**, 2588–2600 https://doi.org/10.1091/mbc.e11-04-0362
86 Zoncu, R., Perera, R.M., Sebastian, R., Nakatsu, F., Chen, H., Balla, T. et al. (2007) Loss of endocytic clathrin-coated pits upon acute depletion of phosphatidylinositol 4,5-bisphosphate. *Proc. Natl Acad. Sci. U.S.A.* **104**, 3793–3798 https://doi.org/10.1073/pnas.0611733104
87 Carroll, S.Y., Stimpson, H.E.M., Weinberg, J., Toret, C.P., Sun, Y. and Drubin, D.G. (2012) Analysis of yeast endocytic site formation and maturation through a regulatory transition point. *Mol. Biol. Cell* **23**, 657–668 https://doi.org/10.1091/mbc.e11-02-0108
88 Mettlen, M., Stoeber, M., Loerke, D., Antonescu, C.N., Danuser, G. and Schmid, S.L. (2009) Endocytic accessory proteins are functionally distinguished by their differential effects on the maturation of clathrin-coated pits. *Mol. Biol. Cell* **20**, 3251–3260 https://doi.org/10.1091/mbc.e09-03-0256
89 Loerke, D., Mettlen, M., Yarar, D., Jaqaman, K., Jaqaman, H., Danuser, G. et al. (2009) Cargo and dynamin regulate clathrin-coated pit maturation. *PLoS Biol.* **7**, e57 https://doi.org/10. 1371/journal.pbio.1000057
90 Ford, M.G.J., Mills, I.G., Peter, B.J., Vallis, Y., Praefcke, G.J.K., Evans, P.R. et al. (2002) Curvature of clathrin-coated pits driven by epsin. *Nature* **419**, 361–366 https://doi.org/10.1038/nature01020
91 Saleem, M., Morlot, S., Hohendahl, A., Manzi, J., Lenz, M. and Roux, A. (2015) A balance between membrane elasticity and polymerization energy sets the shape of spherical clathrin coats. *Nat. Commun.* **6**, 6249 https://doi.org/10.1038/ncomms7249
92 Dannhauser, P.N., Platen, M., Böning, H., Ungewickell, H., Schaap, I.A.T. and Ungewickell, E.J. (2015) Effect of clathrin light chains on the stiffness of clathrin lattices and membrane budding. *Traffic* **16**, 519–533 https://doi.org/10.1111/tra.12263
93 Redlingshöfer, L., McLeod, F., Chen, Y., Camus, M.D., Burden, J.J., Palomer, E. et al. (2020) Clathrin light chain diversity regulates membrane deformation in vitro and synaptic vesicle formation in vivo. *Proc. Natl Acad. Sci. U.S.A.* **117**, 23527–23538 https://doi.org/10.1073/pnas.2003662117
94 Massol, R.H., Boll, W., Griffin, A.M. and Kirchhausen, T. (2006) A burst of auxilin recruitment determines the onset of clathrin-coated vesicle uncoating. *Proc. Natl Acad. Sci. U.S.A.* **103**, 10265–10270 https://doi.org/10.1073/pnas.0603369103
95 Schlossman, D.M., Schmid, S.L., Braell, W.A. and Rothman, J.E. (1984) An enzyme that removes clathrin coats: purification of an uncoating ATPase. *J. Cell Biol.* **99**, 723–733 https://doi.org/10.1083/jcb.99.2.723
96 Wu, X., Zhao, X., Baylor, L., Kaushal, S., Eisenberg, E. and Greene, L.E. (2001) Clathrin exchange during clathrin-mediated endocytosis. *J. Cell Biol.* **155**, 291–300 https://doi.org/10.1083/jcb.200104085
97 Loerke, D., Wienisch, M., Kochubey, O. and Klingauf, J. (2005) Differential control of clathrin subunit dynamics measured with EW-FRAP microscopy. *Traffic* **6**, 918–929 https://doi.org/10.1111/j.1600-0854.2005.00329.x
98 Avinoam, O., Schorb, M., Beese, C.J., Briggs, J.A.G. and Kaksonen, M. (2015) Endocytic sites mature by continuous bending and remodeling of the clathrin coat. *Science* **348**, 1369–1372 https://doi.org/10.1126/science.aaa9555
99 Sousa, R., Liao, H.S., Cuéllar, J., Jin, S., Valpuesta, J.M., Jin, A.J. et al. (2016) Clathrin-coat disassembly illuminates the mechanisms of Hsp70 force generation. *Nat. Struct. Mol. Biol.* **23**, 821–829 https://doi.org/10.1038/nsmb.3272
100 Picco, A., Mund, M., Ries, J., Nédélec, F. and Kaksonen, M. (2015) Visualizing the functional architecture of the endocytic machinery. *eLife* **4**, e04535 https://doi.org/10.7554/elife.04535
101 Collins, A., Warrington, A., Taylor, K.A. and Svitkina, T. (2011) Structural organization of the actin cytoskeleton at sites of clathrin-mediated endocytosis. *Curr. Biol.* **21**, 1167–1175 https://doi.org/10.1016/j.cub.2011.05.048
102 Carlsson, A.E. and Bayly P, V. (2014) Force generation by endocytic actin patches in budding yeast. *Biophys. J.* **106**, 1596–1606 https://doi.org/10.1016/j.bpj.2014.02.035
103 Dmitrieff, S. and Nédélec, F. (2015) Membrane mechanics of endocytosis in cells with turgor. *PLoS Comput. Biol.* **11**, e1004538 https://doi.org/10.1371/journal.pcbi.1004538
104 Ayscough, K.R., Stryker, J., Pokala, N., Sanders, M., Crews, P. and Drubin, D.G. (1997) High rates of actin filament turnover in budding yeast and roles for actin in establishment and maintenance of cell polarity revealed using the actin inhibitor latrunculin-A. *J. Cell Biol.* **137**, 399–416 https://doi.org/10.1083/jcb.137.2.399
105 Fujimoto, L.M., Roth, R., Heuser, J.E. and Schmid, S.L. (2000) Actin assembly plays a variable, but not obligatory role in receptor-mediated endocytosis. *Traffic* **1**, 161–171 https://doi.org/10.1034/j.1600-0854.2000.010208.x
106 Lamaze, C., Fujimoto, L.M., Yin, H.L. and Schmid, S.L. (1997) The actin cytoskeleton is required for receptor-mediated endocytosis in mammalian cells. *J. Biol. Chem.* **272**, 20332–5 https://doi.org/10.1074/jbc.272.33.20332
107 Grassart, A., Cheng, A.T., Hong, S.H., Zhang, F., Zenzer, N., Feng, Y. et al. (2014) Actin and dynamin2 dynamics and interplay during clathrin-mediated endocytosis. *J. Cell Biol.* **205**, 721–735 https://doi.org/10.1083/jcb.201403041
108 Li, D., Shao, L., Chen, B.-C., Zhang, X., Zhang, M., Moses, B. et al. (2015) Extended-resolution structured illumination imaging of endocytic and cytoskeletal dynamics. *Science.* **349**, aab3500 https://doi.org/10.1126/science.aab3500
109 Akamatsu, M., Vasan, R., Serwas, D., Ferrin, M.A., Rangamani, P. and Drubin, D.G. (2020) Principles of self-organization and load adaptation by the actin cytoskeleton during clathrin-mediated endocytosis. *eLife* **9**, e49840 https://doi.org/10.7554/elife.49840
110 Leyton-Puig, D., Isogai, T., Argenzio, E., van den Broek, B., Klarenbeek, J., Janssen, H. et al. (2017) Flat clathrin lattices are dynamic actin-controlled hubs for clathrin-mediated endocytosis and signalling of specific receptors. *Nat. Commun.* **8**, 16068 https://doi.org/10.1038/ncomms16068
111 Boulant, S., Kural, C., Zeeh, J.C., Ubelmann, F. and Kirchhausen, T. (2011) Actin dynamics counteract membrane tension during clathrin-mediated endocytosis. *Nat. Cell Biol.* **13**, 1124–1132 https://doi.org/10.1038/ncb2307
112 Engqvist-Goldstein, Å.EY., Zhang, C.X., Carreno, S., Barroso, C., Heuser, J.E. and Drubin, D.G. (2004) RNAi-mediated Hip1R silencing results in stable association between the endocytic machinery and the actin assembly machinery. *Mol. Biol. Cell* **15**, 1666–1679 https://doi.org/10.1091/mbc.e03-09-0639

113 Messa, M., Fernández-Busnadiego, R., Sun, E.W., Chen, H., Czapla, H., Wrasman, K. et al. (2014) Epsin deficiency impairs endocytosis by stalling the actin-dependent invagination of endocytic clathrin-coated pits. *eLife* **3**, e03311 https://doi.org/10.7554/elife.03311
114 Skruzny, M., Brach, T., Ciuffa, R., Rybina, S., Wachsmuth, M. and Kaksonen, M. (2012) Molecular basis for coupling the plasma membrane to the actin cytoskeleton during clathrin-mediated endocytosis. *Proc. Natl Acad. Sci. U.S.A.* **109**, E2533–E2542 https://doi.org/10.1073/pnas.1207011109
115 Skruzny, M., Desfosses, A., Prinz, S., Dodonova, S.O., Gieras, A., Uetrecht, C. et al. (2015) An organized Co-assembly of clathrin adaptors Is essential for endocytosis. *Dev. Cell* **33**, 150–162 https://doi.org/10.1016/j.devcel.2015.02.023
116 Frost, A., Perera, R., Roux, A., Spasov, K., Destaing, O., Egelman, E.H. et al. (2008) Structural basis of membrane invagination by F-BAR domains. *Cell* **132**, 807–817 https://doi.org/10.1016/j.cell.2007.12.041
117 Habermann, B. (2004) The BAR-domain family of proteins: a case of bending and binding? *EMBO Rep.* **5**, 250–255 https://doi.org/10.1038/sj.embor.7400105
118 Mim, C., Cui, H., Gawronski-Salerno, J.A., Frost, A., Lyman, E., Voth, G.A. et al. (2012) Structural basis of membrane bending by the N-BAR protein endophilin. *Cell* **149**, 137–145 https://doi.org/10.1016/j.cell.2012.01.048
119 Schöneberg, J., Lehmann, M., Ullrich, A., Posor, Y., Lo, W.T., Lichtner, G. et al. (2017) Lipid-mediated PX-BAR domain recruitment couples local membrane constriction to endocytic vesicle fission. *Nat. Commun.* **8**, 15873 https://doi.org/10.1038/ncomms15873
120 Wu, M., Huang, B., Graham, M., Raimondi, A., Heuser, J.E., Zhuang, X. et al. (2010) Coupling between clathrin-dependent endocytic budding and F-BAR-dependent tubulation in a cell-free system. *Nat. Cell Biol.* **12**, 902–908 https://doi.org/10.1038/ncb2094
121 Itoh, T., Erdmann, K.S., Roux, A., Habermann, B., Werner, H. and De Camilli, P. (2005) Dynamin and the actin cytoskeleton cooperatively regulate plasma membrane invagination by BAR and F-BAR proteins. *Dev. Cell* **9**, 791–804 https://doi.org/10.1016/j.devcel.2005.11.005
122 Meinecke, M., Boucrot, E., Camdere, G., Hon, W.-C., Mittal, R. and McMahon, H.T. (2013) Cooperative recruitment of dynamin and BIN/amphiphysin/Rvs (BAR) domain-containing proteins leads to GTP-dependent membrane scission. *J. Biol. Chem.* **288**, 6651–6661 https://doi.org/10.1074/jbc.m112.444869
123 Antonny, B., Burd, C., De Camilli, P., Chen, E., Daumke, O., Faelber, K. et al. (2016) Membrane fission by dynamin: what we know and what we need to know. *EMBO J.* **35**, 2270–2284 https://doi.org/10.15252/embj.201694613
124 Morlot, S. and Roux, A. (2013) Mechanics of dynamin-mediated membrane fission. *Annu. Rev. Biophys.* **42**, 629–649 https://doi.org/10.1146/annurev-biophys-050511-102247
125 Ingerman, E., Perkins, E.M., Marino, M., Mears, J.A., McCaffery, J.M., Hinshaw, J.E. et al. (2005) Dnm1 forms spirals that are structurally tailored to fit mitochondria. *J. Cell Biol.* **170**, 1021–1027 https://doi.org/10.1083/jcb.200506078
126 Miserey-Lenkei, S., Chalancon, G., Bardin, S., Formstecher, E., Goud, B. and Echard, A. (2010) Rab and actomyosin-dependent fission of transport vesicles at the Golgi complex. *Nat. Cell Biol.* **12**, 645–654 https://doi.org/10.1038/ncb2067
127 Slepnev, V.I. and De Camilli, P. (2000) Accessory factors in clathrin-dependent synaptic vesicle endocytosis. *Nat. Rev. Neurosci.* **1**, 161–172 https://doi.org/10.1038/35044540
128 Watanabe, S., Mamer, L.E., Raychaudhuri, S., Luvsanjav, D., Eisen, J., Trimbuch, T. et al. (2018) Synaptojanin and endophilin mediate neck formation during ultrafast endocytosis. *Neuron* **98**, 1184–1197.e6 https://doi.org/10.1016/j.neuron.2018.06.005
129 McPherson, P.S., Garcia, E.P., Slepnev, V.I., David, C., Zhang, X., Grabs, D. et al. (1996) A presynaptic inositol-5-phosphatase. *Nature* **379**, 353–357 https://doi.org/10.1038/379353a0
130 Cremona, O., Di Paolo, G., Wenk, M.R., Lüthi, A., Kim, W.T., Takei, K. et al. (1999) Essential role of phosphoinositide metabolism in synaptic vesicle recycling. *Cell* **99**, 179–188 https://doi.org/10.1016/s0092-8674(00)81649-9
131 Nández, R., Balkin, D.M., Messa, M., Liang, L., Paradise, S., Czapla, H. et al. (2014) A role of OCRL in clathrin-coated pit dynamics and uncoating revealed by studies of lowe syndrome cells. *eLife* **3**, e02975 https://doi.org/10.7554/elife.02975
132 He, K., Song, E., Upadhyayula, S., Dang, S., Gaudin, R., Skillern, W. et al. (2020) Dynamics of auxilin 1 and GAK in clathrin-mediated traffic. *J. Cell Biol.* **219**, 201908142 https://doi.org/10.1083/jcb.201908142
133 He, K., Marsland, III, R., Upadhyayula, S., Song, E., Dang, S., Capraro, B.R. et al. (2017) Dynamics of phosphoinositide conversion in clathrin-mediated endocytic traffic. *Nature* **552**, 410–414 https://doi.org/10.1038/nature25146
134 Chang-Ileto, B., Frere, S.G., Chan, R.B., Voronov S, V., Roux, A. and Di Paolo, G. (2011) Synaptojanin 1-mediated PI(4,5)P2 hydrolysis is modulated by membrane curvature and facilitates membrane fission. *Dev. Cell* **20**, 206–218 https://doi.org/10.1016/j.devcel.2010.12.008
135 Di Paolo, G. and De Camilli, P. (2006) Phosphoinositides in cell regulation and membrane dynamics. *Nature* **443**, 651–657 https://doi.org/10.1038/nature05185
136 Traub, L.M. (2005) Common principles in clathrin-mediated sorting at the Golgi and the plasma membrane. *Biochim. Biophys. Acta Mol. Cell Res.* **1744**, 415–437 https://doi.org/10.1016/j.bbamcr.2005.04.005
137 Ahle, S. and Ungewickell, E. (1990) Auxilin, a newly identified clathrin-associated protein in coated vesicles from bovine brain. *J. Cell Biol.* **111**, 19–29 https://doi.org/10.1083/jcb.111.1.19
138 Schroder, S., Morris, S.A., Knorr, R., Plessmann, U., Weber, K., Vinh, N.G. et al. (1995) Primary structure of the neuronal clathrin-associated protein auxilin and its expression in bacteria. *Eur. J. Biochem.* **228**, 297–304 https://doi.org/10.1111/j.1432-1033.1995.0297n.x
139 Ungewickell, E., Ungewickell, H., Holstein, S.E.H., Lindner, R., Prasad, K., Barouch, W. et al. (1995) Role of auxilin in uncoating clathrin-coated vesicles. *Nature* **378**, 632–635 https://doi.org/10.1038/378632a0
140 Holstein, S.E., Ungewickell, H. and Ungewickell, E. (1996) Mechanism of clathrin basket dissociation: separate functions of protein domains of the dnaJ homologue auxilin. *J. Cell Biol.* **135**, 925–937 https://doi.org/10.1083/jcb.135.4.925
141 Fotin, A., Cheng, Y., Grigorieff, N., Walz, T., Harrison, S.C. and Kirchhausen, T. (2004) Structure of an auxilin-bound clathrin coat and its implications for the mechanism of uncoating. *Nature* **432**, 649–653 https://doi.org/10.1038/nature03078
142 Braell, W.A., Schlossman, D.M., Schmid, S.L. and Rothman, J.E. (1984) Dissociation of clathrin coats coupled to the hydrolysis of ATP: role of an uncoating ATPase. *J. Cell Biol.* **99**, 735–741 https://doi.org/10.1083/jcb.99.2.734
143 Kalli, A.C., Morgan, G. and Sansom, M.S.P. (2013) Interactions of the auxilin-1 PTEN-like domain with model membranes result in nanoclustering of phosphatidyl inositol phosphates. *Biophys. J.* **105**, 137–145 https://doi.org/10.1016/j.bpj.2013.05.012

Biochemical Journal (2021) **478** 3099–3123
https://doi.org/10.1042/BCJ20200740

144 Park, B.-C., Yim, Y.-I., Zhao, X., Olszewski, M.B., Eisenberg, E. and Greene, L.E. (2015) The clathrin-binding and J-domains of GAK support the uncoating and chaperoning of clathrin by Hsc70 in the brain. *J. Cell Sci.* **128**, 3811–3821 https://doi.org/10.1242/jcs.171058
145 Ungewickell, E., Ungewickell, H. and Holstein, S.E. (1997) Functional interaction of the auxilin J domain with the nucleotide- and substrate-binding modules of Hsc70. *J. Biol. Chem.* **272**, 19594–19600 https://doi.org/10.1074/jbc.272.31.19594
146 Barouch, W., Prasad, K., Greene, L. and Eisenberg, E. (1997) Auxilin-Induced interaction of the molecular chaperone Hsc70 with clathrin baskets. *Biochemistry* **36**, 4303–4308 https://doi.org/10.1021/bi962727z
147 Young, A., Stoilova-McPhie, S., Rothnie, A., Vallis, Y., Harvey-Smith, P., Ranson, N. et al. (2013) Hsc70-induced changes in clathrin-Auxilin cage structure suggest a role for clathrin light chains in cage disassembly. *Traffic* **14**, 987–996 https://doi.org/10.1111/tra.12085
148 Barouch, W., Prasad, K., Greene, L.E. and Eisenberg, E. (1994) ATPase activity associated with the uncoating of clathrin baskets by Hsp70. *J. Biol. Chem.* **269**, 28563–8 PMID:7961802
149 Prasad, K., Barouch, W., Greene, L. and Eisenberg, E. (1993) A protein cofactor is required for uncoating of clathrin baskets by uncoating ATPase. *J. Biol. Chem.* **268**, 23758–23761 https://doi.org/10.1016/s0021-9258(20)80445-1
150 Greene, M.K., Maskos, K. and Landry, S.J. (1998) Role of the J-domain in the cooperation of Hsp40 with Hsp70. *Proc. Natl Acad. Sci. U.S.A.* **95**, 6108–6113 https://doi.org/10.1073/pnas.95.11.6108
151 Xue, Y.-L., Zhou, L., Sun, Y., Li, H., Jones, G.W. and Song, Y. (2017) Steered molecular dynamics simulation of the binding of the bovine auxilin J domain to the Hsc70 nucleotide-binding domain. *J. Mol. Model.* **23**, 320 https://doi.org/10.1007/s00894-017-3453-2
152 Rapoport, I., Boll, W., Yu, A., Böcking, T. and Kirchhausen, T. (2008) A motif in the clathrin heavy chain required for the Hsc70/auxilin uncoating reaction. *Mol. Biol. Cell* **19**, 405–413 https://doi.org/10.1091/mbc.e07-09-0870
153 Xing, Y., Böcking, T., Wolf, M., Grigorieff, N., Kirchhausen, T. and Harrison, S.C. (2010) Structure of clathrin coat with bound Hsc70 and auxilin: mechanism of Hsc70-facilitated disassembly. *EMBO J.* **29**, 655–665 https://doi.org/10.1038/emboj.2009.383
154 Sousa, R. and Lafer, E.M. (2015) The role of molecular chaperones in clathrin mediated vesicular trafficking. *Front. Mol. Biosci.* **2**, 26 https://doi.org/10.3389/fmolb.2015.00026
155 Böcking, T., Aguet, F., Rapoport, I., Banzhaf, M., Yu, A., Zeeh, J.C. et al. (2014) Key interactions for clathrin coat stability. *Structure* **22**, 819–829 https://doi.org/10.1016/j.str.2014.04.002
156 Sousa, R. (2014) Structural mechanisms of chaperone mediated protein disaggregation. *Front. Mol. Biosci.* **1**, 12 https://doi.org/10.3389/fmolb.2014.00012
157 Böcking, T., Aguet, F., Harrison, S.C. and Kirchhausen, T. (2011) Single-molecule analysis of a molecular disassemblase reveals the mechanism of Hsc70-driven clathrin uncoating. *Nat. Struct. Mol. Biol.* **18**, 295–301 https://doi.org/10.1038/nsmb.1985
158 Ferreira, F., Foley, M., Cooke, A., Cunningham, M., Smith, G., Woolley, R. et al. (2012) Endocytosis of G protein-coupled receptors is regulated by clathrin light chain phosphorylation. *Curr. Biol.* **22**, 1361–1370 https://doi.org/10.1016/j.cub.2012.05.034
159 Krantz, K.C., Puchalla, J., Thapa, R., Kobayashi, C., Bisher, M., Viehweg, J. et al. (2013) Clathrin coat disassembly by the yeast Hsc70/Ssa1p and auxilin/Swa2p proteins observed by single-particle burst analysis spectroscopy. *J. Biol. Chem.* **288**, 26721 https://doi.org/10.1074/jbc.m113.491753
160 Rothnie, A., Clarke, A.R., Kuzmic, P., Cameron, A. and Smith, C.J. (2011) A sequential mechanism for clathrin cage disassembly by 70-kDa heat-shock cognate protein (Hsc70) and auxilin. *Proc. Natl Acad. Sci. U.S.A.* **108**, 6927–6932 https://doi.org/10.1073/pnas.1018845108
161 Packschies, L., Theyssen, H., Buchberger, A., Bukau, B., Goody, R. and Reinstein, J. (1997) Grpe accelerates nucleotide exchange of the molecular chaperone dnaK with an associative displacement mechanism. *Biochemistry* **36**, 3417–3422 https://doi.org/10.1021/bi962835l
162 McCarty, J.S., Buchberger, A., Reinstein, J. and Bukau, B. (1995) The role of ATP in the functional cycle of the dnaK chaperone system. *J. Mol. Biol.* **249**, 126–137 https://doi.org/10.1006/jmbi.1995.0284
163 Takeda, S. and McKay, D.B. (1996) Kinetics of peptide binding to the bovine 70 kDa heat shock cognate protein, a molecular chaperone †. *Biochemistry* **35**, 4636–4644 https://doi.org/10.1021/bi952903o
164 Theyssen, H., Schuster, H.-P., Packschies, L., Bukau, B. and Reinstein, J. (1996) The second step of ATP binding to dnaK induces peptide release. *J. Mol. Biol.* **263**, 657–670 https://doi.org/10.1006/jmbi.1996.0606
165 Morgan, J.R., Jiang, J., Oliphint, P.A., Jin, S., Gimenez, L.E., Busch, D.J. et al. (2013) A role for an Hsp70 nucleotide exchange factor in the regulation of synaptic vesicle endocytosis. *J. Neurosci.* **33**, 8009 https://doi.org/10.1523/jneurosci.4505-12.2013
166 Lee, D.-W., Wu, X., Eisenberg, E. and Greene, L.E. (2006) Recruitment dynamics of GAK and auxilin to clathrin-coated pits during endocytosis. *J. Cell Sci.* **119**, 3502–3512 https://doi.org/10.1242/jcs.03092
167 Sousa, R. and Lafer, E.M. (2019) The physics of entropic pulling: a novel model for the Hsp70 motor mechanism. *Int. J. Mol. Sci.* **20**, 2334 https://doi.org/10.3390/ijms20092334
168 Goloubinoff, P. and Rios, P.D.L. (2007) The mechanism of Hsp70 chaperones: (entropic) pulling the models together. *Trends Biochem. Sci.* **32**, 372–380 https://doi.org/10.1016/j.tibs.2007.06.008
169 Rios, P.D.L., Ben-Zvi, A., Slutsky, O., Azem, A. and Goloubinoff, P. (2006) Hsp70 chaperones accelerate protein translocation and the unfolding of stable protein aggregates by entropic pulling. *Proc. Natl Acad. Sci. U.S.A.* **103**, 6166–6171 https://doi.org/10.1073/pnas.0510496103
170 Kirchhausen, T. (2000) Clathrin. *Annu. Rev. Biochem.* **69**, 699–727 https://doi.org/10.1146/annurev.biochem.69.1.699
171 Ramanan, V., Agrawal, N.J., Liu, J., Engles, S., Toy, R. and Radhakrishnan, R. (2011) Systems biology and physical biology of clathrin-mediated endocytosis. *Integr. Biol. (Camb)* **3**, 803–815 https://doi.org/10.1039/c1ib00036e
172 Akisaka, T. and Yoshida, A. (2021) Surface distribution of heterogenous clathrin assemblies in resorbing osteoclasts. *Exp. Cell Res.* **399**, 112433 https://doi.org/10.1016/j.yexcr.2020.112433
173 Royle, S.J. (2012) The role of clathrin in mitotic spindle organisation. *J. Cell Sci.* **125**, 19–28 https://doi.org/10.1242/jcs.094607
174 Hepler, P.K., McIntosh, J.R. and Cleland, S. (1970) Intermicrotubule bridges in mitotic spindle apparatus. *J. Cell Biol.* **45**, 438–444 https://doi.org/10.1083/jcb.45.2.438
175 Elkhatib, N., Bresteau, E., Baschieri, F., Rioja, A.L., van Niel, G., Vassilopoulos, S. et al. (2017) Tubular clathrin/AP-2 lattices pinch collagen fibers to support 3D cell migration. *Science* **356**, eaal4713 https://doi.org/10.1126/science.aal4713
176 Milosevic, I. (2018) Revisiting the role of clathrin-Mediated endoytosis in synaptic vesicle recycling. *Front. Cell Neurosci.* **12**. https://doi.org/10.3389/fncel.2018.00027

177 Casamento, A. and Boucrot, E. (2020) Molecular mechanism of fast endophilin-Mediated endocytosis. *Biochem. J.* **477**, 2327–2345 https://doi.org/10.1042/bcj20190342
178 Milosevic, I., Giovedi, S., Lou, X., Raimondi, A., Collesi, C., Shen, H. et al. (2011) Recruitment of endophilin to clathrin-coated pit necks is required for efficient vesicle uncoating after fission. *Neuron* **72**, 587–601 https://doi.org/10.1016/j.neuron.2011.08.029
179 Bertot, L., Grassart, A., Lagache, T., Nardi, G., Basquin, C., Olivo-Marin, J.-C. et al. (2018) Quantitative and statistical study of the dynamics of clathrin-Dependent and -Independent endocytosis reveal a differential role of EndophilinA2. *Cell Rep.* **22**, 1574–1588 https://doi.org/10.1016/j.celrep.2018.01.039
180 Chanaday, N.L., Cousin, M.A., Milosevic, I., Watanabe, S. and Morgan, J.R. (2019) The synaptic vesicle cycle revisited: new insights into the modes and mechanisms. *J. Neurosci.* **39**, 8209–8216 https://doi.org/10.1523/jneurosci.1158-19.2019
181 Murdoch, J.D., Rostosky, C.M., Gowrisankaran, S., Arora, A.S., Soukup, S.-F., Vidal, R. et al. (2016) Endophilin-A deficiency induces the Foxo3a-Fbxo32 network in the brain and causes dysregulation of autophagy and the ubiquitin-Proteasome system. *Cell Rep.* **17**, 1071–1086 https://doi.org/10.1016/j.celrep.2016.09.058
182 Kasprowicz, J., Kuenen, S., Miskiewicz, K., Habets, R.L.P., Smitz, L. and Verstreken, P. (2008) Inactivation of clathrin heavy chain inhibits synaptic recycling but allows bulk membrane uptake. *J. Cell Biol.* **182**, 1007–1016 https://doi.org/10.1083/jcb.200804162
183 Augustine, G.J., Morgan, J.R., Villalba-Galea, C.A., Jin, S., Prasad, K. and Lafer, E.M. (2006) Clathrin and synaptic vesicle endocytosis: studies at the squid giant synapse. *Biochem. Soc. Trans.* **34**, 68–72 https://doi.org/10.1042/bst0340068
184 Farsi, Z., Gowrisankaran, S., Krunic, M., Rammner, B., Woehler, A., Lafer, E.M. et al. (2018) Clathrin coat controls synaptic vesicle acidification by blocking vacuolar ATPase activity. *eLife* **7**, e32569 https://doi.org/10.7554/elife.32569
185 Calebiro, D. and Godbole, A. (2018) Internalization of G-protein-coupled receptors: implication in receptor function, physiology and diseases. *Best Pract. Res. Clin. Endocrinol. Metab.* **32**, 83–91 https://doi.org/10.1016/j.beem.2018.01.004
186 Ferrandon, S., Feinstein, T.N., Castro, M., Wang, B., Bouley, R., Potts, J.T. et al. (2009) Sustained cyclic AMP production by parathyroid hormone receptor endocytosis. *Nat. Chem. Biol.* **5**, 734–742 https://doi.org/10.1038/nchembio.206
187 Tsao, P.I. and von Zastrow, M. (2000) Type-specific sorting of G protein-coupled receptors after endocytosis. *J. Biol. Chem.* **275**, 11130–11140 https://doi.org/10.1074/jbc.275.15.11130
188 Ferguson, S.S. (2001) Evolving concepts in G protein-coupled receptor endocytosis: the role in receptor desensitization and signaling. *Pharmacol. Rev.* **53**, 1–24 PMID:11171937
189 Zhang, X. and Kim, K.-M. (2017) Multifactorial regulation of G protein-coupled receptor endocytosis. *Biomol. Ther. (Seoul)* **25**, 26–43 https://doi.org/10.4062/biomolther.2016.186
190 Oakley, R.H., Laporte, S.A., Holt, J.A., Barak, L.S. and Caron, M.G. (1999) Association of beta-arrestin with G protein-coupled receptors during clathrin-mediated endocytosis dictates the profile of receptor resensitization. *J. Biol. Chem.* **274**, 32248–32257 https://doi.org/10.1074/jbc.274.45.32248
191 Laporte, S.A., Oakley, R.H., Holt, J.A., Barak, L.S. and Caron, M.G. (2000) The interaction of beta-arrestin with the AP-2 adaptor is required for the clustering of beta 2-adrenergic receptor into clathrin-coated pits. *J. Biol. Chem.* **275**, 23120–6 https://doi.org/10.1074/jbc.m002581200
192 Goodman, O.B., Krupnick, J.G., Santini, F., Gurevich V, V., Penn, R.B., Gagnon, A.W. et al. (1996) β-Arrestin acts as a clathrin adaptor in endocytosis of the β2-adrenergic receptor. *Nature* **383**, 447–450 https://doi.org/10.1038/383447a0
193 McArdle, C.A., Franklin, J., Green, L. and Hislop, J.N. (2002) Signalling, cycling and desensitisation of gonadotrophin-releasing hormone receptors. *J. Endocrinol.* **173**, 1–11 https://doi.org/10.1677/joe.0.1730001
194 Krupnick, J.G. and Benovic, J.L. (1998) The role of receptor kinases and arrestins in G protein-coupled receptor regulation. *Annu. Rev. Pharmacol. Toxicol.* **38**, 289–319 https://doi.org/10.1146/annurev.pharmtox.38.1.289
195 Eichel, K. and von Zastrow, M. (2018) Subcellular organization of GPCR signaling. *Trends Pharmacol. Sci.* **39**, 200–208 https://doi.org/10.1016/j.tips.2017.11.009
196 Qiao, Y., Yang, J., Zhang, X., Liu, Y., Zhang, J., Zong, S. et al. (2004) Characterization of rtSH3p13 gene encoding a development protein involved in vesicular traffic in spermiogenesis. *Cell Res.* **14**, 197–207 https://doi.org/10.1038/sj.cr.7290220
197 Wei-Pang, H. and Han-Chen, H. (2006) Role of microtubule-dependent membrane trafficking in acrosomal biogenesis. *Cell Tissue Res.* **323**, 495–503 https://doi.org/10.1007/s00441-005-0097-9
198 Funaki, T., Kon, S., Tanabe, K., Natsume, W., Sato, S., Shimizu, T. et al. (2013) The Arf GAP SMAP2 is necessary for organized vesicle budding from the trans-Golgi network and subsequent acrosome formation in spermiogenesis. *Mol. Biol. Cell* **24**, 2633–2644 https://doi.org/10.1091/mbc.e13-05-0234
199 Li, S., Qiao, Y., Di, Q., Le, X., Zhang, L., Zhang, X. et al. (2009) Interaction of SH3P13 and DYDC1 protein: a germ cell component that regulates acrosome biogenesis during spermiogenesis. *Eur. J. Cell Biol.* **88**, 509–520 https://doi.org/10.1016/j.ejcb.2009.05.001
200 Ezratty, E.J., Bertaux, C., Marcantonio, E.E. and Gundersen, G.G. (2009) Clathrin mediates integrin endocytosis for focal adhesion disassembly in migrating cells. *J. Cell Biol.* **187**, 733–747 https://doi.org/10.1083/jcb.200904054
201 Chao, W.-T. and Kunz, J. (2009) Focal adhesion disassembly requires clathrin-dependent endocytosis of integrins. *FEBS Lett.* **583**, 1337–1343 https://doi.org/10.1016/j.febslet.2009.03.037
202 Geraldo, S., Simon, A., Elkhatib, N., Louvard, D., Fetler, L. and Vignjevic, D.M. (2012) Do cancer cells have distinct adhesions in 3D collagen matrices and in vivo? *Eur. J. Cell Biol.* **91**, 930–937 https://doi.org/10.1016/j.ejcb.2012.07.005
203 Tawil, N., Wilson, P. and Carbonetto, S. (1993) Integrins in point contacts mediate cell spreading: factors that regulate integrin accumulation in point contacts vs. focal contacts. *J. Cell Biol.* **120**, 261–271 https://doi.org/10.1083/jcb.120.1.261
204 Maupin, P. and Pollard, T.D. (1983) Improved preservation and staining of heLa cell actin filaments, clathrin-coated membranes, and other cytoplasmic structures by tannic acid-glutaraldehyde-saponin fixation. *J. Cell Biol.* **96**, 51–62 https://doi.org/10.1083/jcb.96.1.51
205 Borlido, J., Veltri, G., Jackson, A.P. and Mills, I.G. (2008) Clathrin is spindle-associated but not essential for mitosis. *PLoS ONE* **3**, e3115 https://doi.org/10.1371/journal.pone.0003115
206 Fielding, A.B., Willox, A.K., Okeke, E. and Royle, S.J. (2012) Clathrin-mediated endocytosis is inhibited during mitosis. *Proc. Natl Acad. Sci. U.S.A.* **109**, 6572–6577 https://doi.org/10.1073/pnas.1117401109

Biochemical Journal (2021) **478** 3099–3123
https://doi.org/10.1042/BCJ20200740

207 Booth, D.G., Hood, F.E., Prior, I.A. and Royle, S.J. (2011) A TACC3/ch-TOG/clathrin complex stabilises kinetochore fibres by inter-microtubule bridging. *EMBO J.* **30**, 906–919 https://doi.org/10.1038/emboj.2011.15
208 Medendorp, K., Vreede, L., van Groningen, J.J.M., Hetterschijt, L., Brugmans, L., Jansen, P.A.M. et al. (2010) The mitotic arrest deficient protein MAD2B interacts with the clathrin light chain A during mitosis. *PLoS ONE* **5**, e15128 https://doi.org/10.1371/journal.pone.0015128
209 Royle, S.J. and Lagnado, L. (2006) Trimerisation is important for the function of clathrin at the mitotic spindle. *J. Cell Sci.* **119**, 4071–4078 https://doi.org/10.1242/jcs.03192
210 Hood, F.E., Williams, S.J., Burgess, S.G., Richards, M.W., Roth, D., Straube, A. et al. (2013) Coordination of adjacent domains mediates TACC3–ch-TOG–clathrin assembly and mitotic spindle binding. *J. Cell Biol.* **202**, 463–478 https://doi.org/10.1083/jcb.201211127
211 Lin, C.-H., Hu, C.-K. and Shih, H.-M. (2010) Clathrin heavy chain mediates TACC3 targeting to mitotic spindles to ensure spindle stability. *J. Cell Biol.* **189**, 1097–1105 https://doi.org/10.1083/jcb.200911120
212 Rondelet, A., Lin, Y.-C., Singh, D., Porfetye, A.T., Thakur, H.C., Hecker, A. et al. (2020) Clathrin's adaptor interaction sites are repurposed to stabilize microtubules during mitosis. *J. Cell Biol.* **219**, e201907083 https://doi.org/10.1083/jcb.201907083
213 Nixon, F.M., Gutiérrez-Caballero, C., Hood, F.E., Booth, D.G., Prior, I.A. and Royle, S.J. (2015) The mesh is a network of microtubule connectors that stabilizes individual kinetochore fibers of the mitotic spindle. *eLife* **4**, e07635 https://doi.org/10.7554/elife.07635
214 Dickson, R.B. and Willingham, M.C. (1981) Pastan I. alpha 2-macroglobulin adsorbed to colloidal gold: a new probe in the study of receptor-mediated endocytosis. *J. Cell Biol.* **89**, 29–34 https://doi.org/10.1083/jcb.89.1.29
215 Dahlberg, J.E. (1974) Quantitative electron microscopic analysis of the penetration of VSV into L cells. *Virology* **58**, 250–262 https://doi.org/10.1016/0042-6822(74)90159-7
216 Fan, D.P. and Sefton, B.M. (1978) The entry into host cells of sindbis virus, vesicular stomatitis virus and sendai virus. *Cell* **15**, 985–992 https://doi.org/10.1016/0092-8674(78)90282-9
217 Matlin, K.S., Reggio, H., Helenius, A. and Simons, K. (1982) Pathway of vesicular stomatitis virus entry leading to infection. *J. Mol. Biol.* **156**, 609–631 https://doi.org/10.1016/0022-2836(82)90269-8
218 Mercer, J., Schelhaas, M. and Helenius, A. (2010) Virus entry by endocytosis. *Annu. Rev. Biochem.* **79**, 803–833 https://doi.org/10.1146/annurev-biochem-060208-104626
219 Veiga, E. and Cossart, P. (2005) Listeria hijacks the clathrin-dependent endocytic machinery to invade mammalian cells. *Nat. Cell Biol.* **7**, 894–900 https://doi.org/10.1038/ncb1292
220 Veiga, E., Guttman, J.A., Bonazzi, M., Boucrot, E., Toledo-Arana, A., Lin, A.E. et al. (2007) Invasive and adherent bacterial pathogens co-Opt host clathrin for infection. *Cell Host Microbe* **2**, 340–351 https://doi.org/10.1016/j.chom.2007.10.001
221 Bonazzi, M., Vasudevan, L., Mallet, A., Sachse, M., Sartori, A., Prevost, M.-C. et al. (2011) Clathrin phosphorylation is required for actin recruitment at sites of bacterial adhesion and internalization. *J. Cell Biol.* **195**, 525–536 https://doi.org/10.1083/jcb.201105152
222 Pizarro-Cerdá, J., Kühbacher, A. and Cossart, P. (2012) Entry of listeria monocytogenes in mammalian epithelial cells: an updated view. *Cold Spring Harb. Perspect. Med.* **2**, a010009 https://doi.org/10.1101/cshperspect.a010009
223 Veiga, E. and Cossart, P. (2006) The role of clathrin-dependent endocytosis in bacterial internalization. *Trends Cell Biol.* **16**, 499–504 https://doi.org/10.1016/j.tcb.2006.08.005
224 Moreno-Ruiz, E., Galán-Díez, M., Zhu, W., Fernández-Ruiz, E., d'Enfert, C., Filler, S.G. et al. (2009) *Candida albicans* internalization by host cells is mediated by a clathrin-dependent mechanism. *Cell. Microbiol.* **11**, 1179–1189 https://doi.org/10.1111/j.1462-5822.2009.01319.x
225 Almeida, R.A. and Oliver, S.P. (1995) Invasion of bovine mammary epithelial cells by *streptococcus dysgalactiae*. *J. Dairy Sci.* **78**, 1310–1317 https://doi.org/10.3168/jds.s0022-0302(95)76752-2
226 Jevon, M., Guo, C., Ma, B., Mordan, N., Nair, S.P., Harris, M. et al. (1999) Mechanisms of internalization of staphylococcus aureus by cultured human osteoblasts. *Infect. Immun.* **67**, 2677–2681 https://doi.org/10.1128/iai.67.5.2677-2681.1999
227 Fumagalli, M., Camus, S.M., Diekmann, Y., Burke, A., Camus, M.D., Norman, P.J. et al. (2019) Genetic diversity of CHC22 clathrin impacts its function in glucose metabolism. *eLife* **8**, e41517 https://doi.org/10.7554/elife.41517
228 Wakeham, D.E., Abi-Rached, L., Towler, M.C., Wilbur, J.D., Parham, P. and Brodsky, F.M. (2005) Clathrin heavy and light chain isoforms originated by independent mechanisms of gene duplication during chordate evolution. *Proc. Natl Acad. Sci. U.S.A.* **102**, 7209–7214 https://doi.org/10.1073/pnas.0502058102
229 Hoshino, S., Sakamoto, K., Vassilopoulos, S., Camus, S.M., Griffin, C.A., Esk, C. et al. (2013) The CHC22 clathrin-GLUT4 transport pathway contributes to skeletal muscle regeneration. *PLoS ONE* **8**, e77787 https://doi.org/10.1371/journal.pone.0077787
230 Gould, G.W., Brodsky, F.M. and Bryant, N.J. (2020) Building GLUT4 vesicles: CHC22 clathrin's human touch. *Trends Cell Biol.* **30**, 705–719 https://doi.org/10.1016/j.tcb.2020.05.007
231 Camus, S.M., Camus, M.D., Figueras-Novoa, C., Boncompain, G., Sadacca, L.A., Esk, C. et al. (2020) CHC22 clathrin mediates traffic from early secretory compartments for human GLUT4 pathway biogenesis. *J. Cell Biol.* **219**, e201812135 https://doi.org/10.1083/jcb.201812135
232 Dannhauser, P.N., Camus, S.M., Sakamoto, K., Sadacca, L.A., Torres, J.A., Camus, M.D. et al. (2017) CHC22 and CHC17 clathrins have distinct biochemical properties and display differential regulation and function. *J. Biol. Chem.* **292**, 20834–20844 https://doi.org/10.1074/jbc.m117.816256
233 Nossal, R. (2001) Energetics of clathrin basket assembly. *Traffic* **2**, 138–147 https://doi.org/10.1034/j.1600-0854.2001.020208.x
234 Jin, A.J. and Nossal, R. (2000) Rigidity of triskelion arms and clathrin nets. *Biophys. J.* **78**, 1183–1194 https://doi.org/10.1016/s0006-3495(00)76676-8
235 Chen, Z. and Schmid, S.L. (2020) Evolving models for assembling and shaping clathrin-coated pits. *J. Cell Biol.* **219**, e202005126 https://doi.org/10.1083/jcb.202005126
236 Kirchhausen, T. (1993) Coated pits and coated vesicles - sorting it all out. *Curr. Opin. Struct. Biol.* **3**, 182–188 https://doi.org/10.1016/s0959-440x(05)80150-2
237 Jin, A.J. and Nossal, R. (1993) Topological mechanisms involved in the formation of clathrin-coated vesicles. *Biophys. J.* **65**, 1523–1537 https://doi.org/10.1016/s0006-3495(93)81189-5
238 Heuser, J. and Evans, L. (1980) Three-dimensional visualization of coated vesicle formation in fibroblasts. *J. Cell Biol.* **84**, 560–583 https://doi.org/10.1083/jcb.84.3.560

239 Grove, J., Metcalf, D.J., Knight, A.E., Wavre-Shapton, S.T., Sun, T., Protonotarios, E.D. et al. (2014) Flat clathrin lattices: stable features of the plasma membrane. *Mol. Biol. Cell* **25**, 3581–3594 https://doi.org/10.1091/mbc.e14-06-1154
240 Subtil, A., Gaidarov, I., Kobylarz, K., Lampson, M.A., Keen, J.H. and McGraw, T.E. (1999) Acute cholesterol depletion inhibits clathrin-coated pit budding. *Proc. Natl Acad. Sci. U.S.A.* **96**, 6775–6780 https://doi.org/10.1073/pnas.96.12.6775
241 Chen, Y., Yong, J., Martínez-Sánchez, A., Yang, Y., Wu, Y., De Camilli, P. et al. (2019) Dynamic instability of clathrin assembly provides proofreading control for endocytosis. *J. Cell Biol.* **218**, 3200–3211 https://doi.org/10.1083/jcb.201804136
242 Hirst, J., Sahlender, D.A., Li, S., Lubben, N.B., Borner, G.H.H. and Robinson, M.S. (2008) Auxilin depletion causes self-assembly of clathrin into membraneless cages *in vivo*. *Traffic* **9**, 1354–1371 https://doi.org/10.1111/j.1600-0854.2008.00764.x
243 Yim, Y.-I., Scarselletta, S., Zang, F., Wu, X., Lee, D., Kang, Y. et al. (2005) Exchange of clathrin, AP2 and epsin on clathrin-coated pits in permeabilized tissue culture cells. *J. Cell Sci.* **117**, 631–639 https://doi.org/10.1242/jcs.00910
244 Bucher, D., Frey, F., Sochacki, K.A., Kummer, S., Bergeest, J.-P., Godinez, W.J. et al. (2018) Clathrin-adaptor ratio and membrane tension regulate the flat-to-curved transition of the clathrin coat during endocytosis. *Nat. Commun.* **9**, 1109 https://doi.org/10.1038/s41467-018-03533-0
245 Sochacki, K.A., Heine, B.L., Haber, G.J., Jimah, J.R., Prasai, B., Alfonzo-Mendez, M.A. et al. (2020) The structure and spontaneous curvature of clathrin lattices at the plasma membrane. *bioRxiv* https://doi.org/10.1101/2020.07.18.207258
246 Ferguson, J.P., Willy, N.M., Heidotting, S.P., Huber, S.D., Webber, M.J. and Kural, C. (2016) Deciphering dynamics of clathrin-mediated endocytosis in a living organism. *J. Cell Biol.* **214**, 347–358 https://doi.org/10.1083/jcb.201604128
247 Willy, N.M., Ferguson, J.P., Silahli, S., Cakez, C., Hasan, F., Chen, Y. et al. (2019) Endocytic clathrin coats develop curvature at early stages of their formation. *bioRxiv* https://doi.org/10.1101/715219
248 Scott, B.L., Sochacki, K.A., Low-Nam, S.T., Bailey, E.M., Luu, Q., Hor, A. et al. (2018) Membrane bending occurs at all stages of clathrin-coat assembly and defines endocytic dynamics. *Nat. Commun.* **9**, 419 https://doi.org/10.1038/s41467-018-02818-8
249 Maib, H., Ferreira, F., Vassilopoulos, S. and Smythe, E. (2018) Cargo regulates clathrin-coated pit invagination via clathrin light chain phosphorylation. *J. Cell Biol.* **217**, 4253–4266 https://doi.org/10.1083/jcb.201805005
250 Keen, J.H., Willingham, M.C. and Pastan, I.H. (1979) Clathrin-coated vesicles: isolation, dissociation and factor-dependent reassociation of clathrin baskets. *Cell* **16**, 303–312 https://doi.org/10.1016/0092-8674(79)90007-2
251 Schook, W., Puszkin, S., Bloom, W., Ores, C. and Kochwa, S. (1979) Mechanochemical properties of brain clathrin: interactions with actin and alpha-actinin and polymerization into basketlike structures or filaments. *Proc. Natl Acad. Sci. U.S.A.* **76**, 116–120 https://doi.org/10.1073/pnas.76.1.116
252 Nandi, P.K., Pretorius, H.T., Lippoldt, R.E., Johnson, M.L. and Edelhoch, H. (1980) Molecular properties of the reassembled coat protein of coated vesicles. *Biochemistry* **19**, 5917–5921 https://doi.org/10.1021/bi00566a039
253 Woodward, M.P. and Roth, T.F. (1978) Coated vesicles: characterization, selective dissociation, and reassembly. *Proc. Natl Acad. Sci. U.S.A.* **75**, 4394–4398 https://doi.org/10.1073/pnas.75.9.4394
254 Crowther, R.A., Pinch, J.T. and Pearse, B.M.F. (1976) On the structure of coated vesicles. *J. Mol. Biol.* **103**, 785–798 https://doi.org/10.1016/0022-2836(76)90209-6
255 Sorger, P.K., Crowther, R.A., Finch, J.T. and Pearse, B.M. (1986) Clathrin cubes: an extreme variant of the normal cage. *J. Cell Biol.* **103**, 1213–1219 https://doi.org/10.1083/jcb.103.4.1213
256 Heuser, J.E., Keen, J.H., Amende, L.M., Lippoldt, R.E. and Prasad, K. (1987) Deep-etch visualization of 27S clathrin: a tetrahedral tetramer. *J. Cell Biol.* **105**, 1999–2009 https://doi.org/10.1083/jcb.105.5.1999
257 Dannhauser, P.N., Platen, M., Böning, H. and Schaap, I.A.T. (2015) Durable protein lattices of clathrin that can be functionalized with nanoparticles and active biomolecules. *Nat. Nanotechnol.* **10**, 954–957 https://doi.org/10.1038/nnano.2015.206
258 Ferguson, M.L., Prasad, K., Boukari, H., Sackett, D.L., Krueger, S., Lafer, E.M. et al. (2008) Clathrin triskelia show evidence of molecular flexibility. *Biophys. J.* **95**, 1945–1955 https://doi.org/10.1529/biophysj.107.126342
259 Ungewickells, E. and Ungewickell, H. (1991) Bovine brain clathrin light chains impede heavy chain assembly *in vitro**. *J. Biol. Chem.* **266**, 12710–4 https://doi.org/10.1016/s0021-9258(18)98957-x
260 Liu, S.H., Wong, M.L., Craik, C.S. and Brodsky, F.M. (1995) Regulation of clathrin assembly and trimerization defined using recombinant triskelion hubs. *Cell* **83**, 257–267 https://doi.org/10.1016/0092-8674(95)90167-1
261 Wilbur, J.D., Hwang, P.K., Ybe, J.A., Lane, M., Sellers, B.D., Jacobson, M.P. et al. (2010) Conformation switching of clathrin light chain regulates clathrin lattice assembly. *Dev. Cell* **18**, 854–861 https://doi.org/10.1016/j.devcel.2010.04.007
262 Ybe, J.A., Ruppel, N., Mishra, S. and VanHaaften, E. (2003) Contribution of cysteines to clathrin trimerization domain stability and mapping of light chain binding. *Traffic* **4**, 850–856 https://doi.org/10.1046/j.1600-0854.2003.0139.x
263 Ybe, J.A., Perez-Miller, S., Niu, Q., Coates, D.A., Drazer, M.W. and Clegg, M.E. (2007) Light chain C-terminal region reinforces the stability of clathrin heavy chain trimers. *Traffic* **8**, 1101–1110 https://doi.org/10.1111/j.1600-0854.2007.00597.x
264 Musacchio, A., Smith, C.J., Roseman, A.M., Harrison, S.C., Kirchhausen, T. and Pearse, B.M. (1999) Functional organization of clathrin in coats: combining electron cryomicroscopy and X-ray crystallography. *Mol. Cell* **3**, 761–770 https://doi.org/10.1016/s1097-2765(01)80008-3
265 Kovtun, O., Dickson, V.K., Kelly, B.T., Owen, D.J. and Briggs, J.A.G. (2020) Architecture of the AP2/clathrin coat on the membranes of clathrin-coated vesicles. *Sci. Adv.* **6**, eaba8381 https://doi.org/10.1126/sciadv.aba8381
266 Bhave, M., Mino, R.E., Wang, X., Lee, J., Grossman, H.M., Lakoduk, A.M. et al. (2020) Functional characterization of 67 endocytic accessory proteins using multiparametric quantitative analysis of CCP dynamics. *Proc. Natl Acad. Sci. U.S.A.* **117**, 31591–31602 https://doi.org/10.1073/pnas.2020346117
267 Dandey, V.P., Budell, W.C., Wei, H., Bobe, D., Maruthi, K., Kopylov, M. et al. (2020) Time-resolved cryo-EM using spotiton. *Nat. Methods* **17**, 897–900 https://doi.org/10.1038/s41592-020-0925-6

Article

TRANSPARENT PROCESS OPEN ACCESS

THE EMBO JOURNAL

Multi-modal adaptor-clathrin contacts drive coated vesicle assembly

Sarah M Smith[1], Gabrielle Larocque[2,†], Katherine M Wood[1], Kyle L Morris[1,‡], Alan M Roseman[3], Richard B Sessions[4], Stephen J Royle[2,*] & Corinne J Smith[1,**]

Abstract

Clathrin-coated pits are formed by the recognition of membrane and cargo by the AP2 complex and the subsequent recruitment of clathrin triskelia. A role for AP2 in coated-pit assembly beyond initial clathrin recruitment has not been explored. Clathrin binds the β2 subunit of AP2, and several binding sites have been identified, but our structural knowledge of these interactions is incomplete and their functional importance during endocytosis is unclear. Here, we analysed the cryo-EM structure of clathrin cages assembled in the presence of β2 hinge-appendage (β2HA). We find that the β2-appendage binds in at least two positions in the cage, demonstrating that multi-modal binding is a fundamental property of clathrin-AP2 interactions. In one position, β2-appendage cross-links two adjacent terminal domains from different triskelia. Functional analysis of β2HA-clathrin interactions reveals that endocytosis requires two clathrin interaction sites: a clathrin-box motif on the hinge and the "sandwich site" on the appendage. We propose that β2-appendage binding to more than one triskelion is a key feature of the system and likely explains why assembly is driven by AP2.

Keywords clathrin; cryo-electron microscopy; endocytosis; membrane traffic
Subject Categories Membranes & Trafficking; Structural Biology
DOI 10.15252/embj.2021108795 | Received 23 May 2021 | Revised 30 July 2021 | Accepted 3 August 2021 | Published online 6 September 2021
The EMBO Journal (2021) 40: e108795

Introduction

Clathrin-mediated endocytosis (CME) is the major route of entry for receptors and their ligands into cells (Mettlen *et al*, 2018). A clathrin-coated pit is formed at the plasma membrane that selects cargo for uptake into the cell via a clathrin-coated vesicle. Clathrin cannot recognize membrane or cargo itself and so an adaptor protein binds the membrane, selects the cargo, and associates with clathrin leading to pit formation (Fig 1A). Several adaptor proteins have clathrin binding sites and colocalize with clathrin structures in cells but the assembly polypeptide-2 (AP2) complex (α, β2, μ2 and σ2 subunits) is thought to primarily initiate clathrin recruitment.

The recruitment of clathrin by the β2 subunit is an essential step in CME. AP2 and clathrin arrive jointly at the membrane in a ratio of two AP2 complexes per triskelion (Cocucci *et al*, 2012). As the pit matures, the ratio decreases as clathrin polymerizes (Bucher *et al*, 2018). It is assumed that this polymerization—which is an innate property of clathrin triskelia—completes vesicle formation. However, AP2 is named after its ability to promote clathrin cage assembly *in vitro* (Zaremba & Keen, 1983; Pearse & Robinson, 1984), and a fragment of the β2 subunit of AP2, containing the hinge and appendage domains (β2HA), has been shown to promote the polymerization of clathrin (Gallusser & Kirchhausen, 1993; Shih *et al*, 1995; Owen *et al*, 2000). How these *in vitro* observations relate to endocytosis in cells is unclear. One intriguing but often overlooked idea is that AP2, via β2HA, serves a dual role in CME: initially recruiting clathrin to the plasma membrane and then driving coated vesicle assembly.

There are two clathrin-binding locations on β2HA (Fig 1B). The first is a linear peptide motif within the hinge region (Owen *et al*, 2000; Lundmark & Carlsson, 2002), LLNLD, called the clathrin-box motif (CBM). The second clathrin-binding location is within the β2-appendage domain, however, its precise nature is debated (Chen & Schmid, 2020). The appendage domain has two sites that interact distinctly with different binding partners (Owen *et al*, 2000; Edeling *et al*, 2006; Schmid *et al*, 2006). The first, termed the sandwich (or side) domain, which surrounds Tyr 815, binds AP180, amphiphysin and eps15. A second site, termed the platform (or top) domain, surrounds residues Y888 and W841 (Fig 1B). This binds the adaptor proteins epsin, β-arrestin and autosomal recessive hypercholesterolemia (ARH) protein and functions independently from the sandwich domain. The roles of these sites in clathrin binding remain to be clarified. *In vitro* pull-down experiments highlight the potential

1 School of Life Sciences, University of Warwick, Coventry, UK
2 Centre for Mechanochemical Cell Biology, Warwick Medical School, University of Warwick, Coventry, UK
3 Division of Molecular and Cellular Function, School of Biological Sciences, Faculty of Biology, Medicine and Health, Manchester Academic Health Science Centre, University of Manchester, Manchester, UK
4 School of Biochemistry, University of Bristol, Bristol, UK
*Corresponding author. Tel: +44 24 7615 1931; E-mail: s.j.royle@warwick.ac.uk
**Corresponding author. Tel: +44 24 7652 2461; E-mail: corinne.smith@warwick.ac.uk
†Present address: Cellular Signalling and Cytoskeletal Function Laboratory, The Francis Crick Institute, London, UK
‡Present address: Diamond Light Source Ltd, Harwell Science & Innovation Campus, Didcot, UK

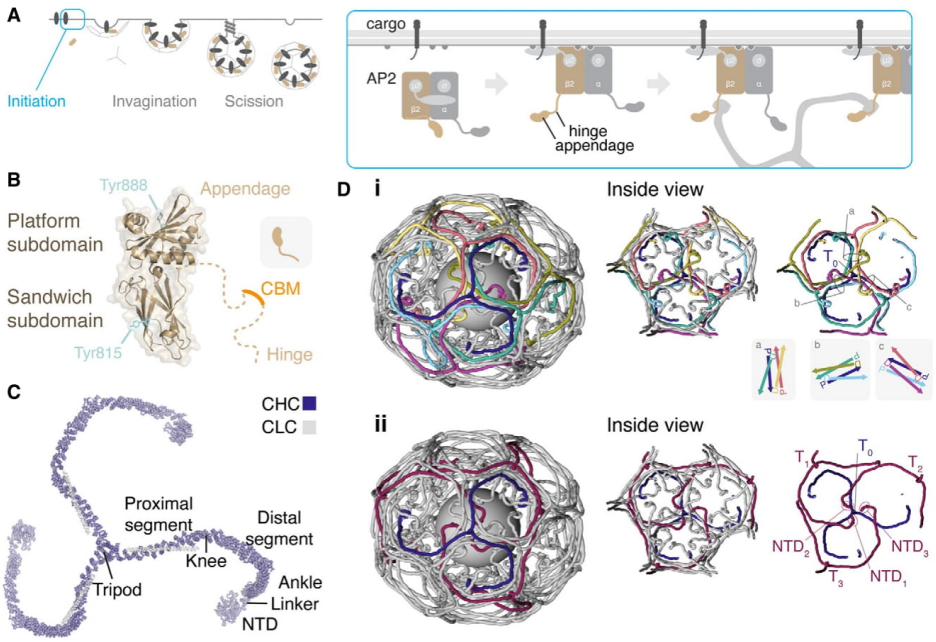

Figure 1. Structural view of clathrin assembly during endocytosis.

A Schematic diagram of clathrin-mediated endocytosis. The AP2 complex opens when it engages cargo and PI(4,5)P2, the β2 hinge and appendage (β2HA) become available for clathrin binding, initiating pit formation.

B Structure of β2HA (PDB code: 2G30). The appendage is divided into platform and sandwich subdomain, each with a tyrosine residue previously identified to be important for clathrin binding. The unstructured hinge region contains a clathrin-box motif (CBM, LLNLD) which binds the N-terminal domain (NTD) of clathrin heavy chain.

C Structure of a clathrin triskelion (PDB code: 3IYV). Three clathrin heavy chains (CHC) each with an associated light chain (CLC) are trimerized at their C-termini forming a tripod. Each leg is divided into proximal and distal segments, an ankle region and NTD.

D Clathrin assemblies. (i) An indigo triskelion is shown engaged with six other triskelia in a hexagonal barrel, coating a vesicle. Each edge is made from four leg segments for four different triskelia: two antiparallel proximal (P) regions on the outer surface and two antiparallel distal (D) regions below. Three edges (a–c) are shown schematically. (ii) The tripod of this triskelion (T_0) is at a vertex, and below that, three NTDs (NTD_{1-3}) are arranged, contributed by triskelia (purple) whose tripods are two or three edges away (T_{1-3}). Right panels show the view from the vesicle towards the vertex. The positions of triskelia were mapped by downsampling the carbon backbones in 3IYV by 5 residues and smoothing their position in 3D space using a 25 residue window in IgorPDB. CLCs have been removed for clarity.

importance of both Y888 and Y815 for clathrin binding but reports differ on their relative contribution (Owen *et al*, 2000; Edeling *et al*, 2006; Schmid *et al*, 2006).

Our structural understanding of how clathrin engages with AP2 is incomplete. The N-terminal domain (NTD, Fig 1C) of clathrin heavy chain is a seven-bladed β-propeller with four adaptor protein binding sites (Willox & Royle, 2012). Atomic structures have revealed that CBMs bind promiscuously to these sites, with the AP2 CBM binding to the "CBM site" between blades 1 and 2 and also to the "arrestin site" between blades 4 and 5 (Muenzner *et al*, 2017). The location where β2-appendage binds clathrin is uncertain. Knuehl *et al* (2006) used biochemical approaches and yeast-2-hybrid studies to identify residues C682 and G710 on the heavy chain ankle region as a potential location for β2-appendage. Another potential location is where transforming acidic coiled-coil 3 (TACC3) binds clathrin (residues 457–507; Burgess *et al*, 2018; Hood *et al*, 2013). However, a full picture of how the β2HA interacts with assembled clathrin, central to the mechanism of clathrin recruitment, remains elusive.

Recently, two structural studies have visualized contradictory modes of binding for the β2-appendage in clathrin assemblies. Using cryo-electron tomography, Kovtun *et al* investigated the structure of assembled clathrin and a form of AP2 lacking the alpha appendage and hinge region on lipid membranes containing cargo peptides and PI(4,5)P2 (Kovtun *et al*, 2020). They observed density beneath the clathrin vertex enclosed by one terminal domain and the ankle regions of two triskelion legs (see Fig 1D for orientation). In contrast, Paraan *et al* isolated native coated vesicles from bovine brain and obtained a structure using single particle analysis. They observed density consistent with the β2-appendage, however it was

in a different location, between two adjacent terminal domains (Paraan *et al*, 2020).

In order to address the paradox, we have analysed the structure of purified clathrin bound to the β2HA using single particle cryo-EM approaches. We find that the β2-appendage binds in at least two positions on clathrin, within the same sample, demonstrating that multi-modal binding is a fundamental property of clathrin-AP2 interactions and reconciling the differing observations in the literature. Our functional analysis of β2HA-clathrin interactions reveals that endocytosis requires hinge and appendage interaction sites, with the Tyr 815 sandwich site being more important for productive vesicle formation than the Tyr 888 platform site. In consolidating all available structural and functional information, we find that β2-appendage binding to more than one clathrin triskelion is a key feature of the system and likely explains how clathrin assembly is driven by AP2.

Results

The appendage of β2 is critical for coated vesicle formation

We previously developed a strategy to trigger clathrin-coated vesicle formation in cells, termed "hot-wired endocytosis" (Wood *et al*, 2017). It works by inducibly attaching a clathrin-binding protein (clathrin "hook") to a plasma membrane "anchor" using an FKBP-rapamycin-FRB dimerization system; and this is sufficient to trigger endocytosis (Fig 2A). Using the hinge and appendage of the β2 subunit of the AP2 complex (FKBP-β2HA-GFP) as a clathrin hook allows us to examine endocytosis that is driven by the interaction of β2HA and clathrin, that is, independent of other clathrin-adaptor interactions. Hot-wired endocytosis can be detected in live cells by visualizing the formation of intracellular bright green puncta that also contain an antibody to the extracellular portion of the anchor. These puncta move inside the cell, away from the plasma membrane and we have shown previously that they are clathrin-coated vesicles that have pinched off from the surface and are competent for traffic inside the cell (Wood *et al*, 2017). Using FKBP-β2HA-GFP as a clathrin hook, the formation of numerous puncta was observed, while a control construct (FKBP-GFP) elicited no response (Fig 2B and C).

An analogous construct from the AP3 complex, FKBP-β3HA-GFP, with the hinge and appendage of β3, was not competent for hot-wiring (Fig 2B and C). This is a surprising result for two reasons: first, the clathrin-box motif in the hinge of β3 binds clathrin *in vitro* (Dell'Angelica *et al*, 1998), and second, we had assumed that the role of the clathrin hook in the hot-wiring system was solely to recruit clathrin initially, with downstream polymerization being driven by clathrin alone.

To investigate this result in more detail, we tested whether the hinges of β2 or β3 were competent for hot-wiring. Despite the presence of a clathrin-box motif in both hinges, with the appendage domains removed neither FKBP-β2H-GFP nor FKBP-β3H-GFP was able to induce endocytosis (Fig 2B and C). Next, we transplanted the appendage of β3 onto the β2 hinge, and the appendage of β2 onto the β3 hinge. We observed hot-wiring with FKBP-β3Hβ2A-GFP but not with FKBP-β2Hβ3A-GFP (Fig 2B and C). Thus, the β2 appendage was able to drive endocytosis with a β3 hinge but the β2 hinge alone or in the presence of the β3 appendage could not. These results indicate firstly that the β2 appendage is critical for endocytosis and that the β3 appendage cannot substitute for this activity. Secondly, hooks containing a clathrin-box motif are not sufficient for vesicle formation. This suggested to us that the β2 appendage is active in clathrin polymerization.

Structure of clathrin-β2HA minicoat cages

If the β2 appendage contributes to clathrin polymerization, the nature of its interaction with assembled clathrin is of particular interest. In order to investigate this, we analysed cryo-electron micrographs of clathrin assembled in the presence of β2HA (Fig EV1A–G). Saturation of β2HA binding sites on clathrin was achieved using a 60-fold molar excess of β2HA (Fig EV1A and B). Of the 57,528 particles analysed, 29% of the total particle data set (16,641 particles) was occupied by the minicoat class of cages (Fig EV1C–G). Subsequent extensive supervised and unsupervised 3D classifications identified the particles most stably associated with the minicoat cage architecture (Appendix Figs S1 and S2). These 13 983 minicoat particles were refined to a gold standard resolution of 9.1 Å (Appendix Fig S3).

In order to locate β2HA within the map density, we compared the β2HA-clathrin map to a map of clathrin cages assembled in the absence of β2HA. While a difference map did reveal density in a location just above the terminal domains, it was not well-defined (Fig 3A and B). We therefore conducted a voxel-by-voxel comparison between the two maps to locate statistically significant differences (Young *et al*, 2013). This method allows the location of differences to be determined with confidence but does not define the shape of difference density. This enabled us to evaluate the entire minicoat particle data set globally for potential β2HA binding locations. The results of this analysis confirmed a significant difference just above the terminal domains (Fig 3C). We also noted significant differences in some other areas, away from β2HA, that may be related to triskelion leg movements or other conformational changes upon β2HA binding.

Finding β2HA in clathrin-β2HA minicoats

Our global difference analysis suggested that the β2HA was indeed bound to the cages but not well-resolved. Association of β2HA with clathrin cages may increase sample heterogeneity either through effects on the cage structure itself or through variations in mode of binding, ultimately affecting resolution. In addition, clathrin terminal domain flexibility may result in weaker density in the terminal domain and linker region (Fotin *et al*, 2004; Morris *et al*, 2019). We therefore used signal subtraction to reduce the dominance of the strong features of the outer clathrin cage in order to classify the weaker terminal domain signal more precisely (Bai *et al*, 2015) (Appendix Fig S4). 13,983 particles of the inner region of the minicoat cage were classified into 20 classes, with occupancy ranging from 1.4 to 12.2%, reflecting the heterogeneity of this cage region. Particles belonging to each class were refined individually to a higher resolution (Fig EV2). The outputs of the individual refinements (each at contour level σ3) varied in the quality and completeness of the terminal domain density. However in two classes, 15 and 18, distinct density consistent with bound β2HA was observed.

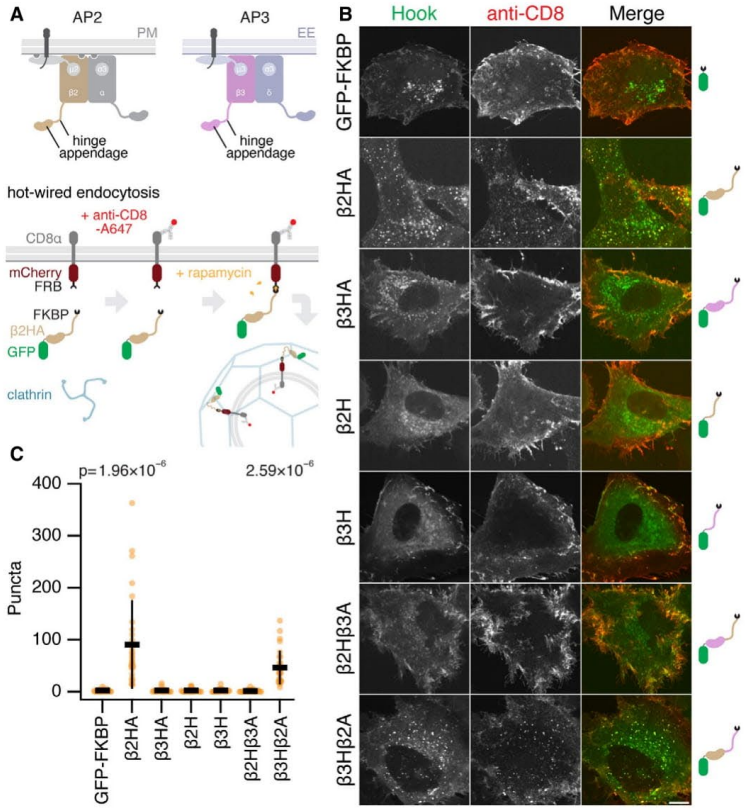

Figure 2. The β2 appendage is crucial for hot-wired clathrin-mediated endocytosis.

A Schematic diagram of hot-wired endocytosis. Under normal conditions the AP2 complex engages with cargo and PI(4,5)P2 at the plasma membrane (PM) and the β2 hinge and appendage become available for clathrin engagement. AP3 acts analogously at the early endosome (EE). In hot-wired endocytosis a clathrin hook, e.g. β2 hinge and appendage (FKBP-β2HA-GFP) is attached to a plasma membrane anchor CD8-mCherry-FRB inducibly by rapamycin application. Endocytosis is measured by uptake of a fluorescent antibody that binds the plasma membrane anchor.

B Representative confocal micrographs of cells expressing the plasma membrane anchor (CD8-mCherry-FRB) and the indicated hooks (green). Cells were incubated with anti-CD8-Alexa647 (red) and treated with rapamycin (200 nM, 15 min). Endocytic vesicles coinciding in both green and red channels (yellow in merge) were quantified in B. Scale bar, 10 μm.

C Scatter dot plot shows the number of intracellular GFP-positive vesicles that contained anti-CD8 Alexa647 per cell, bars indicate mean ± SD. Number of experiments = 3. *P*-values from Dunnett's *post hoc* test that were < 0.1 are shown above.

In the case of class 15, these densities were in a different location to that shown by our global analysis, on alternate terminal domains within a polyhedral face (Fig EV3A–D). Comparison of equivalent positions in a minicoat cage without adaptor bound demonstrated that the densities present at the terminal domains were a consequence of β2HA binding (Fig EV3A and B). Looking at adjacent polyhedral faces, for a given hub region where 3 terminal domains (from separate triskelia) converge, two terminal domains are engaged in an interaction with a single β2-appendage leaving one terminal domain unoccupied (Fig EV3C). Interestingly, β2HA density was not present at any of the 4 hubs in the minicoat cage where 3 pentagonal faces join. This class was refined further using localized reconstruction (described below).

For class 18, density could be seen on every terminal domain in all the hexagonal faces of the minicoat volume, but was less well-resolved (Fig 4A and B). In contrast to class 15 these densities lay parallel to the terminal domain beta-propeller and did not contact neighbouring terminal domains. We used localized reconstruction

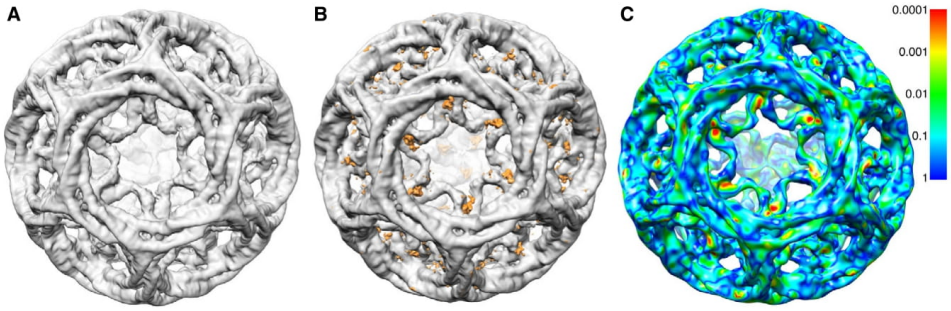

Figure 3. Global difference analysis of clathrin-β2HA compared to clathrin alone.

A Unsharpened cryo-EM map of clathrin-β2HA minicoat cage architecture at 9.1 Å resolution.
B Difference map of clathrin-β2HA minicoat and clathrin-only minicoat. Differences in density are shown in orange.
C Clathrin-β2HA and clathrin-only minicoat maps. Statistically significant differences are shown on a rainbow colour scheme (see inserted panel) with red, orange, yellow and green being the areas of significant difference. The light blue and dark blue areas indicate regions where the significance is below our threshold, or there is no significant difference between the two maps. The regions with the most significant difference density at $P < 0.0005$ (in red) were interpreted as the binding site of β2HA. Other regions show significant differences due to conformation changes related to binding. The contour level of all maps is 3.0 times sigma above the mean of the map. All images were created in UCSF Chimera (Pettersen *et al*, 2004).

(Ilca *et al*, 2015; Morris *et al*, 2019) to improve the resolution of the hexagonal faces from this class of minicoat particles. Rigid-body fitting of the clathrin terminal domain atomic structure revealed surplus density on either side of the beta-propeller structure (Fig 4C). The location of this density is consistent with our earlier global difference analysis. The surplus density at either side of the terminal domain was large enough to accommodate the atomic structure of the β2-appendage (Fig 4C) but could not support an unambiguous fit of this structure.

Resolving β2HA in the minicoat hub substructure

Having established through our analysis of whole cages that β2HA has at least two different binding locations on assembled clathrin, we next improved the resolution of the most defined density for β2HA by making use of the local symmetry present within the cages. We extracted and refined the hub regions from each vertex of the minicoat cage particles belonging to Class 15 (Fig EV2), using localized reconstruction within RELION (Ilca *et al*, 2015). Using this approach we refined a total of 26,624 minicoat hub regions to a global resolution of 9.6 Å (Fig EV4A–I). This resulted in a considerable improvement in resolution when compared to the whole-cage particles of Class 15 which refined to 19.8 Å (Fig EV2). Hubs surrounded by three pentagonal faces, which did not show additional density, were excluded from this refinement. A difference map and statistical comparison confirmed the presence of density due to β2HA (Fig 5A–D). We also found that separating the hubs according to whether the β2HA density linked terminal domains emerging from two pentagonal faces or from one pentagonal face and one hexagonal face resulted in improved map definition (Fig EV3C and D). These two classes were refined separately to global resolutions of ~10 Å (10.5 Å for P-P hubs and 10.1 Å for H-P hubs, Fig EV4B and C), consistent with the reduced number of particles in each subset. Despite this slightly lower resolution, the β2HA density in these maps was more clearly defined than in previous maps, with an intensity equal to the adjoining terminal domains (at contour level σ3), and a 1:2 β2HA:terminal domain binding ratio for both hub volumes (Fig EV4A–C).

Defining β2-appendage interactions with clathrin terminal domains

The improved definition of the β2HA density in the P-P hubs allowed us to carry out rigid-body fitting of the atomic structures of β2-appendage (PDB 1E42; Owen *et al*, 2000) and clathrin terminal domain (PDB 1BPO; ter Haar *et al*, 1998). The optimal orientation of the β2-appendage was found by selecting the fit with the greatest occupation of density (Fig 6A and C). A molecular model of the clathrin heavy chain formed from the model of Morris *et al* (6SCT) and the terminal domain X-ray structure of ter Haar *et al* (1BPO) was fitted into the P-P hub map using a combination of manual fitting and FlexEM (ter Haar *et al*, 1998; Topf *et al*, 2008; Joseph *et al*, 2016; Morris *et al*, 2019). Based on this fit, the alignment of the β2-appendage and the terminal domains was then optimized according to predicted intermolecular interaction energies calculated using the programme BUDE to determine a plausible binding interface (Fig 6D and E). The resulting model has been deposited as 7OM8.pdb.

We then conducted a systematic analysis of the potential contribution residues at the interface made to binding energy using the programme BudeAlaScan (BAlaS; Ibarra *et al*, 2019; Wood *et al*, 2020) which performs computational alanine scanning (Table 1). In addition to looking at single residues we examined the effect of multiple weaker interactions to define residue clusters that, through a cooperative effect, may prove important for binding. As a control, we performed a similar analysis with the α-appendage domain

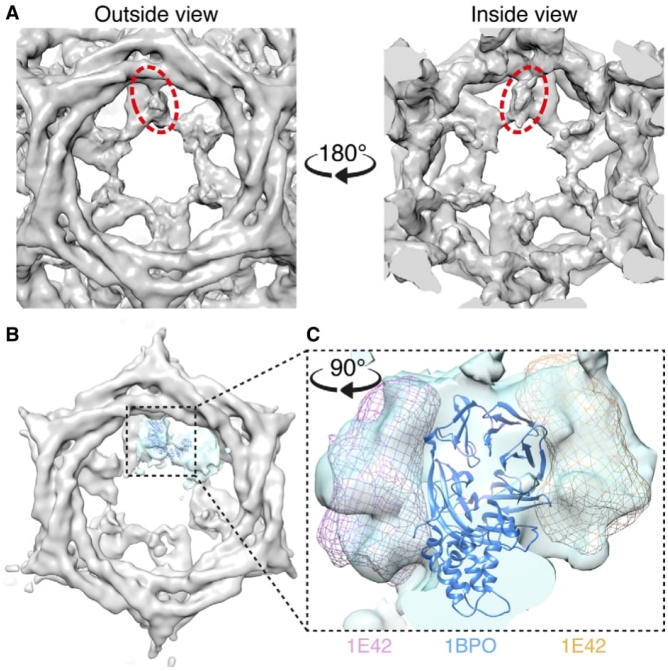

Figure 4. Unattributed density in hexagonal faces of clathrin minicoats.

A Close-up view of the unattributed density on each terminal domain in a given hexagonal face of the clathrin-β2HA minicoat cage that was resolved from particles belonging to class 18. Views from outside and inside a given hexagonal face are shown (left and right, respectively). Example densities are highlighted in dashed red ellipses.

B Using localized reconstruction (Ilca *et al*, 2015), all hexagonal faces from the minicoat cage shown in panel A were extracted and averaged resulting in a 19 Å map. A single terminal domain and connecting linker and ankle region, is highlighted in cyan, with the atomic model of clathrin terminal domain β-propeller structure (PDB 1BPO) rigid body fitted into the density (shown in dark blue).

C Rigid-body fitting of the clathrin terminal domain atomic structure (shown in dark blue) revealed surplus density on either side of the β-propeller structure, which was large enough to accommodate the atomic structure of the β2-adaptin appendage (PDB 1E42, shown as pink and orange wireframes) but not sufficiently defined to support an unambiguous fit to the density. All images were created, and rigid-body fitting was conducted, in UCSF Chimera (Pettersen *et al*, 2004).

which does not bind clathrin. These results predict that residue Tyr 815 on the β2-appendage makes the largest contribution (14 kJ mol^{-1}) with Asp 812, Gln 804 and Lys 759 contributing at or above a 5 kJ mol^{-1} threshold at that interface. There were also contributions from Glu 847 and Arg 904 at the 888 platform domain interface with a second terminal domain. Tyr 888 itself, implicated in adaptor interactions with the β2-appendage, does not form contacts with the terminal domain in our model. In the control experiments with the α-appendage, only Glu 849 showed a contribution > 5 kJ mol^{-1} (7.2 kJ mol^{-1}).

A similar analysis looking at the terminal domain interactions showed only two residues contributing more than 5 kJ mol^{-1} to the 815 sandwich interface; Thr 235 and Trp 164, while three terminal domain residues contributed more than 5 kJ mol^{-1} to the 888 platform domain interface; Lys 140, Asp 187 and Lys 189. In the alpha appendage controls, three residues contributed more than 5 kJ mol^{-1}; Lys 140, Trp 164 and Lys 189. In all cases, there were no contributions comparable to that of Tyr 815. This suggested that individual residue interactions are less important for terminal domain binding, so we investigated potential cooperativity from groups of weaker-binding residues. We performed a constellation analysis using BAlaS for residues with an interaction energy greater than 3 kJ mol^{-1}. This showed that cooperative clusters formed at the interfaces between the terminal domains and both the 815 sandwich and 888 platform domains (Table 2 and Fig 6B). At the 815 sandwich domain, these complementary clusters involved β2 appendage residues Lys 759, Gln 804, Asp 812 and Tyr 815 and terminal domain residues Asp 159, Lys 161 and Trp 164. At the 888 platform domain interface, the complementary clusters consisted of β2-appendage residues Lys 842, Asn 846, Glu 847 and Glu 849 and terminal domain residues Lys 140, Asp 187 and Lys 189. For the alpha appendage control, there were no cooperative clusters at the

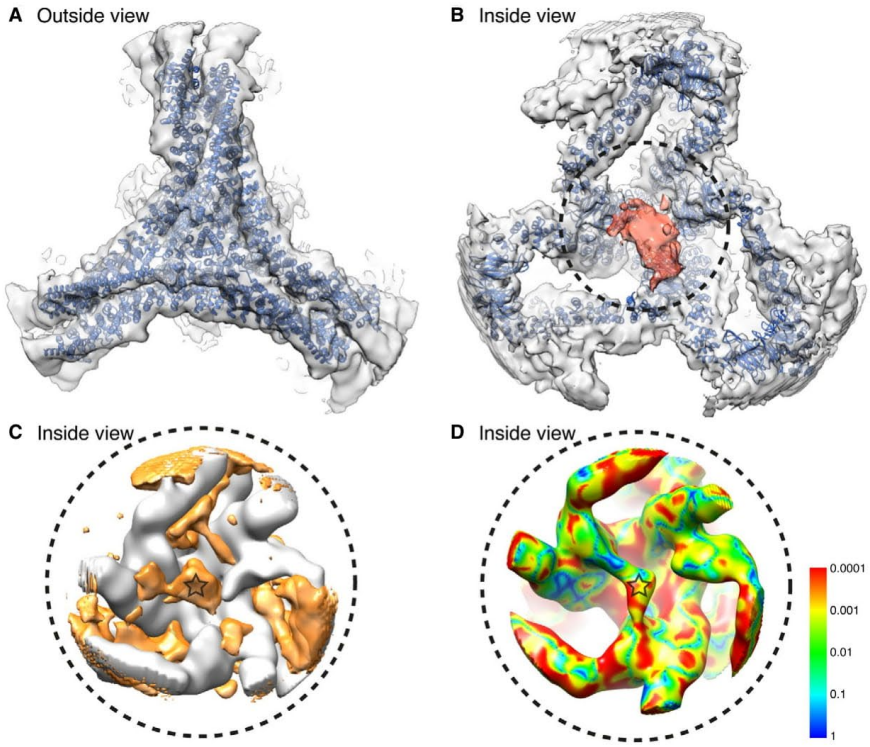

Figure 5. Identification of β2HA in clathrin minicoats.

A 10.5 Å resolution cryo-EM map of clathrin-β2HA minicoat hub region particles belonging to class 15. The hub region atomic model (PDB 6SCT) was flexibly fitted (Topf *et al*, 2008; Joseph *et al*, 2016) into the cryo-EM map (blue).

B Underside view of the cryo-EM map and fitted clathrin model shown in panel A. Density attributed to β2HA is coloured red.

C Difference map of the clathrin-β2HA minicoat and clathrin-only minicoat hub maps. Differences in density are shown in orange. The orange density located at the junction of the three terminal domains (marked with a star) is consistent with the location of β2HA shown in panel B.

D Pixel by pixel comparison between clathrin-β2HA and clathrin-only minicoat hub maps. Statistically significant differences are shown on a rainbow colour scheme (see inserted panel) with red, orange, yellow and green being the areas of significant difference. Red indicates the regions with significant differences at the highest level, $P < 0.0005$. Differences reflect the binding of β2HA and induced movements of the legs. The light blue and dark blue areas indicate regions where the significance is below our threshold, or there is no significant difference between the two maps. The density attributed to β2HA is marked with a star.

888 platform domain but at the 815 sandwich domain some pairs of residues showed high cooperativity (Table 2). Interestingly, in our model Lys 140, Lys 189 and Asp 187 form salt bridge contacts with Glu 847, Glu 849 and Arg 904, respectively. In the α-appendage control, only Glu 849 and Lys 189 form a plausible salt bridge, suggesting a role for Lys 140/Glu 847 and Asp 187/Arg 904 salt bridges in the specificity of this interaction.

In all, this analysis of our proposed model suggests that Tyr 815 plays a key role in β2-appendage clathrin binding, supported by residues Asp 812, Gln 804 and Lys 759. On the terminal domain, residues Thr 235 and Trp 164, supported by Asp 159 and Lys 161 contribute to the interface (Fig 6B,D,E). It also suggests the potential for cooperative clusters of weaker binding interactions to support a binding interface between the 888 platform domain and the terminal domain.

Role of β2 residues 815 and 888 in functional clathrin assembly

Previous work had identified Tyr 815 and Tyr 888 (shown in Fig 1B) as being important for β2HA-clathrin interactions (Edeling *et al*, 2006; Schmid *et al*, 2006). Our model and *in silico* alanine scanning analysis had identified the importance of both the platform and sandwich sites on β2-appendage in this interaction, so we returned to the hot-wired endocytosis system to address their relative functional importance. We had found that the hinge and appendage of β2 or β1 but not β3, were competent for hot-wiring

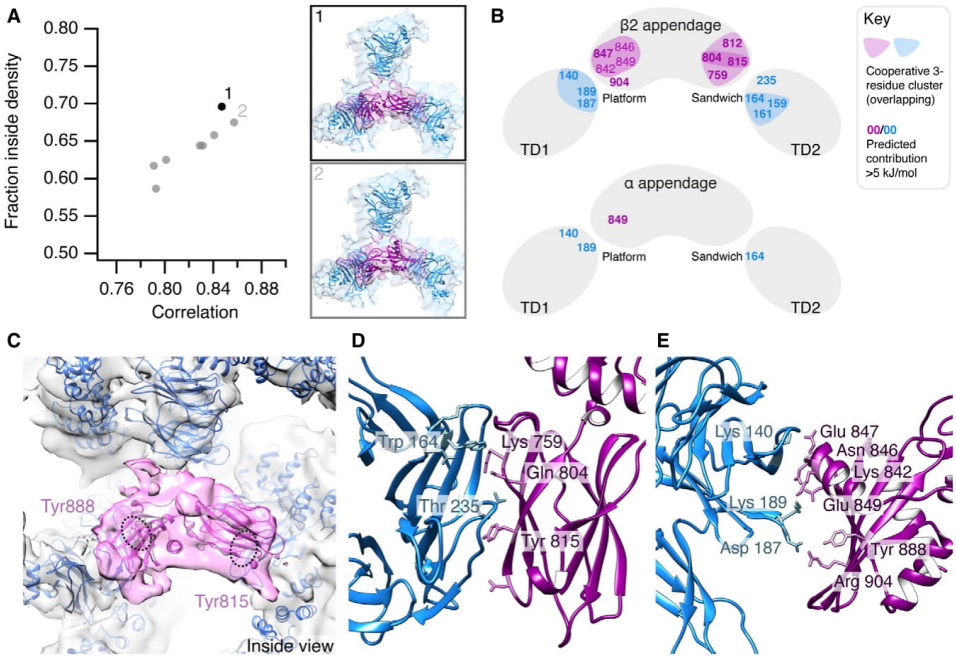

Figure 6. Orientation of β2-appendage with respect to clathrin terminal domains.

A Plot of fraction of atomic structure inside the cryo-EM density (Y-axis) versus correlation of fit (X-axis). The fit with the largest fraction inside density is shown in black. Although it had the second highest correlation value, this orientation yielded the highest hit-rate in the rigid body fitting, accounting for 34% of possible fits calculated. Two possible orientations (panels 1 and 2) of the β2-appendage were determined through rigid body fitting of the atomic structure of Owen *et al*, PDB 1E42 into the P-P minicoat hub volume from class 15.

B Diagrammatic summary of the analysis of binding interfaces using BudeAlaScan (BAlaS). Full results are given in Table 1.

C The selected best fit of the β2-appendage (purple) is shown in the context of the surrounding clathrin legs (Model in blue, density in grey). The atomic structures of Tyr 815 and Tyr 888 are displayed and highlighted in dashed ellipses. In the orientation shown, Tyr 815 is obscured by the β-sheets of the β2-appendage.

D Predicted interface between terminal domain β-propeller (blue) and β2-appendage sandwich or side domain (purple) surrounding Tyr 815.

E Predicted interface between terminal domain β-propeller (blue) and β2-appendage platform or top domain (purple) surrounding Tyr 888.

(Fig 2B and C; Wood *et al*, 2017). Consistent with these results, Tyr 815 and Tyr 888 are conserved in β2 and β1 but missing in β3 (Fig EV5A–D).

Deletion of the clathrin-box motif (ΔCBM) or mutation of Tyr 815 to alanine (Y815A) impaired the ability of FKBP-β2HA-GFP to generate endocytic vesicles (Fig 7A and B). Mutation of Tyr 888 to valine (Y888V), a mutation previously reported to reduce clathrin binding (Schmid *et al*, 2006) had no measurable effect on hot-wiring (Fig 7B). Moreover, the Y888V mutation had no additional effect when combined with ΔCBM, whereas the combination of ΔCBM and Y815A completely ablated hot-wiring (Fig 7B).

These results suggest that functional clathrin-β2HA interactions depend on the clathrin-box motif in the hinge and the sandwich site of the β2 appendage (centred on Tyr 815) while the role of the platform site of the β2 appendage (centred on Tyr 888) is undetectable in this assay.

Discussion

In this paper, we describe two positions in the clathrin cage where β2-appendage binds in the assembled state. These occur within the same sample, demonstrating that multi-modal binding is a fundamental property of clathrin-AP2 interactions. Our functional analysis demonstrated that endocytosis depends on two interactions between β2HA and clathrin. Together these observations provide an explanation for how AP2 drives coated vesicle formation in cells.

Our observation that β2HA can bind in multiple positions on clathrin within the same sample casts a new perspective on the apparently contradictory observations of Kovtun *et al* (2020) and Paraan *et al* (2020), suggesting they instead form part of a wider spectrum of possible β-appendage binding modes. We have summarized these multi-modal clathrin-β2HA interactions in Fig 8. The first location (Class 15) is between two of the three terminal

Table 1. Analysis of binding interfaces using BudeAlaScan (BAlaS): alanine scanning.

Protein	Appendage Residue	ΔΔG (kJ mol^{-1})	Appendage Subdomain	TD Residue	ΔΔG (kJ mol^{-1})	Appendage Subdomain, Terminal Domain (TD)
β2 appendage	Tyr 815	14.4	815 sandwich	Thr 235	7.0	815 sandwich, TD chain Y
	Lys 759	6.4	815 sandwich	Trp 164	6.9	815 sandwich, TD chain Y
	Asp 812	5.9	815 sandwich			
	Gln 804	5.1	815 sandwich			
	Glu 847	7.2	888 platform	Lys 140	7.7	888 platform, TD chain Z
	Arg 904	5.8	888 platform	Asp 187	5.7	888 platform, TD chain Z
				Lys 189	5.7	888 platform, TD chain Z
Control. α appendage mapped onto 815 sandwich domain	Glu 849	7.2	888 platform	Trp 164	6.9	815 sandwich, TD chain Y
				Lys 140	7.0	888 platform, TD chain Z
				Lys 189	6.0	888 platform, TD chain Z
Control. α appendage mapped onto 888 platform domain	Glu 849	6.1	888 platform	Lys 189	5.5	888 platform, TD chain Z

Table 2. Analysis of binding interfaces using BAlaS: constellation analysis for ΔΔG = 3kJ mol^{-1}.

Protein	Constellation	Constellation ΔΔG (kJ mol^{-1})	Summed Individual ΔΔGs (kJ mol^{-1})	Cooperativity (kJ mol^{-1})
β2 appendage (β2-TD)	B759_B804_B815	9.7	25.8	−16.2
	B804_B812_B815	14.1	25.3	−11.2
	B842_B846_B847	3.8	15.1	−11.3
	B842_B846_B849	−2.4	12.3	−14.7
	B842_B847_B849	1.5	15.2	−13.6
	B846_B847_B849	2.3	16.1	−13.8
TD (β2-TD)	Y159_Y161_Y164	−1.4	14.7	−16.1
	Z140_Z187_Z189	3.7	19	−15.3
α (α mapped onto 815 sandwich domain)	A761_A763	−15.1	7.7	−22.8
TD (α mapped onto 815 sandwich domain)	Y161_Y164	−13.8	10	−23.8
	Z140_Z189	−8.9	13	−21.9
(α mapped onto 888 platform domain)	n.a.	n.a.	n.a.	n.a.

domains that sit directly beneath the vertex. The second location (Class 18) that we identified is above the terminal domain and maps closely to the location identified by Kovtun *et al*, where the appendage faces CHC repeat 2 from one triskelion and CHC repeat 1 of another. The third location, described by Paraan *et al* is analogous to our Class 15 in that two terminal domains are linked, but they are adjacent domains within a hexagonal face rather than being beneath a cage vertex (Fig 8A and B). A common feature of all three modes is the potential for β2HA to cross-link clathrin triskelia.

In the first and third modes, the sandwich site and platform site of the β2-appendage are positioned to make interactions with two distinct terminal domains. Whereas in the second mode, according to the best fit of the β2-appendage reported by Kovtun *et al* (2020), neither site faces clathrin; although we note that the second highest scoring fit would place the platform site in apposition to CHC repeat 2. This region contains Cys 682 and Gly 710, previously identified as important for binding β2- and GGA-appendages (Knuehl *et al*, 2006).

In comparing our results with those of Kovtun *et al* and Paraan *et al*, we see that differing sample conditions such as inclusion of membrane and cargo (Kovtun *et al*, 2020) or use of coated vesicles purified from source (Paraan *et al*, 2020) do not explain differences in β-appendage binding location since in our study with only two purified protein components we see multiple binding locations that

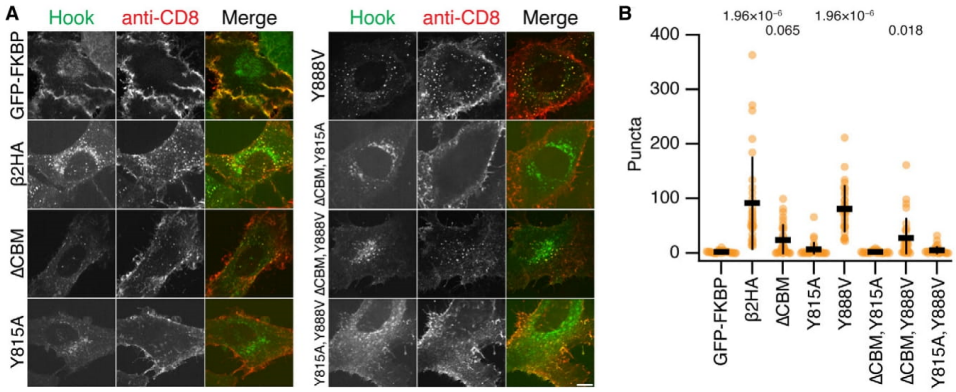

Figure 7. Functional test of importance of Tyr 815 and Tyr 888 to CCV formation.

A Representative confocal micrographs of cells expressing the plasma membrane anchor (CD8-mCherry-FRB) and the indicated hooks (green). Cells were incubated with anti-CD8-Alexa647 (red) and treated with rapamycin (200 nM, 15 min). Vesicles coinciding in both green and red channels (yellow in merge) were quantified in B. Scale bar, 10 μm.

B Scatter dot plot shows the number of intracellular GFP-positive vesicles that contained anti-CD8 Alexa647 per cell, bars indicate mean ± SD. *P*-values from Dunnett's *post hoc* test that were <0.1 are shown above. Note that these results are from the same experimental series as Fig 1 and that the negative and positive control data (GFP-FKBP and FKBP-β2HA-GFP) are as in Fig 1.

either confirm (Kovtun *et al*, 2020) or are similar to (Paraan *et al*, 2020) those seen in more complex systems. One interpretation of this is that the long linker domain on β2-adaptin permits the β-appendage to move freely, even within a coated vesicle, and form stable interactions unencumbered by the need for additional components or a specific orientation. Further structural and functional studies in systems that more closely reflect the physiological environment will be needed to confirm this.

The location of the β2-hinge is unknown in all three modes of binding. The clathrin-box motif in the hinge has been shown to interact as an extended peptide slotted between blades 1 and 2 or between blades 4 and 5 of the beta-propeller at clathrin heavy chain's N-terminal domain (ter Haar *et al*, 2000; Zhuo *et al*, 2015; Muenzner *et al*, 2017). At the current resolution, density relating to a peptide in such an extended conformation would be very hard to distinguish, and the promiscuous nature of clathrin-box motif binding reduces the observable density further. However, we know that the interaction of this motif is essential for coated vesicle formation possibly because it is involved in initial clathrin recruitment. Assuming that it maintains contact with the terminal domain as the coat forms, all three modes of binding allow for β2HA to make contact with clathrin heavy chains from up to three distinct triskelia.

Our hot-wiring results indicate that for endocytosis to proceed, the two most important sites on β2HA are the sandwich site and the clathrin-box motif in the hinge, with no detectable contribution from the platform site. Previous biochemical experiments investigated the importance of Tyr 815 in the sandwich site and Tyr 888 in the platform site in the interaction of β2HA with clathrin (Owen *et al*, 2000; Edeling *et al*, 2006; Schmid *et al*, 2006). Owen *et al* (2000) and Schmid *et al* (2006) showed a significant effect on clathrin binding to the β-appendage and hinge when Tyr 888 was altered to Val. In experiments where Tyr 815 was altered to Ala, Edeling *et al* (2006) showed that the effect on clathrin binding was most apparent when the hinge region was either absent, or the clathrin-binding motif within the hinge was deleted or mutated. While these experiments used brain extract for binding, where indirect interactions via other proteins known to bind both clathrin and β2HA remain a possibility, they nonetheless support our conclusion that the sandwich site, in partnership with the CBM domain within the β-adaptin hinge, is required for clathrin polymerization in functional coat formation. Our *in silico* analysis indicates that, in one mode, the platform site of β2HA does make contact with the terminal domain, and that two pairs of salt bridges (Lys140/Glu847 and Asp187/Arg904) may stabilise this interaction. We interpret our hot-wiring results to mean that this contact occurs only after binding of the hinge and the sandwich site. Further studies testing the effect of mutagenesis at this interface would help determine whether clathrin binding at this site is of functional importance. Such a cooperative role would allow interaction with other adaptor and accessory proteins such as epsin, β-arrestin and ARH at the platform domain (Schmid *et al*, 2006), creating flexibility to recruit the additional cargo associated with these adaptors to the growing vesicle.

All available data thus suggest that the β2 subunit of AP2 has a dual function in first recruiting clathrin to the membrane and then driving coated vesicle formation by promoting clathrin polymerization. The alternative model, where β2 only recruits clathrin and clathrin self-assembles in the absence of contribution of the adaptors, is highly unlikely. First, a single clathrin-box motif, which is sufficient to bind clathrin *in vitro* is not sufficient to induce coated vesicle formation in the hot-wiring assay. Second, under the alternative model, the requirement for the appendage in addition to the

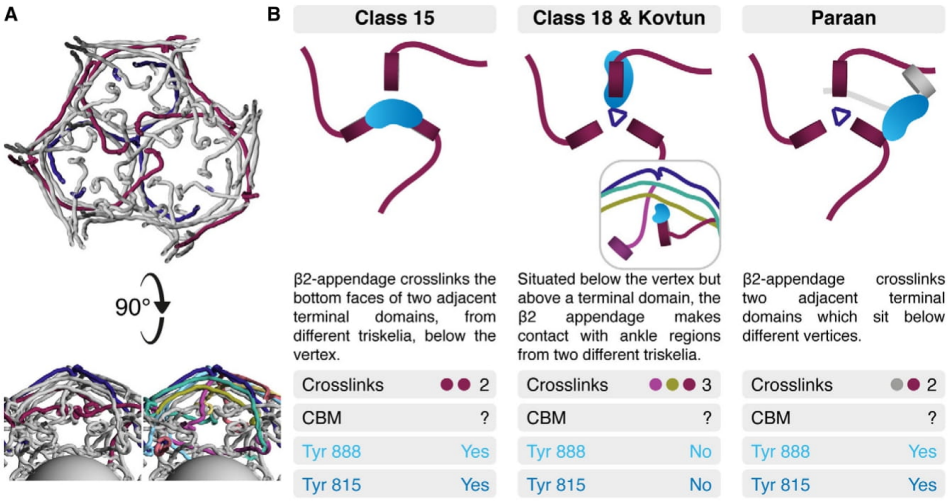

Figure 8. Summary of multi-modal clathrin-β2HA interactions.

A For orientation, an indigo triskelion and the three NTDs situated below its vertex are shown, contributed by maroon-coloured triskelia (viewed from the vesicle, towards the vertex). A "side view" with the same colouring and with alternative colouring (also used in panel B) where the six triskelia that interact with the indigo triskelion are depicted (below).

B Three modes of binding reported in this study and in two recent studies (Kovtun *et al*, 2020; Paraan *et al*, 2020). Common and contrasting features of each binding mode are shown. The inset in Class 18 & Kovtun shows the side view from A. Each panel indicates the number of cross-links, whether CBM density was observed and whether Tyr 888 and Tyr815 are in an orientation likely to bind to the terminal domain.

hinge would mean that both interactions must occur on one triskelion exclusively. The multiple modes of binding described from cryo-EM data all feature triskelia cross-linking and therefore make this model improbable.

The multi-modal nature of β2HA-clathrin interactions that cross-link triskelia raise the question of whether other adaptors have the same property. Alternative adaptors such as epsin, β-arrestin and AP180 have multiple motifs that interact with clathrin or with AP2 (Traub, 2009; Smith *et al*, 2017). This suggests that they may also be able to contribute to initial recruitment and to cross-linking during assembly. In the case of epsin, the linear unstructured domain alone is capable of forming coated pits *in vitro* (Dannhauser & Ungewickell, 2012) and forming vesicles in cells using hot-wired endocytosis (Wood *et al*, 2017). The interpretation of these experiments was simply that epsin recruited clathrin and then clathrin self-assembled into a cage. It is possible that this region of epsin may also cross-link triskelia and thereby contribute to coat formation. If this is the case, it suggests a mechanism whereby adaptor proteins included in a growing coat can enhance clathrin polymerization and thereby stabilize, or even accelerate, coated vesicle formation. Since epsin, β-arrestin and AP180 also bring cargo to the growing vesicle, this has implications for understanding how particular cargos may, through their associated adaptor, increase the likelihood of completion of a growing vesicle and consequently drive forward their own internalization.

Materials and Methods

Molecular biology

The hinge and appendage of the human β2 subunit of the AP2 complex (designated β2HA), corresponding to residues 616–951 of the long isoform, was used for all experiments. Numbering of residues in the appendage is after the structure of β2-appendage which uses the numbering of the shorter isoform, ending at residue 937 (Owen *et al*, 2000).

CD8-mCherry-FRB, FKBP-β2HA-GFP, FKBP-β3HA-GFP, FKBP-β2HA(Y815A)-GFP, FKBP-β2HA(ΔCBM)-GFP and FKBP-β2HA (ΔCBM,Y815A)-GFP were described previously (Wood *et al*, 2017). The Y888V mutation was added by site-directed mutagenesis to FKBP-β2HA-GFP, FKBP-β2HA(Y815A)-GFP and FKBP-β2HA (ΔCBM)-GFP. FKBP-β2H-GFP was made by substituting β2-hinge (616–704) in place of β2HA in FKBP-β2HA-GFP using BamHI and AgeI. Similarly, FKBP-β3H-GFP was made by substituting β3-hinge (702–859) in FKBP-β3HA-GFP using PspOMI and AgeI. FKBP-β2Hβ3A-GFP was made by inserting the β3-appendage (860–1,094) into FKBP-β2A-GFP via SalI and NotI. FKBP-β3Hβ2A-GFP was made by inserting the β2-appendage (705–951) into FKBP-β3 hinge-GFP via SalI and NotI. Plasmid to express GST-β2HA in bacteria was available from previous work (Hood *et al*, 2013).

Cell culture and light microscopy

HeLa cells (Health Protection Agency/European Collection of Authenticated Cell Cultures, #93021013) were kept in DMEM supplemented with 10% FBS and 100 U ml^{-1} penicillin/streptomycin at 37°C and 5% CO_2. DNA transfection was performed with Genejuice (Merck Millipore) using the manufacturer's protocol. HeLa cells were transfected with CD8-mCherry-FRB and one of the hooks (GFP-FKBP, FKBP-β2HA-GFP, FKBP-β3HA-GFP, FKBP-β2H-GFP, FKBP-β3H-GFP, FKBP-β2Hβ3A-GFP, FKBP-β3Hβ2A-GFP, FKBP-β2HA(ΔCBM)-GFP, FKBP-β2 HA(Y815A)-GFP, FKBP-β2HA (Y888V)-GFP, FKBP-β2HA(ΔCBM,Y815A)-GFP, FKBP-β2HA(ΔCBM, Y888V)-GFP or FKBP-β2HA(Y815A,Y888V)-GFP).

After 24 h, the cells were put on coverslips. The next day, surface CD8 was labelled with 10 μg ml^{-1} AlexaFluor647-anti-CD8 antibody (Bio-Rad, MCA1226A647) at 37°C for 5 min. To induce dimerization of the hook to the CD8, the medium was changed for DMEM with 200 nm rapamycin (Alfa Aesar) for 15 min at 37°C. The cells were then fixed with fixation buffer (4% formaldehyde, 4% sucrose, 80 mM K-PIPES, 5 mM EGTA, 2 mM $MgCl_2$, pH 6.8) for 10 min at RT. The coverslips were rinsed 4 × 5 min with PBS and mounted in Mowiol and DAPI.

Cells were imaged using a spinning disc confocal system (Ultraview Vox; PerkinElmer) with a 100× 1.4 NA oil-immersion objective. Images were captured in Volocity using a dual-camera system (ORCA-R2; Hamamatsu) after excitation with lasers of wavelength 488 and 640 nm.

Image analysis

The images acquired were duplicated and thresholded to isolate vesicular structures. To analyse only coinciding structures, thresholded images were multiplied with one another using the "Image calculator" plugin in FIJI and the vesicular structures measuring between 0.03 μm^2 and 0.8 μm^2 and of 0.3-1 circularity were counted in the resulting image using the "analyse particles" plugin. A one-way ANOVA with Dunnett's *post hoc* test was performed using GFP-FKBP as control.

Buffer compositions

HKM buffer: 25 mM HEPES pH 7.2, 125 mM potassium acetate, 5 mM magnesium acetate. Tris buffer: 1 M Tris pH 7.1, 1 mM EDTA, 1 mM DTT. Ficoll/Sucrose buffer: 6.3% w/v Ficoll PM 70, 6.3% w/v sucrose in HKM pH 7.2. Saturated ammonium sulphate: excess ammonium sulphate dissolved in 10 mM Tris pH 7, 0.1 mM EDTA. Polymerization buffer: 100 mM MES pH 6.4, 1.5 mM $MgCl_2$, 0.2 mM EGTA. Depolymerization buffer: 20 mM TEA pH 8.0, 1 mM EDTA, 1 mM DTT. Purification buffer: 20 mM HEPES pH 7.2, 200 mM NaCl. Elution buffer: 20 mM HEPES pH 7.0, 200 mM NaCl, 10 mM reduced glutathione. Prescission buffer: 50 mM tris–HCl pH 7.0, 150 mM NaCl, 1 mM EDTA, 1 mM DTT.

Protein expression and purification

Clathrin was purified from pig brain clathrin-coated vesicles (see detailed method in Rothnie *et al*, 2011 Supporting Information). Clathrin cages were assembled for harvesting by dialyzing the purified triskelia into polymerization buffer at 4°C and then harvested by ultracentrifugation. Pellets containing clathrin cages were resuspended in a small volume of polymerization buffer. Concentration of clathrin cages was assayed by A_{280} of triskelia to avoid the effects from light scattering.

β2HA was expressed as a GST-β2HA fusion protein in *Escherichia coli* strain, BL21. Bacteria were grown at 37°C to an OD_{600} of 0.6 and then induced with 0.8 mM IPTG at 20°C overnight. Cells were harvested and resuspended in purification buffer (supplemented with Complete Protease Inhibitor Cocktail tablet as per Roche Applied Science instructions) and lysed by sonication. The soluble fraction was obtained by centrifugation at 75,400 *g* for 30 min. GST-β2HA was purified from the soluble fraction using glutathione resin (GE Healthcare) and GST-β2HA was displaced from the glutathione resin using elution buffer. The GST tag was removed by a GST fusion 3C protease (Prescission, GE Healthcare) by dialysing GST-β2HA with GST fusion 3C protease, in prescission buffer, overnight at 4°C. The fusion protease was removed using glutathione resin and the cleaved β2HA was collected in the flow-through. Cleaved β2HA was concentrated and loaded onto a HiLoad Superdex 200 (equilibrated in purification buffer) for further purification via size exclusion chromatography. Fractions containing purified β2HA were pooled and concentrated on Vivaspin columns (Sartorius).

β2HA-clathrin complex preparation

To identify the maximum amount of β2HA that could bind the clathrin cages, increasing molar amounts of β2HA was reconstituted with 3 μM clathrin in depolymerization buffer at 4°C and subsequent dialysis overnight into polymerization buffer at 4°C. The β2HA-clathrin cage complexes were harvested by centrifugation at 230,000 *g* for 30 min and concentrated 10-fold by pellet resuspension into a small volume of polymerization buffer. The protein composition of the resuspended pellets was analysed by SDS–PAGE and densitometry in ImageJ (Schneider *et al*, 2012).

Negative stain transmission electron microscopy

Clathrin cages reconstituted in the presence of 180 μM β2HA were screened under negative stain. Assembled β2HA-clathrin cage complexes (5 μl of 1 μM) were pipetted onto a glow-discharged formvar carbon 300-mesh copper grid (Agar Scientific) and incubated for 1 min at room temperature. Excess sample was removed by blotting with Whatman filter paper and 5 μl of 1% (w/v) uranyl acetate stain was subsequently applied to the grid and left to incubate for 1 min at room temperature. Excess negative stain was removed by blotting with Whatman filter paper. Samples were imaged using a JEOL 2100Plus and Gatan OneView IS at 200 keV.

Cryo-electron microscopy

3 μl of β2HA clathrin cage complexes (clathrin at 9 μM) were applied to glow-discharged 300-mesh copper Quantifoil R1.2/1.3 grids and blotted at 4°C and > 90% humidity for 4.5 s before plunging into an ethane/propane mix (80%/20%) liquefied and cooled by liquid nitrogen using a Leica EM GP automated plunge freezing device.

Cryo-electron micrographs were collected as movies using a Titan Krios and Falcon III detector (Leicester Institute of Structural and Chemical Biology), operating at 300 keV. EPU was used for automated data collection, movies were acquired at a total dose of 64 e^{-} Å^{-2} over 1 s at a dose rate of 1.65 e^{-} Å^{-2} s^{-1} with a magnified pixel size of 1.39 Å px^{-1} using a 1 µm beam and 70 µm C2 aperture. Three images were acquired per hole with some illumination of the carbon support. Micrographs were targeted for collection between 1.1 and 2 µm defocus.

Data processing

Beam-induced motion of the specimen was anisotropically corrected, with and without dose-weighting, using MotionCor2 (Li *et al*, 2013). The contrast transfer function of the motion-corrected summed micrographs was estimated from non-dose-weighted micrographs using gctf v1.06 (Zhang, 2016) employing equiphase averaging and validation functions. RELION v3.0.5 (Scheres, 2012) was used for particle picking, extraction, and all classifications and refinements. 57,528 particles were manually picked from the non-dose-weighted, motion-corrected micrographs and then extracted at a binned pixel size of 10.8 Å px^{-1}. Reference-free 2D classification, over 25 iterations, was first used to analyse the quality of the extracted particles. The highest quality classes, containing 51,133 particles, were selected for further 3D classification. As previously described, supervised asymmetric 3D classification successfully sorted the particles into ten structural classes (Morris *et al*, 2019). The particles associated with the minicoat cage type, which produced the highest quality 3D classification output, were selected for subsequent hierarchical, supervised 3D classifications to identify the particles most stably associated with this particular cage geometry (Appendix Fig S1). Further unsupervised 3D classification of these stable minicoat particles subdivided the particles into 3 classes and was carried out using a regularization parameter (*T*) of 4, no imposed symmetry and no mask (Appendix Fig S2). 3D auto refinement of the most stable minicoat particles (at 10.8 Å px^{-1}, without symmetry imposed) yielded a 24 Å minicoat volume. These particles were reextracted from non-dose-weighted micrographs with a box size of 500 px and a pixel size of 2.78 Å px^{-1}; large enough to include clathrin cages over 1,000 Å diameter. The minicoat cage architecture was refined at 2.78 Å px^{-1} (i.e. binned twofold) without imposing symmetry. The refinement reference (from the previous 3D auto refinement of minicoat particles) was low pass filtered to 40 Å. Since the output volume was a minicoat with mixed handedness, an unsupervised 3D classification was conducted on the minicoat particles (no symmetry imposed, and no alignment of particles). Only the minicoat particles contributing to volumes that had 100% surface density were saved and used in subsequent processing. These particles were refined as described for the previous 3D auto refinement, and yielded a 11.7 Å volume. A mask was generated from this C_1 reconstruction at 3σ, extended and softened by 2 and 9 px. This mask was employed in subsequent C_1 refinements that used dose-weighted minicoat particles, solvent flattening and a Gaussian noise background. Reconstructions with and without imposed symmetry correlated well.

Resolution of each reconstruction was estimated using the gold standard Fourier shell correlation (FSC) measurement within a mask created from the refinement volume (using threshold value of 3σ, expanded by 2 px to 4 px and softened by 9 px). The MTF of the Falcon III camera (operated at 300 keV) was applied and the B factor of the map was automatically calculated if the resolution exceeded 10 Å. In instances, where sub-10 Å refinements were calculated, a user-defined B factor value was given.

In order to identify β2HA in the minicoat volume we subtracted the signal contributed by the outer coat region and subsequently conducted a masked, unsupervised 3D classification on the signal-subtracted inner cage region (Appendix Fig S4) with a regularization parameter (*T*) of 20 tetrahedral (T) symmetry imposed and no alignment of particles calculated. The mask was created from the tetrahedral refinement volume using a threshold value of 3σ, expanded by 5 px and softened by 9 px. The particles contributing to each of the 20 classes were saved separately and refined with *T* symmetry imposed. Qualitative analysis of the individual refinement outputs (visualized at contour level 3σ), identified two classes that possessed strong additional density that was not present in reconstructions calculated using signal from the whole cage (i.e. prior to signal subtraction) *or* in a minicoat cage volume reconstructed *without* adaptor protein present.

Localized subparticle extraction and reconstruction

To improve the resolution of the strong additional density resolved after masked 3D classifications of signal-subtracted minicoat particles, we performed localized reconstruction (Ilca *et al*, 2015) as previously described for single particle data sets of clathrin cages (Morris *et al*, 2019). Hub regions were extracted and recentred as new subparticles in 350 px boxes from whole minicoat cage particles. Each of the extracted hub subparticles were reconstructed separately to serve as references in subsequent refinements.

All refinements were conducted in C_1 with masking applied from a 3σ extended 2 px and softened 9 px mask (3σ/e2/s9). Global resolution of the hub region was estimated as described previously using the gold standard FSC approach (within a mask 3σ/e2/s9). The refinement was found to have converged at 9.6 Å. Local resolution estimations were made using ResMap (Kucukelbir *et al*, 2014) revealing lower resolutions in the terminal domain regions of the minicoat hub. To improve the quality of the β2HA density located between the terminal domains under the hub vertex, the hub subparticles were classified based on whether the β2HA density connected terminal domains from two separate pentagonal faces (PP) or connected a hexagonal and pentagonal face (HP). Compared to the whole-cage volume (post-signal subtraction), the resolution of the β2HA (and neighbouring clathrin heavy chain regions) is improved, allowing PDBs of the clathrin heavy chain (residues 1–361, 362–487 and 488–834) to be fitted into the hub volume.

Global difference analysis

Student's *t*-test was used to determine the significance of differences between two structures, using SPIDER and the programmes of Milligan and Flicker as previously published (Milligan & Flicker, 1987; Frank *et al*, 1996; Young *et al*, 2013). In order to do this, independent maps of each structure (four in the case of whole cages, three for the hubs) were created using RELION. The -split command in the relion_star_handler script was used to divide the data into separate sets, taking care to distribute images of particles evenly from each micrograph and therefore the defocus spread. A low pass Fourier filter, 11 Å in the case of whole cages and 12 Å for the hubs,

was applied to the maps. In order to avoid potential false differences due to variations in the quality of the two structures solved, or random effects such as the sampling of defocus values, the two structures were scaled together in reciprocal space by calculating their radial amplitude-profiles. A reciprocal-space scaling profile was calculated by comparing the amplitude profile of the clathrin-only map with the β-adaptin map (Young *et al*, 2013). Using this, all the β-adaptin sub-maps were rescaled to fit the profile of the clathrin-only map. These maps were used to calculate an average and variance for each structure. The per voxel value of t and the significance of differences was computed from these, using the appropriate degrees of freedom. Many regions had significant differences with $P < 0.05$. Regions we have interpreted to show direct density differences relating to ligand binding have $P < 0.0001$. The images show the original maps, with the value of P coloured onto the surface according to the scale shown.

Redocking the adaptor proteins

Initially, the β2-appendage protein structure (1E42) was docked by fitting into the unoccupied density in the β2HA-clathrin map. However, this led to an overlap of residues between the C-terminal domain and its neighbouring terminal domain, while leaving a gap at the putative interface between the N-terminal domain and a second local terminal domain. The docking programme BUDE (McIntosh-Smith *et al*, 2012, 2015) was used to refine this structure as follows. The complex was centred on the centre-of-coordinates of the β2-appendage and the complex split into clathrin as the receptor and β2-appendage as the ligand. The docking grid was defined: −10 to 10 in 2° increments for rotation and −10 to 10 in 1 Å increments for translation. A genetic algorithm, EMC (Abraham *et al*, 2015), sampling 1.1 million poses was used to find low energy poses.

The best pose was inspected and new rotamers chosen for a few interfacial sidechains to optimize putative interfacial interactions (β2-appendage: R732, R759, N846, E849, E882; clathrin: R188) and the above docking procedure repeated. Next, Gromacs 2019.4 (Abraham *et al*, 2015) was used to parameterize the complex with the Amber99SB-ildn (Lindorff-Larsen *et al*, 2010) forcefield at pH 7 and place it in box of TIP3P water containing 0.15 m NaCl. A short energy minimization (200 steps of steepest descents) was performed to remove bad intermolecular atom-atom contacts, permitted by BUDE's very soft empirical free energy forcefield, and yield the finished model.

The initial α-appendage complex was prepared by superimposing the α-appendage (1B9K) on the β2-appendage C-terminal domain of the finished complex. This preliminary model of the α-appendage complex was subjected to the same docking and minimization procedure described above. Because the angle between the platform and sandwich domains of the α-appendage is smaller, we also prepared complexes where either the platform or sandwich domain of the α-appendage (1B9K) were directly superimposed onto the corresponding region of the β2-appendage domain of the finished complex using the Matchmaker function in UCSF Chimera.

In silico alanine scanning

The two energy-minimized complexes and the individual platform and sandwich domain α-appendage complexes were presented to the BAlaS server http://balas.app (Wood *et al*, 2020). The three clathrin domains were assigned as the receptor and the appendages (either β2 or α) as the ligand. Alanine scanning and constellation calculations were performed and the results downloaded.

Figure preparation

Maps and models were visualized using UCSF Chimera (Pettersen *et al*, 2004). Simplified views of triskelia were generated using IgorPDB and 3IYV. Microscopy figures and plots were made Fiji and Igor Pro (WaveMetrics Inc.). All figures were assembled in Adobe Illustrator.

Data availability

EM maps supporting this study have been deposited in the Electron Microscopy Data Bank with accession codes EMD-12980, EMD-12981, EMD-12983 and EMD-12984 (relating to Figs 4B and C, 4A, 3 and 5, respectively). Particle stacks associated with EMD-12980, EMD-12983 and EMD-12984 were deposited to EMPIAR as 10784, 10779 and 10783, respectively. The fitted model of clathrin terminal domains and β2-appendage has been deposited in the protein data bank as 7OM8.pdb. Original models of both the clathrin terminal domain [1BPO.pdb, (ter Haar *et al*, 1998)] and β2-appendage [1E42.pdb, (Owen *et al*, 2000)] were used to generate the fitted model with only the interfaces between the protein molecules remodelled. No intermolecule clashes have been identified in the fitted model. The intramolecule clashes and geometric outliers are historical.

Expanded View for this article is available online.

Acknowledgements
SMS and CJS thank UKRI Biotechnology and Biological Sciences Research Council (BBSRC) for support (BB/N008391/1). CJS was a Royal Society Leverhulme Trust Senior Research Fellow. KMW is funded by MRC Doctoral Training Partnership grant MR/N014294/1. We acknowledge the Midlands Regional Cryo-EM Facility at the Leicester Institute of Structural and Chemical Biology (LISCB), major funding from MRC (MC_PC_17136) and thank Christos Savva and T. J. Ragan for assistance with data collection. Sample preparation and development was supported by Saskia Bakker, Warwick Advanced Bioimaging Research Technology Platform, using equipment funded by BBSRC ALERT14 award BB/M01228X/1 and MRC award reference MC_PC_17136. We thank Laura Wood and Miguel Hernández González for early work on this project.

Author contributions
SMS carried out structural biology experiments and contributed to the manuscript writing and figure preparation. GL conducted hot-wiring experiments contributed to the manuscript writing and figure preparation. KMW carried out structural biology experiments and contributed to the manuscript writing. KLM contributed to structural analysis and manuscript writing. AMR carried out structure comparisons and contributed to the manuscript writing. RBS carried out model building and contributed to the manuscript writing. SJR contributed to data interpretation, manuscript writing and figure preparation. CJS contributed to data interpretation, structural analysis and wrote the final draft, which was approved by all authors.

Conflict of interest
The authors declare that they have no conflict of interest.

References

Abraham MJ, Murtola T, Schulz R, Páll S, Smith JC, Hess B, Lindahl E (2015) GROMACS: high performance molecular simulations through multi-level parallelism from laptops to supercomputers. *SoftwareX* 1–2: 19–25

Bai X, Rajendra E, Yang G, Shi Y, Scheres SHW (2015) Sampling the conformational space of the catalytic subunit of human γ-secretase. *Elife* 4: e11182

Bucher D, Frey F, Sochacki KA, Kummer S, Bergeest J-P, Godinez WJ, Kräusslich H-G, Rohr K, Taraska JW, Schwarz US *et al* (2018) Clathrin-adaptor ratio and membrane tension regulate the flat-to-curved transition of the clathrin coat during endocytosis. *Nat Commun* 9: 1109

Burgess SG, Mukherjee M, Sabir S, Joseph N, Gutiérrez-Caballero C, Richards MW, Huguenin-Dezot N, Chin JW, Kennedy EJ, Pfuhl M *et al* (2018) Mitotic spindle association of TACC3 requires Aurora-A-dependent stabilization of a cryptic α-helix. *EMBO J* 37: e97902

Chen Z, Schmid SL (2020) Evolving models for assembling and shaping clathrin-coated pits. *J Cell Biol* 219: e202005126

Cocucci E, Aguet F, Boulant S, Kirchhausen T (2012) The first five seconds in the life of a clathrin-coated pit. *Cell* 150: 495–507

Dannhauser PN, Ungewickell EJ (2012) Reconstitution of clathrin-coated bud and vesicle formation with minimal components. *Nat Cell Biol* 14: 634–639

Dell'Angelica EC, Klumperman J, Stoorvogel W, Bonifacino JS (1998) Association of the AP-3 adaptor complex with clathrin. *Science* 280: 431–434

Edeling MA, Mishra SK, Keyel PA, Steinhauser AL, Collins BM, Roth R, Heuser JE, Owen DJ, Traub LM (2006) Molecular switches involving the AP-2 beta2 appendage regulate endocytic cargo selection and clathrin coat assembly. *Dev Cell* 10: 329–342

Fotin A, Cheng Y, Sliz P, Grigorieff N, Harrison SC, Kirchhausen T, Walz T (2004) Molecular model for a complete clathrin lattice from electron cryomicroscopy. *Nature* 432: 573–579

Frank J, Radermacher M, Penczek P, Zhu J, Li Y, Ladjadj M, Leith A (1996) SPIDER and WEB: processing and visualization of images in 3D electron microscopy and related fields. *J Struct Biol* 116: 190–199

Gallusser A, Kirchhausen T (1993) The beta 1 and beta 2 subunits of the AP complexes are the clathrin coat assembly components. *EMBO J* 12: 5237–5244

ter Haar E, Harrison SC, Kirchhausen T (2000) Peptide-in-groove interactions link target proteins to the beta-propeller of clathrin. *Proc Natl Acad Sci USA* 97: 1096–1100

ter Haar E, Musacchio A, Harrison SC, Kirchhausen T (1998) Atomic structure of clathrin. *Cell* 95: 563–573

Hood FE, Williams SJ, Burgess SG, Richards MW, Roth D, Straube A, Pfuhl M, Bayliss R, Royle SJ (2013) Coordination of adjacent domains mediates TACC3-ch-TOG-clathrin assembly and mitotic spindle binding. *J Cell Biol* 202: 463–478

Ibarra AA, Bartlett GJ, Hegedüs Z, Dutt S, Hobor F, Horner KA, Hetherington K, Spence K, Nelson A, Edwards TA *et al* (2019) Predicting and experimentally validating hot-spot residues at protein-protein interfaces. *ACS Chem Biol* 14: 2252–2263

Ilca SL, Kotecha A, Sun X, Poranen MM, Stuart DI, Huiskonen JT (2015) Localized reconstruction of subunits from electron cryomicroscopy images of macromolecular complexes. *Nat Commun* 6: 8843

Joseph AP, Malhotra S, Burnley T, Wood C, Clare DK, Winn M, Topf M (2016) Refinement of atomic models in high resolution EM reconstructions using Flex-EM and local assessment. *Methods* 100: 42–49

Knuehl C, Chen C-Y, Manalo V, Hwang PK, Ota N, Brodsky FM (2006) Novel binding sites on clathrin and adaptors regulate distinct aspects of coat assembly. *Traffic* 7: 1688–1700

Kovtun O, Dickson VK, Kelly BT, Owen DJ, Briggs JAG (2020) Architecture of the AP2/clathrin coat on the membranes of clathrin-coated vesicles. *Sci Adv* 6: eaba8381

Kucukelbir A, Sigworth FJ, Tagare HD (2014) Quantifying the local resolution of cryo-EM density maps. *Nat Methods* 11: 63–65

Li X, Mooney P, Zheng S, Booth CR, Braunfeld MB, Gubbens S, Agard DA, Cheng Y (2013) Electron counting and beam-induced motion correction enable near-atomic-resolution single-particle cryo-EM. *Nat Methods* 10: 584–590

Lindorff-Larsen K, Piana S, Palmo K, Maragakis P, Klepeis JL, Dror RO, Shaw DE (2010) Improved side-chain torsion potentials for the Amber ff99SB protein force field. *Proteins* 78: 1950–1958

Lundmark R, Carlsson SR (2002) The beta-appendages of the four adaptor-protein (AP) complexes: structure and binding properties, and identification of sorting nexin 9 as an accessory protein to AP-2. *Biochem J* 362: 597–607

McIntosh-Smith S, Price J, Sessions RB, Ibarra AA (2015) High performance in silico virtual drug screening on many-core processors. *Int J High Perform Comput Appl* 29: 119–134

McIntosh-Smith S, Wilson T, Ibarra AA, Crisp J, Sessions RB (2012) Benchmarking energy efficiency, power costs and carbon emissions on heterogeneous systems. *Comput J* 55: 192–205

Mettlen M, Chen P-H, Srinivasan S, Danuser G, Schmid SL (2018) Regulation of clathrin-mediated endocytosis. *Annu Rev Biochem* 87: 871–896

Milligan RA, Flicker PF (1987) Structural relationships of actin, myosin, and tropomyosin revealed by cryo-electron microscopy. *J Cell Biol* 105: 29–39

Morris KL, Jones JR, Halebian M, Wu S, Baker M, Armache J-P, Avila Ibarra A, Sessions RB, Cameron AD, Cheng Y *et al* (2019) Cryo-EM of multiple cage architectures reveals a universal mode of clathrin self-assembly. *Nat Struct Mol Biol* 26: 890–898

Muenzner J, Traub LM, Kelly BT, Graham SC (2017) Cellular and viral peptides bind multiple sites on the N-terminal domain of clathrin. *Traffic* 18: 44–57

Owen DJ, Vallis Y, Pearse BM, McMahon HT, Evans PR (2000) The structure and function of the beta 2-adaptin appendage domain. *EMBO J* 19: 4216–4227

Paraan M, Mendez J, Sharum S, Kurtin D, He H, Stagg SM (2020) The structures of natively assembled clathrin-coated vesicles. *Sci Adv* 6: eaba8397

Pearse BM, Robinson MS (1984) Purification and properties of 100-kd proteins from coated vesicles and their reconstitution with clathrin. *EMBO J* 3: 1951–1957

Pettersen EF, Goddard TD, Huang CC, Couch GS, Greenblatt DM, Meng EC, Ferrin TE (2004) UCSF Chimera–a visualization system for exploratory research and analysis. *J Comput Chem* 25: 1605–1612

Rothnie A, Clarke AR, Kuzmic P, Cameron A, Smith CJ (2011) A sequential mechanism for clathrin cage disassembly by 70-kDa heat-shock cognate protein (Hsc70) and auxilin. *Proc Natl Acad Sci USA* 108: 6927–6932

Scheres SHW (2012) RELION: implementation of a Bayesian approach to cryo-EM structure determination. *J Struct Biol* 180: 519–530

Schmid EM, Ford MGJ, Burtey A, Praefcke GJK, Peak-Chew S-Y, Mills IG, Benmerah A, McMahon HT (2006) Role of the AP2 beta-appendage hub in recruiting partners for clathrin-coated vesicle assembly. *PLoS Biol* 4: e262

Schneider CA, Rasband WS, Eliceiri KW (2012) NIH Image to ImageJ: 25 years of image analysis. *Nat Methods* 9: 671–675

Shih W, Gallusser A, Kirchhausen T (1995) A clathrin-binding site in the hinge of the beta 2 chain of mammalian AP-2 complexes. *J Biol Chem* 270: 31083 – 31090

Smith SM, Baker M, Halebian M, Smith CJ (2017) Weak molecular interactions in clathrin-mediated endocytosis. *Front Mol Biosci* 4: 72

Topf M, Lasker K, Webb B, Wolfson H, Chiu W, Sali A (2008) Protein structure fitting and refinement guided by cryo-EM density. *Structure* 16: 295 – 307

Traub LM (2009) Tickets to ride: selecting cargo for clathrin-regulated internalization. *Nat Rev Mol Cell Biol* 10: 583 – 596

Willox AK, Royle SJ (2012) Functional analysis of interaction sites on the N-terminal domain of clathrin heavy chain. *Traffic* 13: 70 – 81

Wood CW, Ibarra AA, Bartlett GJ, Wilson AJ, Woolfson DN, Sessions RB (2020) BAlaS: fast, interactive and accessible computational alanine-scanning using BudeAlaScan. *Bioinformatics* 36: 2917 – 2919

Wood LA, Larocque G, Clarke NI, Sarkar S, Royle SJ (2017) New tools for 'hot-wiring' clathrin-mediated endocytosis with temporal and spatial precision. *J Cell Biol* 216: 4351 – 4365

Young A, Stoilova-McPhie S, Rothnie A, Vallis Y, Harvey-Smith P, Ranson N, Kent H, Brodsky FM, Pearse BMF, Roseman A *et al* (2013) Hsc70-induced changes in clathrin-auxilin cage structure suggest a role for clathrin light chains in cage disassembly. *Traffic* 14: 987 – 996

Zaremba S, Keen JH (1983) Assembly polypeptides from coated vesicles mediate reassembly of unique clathrin coats. *J Cell Biol* 97: 1339 – 1347

Zhang K (2016) Gctf: Real-time CTF determination and correction. *J Struct Biol* 193: 1 – 12

Zhuo Y, Cano KE, Wang L, Ilangovan U, Hinck AP, Sousa R, Lafer EM (2015) Nuclear magnetic resonance structural mapping reveals promiscuous interactions between clathrin-box motif sequences and the N-terminal domain of the clathrin heavy chain. *Biochemistry* 54: 2571 – 2580